Imperial College London
Imperial College of Science, Technology and Medicine
Department of Aeronautics

Influence of coherent structures on the near- and far-field evolution of an axisymmetric turbulent jet

Massimiliano Breda

Submitted in part fulfilment of the requirements for the degree of
Doctor of Philosophy

October 2018

I hereby declare that this thesis, and the research it refers to, are entirely my own work and has not been submitted for any other award. Where other sources of information have been used, they have been acknowledged and fully referenced.

Mr Massimiliano Breda

London (United Kingdom)

October 2018

Copyright Declaration

The copyright of this thesis rests with the author and is made available under a Creative Commons Attribution Non-Commercial No Derivatives licence. Researchers are free to copy, distribute or transmit the thesis on the condition that they attribute it, that they do not use it for commercial purposes and that they do not alter, transform or build upon it. For any reuse or redistribution, researchers must make clear to others the licence terms of this work.

‘Passi tutto il tempo alla ricerca di qualcosa ma forse cercavi qualcuno che ti facesse conoscere te stesso’

(April 2018)

‘Secondo me i giovani devono partire, devono andar via, ma per curiosità e non per disperazione. E poi devono tornare. I giovani devono andare per capire com’è il resto del mondo, ma anche per un’altra cosa, ancora più importante, per capire se stessi.‘

Renzo Piano (August 2013)

Abstract

The role of the initial conditions in affecting the near field and the evolution of an axisymmetric turbulent jet towards the far field is examined. The jet's near-field coherent structures are manipulated with the aid of noncircular geometries of identical open area D_e^2, including a square and fractal exit, for comparison with a classical round orifice. The flow is studied between 0 and $26D_e$ with the aid of planar particle image velocimetry (PIV), hot-wire anemometry and tomographic PIV. This study shows that the fractal orifice significantly changes the near-field properties of the jet, breaking-up the coherent structures and affects the entrainment of background (quiescent) fluid into the turbulent stream. Despite the different state of coherence, it is found that many of the jet's turbulent characteristics scale with the number of eddy turnover times rather than simply the streamwise coordinates.

Investigating the jet's evolution towards the self-similar state, the presence of non-equilibrium dissipation was found for all jets studied, concurrent to self-similar scalings for mean velocity and Reynolds stresses.

The thesis is concluded by analysing the turbulent/non-turbulent interface (TNTI) and the fine scales of round and fractal jets at various streamwise locations. In the near field, the exit geometry appears to primarily impact on the inner interface, separating the laminar core from the turbulent stream, rather than the outer interface between the jet and the background fluid. Moreover, analysing the fine scales of the flow, the presence of two interfaces in the near field constrains the development of the turbulent properties and the jets appear as if only "local" strain was present. Finally, the evolution of the jet properties and of the small scales of the flow from the TNTI towards the turbulent bulk is examined, which suggests that the TNTI has a thickness of one longitudinal Taylor lenghtscale λ_f.

Acknowledgements

I would like to express my gratitude to my supervisor Dr Oliver R. H. Buxton for giving me the opportunity to be here and giving me guidance during this work, whilst leaving me enough freedom to take many independent decisions and to work autonomously. Moreover, he has supported many travels to conferences, which proved meaningful in terms of quality of the talks, the attendees and locations. I will never forget my experiences in Bertinoro (Italy), Seville (Spain), Chicago (USA) and Busan (South Korea). I would like to thank also Dr Gioacchino Cafiero. His teaching and counselling on the tomographic PIV technique has been invaluable, as much as the fun times outside the university. I would like to thank also the technicians that supported me in my project (in no particular order): Roland, Ian, Mark, Keith, Fortune, Alan and Gary. Finally, a big thank for all the friends and people that I met during this project. I thank Callum for being a fun housemate, Matteo, Federico and Lorenzo for making this PhD experience fun as well. I also thank the Multisolve lot (Marilia, Edu, Felipe, Pawel, Kostas) for the help and the good times spent at Imperial College.

Vorrei infine dedicare questo lavoro ai miei genitori, alla loro grande fiducia e illimitato supporto durante questo lungo viaggio e a mia sorella per essere stata sempre presente e per avermi fatto conoscere nuovi scorci londinesi. Infine, vorrei dedicare questo lavoro a Francesca per esserci sempre stata e per il supporto nei momenti difficili del mio dottorato e della mia vita.

Un pensiero finale a chi mi vide partire piú di otto anni fa e che non ha potuto vedermi tornare a casa. Sarete sempre nel mio cuore.

Massimiliano Breda gratefully acknowledges EPSRC for funding through EPSRC Grant No. EP/L023520/1.

Contents

Abstract **8**

Acknowledgements **9**

1 Introduction **27**

1.1 Motivation 27

1.2 Literature Review 28

1.2.1 Coherent structures and initial conditions 29

1.2.2 Jet's evolution from near to far field 31

1.2.3 TNTI and small scales 33

1.3 Objectives and approach 38

2 Methodology **40**

2.1 Nomenclature and coordinate system 40

2.2 Jet structure 41

2.3 Planar PIV 43

2.4 Hot-wire Anemometry 46

2.5 Tomographic PIV 48

2.5.1 Ghost particles . . . 53
2.6 Spatial Resolution . . . 54
2.7 Uncertainties . . . 56

3 Breaking up of coherent structures with fractal geometry 58

3.1 Definition . . . 58
3.2 2D evaluation . . . 59
3.3 3D evaluation . . . 62
3.4 Noncircular geometries' axis-switching . . . 68

4 Jet evolution due to coherent structures 71

4.1 Delay of development of jet properties . . . 71
4.2 Rescaling streamwise distance into eddy turnover times . . . 72
4.3 Evaluation of entrainment and mixing . . . 75
4.4 Time-averaged Momentum Equation . . . 79
4.5 Self-similarity and microscales . . . 87
4.6 Previous works on $\varepsilon \sim x^{-4}$ . . . 105
4.6.1 Initial conditions . . . 105
4.6.2 Spatial resolution . . . 107

5 The evolution of the small-scale properties and the behaviour of the TNTI at different streamwise locations 111

5.1 Detection of the TNTI . . . 112
5.2 Properties of TNTI . . . 117
5.3 Fractal dimension of the TNTI . . . 120

5.4 State of the microscales of the jet . . . 123

5.4.1 Unfolding of the jpdf of Q and R . . . 123

5.4.2 Evolution of enstrophy and strain production . . . 127

5.4.3 Strain-vorticity coupling . . . 128

5.4.4 Scale-dependence of alignments $|\hat{\boldsymbol{e}}_i \cdot \hat{\boldsymbol{\omega}}|$ . . . 133

5.4.5 Concluding remarks on the alignment $|\hat{\boldsymbol{e}}_i \cdot \hat{\boldsymbol{\omega}}|$ . . . 142

5.4.6 Evolution of the symmetric and skew-symmetric parts of the $Q-R$ invariants . . . 148

5.5 Evolution of jet's lengthscales from the TNTI into the turbulent bulk . . . 152

5.6 Small scale evolution across the TNTI . . . 156

5.7 Chapter summary . . . 159

6 Conclusions and future work **165**

6.1 Conclusions . . . 165

6.2 Future Work . . . 167

Bibliography **169**

List of Tables

2.1 Spatial resolution of LPIV experiments (worst case) in terms of equivalent diameter and Kolmogorov lengthscale. The estimate of the dissipation rate (and as a conseuquence of η) is later discussed in section 2.6. 45

2.2 Processing details for Planar and Tomographic PIV. The worst case scenario for the spatial resolution is reported. 55

2.3 Uncertainty of the massflow meter, PIV and hot-wire anemometry at different Re_G N.B. the procedure for calculating the uncertainty estimates of the PIV and hot-wire anemometry is presented at the end of this chapter. . 57

4.1 Table of terms used to calculate the entrainment parameter α 78

List of Figures

1.1 Sketch of the TNTI and entrainment processes. Figure reproduced from Bisset et al. (2002), with the permission of Journal of Fluid Mechanics. . . 33

1.2 Physical meaning of various spaces spanned by the VGT invariants and their constituent parts, as reproduced from da Silva and Pereira (2008). In (a) the four sectors of the jpdf of Q and R are shown in blue. The black line indicates the discriminant line $D = 0$. In (b) the jpdf of Q_s and R_s is shown. In (c) the jpdf of $-Q_s$ and Q_ω is shown. 36

2.1 (a) Jet's coordinate system for planar and tomographic PIV data and (b) velocity components. 41

2.2 Schematic of the jet facility with orifice attached to the exit. 43

2.3 Exit geometries studied. The aspect ratio $\mathcal{AR}$ between major and minor axis is shown. 43

2.4 A typical PIV system. Figure reproduced from Raffel et al. (2007). 44

2.5 Schematics of areas studied with planar PIV. 45

2.6 (a) Example of single hot wire (Manual of Dantec Dynamics) and (b) example of calibration in the near field of the round jet. 47

2.7 Tomographic PIV set up. Figure reproduced from Elsinga et al. (2006). . . 48

2.8 Top view schematics of imaging model used for tomographic reconstruction. Figure reproduced from Elsinga et al. (2006). 51

2.9 Schematics of volumes studied with TPIV. 52

2.10 Processing time of a single TPIV time step in DaVis. The computer has two processors Intel(R) Xeon(R) CPU ES-2690 v2 at 3 GHz and 128 GB of RAM. 53

3.1 PIV images for visualisation purposes only, the Kelvin-Helmholtz vortex rings are indicated by the white arrows. N.B. for clarity the co-flow was switched off when capturing these images. 59

3.2 Schematic of the two point correlation $R_{u_r x}(x, r, \xi)$. The round jet taken as an example is generated by the nozzle contraction. 60

3.3 Two point correlation $R_{u_r x}$ as a function of increasing streamwise increment ξ at $x/D_e = 3$ at $Re_G = 10,000$ (LPIV data). 61

3.4 Two point correlation R_{ii_r} in the radial direction before (a) and after (b) the shear layer has coalesced at $Re_G = 10,000$. In both the correlation is calculated at the shear layer, located as the radial location at which $u'_x(x)$ is maximum. Positive ψ is directed towards the centre, while negative ψ towards the irrotational background flow. 62

3.5 Mean vorticity $|\overline{\omega}|$ at $x/D_e = 2$ and $Re_G = 10,000$. The exit geometry is shown in the background in grey. The major axis is shown by the black line, while the minor one by the white line. 63

3.6 Azimuthal mean vorticity at $x/D_e = 2$ and $Re_G = 10,000$ (TPIV data). . . 64

3.7 Radial and streamwise mean vorticity at $x/D_e = 2$ and $Re_G = 10,000$ (TPIV data). 66

3.8 Instantaneous azimuthal vorticity for (a) round and (b) fractal jet (TPIV data, $Re_G = 10,000$). 67

3.9 Instantaneous (a) streamwise and (b) radial vorticity for the fractal jet (TPIV data, $Re_G = 10,000$). 67

3.10 (a) Jet half-width $r_{1/2}$ for various jets. The location of the axis-switch of the noncircular geometries is shown by a dashed line ($Re_G = 10,000$ and LPIV data). (b) Mean streamwise vorticity ω_x at $x/D_e = 2$ and $Re_G = 10,000$ (TPIV data). The opposite-signed vortex regions leading to the axis-switching are shown by the arrows. 69

3.11 Schematics of the jets fitted with tabs that promoted and halted axis-switching (Zaman, 1996). 69

4.1 Streamwise r.m.s. of streamwise velocity fluctuations in the near field at $Re_G = 10,000$ (LPIV data). A marker is plotted every 5 data points to avoid clutter. 72

4.2 (a) Number of eddies overturned in the time taken for the flow to advect distance x, N_{e_x}, as calculated in eq. (4.1) from the shear layer (HW data), centreline velocity (HW data) and characteristic jet velocity (PIV data) at $Re_G = 10,000$. (b) N_{e_x} calculated with the mean velocity at the shear layer at $Re_G = 31,000$ (HW data). 73

4.3 Volume flux evolution in terms of x (a), N_{e_x} (b) and compensated by the initial volumetric flow rate (c) at $Re_G = 10,000$ (LPIV data). The mean value between the major and minor axes at the same streamwise location is shown in magenta and yellow. A marker is plotted every 10 points. Note that $N_{e_x} = 0$ corresponds to the streamwise location $x/D_e = 1$. 75

4.4 (a) Entrainment parameter α as a function of x for the various jets at $Re_G = 10,000$. (b) Streamwise spatial gradient of the volume flux as a function of N_{e_x} for the various jets (LPIV data). Note that $N_{e_x} = 0$ corresponds to the streamwise location $x/D_e = 1$. One marker is plotted every 10 data points to avoid clutter. 76

4.5 Spreading rate $dr_{1/2}/dx$ of the various jets at (a)$Re_G = 3,000$ and $Re_G = 10,000$ (Breda and Buxton, 2017). Trend lines are shown in magenta and one marker is plotted every 10 points to avoid clutter (LPIV data). 79

4.6 Terms of (4.8) for the various jets in the shear layer, where the near-field coherent motions reside at $Re_G = 10,000$ (HPIV data). One marker plotted every 20 points to avoid clutter. The location of peak $u'_x(x)$ is chosen to locate the shear layer. 80

4.7 a) $\overline{U}_x \frac{\partial \overline{U}_x}{\partial x}$ along the centreline and (b) $\overline{u_x u_r}/r$ in the shear layer at $Re_G = 10,000$ (HPIV data). One marker plotted every 20 points to avoid clutter. 81

4.8 (a) $\partial(\overline{u_x u_r})/\partial r$ along the centreline and (b) $\overline{U}_r \frac{\partial \overline{U}_x}{\partial r}$ along the shear layer as a function of N_{e_x} calculated for the various jets at $Re_G = 10,000$ (HPIV data). 82

4.9 Evolution of $\overline{U_r}\partial\overline{U_x}/\partial r$ with N_{e_r} for the various jets in the shear layer at $Re_G = 10,000$ (LPIV data). One marker plotted every 20 points to avoid clutter. (b) Evolution of N_{e_r} with respect to N_{e_x}. 83

4.10 Variation of (a) $\partial\overline{u_x^2}/\partial x$ and of (b) $\overline{u_x u_r}/r$. The expected far-field trend is shown by a red dashed line. (HPIV data, $Re_G = 10,000$) 85

4.11 Variation of (a) $\overline{U_x}\partial\overline{U_x}/\partial x$, (b) $\overline{U_r}\partial\overline{U_x}/\partial r$ and (c) $\partial\overline{u_x u_r}/\partial r$. The expected far-field trend is shown by a red dashed line (HPIV data and $Re_G = 10,000$). 86

4.12 Centreline mean streamwise velocity as a function of x (LPIV data). The velocity is multiplied by x so that the self-similar state will be shown by a constant horizontal trend. Only 10% of the points are shown to avoid clutter. 92

4.13 Radial profiles of $\overline{U_x}$ at various streamwise locations and at $Re_G = 10,000$ (LPIV data), normalised by centreline value. 92

4.14 Radial profiles of $\overline{u_x u_r}$ at various streamwise locations and at $Re_G = 10,000$ (LPIV data), normalised by the centreline velocity (top) and by the a local quantity (bottom). 93

4.15 (a) Dissipation and (b) $r_{1/2}/K_s\overline{U}_{cl}$ as a function of x for the far fields of the various jets at $Re_G = 10,000$ (HPIV data). 95

4.16 (a) Dissipation premultiplied by $(x - x_0/D_e)^4$ (top), premultiplied by $(x - x_0/D_e)^3$ (bottom) and (b) $r_{1/2}/K_s\overline{U}_{cl}$ as a function of x for the far fields of the various jets at $Re_G = 10,000$ (HPIV data). 95

4.17 Jet half-width premultiplied by $(x/D_e)^{-1}$ so that the self-similar state will be shown by a constant horizontal line (LPIV data). 98

4.18 (a) u'_x/q as a function of x and (b) C_ε (from the corrected ε) as a function of $Re_G^{1/2}/Re_{\lambda_f}$ for the various jets in the region $23.5 \leq x/D_e \leq 26$ at $Re_G = 10,000$ (HPIV data). 99

4.19 Ratio between dissipation calculated assuming local isotropy ε_{iso} and assuming local axisymmetry ε_{axi} at $Re_G = 10,000$ at the jet centreline (HPIV data). 101

4.20 Re_{λ_f} and C_ε at $Re_G = 10,000$ (black) and $Re_G = 31,000$ (blue) (HW data). 102

4.21 Premultiplied energy spectra a $x/D_e = 25$ at jet centre-line, (HW data). . . 103

4.22 (a) Variation of Re_{λ_f} with streamwise distance for an axisymmetric jet. (b) Variation of dissipation constant. Data reproduced from the work of Mi and Nathan (2010) for axisymmetric round jets emitted from orifices at $Re_G = 13,000$ (based on the current definition of D_e) and acquired with a hot-wire. 104

4.23 Reproduction of *Figure 2* from Friehe et al. (1972). The markers represent the following data: ■ unpublished work of LaRue and Friehe (1971) ($Re_G = 18,000$), ● Friehe et al. (1972) ($Re_G = 106,000$), ♦ Gibson (1963) ($Re_G = 440,000$), ▲ ($Re_G = 330,000$) and ▼ ($Re_G = 514,000$) from a private communication with F. H. Champagne (1971). Please note the round jet diameter in the original works D was converted to the equivalent diameter as in the current work. The variable U_0 represent the jet exit velocity in the experiments. 106

4.24 Data from the work of Burattini et al. (2005b) acquired with a hot-wire and at $Re_G = 115,000$. Jet emitted from a round nozzle. Dissipation was estimated converting the Kolmogorov length scale reported in Table IV into dissipation as $\varepsilon = \nu^3/\eta^4$. The variable l_w represents the hot-wire length and the round jet diameter is rescaled in terms of equivalent diameter D_e. 107

4.25 Data from Mi and Nathan (2010), acquired with hot-wire and at $Re_G = 13,000$. Jet emitted from sharp orifices. Dissipation is calculated from *Figure 11c* of the original work. Please note the round jet diameter D has been converted to the equivalent diameter D_e of this work. 108

4.26 Data of *homogeneous* dissipation (eq. (4.49)) from *Table 1* of Sadeghi et al. (2015), acquired with a cross-wire probe and at $Re_G = 44,000$. Jet emitted from a round nozzle. The diameter has been converted to equivalent diameter, as stated in the current paper. 109

4.27 Reproduction of *Figure 14* from the work of Mi et al. (2013) (the Kolmogorov scale was then converted into dissipation). The data are acquired with a hot-wire and the jet was emitted by a smooth nozzle. Please note both round jet diameter D and Reynolds number have been rescaled with the equivalent diameter D_e, as the present work. 110

5.1 Example of threshold detection based on the turbulent area. Figure reproduced from Zhou and Vassilicos (2017) with the permission of the Journal of Fluid Mechanics. 114

5.2 $\overline{\omega^{2^*}}$ at various streamwise locations for the round jet, compensated by the mean bulk η (a, b, c) and λ_f (d, e, f). The change of growth rate are shown with the dashed magenta lines (TPIV data and $Re_G = 10,000$). 115

5.3 Mean conditional interface for round and fractal jet at $x/D_e = 2$ (TPIV data, $Re_G = 10,000$). 117

5.4 $\overline{\hat{r}}(\theta)$ for round and fractal jet at $x/D_e = 2$. (TPIV data and $Re_G = 10,000$) 118

5.5 (a) P.d.f. of $\hat{r}$ for round ($\circ$) and fractal ($*$) jet. (b) P.d.f. of fluctuations of the TNTI based on the angular mean radial distance (same legend applied). Here the abscissa has been oriented so that positive represents the turbulent zone, whilst negative represents non-turbulent areas (either in the jet core or in the quiescent background). TPIV data at $x/D_e = 2$ and $Re_G = 10,000$. 119

5.6 P.d.f. of velocity fluctuations at the interface based on the mean interface velocity at the inner and outer interface for round ($\circ$) and fractal jet ($*$). ($x/D_e = 2$, $Re_G = 10,000$). 120

5.7 ITNTI of the round jet from a single time step at $x/D_e = 2$ with varying box size: (a) $B_s = 0.03D_e$, (b) $B_s = 0.08D_e$ and (c) $B_s = 0.16D_e$. The boxes containing the TNTI are shown in red. (TPIV data and $Re_G = 10,000$) 121

5.8 Box counting of different interfaces at various streamwise locations for round ($\circ$) and fractal ($*$) jets (TPIV data ad $Re_G = 10,000$). 122

5.9 Jpdf of Q and R for the round and fractal jet (TPIV data and $Re_G = 10,000$). Isocontours range from 10^{-4} to 10^{0}. The regions of positive and negative D (the discriminant of the velocity gradient tensor) are separated by a black dashed line. (TPIV data, $Re_G = 10,000$) 124

5.10 P.d.f. of $s_{ij}s_{ij}$ for round jet (-) and fractal jet (- -) a various streamwise locations. An insert with a close up of the peaks of the pdf is added. . . . 127

5.11 P.d.f. of enstrophy and strain for round jet (-) and fractal jet (- -). (TPIV data at $Re_G = 10,000$) 128

5.12 Pdf of the spatial evolution of $\omega^2 s_i \cos^2(\boldsymbol{e_i}, \boldsymbol{\omega})$ for round jet (-) and fractal jet (- -). TPIV data at $Re_G = 10,000$. 129

5.13 Pdf of the eigenvalues s_i for round jet (-) and fractal jet (- -). TPIV data and $Re_G = 10,000$. 130

5.14 Pdf of the spatial evolution of the alignment of the vorticity vector with the eigenvectors of the strain-rate tensor for the round jet (-) and the fractal jet (- -). (TPIV data and $Re_G = 10,000$). 131

5.15 Example of turbulent lengthscales (a) constrained between the OTNTI and the ITNTI and (b) unconstrained (Round jet, TPIV data and $Re_G = 10,000$). The turbulent area is shaded in light blue. (c) Pdf of the fluctuations of $\mathcal{L}_\omega$ with respect to its mean $\overline{\mathcal{L}_\omega}$. 137

5.16 Alignment between the eigenvectors $\boldsymbol{e_i}$ of the strain rate and the vorticity unit vector $\boldsymbol{\omega}$ at $x/D_e = 2$. Round jet (R) at the top and fractal jet (F) at the bottom. The colour scheme represents $|\hat{\boldsymbol{e_1}} \cdot \hat{\boldsymbol{\omega}}|$, $|\hat{\boldsymbol{e_2}} \cdot \hat{\boldsymbol{\omega}}|$ and $|\hat{\boldsymbol{e_3}} \cdot \hat{\boldsymbol{\omega}}|$. (TPIV data and $Re_G = 10,000$) 138

5.17 Alignment between the eigenvectors $\boldsymbol{e_i}$ of the strain rate and the vorticity unit vector $\boldsymbol{\omega}$ at $x/D_e = 10$. Round jet (R) at the top and fractal jet (F) at the bottom. The colour scheme represents $|\hat{\boldsymbol{e_1}} \cdot \hat{\boldsymbol{\omega}}|$, $|\hat{\boldsymbol{e_2}} \cdot \hat{\boldsymbol{\omega}}|$ and $|\hat{\boldsymbol{e_3}} \cdot \hat{\boldsymbol{\omega}}|$. (TPIV data and $Re_G = 10,000$) 139

5.18 Alignment between the eigenvectors $\boldsymbol{e_i}$ of the strain rate and the vorticity unit vector $\boldsymbol{\omega}$ at $x/D_e = 25$. Round jet (R) at the top and fractal jet (F) at the bottom. The colour scheme represents $|\hat{\boldsymbol{e_1}} \cdot \hat{\boldsymbol{\omega}}|$, $|\hat{\boldsymbol{e_2}} \cdot \hat{\boldsymbol{\omega}}|$ and $|\hat{\boldsymbol{e_3}} \cdot \hat{\boldsymbol{\omega}}|$. (TPIV data and $Re_G = 10,000$) 140

5.19 Pdf of the alignment $|\hat{\boldsymbol{e_i}} \cdot \hat{\boldsymbol{\omega}}|$ from the turbulent bulk (-) and from regions of intense swirling $\lambda_{ci} > 3.5\lambda'_{ci}$ (- -) (TPIV data, $Re_G = 10,000$). 141

5.20 Pdfs of $s_{ij}s_{ij}$ for the round jet conditioned to various angles of alignment. (TPIV data, $Re_G = 10,000$). 145

5.21 Pdfs of $s_{ij}s_{jk}s_{ki}$ for the round jet conditioned to various angles of alignment. (TPIV data, $Re_G = 10,000$). Legend as in fig. 5.20. 146

5.22 Pdfs of $\omega_i s_{jk} \omega_j$ for the round jet conditioned to various angles of alignment. (TPIV data, $Re_G = 10,000$). Legend as in fig. 5.20. 147

5.23 Jpdf of Q_ω and Q_s for round and fractal jet (TPIV data and $Re_G = 10,000$). Isocontours range from 10^{-4} to 10^0. 148

5.24 Jpdf of Q_s and R_s for round and fractal jet (TPIV data and $Re_G = 10,000$). Isocontours range from 10^{-4} to 10^0. In (a), the eigenvalues $s_1 : s_2 : s_3$ corresponding to each dashed line are shown. Legend as in fig. 5.23. 149

5.25 Jpdf of s_2^* and Q_s for round and fractal jet (TPIV data and $Re_G = 10,000$). Isocontours range from 10^{-4} to 10^0. Legend as in fig. 5.23. 151

5.26 Jpdf of s_2^* and Q_ω for round and fractal jet (TPIV data and $Re_G = 10,000$). Isocontours range from 10^{-4} to 10^0. Legend as in fig. 5.23. 151

5.27 Evolution of of the ratio between bulk λ_f and η for round ($\circ$) and fractal jet ($*$) ($Re_G = 10,000$, TPIV data). 153

5.28 Evolution of (a) local Kolmogorov and of (b) local Taylor lengthscale for round ($\circ$) and fractal jet ($*$) ($Re_G = 10,000$, TPIV data). 154

5.29 Evolution of (a) $\hat{\lambda_f}/\hat{\eta}$ and of (b) $Re_{\hat{\lambda_f}}$ for round ($\circ$) and fractal jet ($*$) ($Re_G = 10,000$, TPIV data). The legend is the same as fig. 5.28 155

5.30 Evolution of (a) K_1, (b) K_2 and (c) K_3 for round ($\circ$) and fractal jet ($*$) ($Re_G = 10,000$, TPIV data). The legend is the same as fig. 5.28 156

5.31 Example of an area probed between 15-20 η at $x/D_e = 2$ (black). The ITNTI is shown in red and the OTNTI in blue (Round jet, TPIV data, $Re_G = 10,000$). 157

5.32 Evolution of $s_{ij}s_{jk}s_{ki}$ across TNTI (TPIV data, $Re_G = 10,000$). The data are presented for the round jet only, but comparable results are found for the fractal jet too. The legend in (d) is valid for the rest of the plot of this section. 161

5.33 Jpdf of $-s_{ij}s_{jk}s_{ki}$ and $\omega_i s_{ij}\omega_j$. Isocontour 10^{-4} and the data are from round jet (comparable behaviour for fractal jet). The black dashed line marks where $\omega_i s_{ij}\omega_j = -4/3 s_{ij}s_{jk}s_{ki}$, therefore the data above the line corresponds to $R > 0$ and below the line to $R > 0$. (TPIV data and $Re_G = 10,000$). 162

5.34 Jpdf of Q and R, at a isocontour of 10^{-2} for the round jet (a comparable behaviour is found for the fractal jet as well). (TPIV data and $Re_G = 10,000$).163

5.35 Jpdf of $-Q_s$ and Q_ω, at a isocontour of 10^{-4} for the round jet (a comparable behaviour is found for the fractal jet as well). (TPIV data and $Re_G = 10,000$).164

Chapter 1

Introduction

1.1 Motivation

Axisymmetric jets have attracted numerous studies in the past due to their common use as mixing and thrust producing devices (Ho and Gutmark, 1987). An axisymmetric round jet issuing directly from a contraction produces a flat-topped (top-hat) velocity profile in the near field and develops towards a turbulent state in the far field (whether self-similar or not) by entraining and mixing background (quiescent) fluid into the turbulent stream, whilst the latter evolves losing "memory" of the initial conditions that generated it. Entrainment describes a process through which there is an exchange of momentum, energy, vorticity, mass and other properties between the surrounding fluid and the turbulent stream across a sharp interface (the so-called turbulent/non-turbulent interface). This process can take place in two ways, through engulfment (ingestion of irrotational fluid into the turbulent stream) and nibbling (small scale diffusion across the interface). The first one is a large-scale process (Yule, 1978) and hence it is influenced by the state of the coherent structures, whilst the latter is a small-scale phenomenon.

In this thesis, the aim is to gather a deeper understanding on the large scale structures, on how they influence entrainment and on how they affect the evolution of an axisymmetric jet towards the far field. This is done by comparing a "classic" round jet with other

noncircular exit geometries. In particular, a fractal geometry was chosen. In fact, fractal geometries have been proven before to lead to a break-up of the coherent structures for a variety of flows, including jets (Cafiero et al., 2015), wakes (Nedić et al., 2013a) and grid-generated flows (Melina et al., 2016). Therefore, comparing the effect of round and fractal geometry on the flow physics, it will be possible to evaluate how different states of the coherent structures affect the entrainment and mixing rates in the near field and as a consequence the properties of the turbulent/non-turbulent interface, which is observed to scale with the microscales of the flow (i.e. the Taylor or the Kolmogorov lengthscales). The different entrainment and mixing rates may also affect the evolution towards the self-similar state, since George (1989) suggested that the growth rate of a jet is strongly dependent on the state of the coherent structures. Entraining and mixing "memoryless" background fluid, the turbulent stream starts transitioning to a *self-similar* state, where the profiles of its quantities at various streamwise locations (i.e. velocity, dissipation, etc.) are the same once re-scaled in terms of local quantities (i.e. centreline velocity and jet half-width, which all vary as a power law with the streamwise distance x).

In summary, this thesis will examine the following question: *How do different near field coherent structures impact the development of the jet and the behaviour of the small and large scales of the flow?*

1.2 Literature Review

The literature review will cover the ways that previous works have answered the question above, split as follows:

- Types of initial conditions for an axisymmetric jet affecting the state of the coherent structures and their influence on entrainment and mixing.
- Previous literature about the evolution of an axisymmetric jet from near to far field.

- Previous literature about the TNTI and the small scale dynamics of a turbulent flow.

1.2.1 Coherent structures and initial conditions

Recent works have focused on understanding the role of the initial conditions in affecting the evolution towards self-similarity of various shear flows. As mentioned in section 1.2.1, an axisymmetric round jet issuing directly from a contraction produces a flat-topped ("top hat") velocity profile in the near field and develops towards the far-field state (whether self-similar or not) by entraining and mixing background, quiescent fluid into the turbulent stream. With increasing axial distance the mean velocity profile evolves until it reaches self-similarity. Previous studies have tried to understand how affecting the coherent structures affected the path to reach this self-similar state. Antonia and Zhao (2001) observed that jets with fully developed and "top-hat" mean velocity profiles reached self-similarity (of mean flow and the velocity fluctuations) after the same streamwise distance, and thereby suggested that the state of the coherent structures did not affect the jet's evolution. This has been a popular idea amongst researchers since the work of Townsend (1976). George (1989) made a similar claim, that the mean flow and turbulent fluctuations would exhibit the same self-similar profiles from flow to flow but, contrastingly, he argued that there is a link between the self-similar state of a flow and its coherent structures. He argued that the evolution of other turbulent quantities would not necessarily exhibit the same self-similar profiles when comparing a multitude of different axisymmetric jet flows.

The state of the coherent structures of a round jet (i.e. the Kelvin-Helmholtz vortex ring) is strongly influenced by the initial conditions. These comprise various effects, including global Reynolds number Re_G, type of exit (nozzle, orifice or pipe) and exit geometry (circular or non-circular).

The dependence of the jet's properties on the initial, global Reynolds number Re_G has been studied by Xu et al. (2013) for a jet emitted by a long square pipe. The authors observed that for $Re_G \leq 30,000$ the streamwise decay of the mean velocity, Strouhal

number of the instabilities and spreading rate of the jet were inversely proportional to the Reynolds number whilst they would be independent of Re_G for $Re_G > 30,000$. This was attributed to the different flow conditions at the nozzle exit which affected the downstream large-scale flow structures. Despite the significant near-field differences, the square jet would evolve to axisymmetry whilst transitioning to self-similarity. A similar conclusion was reached by Namer and Ötügen (1988) and Mi et al. (2013), who observed that mixing, evaluated in terms of spreading rate or centreline velocity decay rate, was weakened by increasing the Reynolds number. Hence, in order to study the influence of Re_G on the jet evolution, three Reynolds numbers are considered in the present study: $Re_G = 3,000$ and $Re_G = 10,000$, to study a regime where some properties of the jet are expected to be Re_G-dependent, and $Re_G = 31,000$, where they should not be.

The choice of nozzle/pipe/orifice jet exit also plays an equally important role in affecting the large-scale coherence present in the flow and therefore entrainment and mixing. The rate of entrainment describes the exchange of momentum, energy, vorticity, mass and other properties between the surrounding fluid and the turbulent stream across a sharp interface (the so-called turbulent/non-turbulent interface). This phenomenon, as reviewed by da Silva et al. (2014a), is strongly affected by both large-scale (engulfment) and small-scale processes (nibbling). In the near field, engulfment has been found to be dominant (Yule, 1978), suggesting that affecting the coherent structures will directly alter the entrainment and mixing processes. Mi et al. (2001) investigated the differences in performance between jets with pipe-, contoured nozzle- and orifice-exits, observing that the latter provided the greatest rate of mixing as shown by the highest spreading rate, whilst the pipe-flow jet the lowest. By means of explanation, Mi et al. (2007) concluded that both nozzle and orifice jets generated primary coherent structures (i.e. the Kelvin-Helmholtz vortex rings), however they occurred more rapidly for the orifice flows translating to a higher engulfment rate.

The coherent structures within the near-field of a jet flow may also be manipulated by using non-circular exit geometries. Examples include combining an increased wetted perimeter and number of corners with various-shaped exits ranging from ellipses, triangles,

squares (Gutmark et al., 1989), petals (Shakouchi et al., 2014), crosses and many others (Mi and Nathan, 2010). Despite the extensive literature available, there is no agreement as to how combining non-circular exits with different types of pipe/nozzle/orifice exits affects the large-scale coherence, and as a consequence entrainment and mixing. Mi and Nathan (2010) and Aleyasin et al. (2017), amongst others, tested various noncircular exit shapes, each coming to different conclusions as to how the entrainment and mixing rates varied between the shapes tested. Contrastingly from Mi and Nathan (2010), Shakouchi et al. (2014) found that a 6-petal shaped nozzle with increased wetted perimeter led to an increased rate of mixing compared to the round jet. Gutmark et al. (1989) found that a combination of corners and large wetted perimeter would allow augmenting both entrainment and mixing. These different findings can be attributed to the different type of exit chosen, however all these studies indicated the possibility of improving mixing, once the number of corners and the wetted perimeter were increased. For this reason, a repetitive fractal pattern, based on a square geometry, is proposed in this study, which allows maximising the number of corners and wetted perimeter for a given open area. Such fractal geometry (fractal dimension $D_f = 1.5$ and 3 iterations, as in Nedić et al. (2013b)) has been previously applied to the perimeter of axisymmetric wake-generating plates where a break-up of the coherence, and a reduction of the shedding energy were observed by Nedić et al. (2015).

1.2.2 Jet's evolution from near to far field

As previously mentioned, an axisymmetric jet evolves by entraining background fluid into the turbulent stream and George (1989) suggested that the evolution of various turbulent quantities of a jet would eventually (after a transition region) follow the same self-similar scalings. Crucially, he argued that this was not the case for the rate of dissipation of turbulent kinetic energy and choosing a different dissipation scaling would indeed alter the spreading rate of each particular jet. Building on the work of George (1989), Nedić et al. (2013b) found a rate of dissipation, of an axisymmetric wake with fractal perimeter,

that is not instantaneously in equilibrium with the inertial inter-scale energy transfer rate (non-equilibrium dissipation) persisting until very far away from these wake generators, thereby affecting the spreading rate of the wake. This was discussed further in the work of Goto and Vassilicos (2015), where the authors verified that also in unsteady periodic turbulence there would be a lag between the energy flux and the kinetic energy dissipation rate, showing that they were not instantaneously in balance as indicated according to the Kolmogorov "classical" equilibrium dissipation. Readers are referred to the review article of Vassilicos (2015) for a full exposition on non-equilibrium dissipation. Summarising, if one follows the classical Kolmogorov (equilibrium) theories, C_ε, as in (1.1), is a constant.

$$C_\varepsilon \equiv \frac{\varepsilon \mathcal{L}}{q^3} = \text{constant} \tag{1.1}$$

in which ε is the (local) rate of dissipation of turbulent kinetic energy, q^2 is the (local) turbulent kinetic energy and $\mathcal{L}$ is the (local) integral length scale. However, when non-equilibrium dissipation is present, C_ε is a function of Re_G and the local Reynolds number $Re_{\lambda_f}(x)$ formed from the local r.m.s. velocity fluctuation u' and the (local) Taylor microscale λ_f

$$C_\varepsilon \equiv \frac{\varepsilon \mathcal{L}}{q^3} \sim \frac{Re_G^{1/2}}{Re_{\lambda_f}} \neq \text{constant} \qquad \forall Re_{\lambda_f} = Re_{\lambda_f}(x) \neq \text{constant}. \tag{1.2}$$

Non-equilibrium dissipation was also found in regions of square-fractal element (Hearst and Lavoie, 2014) and regular (Valente and Vassilicos, 2012) grid-generated flows, as well as unsteady homogeneous isotropic turbulence (Goto and Vassilicos, 2015). Differently from the previous cases, in an axisymmetric jet Re_{λ_f} becomes constant in the very far field (Tennekes and Lumley, 1972), therefore a similar evolution to the other shear flows is not necessarily expected. Despite the abundant literature available for the near field and self-preserving state of axisymmetric jets, no studies to the knowledge of the author have covered the approach to complete self-preservation, in which some, but not all, terms of the mean kinetic energy equation may be self-similar.

As discussed, the fractal geometry may impact the state of the large-scale coherent struc-

tures and as a consequence the entrainment and mixing rates. This means that different exit geometries may impact the turbulent/non-turbulent interface through which entrainment takes place and as a result the small scales of the jet.

1.2.3 TNTI and small scales

As discussed at the start of this chapter, entrainment takes place as an exchange of momentum, energy, vorticity, mass and other properties between the surrounding fluid (irrotational) and the turbulent stream (vortical) across the turbulent/non-turbulent interface (TNTI) (da Silva et al., 2014a). The latter can be defined as a fluctuating interfacial layer, which matches the weakly turbulent fluctuations to weak low-frequency external fluctuations with larger scales (i.e. irrotational). In other words, a layer where the gradients of vorticity fluctuations are maximal (Phillips, 1955). As shown in fig. 1.1, this process takes place as engulfment (large-scale ingestion of irrotational fluid) or nibbling (small-scale viscous diffusion). These two processes do not exclude each other and based on the state of the coherent structures one may be more important than the other one. Establishing which process is dominant across the evolution of the jet is somewhat open

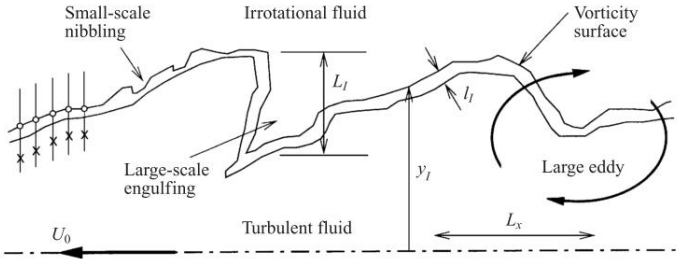


Figure 1.1: Sketch of the TNTI and entrainment processes. Figure reproduced from Bisset et al. (2002), with the permission of Journal of Fluid Mechanics.

to debate (da Silva et al., 2014a), since some authors have suggested that in turbulent jets engulfment is dominant, whilst others have pointed to nibbling. Dahm and Dimotakis (1987); Dimotakis (2000) suggested that engulfment would be the dominant process in the far field of axisymmetric jet and a similar conclusion was reached by Mungal et al. (1991) for diffusion flames. Contrastingly, Westerweel et al. (2005) pointed to nibbling as the dominant entrainment process in the far field of a jet between $x/D_e = 35 - 160$.

In order to better understand the process of entrainment, a deeper understanding of the TNTI is needed both in the near, where engulfment may be dominant, and in the far field, where nibbling may be dominant.

Examining the state of the TNTI has posed significant challenges in the past due to its very small thickness. The first significant work on this topic (Corrsin and Kistler, 1954) suggested the existence of a viscous laminar superlayer (VSL) which matched the irrotational regions to the vortical flow. Corrsin and Kistler (1954) suggested that the thickness of this layer would scale with a viscous lengthscale, usually assumed to be the Kolmogorov lengthscale η. Decades later, numerical and experimental works have suggested that the TNTI is not only composed of the VSL, but also of a turbulent sublayer (TSL) where the vorticity reaches a local maximum and which has a thickness that scales with the Taylor lengthscale λ_f (Bisset et al., 2002; Westerweel et al., 2005) or simply to the radius of the large scale vorticity structures (LVS) near the interface (da Silva and Taveira, 2010). This implies that a full examination of the TNTI has been limited by the high spatial resolution needed to fully resolve the jump of vorticity/velocity between the irrotational fluid and the turbulent stream both in experiments and DNS. Moreover, to the knowledge of the author, the various studies on the TNTI have not covered the influence of the coherent motions (or the lack of it) on its small-scale structure. Since the entrainment process is dominated by engulfment in the near field, a break-up of the coherent structures may change this in favour of nibbling, which is a small-scale phenomenon.

The small scales are important since they describe the state of the small-scale structures of a flow. They have been thought to be well approximated as homogeneous and isotropic (Kolmogorov, 1941; Batchelor, 1953) and their topology has been shown to depend on the behaviour of the velocity gradient tensor (VGT), which can be split into a symmetric and skew-symmetric part (or a strain rate s_{ij} and a rotation tensor ω_{ij}):

$$a_{ij} = \frac{\partial u_i}{\partial x_j} = s_{ij} + \omega_{ij} = \frac{1}{2}\left(\frac{\partial u_i}{\partial x_j} + \frac{\partial u_j}{\partial x_i}\right) + \frac{1}{2}\left(\frac{\partial u_i}{\partial x_j} - \frac{\partial u_j}{\partial x_i}\right) \tag{1.3}$$

Here the flow velocity is split into its mean and fluctuating part following the Reynolds

decomposition $U_i = \overline{U_i} + u_i$. Chong et al. (1990); Chacin and Cantwell (2000) defined the invariants of the VGT, so-called because they remain constant regardless of which coordinate system is used, from the roots of the characteristic equation of a_{ij} written as

$$\xi^3 + P\xi^2 + Q\xi + R = 0, \tag{1.4}$$

where P, Q and R are the invariants. The first invariant P describes the negative trace of the VGT ($P = -a_{ij}$) and is therefore zero for an incompressible flow, hence leaving Q and R to describe the flow topology

$$Q = \frac{1}{4}(\omega_i\omega_i - 2s_{ij}s_{ij}) = Q_\omega + Q_s, \tag{1.5}$$

$$R = -\frac{1}{3}(s_{ij}s_{jk}s_{ki} + \frac{3}{4}\omega_i s_{ij}\omega_j) = R_s + R_\omega, \tag{1.6}$$

where ω_i indicates the $i-th$ component of the vorticity vector. The invariant Q can be considered as the local excess of swirling over strain rate (as discussed by Buxton et al. (2017) amongst others), with its constituent parts Q_ω being half the magnitude of the enstrophy whilst $Q_s = -\varepsilon/4\nu$ is proportional to the turbulent kinetic energy dissipation rate ε.

Since $P = 0$ the states of Q and R can be used to describe the state of an incompressible fluid element. The $Q - R$ space is now analysed in fig. 1.2a. The $Q - R$ space can be divided into four sectors based on the sign of R and of the discriminant of eq. (1.4) $D = Q^3 + 27R^2/4$, which separates purely real solutions ($D < 0$, flow locally straining only) from one real and a pair of complex conjugate pair of roots ($D > 0$, flow locally swirling). In fig. 1.2a, the points of positive D are above the discriminant line, whilst the region of $D < 0$ is below. The four sectors can be therefore defined as follows: sector I: $D > 0, R > 0$ is referred to as the unstable foci where there is enstrophy attenuation; sector II: $D > 0, R < 0$ is referred to as stable foci, where enstrophy amplification takes place; sector III: $D < 0, R < 0$ is referred to as stable nodes; sector III: $D < 0, R > 0$ is referred to as unstable nodes (Soria et al., 1994). The joint probability density function

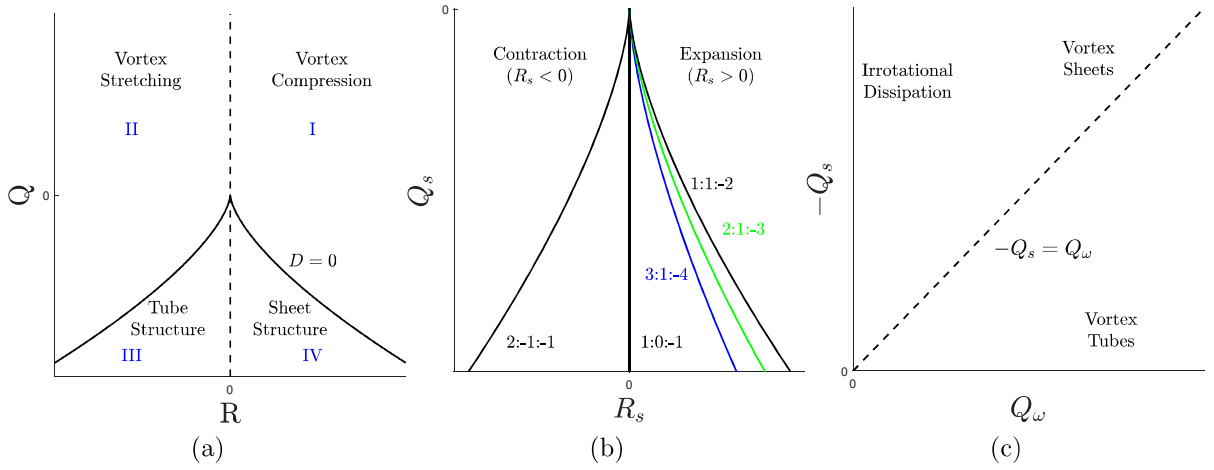


Figure 1.2: Physical meaning of various spaces spanned by the VGT invariants and their constituent parts, as reproduced from da Silva and Pereira (2008). In (a) the four sectors of the jpdf of Q and R are shown in blue. The black line indicates the discriminant line $D = 0$. In (b) the jpdf of Q_s and R_s is shown. In (c) the jpdf of $-Q_s$ and Q_ω is shown.

(jpdf) of Q and R has been found to have a characteristic "tear-drop" shape in a variety of fully developed turbulent flows including homogeneous isotropic turbulence, mixing layers and wall-bounded flows (Soria et al., 1994; Blackburn et al., 1996; Tsinober, 2009; Buxton and Ganapathisubramani, 2010). This "ubiquity" led to the belief the tear-drop shaped jpdf is a universal signature of fine-scale turbulent motions (Chacin and Cantwell, 2000; Elsinga and Marusic, 2010). Despite these studies being conducted in regions of fully developed turbulence, this tear-drop shaped jpdf has also been found in regions where the coherent motions of the flow are still present for grid generated flows and in the flow past a square cylinder (Gomes-Fernandes et al., 2014; Buxton et al., 2017), which pointed to the possibility of this tear-drop shape being a "universal" signature of turbulent flows in general.

A great deal of information is also available from the jpdf of Q_s and R_s (fig. 1.2b), which is useful to analyse the geometry of the local straining. In fact, this jpdf links Q_s, which is proportional to the turbulent kinetic energy dissipation rate ($Q_s = -\varepsilon/4\nu$), and R_s, which is indicative of strain-rate production ($R_s > 0$) and of strain-rate destruction ($R_s < 0$). Further, R_s can be linked to the eigenvalues of s_{ij} as $R_s = -s_1 s_2 s_3/3$, where s_1 is the extensive eigenvalue (always positive), s_3 the compressive one (always negative) and s_2 the intermediate one (either positive or negative). Due to incompressibility, the sum of

the three eigenvalues equals zero. As discussed by da Silva and Pereira (2008), based on the ratio of the first two eigenvalues $a = s_2/s_1$, it is possible to define lines of R_s as

$$R_s = -(Q_s)^{3/2} a(1+a)(1+a+a^2)^{-3/2}. \tag{1.7}$$

As summarised by da Silva and Pereira (2008); Blackburn et al. (1996), each line can define a different state of the flow based on the (most common) ratio of the triplet $s_1 : s_2 : s_3$ as follows: 2:-1:-1 (axisymmetric contraction), 1:0:-1 (two-dimensional flow), 3:1:-4 (biaxial stretching, as modelled by Ashurst et al. (1987)) and 1:1:-2 (axisymmetric stretching). In general it has been found that in many turbulent flows there is a preference for $R_s > 0$ and $Q_s < 0$ indicating sheet-like structures, or simply a flow behaving locally like a jet parallel to $\boldsymbol{e_3}$, impinging on the $\boldsymbol{e_1} - \boldsymbol{e_2}$ plane (Gomes-Fernandes et al., 2014). Here, $\boldsymbol{e_1}$, $\boldsymbol{e_2}$ and $\boldsymbol{e_3}$ are the eigenvectors of s_{ij} corresponding to s_1, s_2 and s_3 respectively. Previous studies have indicated that the most probable geometry of a turbulent flow follows the triplets 3:1:-4 or 2:1:-3 (Ooi et al., 1999; Soria, 1996; Blackburn et al., 1996; Ashurst et al., 1987).

Another important space is the one between Q_s and Q_ω, as shown in fig. 1.2c, which is associated with the topology of the turbulent kinetic energy dissipation and anisotropy. Usually, the points near the abscissa are associated with body rotation and little energy dissipation. These are described as "vortex tubes". The points associated with high dissipation and little rotation are associated with irrotational dissipation outside these vortex tubes (da Silva and Pereira, 2008). The 45° line represents points of high dissipation and rotation described as "vortex sheets". Based on the type of flow, authors found that the majority of points tended to be aligned with the abscissa or with the 45° line (Ooi et al., 1999; Soria et al., 1994; Blackburn et al., 1996).

Summarising, the three jpdfs discussed allow studying the small-scale structure of a turbulent flow and understanding how the flow structure varies moving from the edge of the TNTI into the turbulent bulk. A study on this latter topic was done for a planar jet by da Silva and Pereira (2008, 2009), who found, for example, that in the $Q - R$ space

at the interface all points would be located under the discriminant line D, as expected due to the fact that strain product dominated over enstrophy and therefore $Q < 0$ at all times. However, moving into the turbulent zone, the characteristic fully developed tear-drop shape was recovered at a distance of 12.8 Kolmogorov lengthscales η inside the turbulent bulk.

1.3 Objectives and approach

This thesis aims to investigate how different states of the coherent structures affect the near field and the evolution of an axisymmetric jet. Previous studies have reached contrasting conclusions on how different initial conditions will affect entrainment and mixing rates. It is through this entrainment and mixing that a jet will develop towards an axisymmetric, self-similar state in the far field according to the simple time averaged momentum equation (TAME). However, the effects on the TNTI and on the evolution towards the self-similar state are yet to be unveiled. George (1989) is clear that the rate of dissipation of turbulent kinetic energy plays an important role in the evolution of these jets in the self-similar region, which has been verified in recent years with the discovery of the non-equilibrium dissipation law. Moreover, the state of the self-similarity at the microscales may vary based on the initial state of the coherent structures.

Therefore, this thesis will explore the impact of the coherent structures on the overall development of the jet. Moreover, analysing both round and fractal jets (where the coherent structures may be proven to be broken-up by the exit geometry chosen in this study) will allow comparing different properties and how they are linked to their initial conditions.

Planar Particle Image Velocimetry (PIV) is initially used to assess the state of the flow spatially and draw conclusions on which areas of the flow should be studied. Subsequently, constant temperature hot-wire anemometry is deployed to evaluate the temporal properties of the jet. The thesis is concluded by measuring the three dimensional properties of

the jet with tomographic PIV at various streamwise location downstream to evaluate the evolution of the TNTI and of the jet's small-scale properties. The choice of this technique is dictated by the need for acquiring three dimensional-three component (3D-3C) data without relying on any assumption (i.e. Taylor's frozen flow hypothesis), to study the jet properties near the exit.

The thesis will therefore assess the following questions:

- *Does the fractal geometry break-up the coherent structures of an axisymmetric turbulent jet? (chapter 3)*
- *How do different states of the coherent structures affect the evolution of the jet towards the self-similar state? (chapter 4)*
- *How do the different states of the coherent structures affect the evolution of the TNTI and of the small scale dynamics? (chapter 5)*

Chapter 2

Methodology

This chapter describes the methodology and procedures undertaken in the course of the research.

2.1 Nomenclature and coordinate system

The data from the particle image velocimetry (PIV) are acquired in a Cartesian coordinate system. Across the whole work, the coordinate system is defined with x as the streamwise component and y and z the orthogonal ones. The instantaneous velocities are U, V and W respectively. In some parts of the work, the Cartesian coordinate system has been converted to a cylindrical one. In that case, r is used to indicate the radial component, whilst θ indicates the azimuthal one. In the potential core, where the round jet has a "top-hat" velocity profile, the location of the jet centre was determined as the minimum value of the rms of the streamwise velocity fluctuations between the two peaks at the shear layers. After the shear layers met, the location of the jet centre was determined by fitting a Gaussian curve to the streamwise mean velocity profile to find the maximum value. The instantaneous velocity components were then converted to U_x, U_r and U_θ, as shown in fig. 2.1. Mean (time-average) and fluctuating velocity are decomposed following

the Reynolds decomposition:

$$U_i = \overline{U_i} + u_i. \tag{2.1}$$

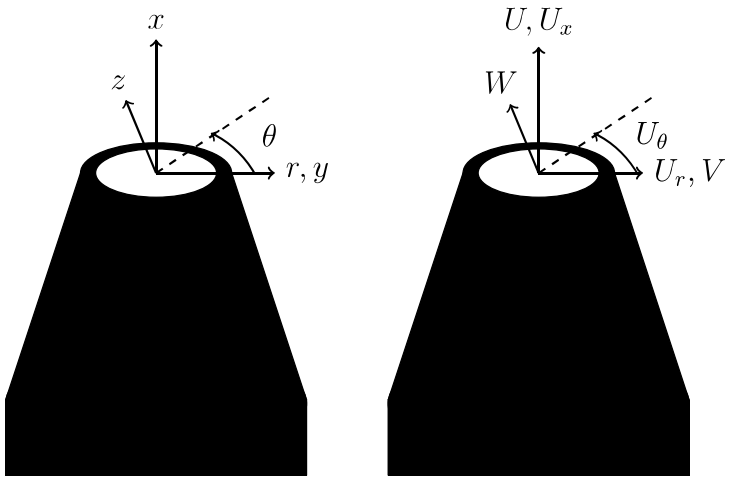


Figure 2.1: (a) Jet's coordinate system for planar and tomographic PIV data and (b) velocity components.

2.2 Jet structure

The flow was generated by an open jet facility at Imperial College London, designed and built specifically for this project, in which the working fluid was air. The flow is conditioned with a honeycomb (hexagonal cells, aspect ratio = 1) and two screens of decreasing mesh size, before it enters a 5^{th} order polynomial contraction. The distance between the first and second grid is 30 mesh lengths (as suggested by Lindgren and Johansson (2002)), whilst that between the second screen and the nozzle is 270 mesh (the finer, downstream mesh) lengths, in order to let the turbulence intensity decay (Mazellier and Vassilicos (2010) suggested that 150 mesh lengths could be potentially sufficient to let the perturbances decay, but in the present case 270 were found to be necessary to minimise the turbulence intensity). A schematic is provided in fig. 2.2. The exit flow is found to have a sharp "top-hat" mean velocity profile and turbulence intensity $< 1\%$. Three different orifices (round, square and fractal) of thickness 0.1 mm and of identical

open area (D_e^2) are attached to the nozzle, as shown in fig. 2.3. Each jet thus has the same exit flow velocity U_e for a given volumetric flow rate,

$$D_e = \sqrt{\text{Exit area}} = 15.8\,\text{mm} \qquad U_e = \frac{\text{Volumetric flow rate}}{\text{Exit area}}. \tag{2.2}$$

Apart from the jet exit shape, all the conditions of the jets are kept the same, since Iyogun and Birouk (2009) showed that nozzle shape and contraction can strongly affect entrainment and mixing and in this way the only differences will be due to the exit geometry. Two Reynolds numbers, defined as

$$Re_G = \frac{U_e D_e}{\nu}, \tag{2.3}$$

of $Re_G = 3,000$ ($U_e = 2.98\,\text{m/s}$) and $Re_G = 10,000$ ($U_e = 9.93\,\text{m/s}$) were chosen, where different regimes of Kelvin-Helmholtz vortices were expected in order to test the Re_G-dependence (which should hold for $Re_G \lesssim 30,000$).

The flow rates through the jet were carefully controlled using an Omega FMA-26 mass flow controller to ensure that these operating conditions were repeatable. As suggested by the manufacturer, the uncertainty regarding the consistency of the flow at the jet exit was estimated to be less than 1%, as detailed in table 2.3. The calculation procedure for the uncertainties is detailed later on in this chapter of the thesis.

Various testing methodologies were used to study the flow. An initial testing campaign of low resolution planar PIV (LPIV) was used to characterise the flow. This was followed by a high resolution PIV (HPIV) experiment to study the dissipation of the jet. Subsequently, hot-wire anemometry (HW) was completed in the far field and in the near field to study the temporal properties of the jet. In these 2D experiments, $U - V$ velocity components from the Cartesian coordinate system correspond to $U_x - U_r$ in the cylindrical one. Finally, tomographic PIV (TPIV) was completed to study the three dimensional properties of the round and fractal jet only. This time the Cartesian velocity components $U - V - W$ were converted to $U_x - U_r - U_\theta$.

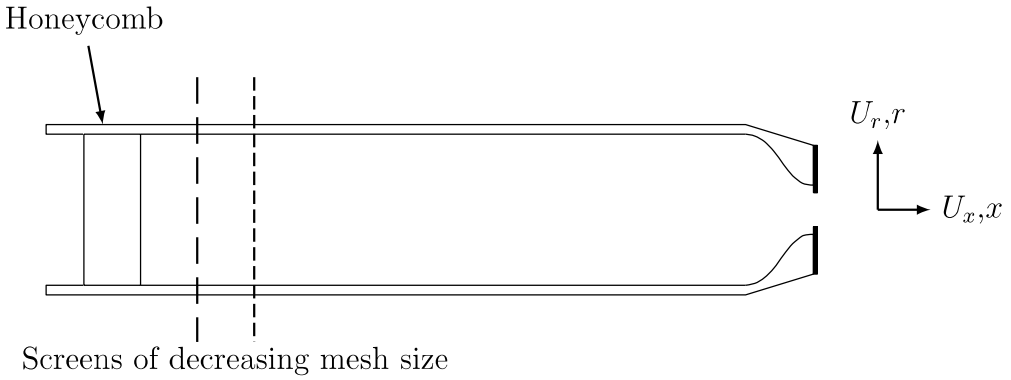
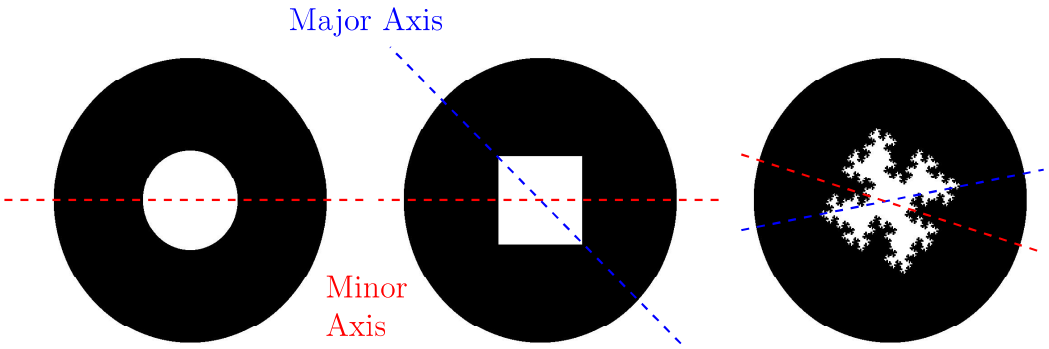


Figure 2.2: Schematic of the jet facility with orifice attached to the exit.



(a) Round ($\mathcal{AR}$= 1) (b) Square ($\mathcal{AR}$= $\sqrt{2}$) (c) Fractal ($\mathcal{AR}$= 2.5)

Figure 2.3: Exit geometries studied. The aspect ratio $\mathcal{AR}$ between major and minor axis is shown.

Now, the different testing campaigns are examined in detail.

2.3 Planar PIV

Particle image velocimetry (PIV) has seen an increasing use in the past decade thanks to its ability to instantaneously measure many points (in the order of $10^3 - 10^5$) at a sufficiently high spatial resolution to resolve the strain-rate and the rate of rotation (Westerweel et al., 2013). Planar PIV allows measuring the 2D properties of a jet in a specific region of the flow. As discussed by Raffel et al. (2007), a PIV system consists of a number of cameras, optical lenses, mirrors, a laser and a flow seeded with illuminated particles. A typical PIV system is shown in fig. 2.4.

A planar PIV experiment involves (usually) a single camera and it allows the measure-

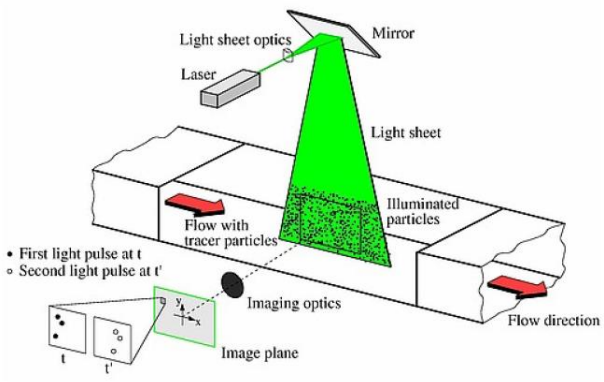


Figure 2.4: A typical PIV system. Figure reproduced from Raffel et al. (2007).

ment of the two-dimensional/two-component (2D-2C) velocity vector across the field of view acquired. In this experiment, a 4 Megapixel camera Imager SX was mounted on a Minitec structure, where its position could be adjusted based on the streamwise location studied. A lens of type AF DC-Nikkor 105 mm f/2D (f-number f/16) was used. The flow was illuminated with a double cavity Nd:YAG low speed laser running at 15 Hz. A seeded low speed co-flow (speed of ≈ 0.1 m/s) was added to the facility to avoid biasing the experiments as background fluid is entrained into the jet and to be able to resolve the edge of the jet. The seeding material chosen was a vestonsint 2159 powder, which combined a good light scattering behaviour and a long enough presence of the co-flow in the background before decaying to complete the acquisition. The particles of this particular powder had diameter of $d_p \approx 10\,\mu$m. The Stokes number is defined as

$$St = \frac{\tau_s}{\tau_f} = 0.18, \quad \tau_s = d_p^2 \frac{\rho_p}{18\mu} = 5 \cdot 10^{-5}\,\text{s}, \tag{2.4}$$

where τ_s is the relaxation time as a function of particle diameter, particle density ρ_p and fluid (in this case air) dynamic viscosity μ. The requirement for the particles to faithfully track the flow is $St \ll 1$, which is the case for this powder. The response time of the flow τ_f was estimated as the Kolmogorov time scale $\tau_f = (\nu/\varepsilon)^{0.5}$. The time delay dt between the two consecutive low-speed PIV frames was set at each station and for each jet (due to the different flow velocities) so that the travel of the particles was between 12 and 15 pixels.

The flow is studied between 0 and $23D_e$ and the laser sheet was placed across the centre line of the jets on the $x-r$ plane, as shown in fig. 2.5. In order to cover this region, four fields of view were imaged with an overlap of approximately 1 D_e. For the noncircular geometries, the flow was imaged across both major and minor axes.

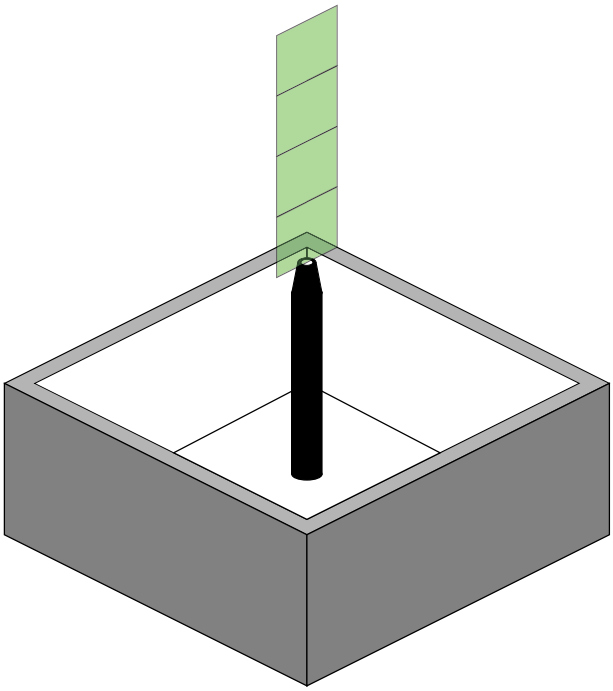


Figure 2.5: Schematics of areas studied with planar PIV.

Table 2.1: Spatial resolution of LPIV experiments (worst case) in terms of equivalent diameter and Kolmogorov lengthscale. The estimate of the dissipation rate (and as a conseuquence of η) is later discussed in section 2.6.

	Round	Square	Fractal
$0-6D_e$	22η $(0.03D_e)$	24η $(0.03D_e)$	22η $(0.03D_e)$
$6-12D_e$	17η $(0.03D_e)$	18η $(0.03D_e)$	18η $(0.03D_e)$
$12-18D_e$	14η $(0.03D_e)$	15η $(0.03D_e)$	15η $(0.03D_e)$
$18-23D_e$	11η $(0.03D_e)$	11η $(0.03D_e)$	12η $(0.03D_e)$

In total, 1,500 images were acquired per jet configuration for each of the four regions at various streamwise locations. The fields of view were of size of approximately $9D_e \times 6.7D_e$. The postprocessing was done on the commercial software DaVis. An initial interrogation area of 64×64 pixels was used to process the images recursively with a final window size of 16×16 pixels. Between each multi-pass iteration, the option *smoothing* was set to optimal (default) to reduce noise and a median filter removed the outliers in each 5×5

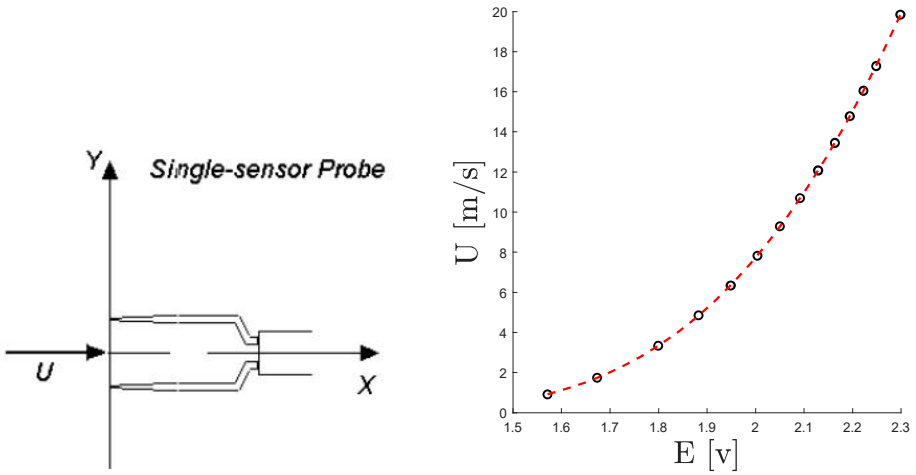
pixels window. A 50 % overlap between adjacent interrogation areas was used leading to a final vector spacing of $0.03D_e$ across all jet configurations. The spatial resolution of each streamwise test is detailed in table 2.1. Spurious vectors were removed and replaced using a similar scheme to Westerweel and Scarano (2005), but the total number of spurious vectors was always found to be less than 4 %. Following the preliminary results of the testing campaign, highly resolved planar 2D2C PIV (HPIV) was performed to investigate the velocity gradients in the near field (2-5 D_e) and in the "far field" (23-26 D_e, where the Reynolds stress profiles are self-similar) at $Re_G = 10,000$. This time, a final interrogation area of 12 × 12 pixels with 50 % overlap was used. This led to a vector spacing of $0.013D_e$ and a spatial resolution of 3.7 Kolmogorov length scales (η) in the far field (after dissipation was corrected following the methodology of Tanaka and Eaton (2007), further details are given in chapter 4) and ranged between 0.08-0.12 longitudinal length scales (λ_f). Further details about the calculation of these length scales are given at the end of this chapter.

2.4 Hot-wire Anemometry

Constant temperature hot-wire anemometry has extensively been used in fluid research due to its excellent signal to noise ratio and frequency response. This technique involves placing a probe inside the flow and measuring the fluctuating electric signal needed to keep the wire at constant temperature in response to the fluctuating convective heating experienced by the wire. This is then converted into a velocity signal with a velocity calibration. In order to obtain one, a voltage is acquired by the hot-wire together with, for example, measurements of velocity from a pitot static tube, ideally in the free stream or in a suitable location where the velocity is known to be the same between the hot-wire and the pitot (i.e. the core of a jet). The calibration is then found by calculating the coefficients C of a 4^{th} order polynomial

$$U = C_0 + C_1E + C_2E^2 + C_3E^3 + C_4E^4, \tag{2.5}$$

where U is the measured velocity and E the voltage. This formula is then applied to the acquired data. An example is shown in fig. 2.6b. As detailed by Dantec, the manufacturer



(a) (b)

Figure 2.6: (a) Example of single hot wire (Manual of Dantec Dynamics) and (b) example of calibration in the near field of the round jet.

of the current hot-wire probes, an increase in temperature of 1 °C can lead to a measurement error of 2%. Despite the lack of windows in the laboratory and, as a consequence, the relatively small temperature variation within it, the hot-wire was re-calibrated after each run of experiments and the temperature was monitored during each run to check it was less than 1 °C different from the temperature the test started with.

In this work, single hot-wire (as in fig. 2.6a) constant temperature anemometry (CTA) was conducted, with an acquisition time of 30 seconds per probe location and a sampling rate of 100 kHz, which was subsequently low-pass filtered at 30 kHz. Gold-plated 55P01 Dantec hot wires were used, the ratio between wire length and diameter was 250 (wire diameter 5 μm, worst case spatial resolution of 1.25 mm $\approx 20\eta$ in the near field and $\approx 12\eta$ in the region $23-26x/D_e$), the overheat ratio was set at 0.8 and the square wave response was above 40 kHz. Comte-Bellot (1976) suggested that a ratio between wire-length and diameter of 200 is necessary to minimise the conductive heat errors. Therefore, the present hot-wire is appropriate to study a turbulent flow. The data were acquired in the near field (0-6 D_e) and in the "far field" (24-26 x/D_e) at $Re_G = 10,000$. A series of points across a radial extent including the jet centreline and the shear layers were acquired at

each streamwise location spaced radially by 1 mm. A final set of experiments was also conducted in the far field at $Re_G = 31,000$ in the same manner.

The testing campaign was concluded with tomographic PIV.

2.5 Tomographic PIV

Tomographic PIV (TPIV) was developed in the Netherlands in 2006 (Elsinga et al., 2006) and it has seen an increasing popularity since then due to its ability to reconstruct the complete three dimensional velocity vector in a volume of a flow. TPIV requires a more complex arrangement compared to planar PIV, since this time the field of view (FOV) is captured by four different cameras (a standard set-up) and a laser volume needs to be generated. An example of the experimental arrangement and of the processing strategy is shown in fig. 2.7.

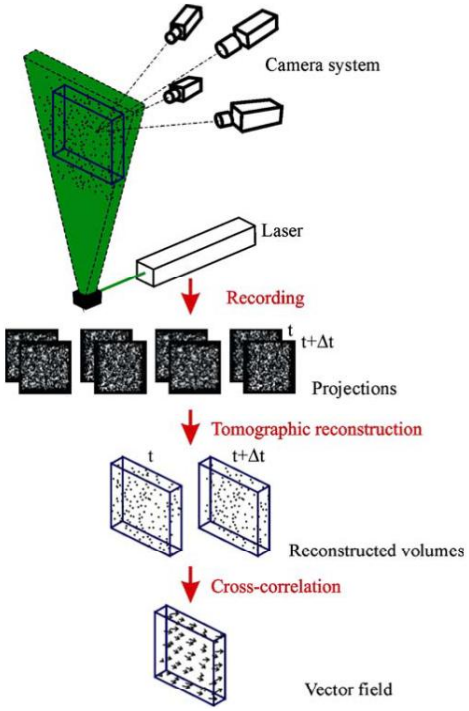


Figure 2.7: Tomographic PIV set up. Figure reproduced from Elsinga et al. (2006).

Generating a volume rather than a laser sheet has important consequences on the spatial resolution that can be achieved by a particular experiment. In fact, differently from a

planar PIV arrangement where a seeding density of 0.15 ppp (particle per pixel) is accepted for a plane, for a TPIV experiment the seeding density should not be greater than 0.05 ppp (Michaelis et al., 2010) for the interrogated volume since otherwise the quality of the volume reconstruction from the four FOVs (cross-correlation) will be severely affected. However, this will also reduce the spatial resolution that can actually be achieved compared to a standard planar PIV experiment. Therefore, reducing the volume thickness allows improving the spatial resolution, which becomes important to study the small-scale structure of a flow. In this research, the TPIV experiment was performed to study the small-scale structure of a turbulent jet and therefore the laser volume thickness was set to be 5 mm (of which ≈ 3 mm was retained after the postprocessing later described) with a variable aperture slit in order to compromise between a reasonable spatial resolution and thick enough volume depth.

Now a brief review of the steps needed to complete a TPIV experiment is given. First, a laser volume is generated by the same double cavity Nd:YAG low speed laser running at 15 Hz, the images are acquired with four cameras, 4 Megapixel Imager SX fitted with four lenses of type AF DC-Nikkor 105 mm f/2D (f-number f/16). An optical calibration is performed by traversing a dotted plate across the whole volume at the positions $\tilde{x} =$ 0 mm, 5 mm[1] and 10 mm and acquiring an image from the cameras in each step. The commercial software Davis was then used to generate the optical three-dimensional calibration knowing the distance between the three streamwise views. However, this first calibration can suffer a calibration error sometimes of the order of 2 pixels. The calibration error arises in the reconstruction step, when each voxel position in space is mapped to a camera pixel position. Here, a voxel represents a three dimensional unit, corresponding to the 3D counterpart of a pixel. In order to achieve a volume reconstruction of high quality, the calibration error needs to be within 0.1 pixels (Elsinga et al., 2006), however this can be difficult to achieve with the optical calibration only. Therefore, in order to improve the calibration quality, a volume self-calibration was completed as discussed by Wieneke (2008). This process involves acquiring a sequence of PIV images and triangu-

[1]Here, $\tilde{x} = 5$ mm is the approximate centre of the laser volume at a given measurement station.

lating the particles, evaluating the error through a disparity map. Here, the 3D position of the particles is calculated in small subvolumes within the reconstructed volume and the triangulation error (i.e. the disparity between the predicted position calculated between different cameras) is averaged inside them. Knowing this error, it is possible to correct the calibration and bring the error down to the required level. In order to have an homogeneous disparity map, the images were recorded running the coflow only. After these initial calibrations, images were acquired switching both coflow and jet on. The TPIV images were processed using the MART algorithm (6 iterations), a multiplicative algebraic reconstruction (Herman and Lent, 1976). This process works as follow. The object is reconstructed as a discretised 3D array of light intensity in physical space $E(X, Y, Z)$ from its projections on the CCD arrays. This problem is under-determined and a lower seeding density usually leads to a better reconstruction. The relationship between the intensity of the i^{th} pixel with image coordinates (x_i, y_i) and the light intensity distribution of the j^{th} voxel in the 3D physical space is given by the linear equation:

$$\sum_{j \in N_i} \omega_{i,j} E(X_i, Y_j, Z_j) = I(x_i, y_i), \tag{2.6}$$

where N_i is the voxel's neighbourhood around the line of sight of the i^{th} pixel (x_i, y_i) through the volume. The weighting coefficient $\omega_{i,j}$ describes the contribution of the j^{th} voxel with intensity $E(X_i, Y_j, Z_j)$ to the pixel intensity $I(x_i, y_i)$ and it is calculated as the volume fraction intersected by the line of sight with the considered voxel. A schematic is shown in fig. 2.8. This process is then completed with an iterative implementation with a predictor-corrector technique and it requires non-zero/uniform initial conditions.

In order to improve the quality of the reconstruction of the images, a dark background previously acquired was subtracted. Sliding minimum subtraction, Gaussian smoothing using a 3×3 pixels kernel to reduce the background noise and sharpening to reduce the number of "ghost particles" (a brief review on ghost particles is given at the end of the section) were also performed on the raw images, allowing the particle diameter to be of the order of 2 pixels and the ppp to be within 0.04 and 0.05. In order to

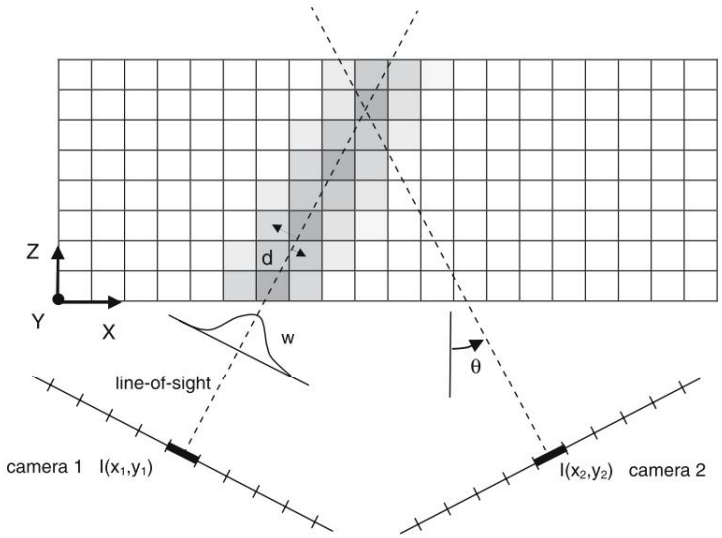


Figure 2.8: Top view schematics of imaging model used for tomographic reconstruction. Figure reproduced from Elsinga et al. (2006).

reduce the postprocessing time sparse cross-correlation (Discetti and Astarita, 2012) was implemented.

The tomographic PIV (TPIV) experiments were conducted at $x/D_e = 2$, $x/D_e = 10$ and $x/D_e = 25$ to study the spatial three dimensional statistics of the jet, as shown in fig. 2.9. The three regions were chosen to study the jet in three different phases: at $x/D_e = 2$, when it is starting to develop, at $x/D_e = 10$, after the shear layers have met, and at $x/D_e = 25$, where the jet is expected to be self-similar at the mean velocity and Reynolds stresses. The laser volume was produced as before at 15 Hz and the image processing was done in DaVis 8.4.

The vectors were reconstructed in three steps: an initial recursive direct correlation[2], followed by two iterations of motion tracking enhancement (MTE) (Novara et al., 2010) to reduce the number of ghost particles and a final recursive direct correlation[3]. A summary of the processing steps together with the computational time is provided in fig. 2.10.

Finally, in order to correct the non-zero divergence of the resultant velocity fields, the data

[2]The first recursive direct correlation was done in steps of specific correlation volume voxel size (passes): $160 \times 160 \times 160(10) \rightarrow 96 \times 96 \times 96(2) \rightarrow 64 \times 64 \times 64(2)$. The volume overlap was 75%.

[3]The second recursive direct correlation was: $160 \times 160 \times 160(10) \rightarrow 96 \times 96 \times 96(2) \rightarrow 64 \times 64 \times 64(2) \rightarrow 48 \times 48 \times 48(2)$. The volume overlap was 75%.

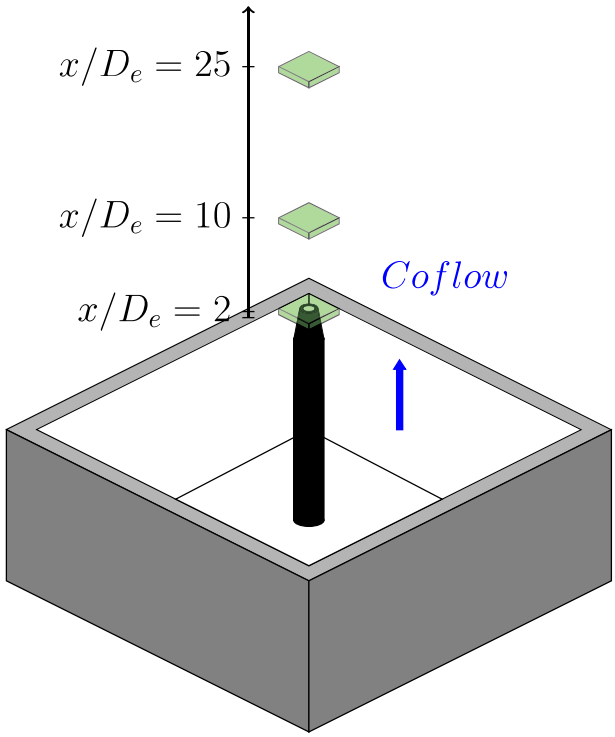


Figure 2.9: Schematics of volumes studied with TPIV.

were corrected using the divergence correction scheme (DCS) as in De Silva et al. (2013). This non-zero divergence is due to experimental noise and, as shown by Buxton et al. (2011a), it can significantly alter the VGT invariants (section 1.2.3), obscuring the shape for example of the $Q - R$ joint probability density function (jpdf). The DCS scheme is based on a non-linear optimisation based constraint which minimally alters the acquired velocity field, whilst restricting the magnitude of the divergence to a maximum tolerance. The objective function to be minimised is the ensemble average of the "turbulent kinetic energy" added to the measured velocity field, i.e. $\tilde{k} = \sum_{i=1}^{3} \langle (U_i - \overline{U}_i) \rangle$, where the velocity is split following the Reynolds decomposition as:

$$U_i = \overline{U}_i + u_i. \tag{2.7}$$

The divergence error was set to be $|\partial \tilde{u}_i / \partial x_i \leq 10 s^{-1}|$ [4] after a convergence study, which led to an average $\tilde{k}/\overline{U}_{cl} < 5\%$ (compensated by the jet streamwise centreline velocity).

[4]The notation $\tilde{\cdot}$ is used to denote the corrected velocity field for tomographic PIV after the DCS is applied. Later it is dropped since the analysis on the 3D-3C data is based solely on the corrected fields.

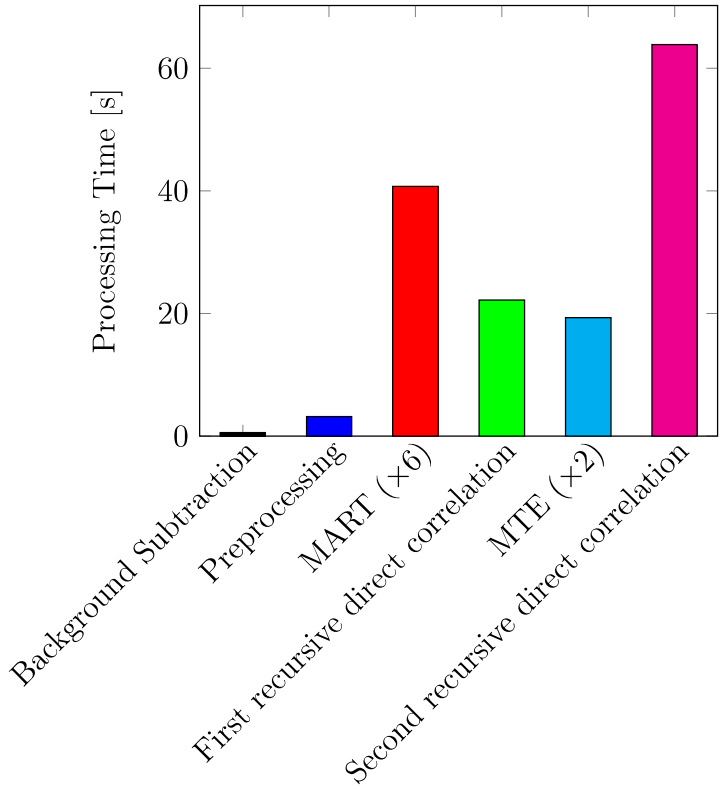


Figure 2.10: Processing time of a single TPIV time step in DaVis. The computer has two processors Intel(R) Xeon(R) CPU ES-2690 v2 at 3 GHz and 128 GB of RAM.

2.5.1 Ghost particles

Ghost particles, as discussed by Maas et al. (1993), are formed at the intersection of line of sight where multiple particles are simultaneously present. They consist of spurious intensity peaks and they are reconstructed together with actual particles. On one side, they cause an underestimate of the "actual" particle displacement gradient magnitude (Elsinga et al., 2011). On the other, ghost particles subtract energy from the actual particles, reducing their accuracy (Elsinga et al., 2011). Differently from the "true" particles, the ghost ones only appear at "random" in one of the two frames used to reconstruct a TPIV volume. Hence, the previously mentioned MTE method is highly effective in predicting the position of an original particle in the two frames and in identifying whether a ghost particle is present due to its random appearance in one of the two frames only.

2.6 Spatial Resolution

The spatial resolution of the different experiments was evaluated in different ways, based on the dimensions and components of velocity available. For the TPIV, the dissipation rate ε was calculated using all nine velocity gradients as detailed in George and Hussein (1991)

$$\varepsilon = \nu\Bigg\{2\Bigg[\left\langle\left(\frac{\partial u}{\partial x}\right)^2\right\rangle+\left\langle\left(\frac{\partial v}{\partial y}\right)^2\right\rangle+\left\langle\left(\frac{\partial w}{\partial z}\right)^2\right\rangle\Bigg]+\Bigg[\left\langle\left(\frac{\partial u}{\partial y}\right)^2\right\rangle+\left\langle\left(\frac{\partial v}{\partial x}\right)^2\right\rangle+\left\langle\left(\frac{\partial u}{\partial z}\right)^2\right\rangle + \left\langle\left(\frac{\partial w}{\partial x}\right)^2\right\rangle+\left\langle\left(\frac{\partial v}{\partial z}\right)^2\right\rangle+\left\langle\left(\frac{\partial w}{\partial y}\right)^2\right\rangle\Bigg] + 2\Bigg[\left\langle\frac{\partial u}{\partial y}\frac{\partial v}{\partial x}\right\rangle+\left\langle\frac{\partial u}{\partial z}\frac{\partial w}{\partial x}\right\rangle+\left\langle\frac{\partial v}{\partial z}\frac{\partial w}{\partial y}\right\rangle\Bigg]\Bigg\}. \tag{2.8}$$

Here the velocity components are reported in a Cartesian coordinate system as in the original work. From eq. (2.8), the Kolmogorov lengthscale was estimated as $\eta = (\nu^3/\varepsilon)^{1/4}$. The transverse Taylor lengthscale λ_g was calculated as in Goto and Vassilicos (2016) inserting the dissipation rate ε calculated in eq. (2.8) and subsequently converted into the longitudinal λ_f as

$$\lambda_g = \sqrt{10\nu\frac{q^2}{\varepsilon}}, \tag{2.9}$$

$$\lambda_f = \sqrt{2}\lambda_g = \sqrt{20\nu\frac{q^2}{\varepsilon}}, \tag{2.10}$$

where q^2 is the turbulent kinetic energy, calculated from the root-mean-square of the velocity fluctuations. Across this thesis, the root-mean-square of a variable will be indicated by primed quantities, i.e. $u' \equiv \sqrt{\overline{uu}}$.

The computation of ε yields to a spatial resolution (worst case) for the TPIV experiment of 11 η at $x/D_e = 2$, of 9η at $x/D_e = 10$ and of 5η at $x/D_e = 25$. In terms of the longitudinal Taylor lengthscale, the spatial resolution ranged between 0.3 and $0.1\lambda_f$ at the three locations studied.

For the HPIV test, the dissipation rate in the far field was calculated assuming the flow would be locally axisymmetric (George and Hussein, 1991) around the x-axis and the

longitudinal Taylor lengthscale was estimated as in eq. (2.10)

$$\varepsilon = \nu\Big[-\left\langle \left(\frac{\partial u}{\partial x}\right)^2 \right\rangle + 2\left\langle \left(\frac{\partial u}{\partial y}\right)^2 \right\rangle + 2\left\langle \left(\frac{\partial v}{\partial x}\right)^2 \right\rangle + 8\left\langle \left(\frac{\partial v}{\partial y}\right)^2 \right\rangle \Big], \tag{2.11}$$

$$q^2 = \frac{u'^2 + v'^2 + w'^2}{2} = \frac{u'^2 + 2v'^2}{2}, \tag{2.12}$$

where q^2 is calculated assuming axisymmetry ($v' = w'$).

Additionally, a HPIV test was conducted in the near field, $2 \leq x/D_e \leq 6$, in order to estimate the dissipation rate since a spatial resolution that is twice as fine as that of the TPIV in the near field could be achieved. The resolution of this HPIV data was estimated to be between $6 - 13\eta$. The dissipation rate estimated from the TPIV data set and the HPIV data set, using the assumption of local axisymmetry (George and Hussein, 1991), were found to differ by up to 50% due to the coarse spatial resolution of the TPIV. In fact both estimates of dissipation are likely to be underestimates since a resolution of $\sim 3\eta$ is considered necessary to resolve the dissipative scales of a turbulent flow (Worth et al., 2010; Buxton et al., 2011b). Nevertheless, in terms of the longitudinal Taylor lengthscale λ_f (computed from the HPIV dataset), the spatial resolution of the TPIV was always less than $0.4\lambda_f$, which is deemed more than sufficient to resolve the large-scale vortical structures. A similar spatial resolution of $\approx 0.4\lambda_f$ was also achieved with the hot-wire in the near field.

Table 2.2: Processing details for Planar and Tomographic PIV. The worst case scenario for the spatial resolution is reported.

	LPIV	HPIV	TPIV
Initial interrogation window	64×64 pixels	64×64 pixels	$160 \times 160 \times 160$ voxels
Final interrogation window	16×16 pixels	12×12 pixels	$48 \times 48 \times 48$ voxels
Overlap	50%	50%	75%
Spatial resolution ("far field")	11η	$\approx 4\eta$	5η
Digital Resolution (px/mm)	16.7	28.0	45.7
Size of Field of View (mm)	141×106	85×63	$33 \times 29 \times 5$

In chapter 4, a correction method for the dissipation estimate is applied to the data at $x/D_e = 23 - 26$. In fact, as shown by Tanaka and Eaton (2007), the inherent noise present in the velocity gradients attributed to the sub-pixel discrimination algorithm in

the PIV processing can be corrected by calculating the dissipation rate from a coarser stencil ($\varepsilon_{2\Delta h}$) and from the fully resolved measurements ($\varepsilon_{\Delta h}$) as

$$\varepsilon = \frac{4\varepsilon_{2\Delta h} - \varepsilon_{\Delta h}}{3}. \tag{2.13}$$

This methodology indicated that the originally calculated spatial resolution for the HPIV test in the far field improved from 5.5 to 3.7η. A summary of the spatial and of the camera digital resolution[5] is reported in table 2.2.

2.7 Uncertainties

Different methodologies were considered to estimate the uncertainties for the various PIV and hot-wire experiments. As detailed by the manufacturer, the uncertainty of the massflow meter was calculated as follows

$$\text{Uncertainty} = \pm 0.4\% \text{ of Reading} + 0.2\% \text{ of Instrument Full Scale.} \tag{2.14}$$

For the low resolution PIV, the convergence of the root-mean-square (r.m.s) of the streamwise velocity fluctuations, u'_x, based on the number of images was checked and an uncertainty band was determined once the values were found to converge. It was found that the r.m.s. would converge after 1,000 images, leading to an error band usually within $\pm 2\%$, but never greater than $\pm 4\%$. For the highly resolved PIV data, the uncertainty was estimated by fitting a parabola to the two-point autocorrelation, $R_{u_x x}$, of the streamwise velocity fluctuations, u_x, in the streamwise direction x, with increment ξ

$$R_{u_x x}(x, r, \xi) = \frac{\langle u_x(x, r) u_x(x + \xi, r) \rangle}{u'_x(x, r) u'_x(x + \xi, r)}. \tag{2.15}$$

As indicated by Pope (2000), a parabolic behaviour is expected by $R_{u_x x}$ as $\xi \to 0$, by the

[5]The digital resolution refers to how close the camera is to the object, whilst the spatial resolution is also a function of the final interrogation window of the PIV cross-correlation.

central limit theorem. Therefore, the difference between $R_{u_x x}(x, r, 0)$ and the parabola fitting at $\xi = 0$, which ideally should be zero, gives an indication of the experimental error. In the regions studied the uncertainty was found to be never greater than $\pm 2\%$. Later at the end of chapter 4, error bars are reported for some quantities such as turbulent kinetic energy and centreline velocity. These were derived through error propagations, which is done by calculating a value of a quantity at a specific location averaging across an increasing number of time steps to see how it oscillates with respect to the value it converges to. A similar approach was used by Baj and Buxton (2017), amongst others. Regarding the estimate of quantities involving the velocity gradients, such as the dissipation rate ε, the data were found to converge within $\pm 2.5\%$. For the hot-wire data, a similar procedure was performed on the autocorrelation of u_x. The uncertainty was found to be less than 5% in the near field and it was less than 1% in the "far field" regions. For the tomographic PIV, the uncertainty is evaluated through the previously mentioned DCS, scheme, which showed that a maximum of 5% of vectors was replaced at the three streamwise locations studied.

Re_G	3,000	10,000	31,000
Massflow meter	$\pm 0.84\%$	$\pm 1.00\%$	$\pm 0.62\%$
PIV (low resolution)	$\pm 2 - 4\%$	$\pm 2 - 4\%$	
PIV (high resolution)		$\pm 2\%$	
Hot-wire		$\pm 2\%$	$\pm 5\%$

Table 2.3: Uncertainty of the massflow meter, PIV and hot-wire anemometry at different Re_G N.B. the procedure for calculating the uncertainty estimates of the PIV and hot-wire anemometry is presented at the end of this chapter.

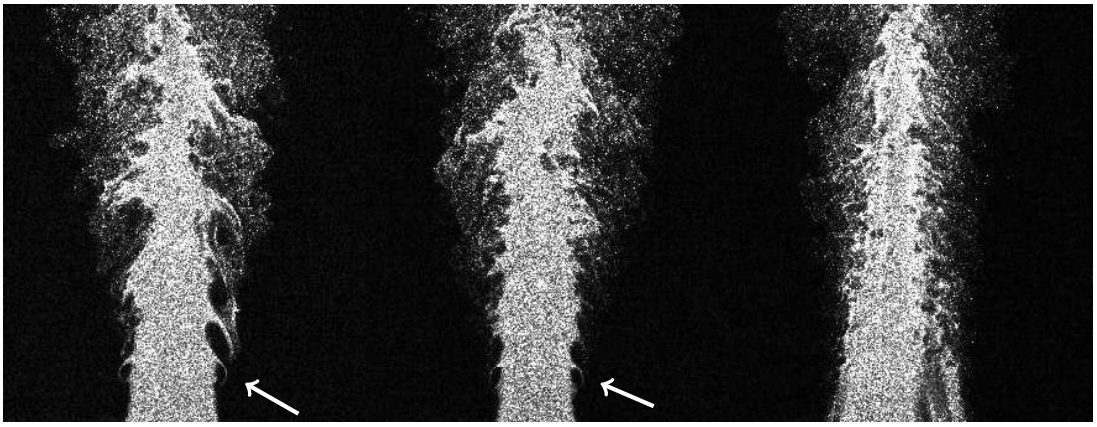
Chapter 3

Breaking up of coherent structures with fractal geometry

In this chapter, the break-up of the coherent structures due to the fractal exit geometry is examined. Part of the findings are published in Breda and Buxton (2017) and Breda and Buxton (2018a).

3.1 Definition

Since the work of Brown and Roshko (1974), the "coherent structures" of a turbulent shear flow have attracted numerous studies, but lacked a formal definition. One of the first authors to provide one was Hussain (1986), which defined them as: *a connected turbulent fluid mass with instantaneously phase-correlated vorticity over its spatial extent.* Visually, coherent structures for a round jet can be identified as a series of vortex rings rolling-up at the jet exit, travelling and bursting further downstream. Therefore, a good way to evaluate the break-up of the coherent structures may be conducting a flow visualisation experiment, like seeding the jet only to verify the presence of the Kelvin-Helmholtz vortex rings as in fig. 3.1. However, flow visualisation itself is not sufficient to discard the presence of structures which meets the definition given above by Hussain (1986); in order



(a) Round (b) Square (c) Fractal

Figure 3.1: PIV images for visualisation purposes only, the Kelvin-Helmholtz vortex rings are indicated by the white arrows. N.B. for clarity the co-flow was switched off when capturing these images.

to evaluate the state of coherent structures, three-dimensional data are needed such that the vorticity can be calculated. However, it may not always be possible to access the full vorticity vector, due to experimental/numerical limitations. Hence, two methodologies are proposed below to evaluate the state of the coherent structures: one based on 2D planar PIV data and one on 3D-3C tomographic PIV data. Henceforth, streamwise velocity U_x, radial velocity U_r and azimuthal velocity U_θ are split into their mean and fluctuating parts, following the Reynolds decomposition.

3.2 2D evaluation

In order to describe the state of the coherent structures, the two point correlation of the velocity fluctuations u_r in the streamwise direction x as a function of a streamwise increment ξ and compensated by the the root-mean square (r.m.s.) of the velocity fluctuations u'_r, as defined in eq. (3.1), was calculated from the 2D planar LPIV data.

$$R_{u_r x}(x, r, \xi) = \frac{\langle u_r(x, r) u_r(x + \xi, r) \rangle}{u'_r(x, r) u'_r(x + \xi, r)} \tag{3.1}$$

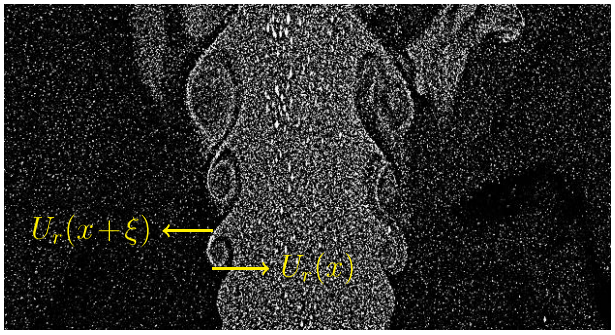


Figure 3.2: Schematic of the two point correlation $R_{u_r x}(x, r, \xi)$. The round jet taken as an example is generated by the nozzle contraction.

Here, the ensemble average $\langle * \rangle$ indicates an average in both time and space of the correlation (within a 3×3 vector box, of approximately $5\eta \times 5\eta$ surrounding the location (x, r) to improve the statistical convergence of the correlation, whilst ensuring the results are insensitive to the size of the box chosen. The 3×3 size was found to be appropriate after a convergence study[1]. This two-point correlation should highlight an anti-correlation (i.e. the change of sign of U_r across some characteristic length scale as shown in the schematic of fig. 3.2), which is associated with the azimuthal component of vorticity of the Kelvin-Helmholtz vortex rings. Hence the lack of it would suggest that the coherent structures have been broken-up.

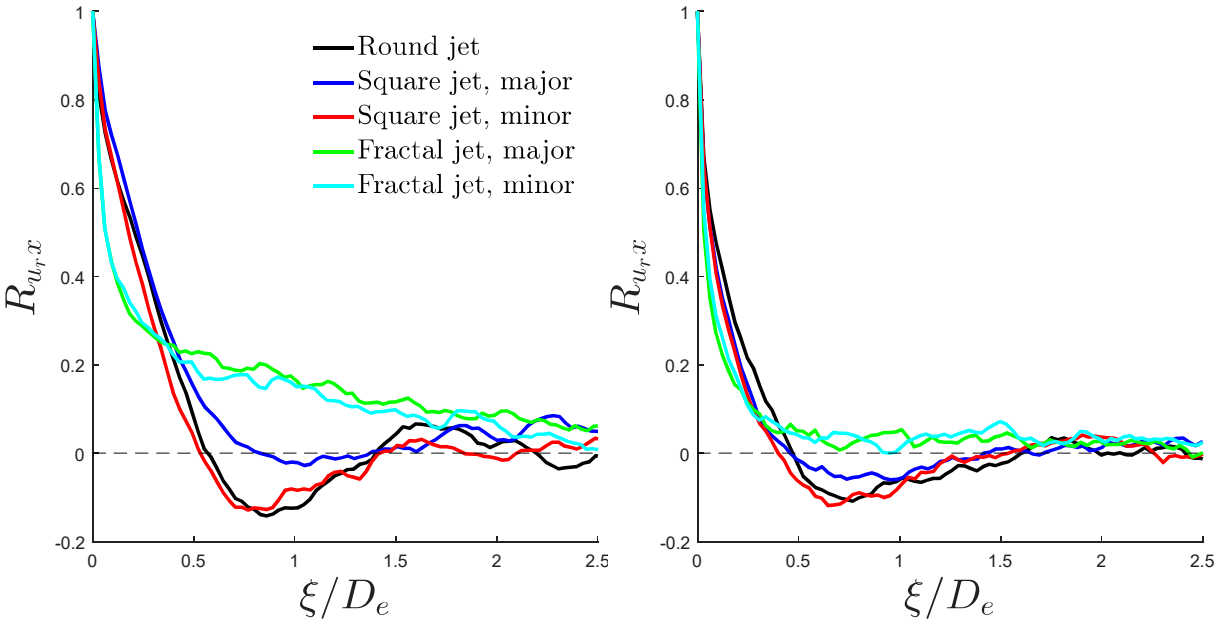
As shown in fig. 3.3, the fractal geometry suppresses the negative anti-correlation at both the centreline and shear layer, where the latter is located at the peak[2] of the r.m.s of the streamwise velocity fluctuations $u'_x(x)$.

To examine the consequences of this suppression of the Kelvin-Helmholtz vortices on the axisymmetric shear layer, the combined correlation of streamwise and radial velocity fluctuations R_{ii_r} is analysed as a function of the radial increment ψ,

$$R_{ii_r}(x, r, \psi) = \frac{\langle u_x(x, r)u_x(x, r + \psi) + u_r(x, r)u_r(x, r + \psi)\rangle}{u'_x(x, r)u'_x(x, r + \psi) + u'_r(x, r)u'_r(x, r + \psi)}, \tag{3.2}$$

[1]Whilst the use of a spatial averaging would certainly affect the conclusions on the small scales, in this case the authors only want to show the effect of exit geometry on the decorrelation of $R_{u_r x}$, which scales with the integral lengthscale.

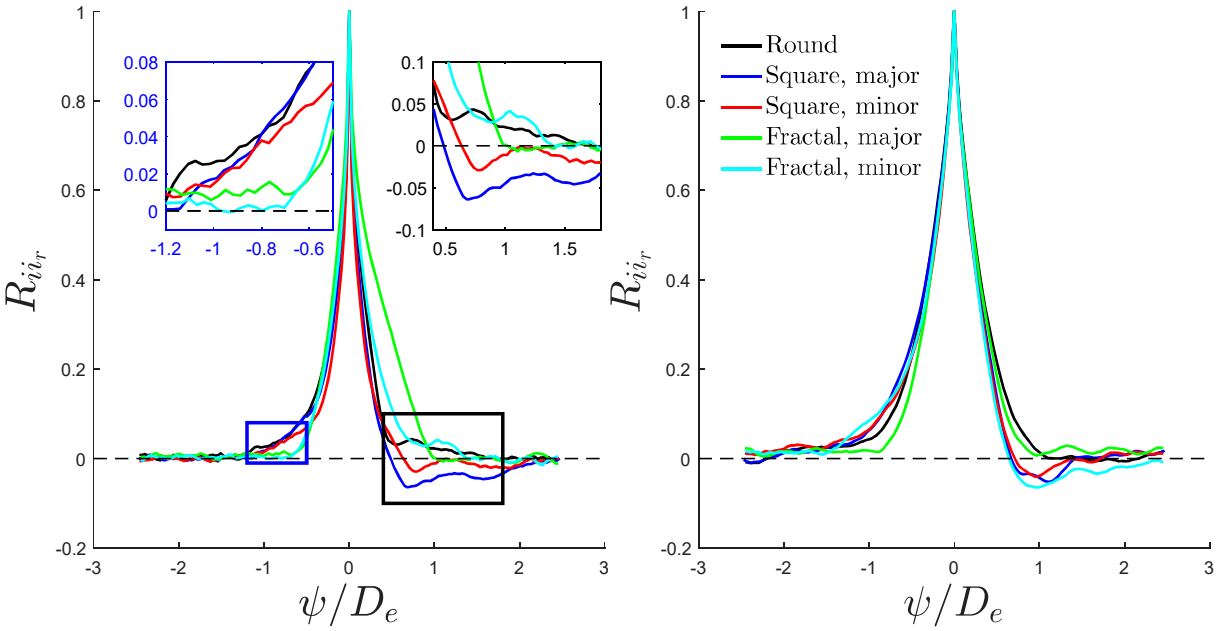
[2]There are two peaks for a given PIV field of view, however the results are comparable between each side of the (approximately, in the case of the fractal jet) axisymmetric shear layer.



(a) Centreline (b) Shear Layer

Figure 3.3: Two point correlation $R_{u_r x}$ as a function of increasing streamwise increment ξ at $x/D_e = 3$ at $Re_G = 10,000$ (LPIV data).

to evaluate the influence of the coherent structures on both streamwise and radial fluctuations. Again, as shown in fig. 3.4, a markedly different behaviour is found between the fractal jet, where it is shown that the near-field coherent structures have been suppressed, and the round and square jets, where the Kelvin-Helmholtz vortex rings are still present as indicated in fig. 3.1. At $x/D_e = 2$, when the correlation is directed towards the irrotational background fluid, the fractal jet is found to decay more rapidly, indicating a thinner shear layer, in part due to the suppression of the coherent structures. When the correlation is directed towards the core, the fractal jet decays more slowly further confirming the observation of a thinner shear layer. In fact, the lack of the Kelvin-Helmholtz vortices reduces the amount of irrotational fluid "moved" towards the jet core, slowing down the growth of the shear layer and the decay of the correlation R_{ii_r}. Despite such differences near the jet exit, at $x/D_e = 11$ the jets show comparable behaviour. Having discussed the potential break-up of the coherent structures due to fractal geometry from two-dimensional data, now this topic is explored through the TPIV results.



(a) $x/D_e = 2$ (b) $x/D_e = 11$

Figure 3.4: Two point correlation R_{ii_r} in the radial direction before (a) and after (b) the shear layer has coalesced at $Re_G = 10,000$. In both the correlation is calculated at the shear layer, located as the radial location at which $u'_x(x)$ is maximum. Positive ψ is directed towards the centre, while negative ψ towards the irrotational background flow.

3.3 3D evaluation

The tomographic PIV data give access to the full 3D vorticity vector. The vorticity is evaluated in polar coordinates

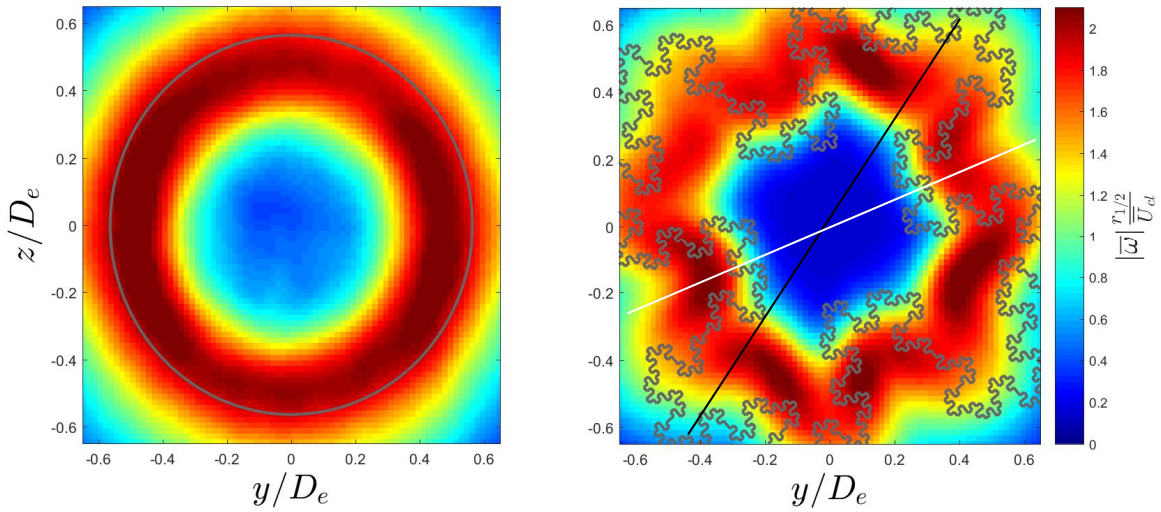
$$\omega = [\omega_r, \omega_\theta, \omega_x]. \tag{3.3}$$

An initial evaluation of the state of the coherence is done by analysing the time averaged mean vorticity in cylindrical coordinates, calculated as:

$$|\overline{\omega}| = \overline{\sqrt{\omega_r^2 + \omega_\theta^2 + \omega_x^2}} \tag{3.4}$$

in the near-field, compensated by the mean streamwise centreline velocity $\overline{U}_{cl}$ and by the jet half-width $r_{1/2}$ defined as:

$$\overline{U}_x(x, r_{1/2}) = 0.5\overline{U}_{cl}(x) \tag{3.5}$$

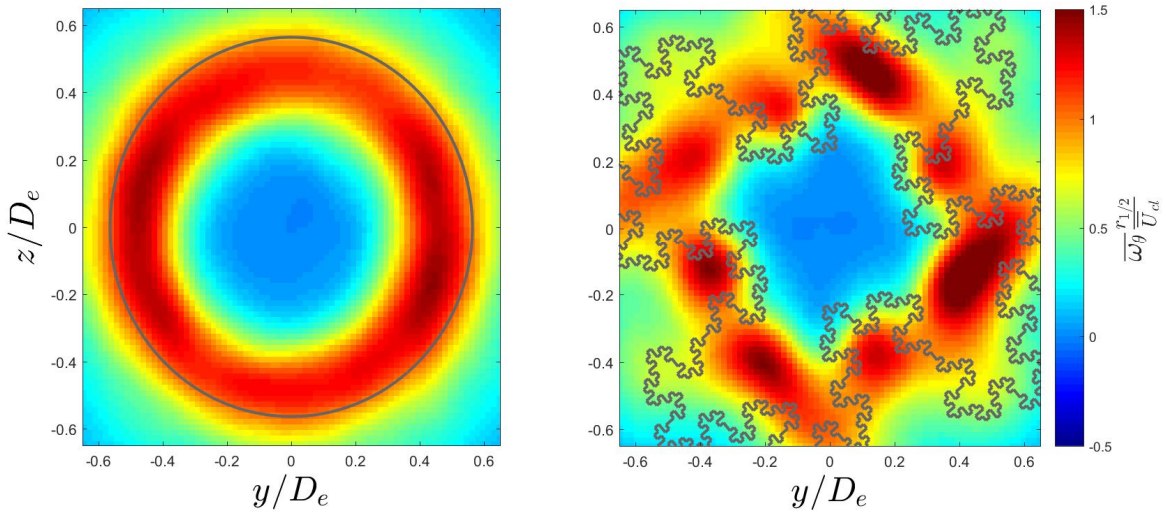


(a) Round (b) Fractal

Figure 3.5: Mean vorticity $|\overline{\omega}|$ at $x/D_e = 2$ and $Re_G = 10,000$. The exit geometry is shown in the background in grey. The major axis is shown by the black line, while the minor one by the white line.

For an axisymmetric jet, it is expected that the coherent structures will lead to a coherent region of vorticity surrounding the jet core, due to the development of the Kelvin-Helmholtz vortex rings. This is found to be the case, as shown in fig. 3.5a. For the fractal jet, it can be observed in fig. 3.5b that the multiscale geometry determines the presence of isolated areas of high absolute magnitude vorticity, even though the jet appears to be largely coherent around its core. However, the single components of the vorticity vector still need to be assessed, since as detailed by Violato and Scarano (2011), modifying the state of the coherent structures with the aid of a chevron nozzle led to a reduction of the azimuthal vorticity ω_θ and to an increase of the streamwise ω_x and radial ω_r vorticity components. Hence, the orientation of the vorticity vector is now evaluated to assess if vorticity remains coherent on at least one of its components. The first one to be investigated is the azimuthal vorticity ω_θ. As shown in fig. 3.6a, the coherence of the round jet is shown by a well defined vortex-ring around the core, which is expected due to the evolution of the Kelvin-Helmholtz vortex rings. Further, it is confirmed that most of the contribution to the vorticity vector is due to its azimuthal component, as visualised in fig. 3.7a and fig. 3.7c

$$|\omega_\theta| \gg |\omega_r| \approx |\omega_x| \approx 0, \tag{3.6}$$



(a) Round (b) Fractal

Figure 3.6: Azimuthal mean vorticity at $x/D_e = 2$ and $Re_G = 10,000$ (TPIV data).

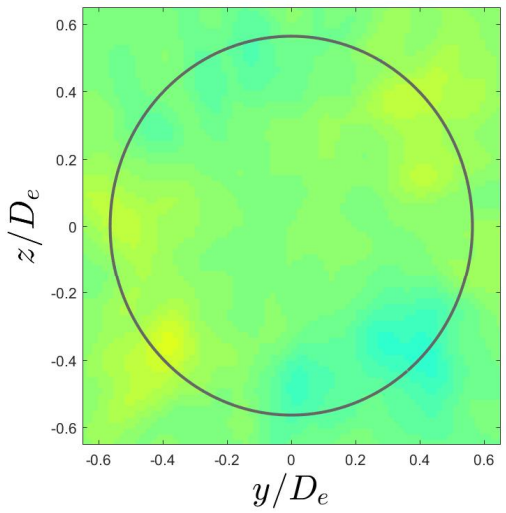
whilst the radial and streamwise components remain negligible. In comparison, the fractal jet is found to have a different behaviour. In fact, its azimuthal vorticity is characterised by patches of high vorticity divided by the fractal geometry, as shown in fig. 3.6b. Moreover, it is found that the patches of high vorticity along the major axis are starting to move inwards towards the centre of the jet. Further, the suppression of coherence leads to the formation of opposite signed radial and streamwise patches of vorticity, with magnitude significantly higher than the round jet, as shown in fig. 3.7b and fig. 3.7d

$$|\omega_\theta| \gtrsim |\omega_r| \gtrsim |\omega_x|. \tag{3.7}$$

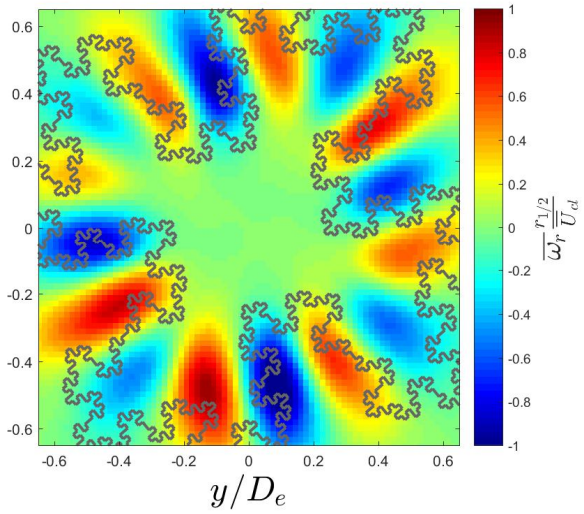
Moreover, the radial vorticity is found to have a comparable magnitude to the azimuthal vorticity, whilst it was almost negligible for the round jet.

Therefore, none of the components of the mean vorticity vector of the fractal jet can be defined as "coherent" in the mean, since the azimuthal vorticity is split into patches whilst streamwise and radial components are divided in opposite-signed regions, which may indicate that the vorticity components are not instantaneously coherent too. Examples of the instantaneous single components of vorticity, which are specifically referenced in the definition of Hussain (1986) for a coherent structure, for the fractal jet are shown in fig. 3.8

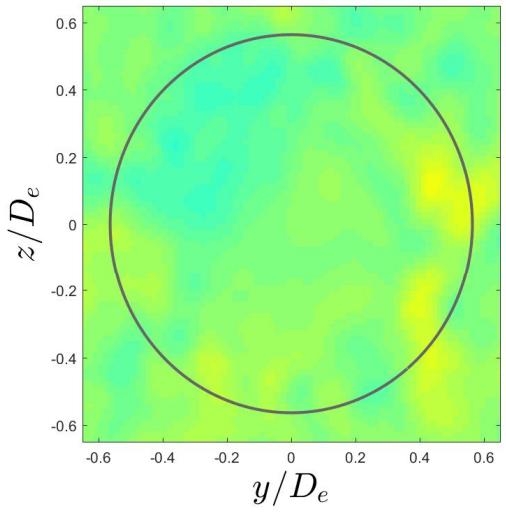
and fig. 3.9. Effectively, the fractal geometry determines a mean transfer of vorticity from the azimuthal towards the radial and streamwise components, due to the break-up of the vortex rings. The transferred vorticity does not lead to the formation of phase-correlated structures, since $\overline{\omega_r}$ and $\overline{\omega_x}$ shows the presence of new opposite signed patches of vorticity which indicates that the formation of instantaneously phase-correlated structures is likely halted. Therefore, the vorticity vector confirms the findings of the 2D LPIV experiment in the previous section, which suggested that the fractal geometry leads to a break-up of the coherent structures. Similar findings have been shown for other turbulent flows, such as jets fitted with a fractal grid (Cafiero et al., 2015), grid-generated flows (Melina et al., 2016) and axisymmetric wakes (Nedić et al., 2013a).



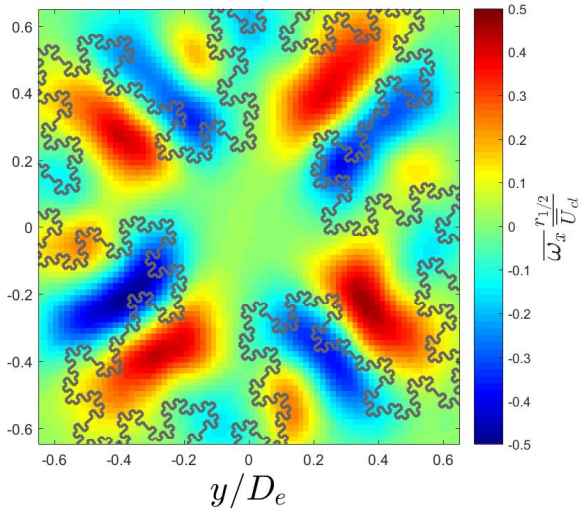
(a) Round



(b) Fractal



(c) Round



(d) Fractal

Figure 3.7: Radial and streamwise mean vorticity at $x/D_e = 2$ and $Re_G = 10,000$ (TPIV data).

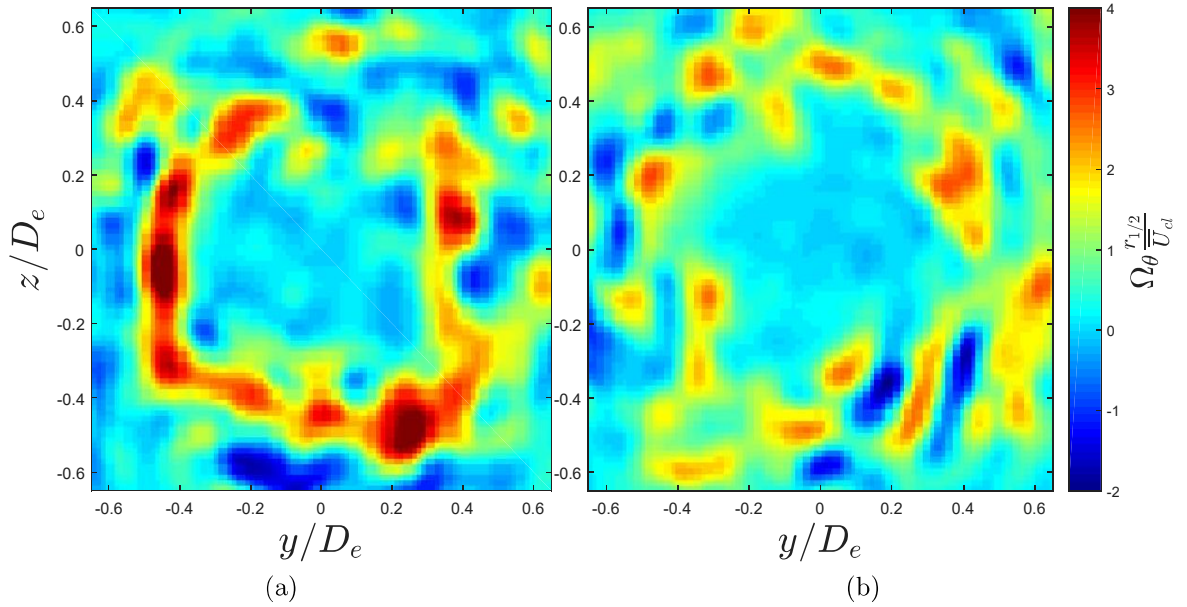


Figure 3.8: Instantaneous azimuthal vorticity for (a) round and (b) fractal jet (TPIV data, $Re_G = 10,000$).

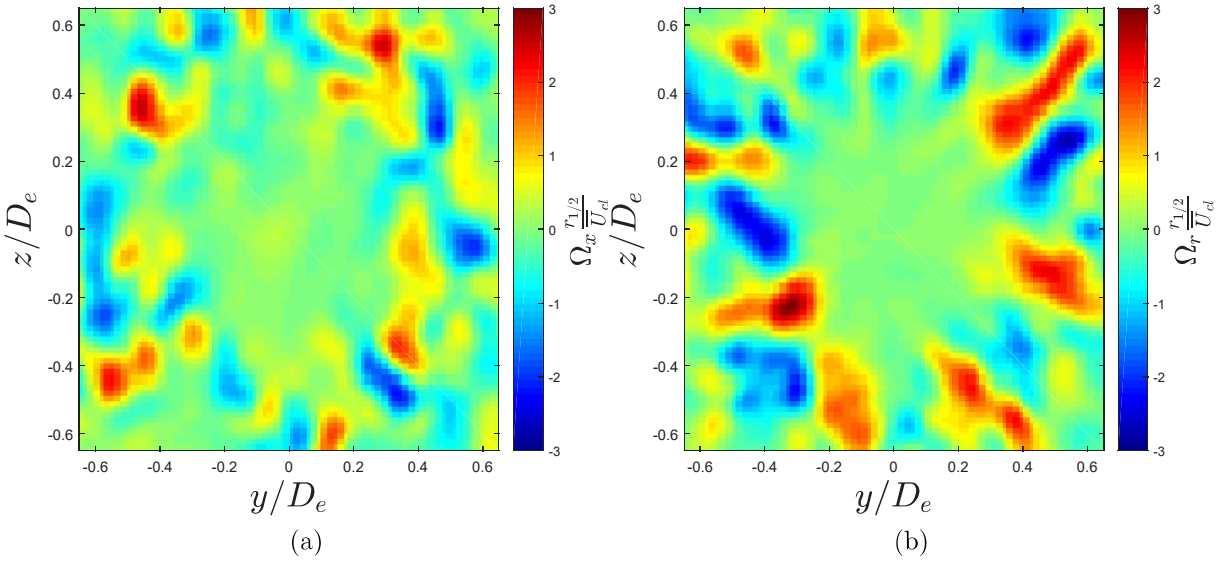


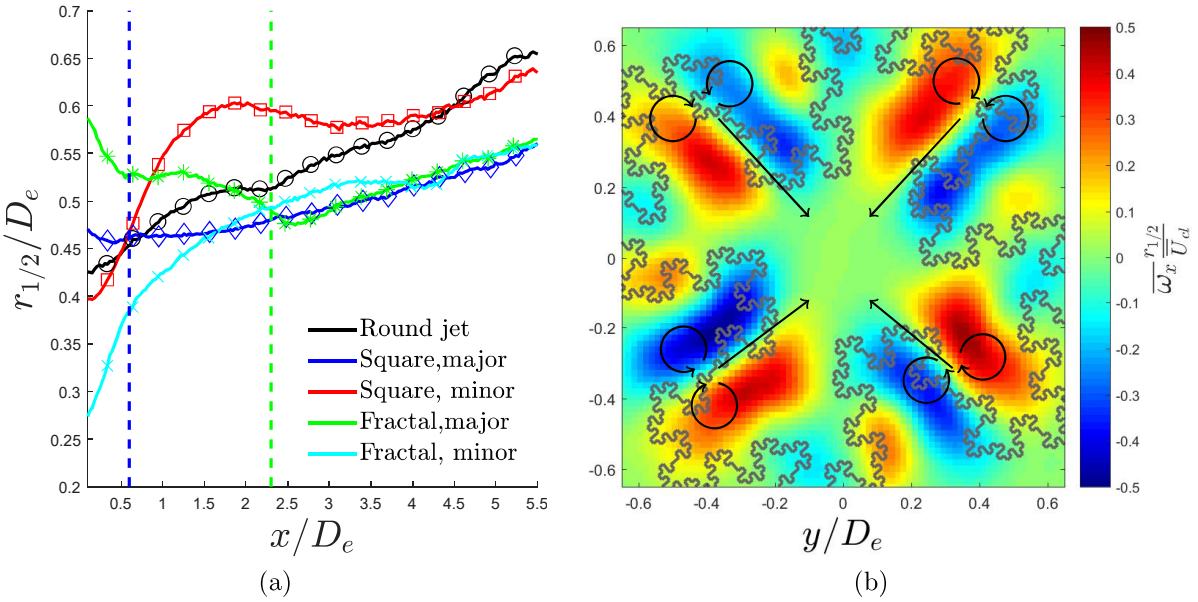
Figure 3.9: Instantaneous (a) streamwise and (b) radial vorticity for the fractal jet (TPIV data, $Re_G = 10,000$).

3.4 Noncircular geometries' axis-switching

As mentioned in the previous section, $\overline{\omega_\theta}$ was found to move inwards towards the jet centre along the major axis in fig. 3.6b, whilst the opposite took place along the minor axis. This suggested the presence of a phenomenon called "axis-switching". The latter, where the major axis of the jet shrinks as the minor one expands, has been found before to be linked to the behaviour of ω_x and ω_θ. It has been previously reported for square jets (Quinn, 1992a; Zaman, 1996), but it has not been observed for jets where the coherent structures were suppressed due to, for example, the fractal geometry. A first observation can be drawn from fig. 3.5b, where it is observed that the regions of high vorticity across the major axis are moving towards the jet centre compared to the exit geometry, while the ones across the minor axis are expanding away from the core. Further, axis-switching is identified for both square and fractal geometry in fig. 3.10a at $x/D_e = 0.6$ and $x/D_e = 2.3$ respectively, where the jet half-width imaged across the major axis becomes smaller than the one at the minor axis. This may somewhat imply that this phenomenon is not influenced by the state of the coherent structures.

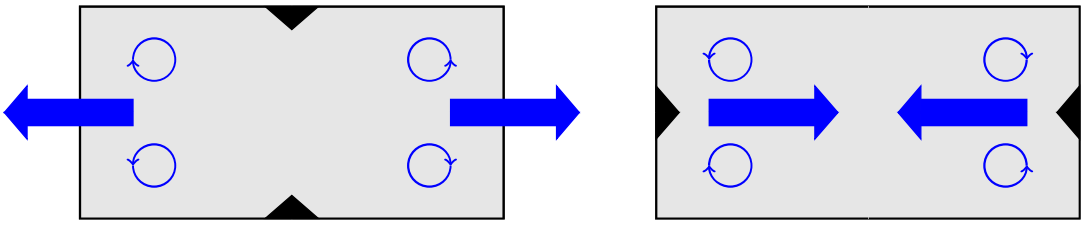
The different location of the crossover could be due to the different AR of the two noncircular geometries. Quinn (1992b), testing rectangular jets of varying AR, found that increasing the aspect ratio moved the location of the crossover further away from the jet exit. Here, it seems this may be the reason for the present study, since the fractal jet, that has the crossover point the farthest away from the jet exit, also has the highest AR. This phenomenon has been found before for various noncircular jets and it was explained through the contribution of ω_θ (Hussain and Husain, 1989) and ω_x (Zaman, 1996). The former was mainly linked to the different induced velocity between the major and the minor axes across an elliptical vortex ring, leading to the faster segments curling up and protruding from the jet core. For the fractal jet at issue, however, this is not found to be the leading cause of axis-switching due to the break-up of the azimuthal vorticity.

The study of Zaman (1996), who tested rectangular jets fitted with tabs alternatively on the major or on the minor axes, suggested that axis-switching would take place only if



(a) (b)

Figure 3.10: (a) Jet half-width $r_{1/2}$ for various jets. The location of the axis-switch of the noncircular geometries is shown by a dashed line ($Re_G = 10,000$ and LPIV data). (b) Mean streamwise vorticity ω_x at $x/D_e = 2$ and $Re_G = 10,000$ (TPIV data). The opposite-signed vortex regions leading to the axis-switching are shown by the arrows.



(a) No axis-switching (b) Axis-switching

Figure 3.11: Schematics of the jets fitted with tabs that promoted and halted axis-switching (Zaman, 1996).

the non-circular geometry emitted regions of opposite-signed streamwise vorticity with the signs as in fig. 3.11b, where flow would be injected towards the jet centre, thereby shrinking the major axis. However, if the signs of the streamwise vorticity were as in fig. 3.11a, the flow would be ejected towards the ambient and therefore axis-switching would not occur. As shown in fig. 3.10b, the fractal geometry generates regions of opposite-signed streamwise vorticity, whose direction makes them inject fluid towards the jet centre, indicating that for this jet the ω_x dynamics is likely responsible for the axis-switching. Of course, ω_x does not exclude a relevant contribution of ω_θ too, since its asymmetrical distribution could also be responsible of this phenomenon. However, the streamwise

vorticity certainly plays the key role of shrinking the major axis, allowing this phenomenon to take place. The streamwise location of the axis-switching appears to be due to the aspect ratio of the jet rather than being linked to the vorticity.

Having established the difference state of coherent structures between round and fractal jet, the entrainment and mixing performances and the subsequent evolution towards the far field of the jets are analysed in the next chapter.

Chapter 4

Jet evolution due to coherent structures

The results presented in this chapter are published in Breda and Buxton (2017) and Breda and Buxton (2018b).

4.1 Delay of development of jet properties

Having established that differently from the round and square jets, the fractal geometry leads to a break-up of the coherent structures, now the evolution of the jets is evaluated. This is first done by evaluating the mean length of the potential core for the three jets, defined as the region where the streamwise fluctuations u'_x are an increasing function of x at the jet centreline. As shown by fig. 4.1, it can be seen that the reduction in u'_x for the fractal jet relative to the round and square jets is due to the extension of the potential core length. In fact, the location of the peak turbulent fluctuations is pushed further downstream from $x/D_e = 6$ (round and square jets) to $x/D_e = 9$ (fractal jet). As mentioned before in chapter 3, this suggests that the fractal jet reduces the energy content in the coherent motions and produces a thinner shear layer that coalesces at the centreline further downstream relative to the other two jets, thereby delaying the development of

the jet's turbulent properties.

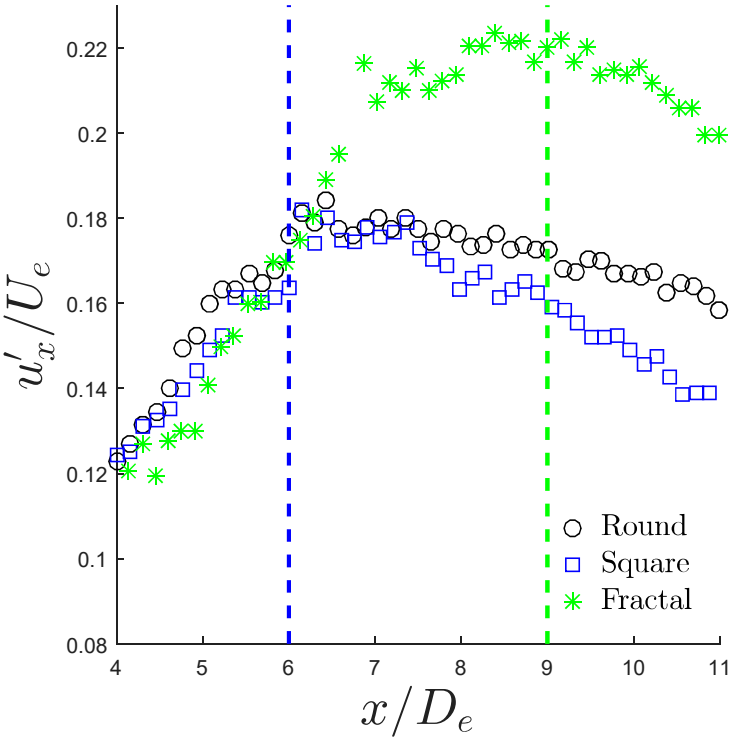


Figure 4.1: Streamwise r.m.s. of streamwise velocity fluctuations in the near field at $Re_G = 10,000$ (LPIV data). A marker is plotted every 5 data points to avoid clutter.

4.2 Rescaling streamwise distance into eddy turnover times

As suggested by Hunt (1994), the turbulent structure of a shear flow is not necessarily independent of the initial conditions, since the advection time for an eddy to travel along the turbulent stream would be linked to its growing (or eddy turnover) time scale. Hence, despite entraining irrotational (and therefore "memoryless") background fluid into the jet stream, the eddies would still be affected by the initial conditions, albeit this "memory" is diluted by continuous entrainment. Fig. 3.1 and fig. 4.1 shows that the fractal geometry has modified the flow physics in the near field, in particular by suppressing the large-scale coherence embedded into the flow, thereby delaying the coalescence of the axisymmetric shear layer. Therefore, these jet physics are now revisited in terms of the advection time

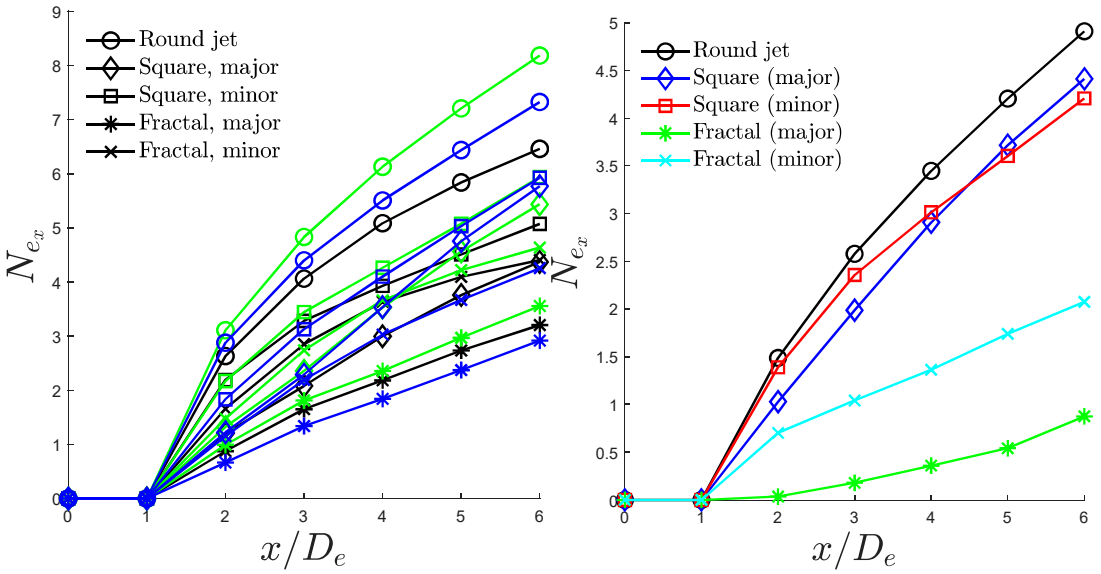


Figure 4.2: (a) Number of eddies overturned in the time taken for the flow to advect distance x, N_{e_x}, as calculated in eq. (4.1) from the shear layer (HW data), centreline velocity (HW data) and characteristic jet velocity (PIV data) at $Re_G = 10,000$. (b) N_{e_x} calculated with the mean velocity at the shear layer at $Re_G = 31,000$ (HW data).

scale (which is a function of the mean velocity) compensated by the local eddy turnover time (which is a function of the eddies' velocity and length scales), defining a new quantity N_{e_x} as

$$N_{e_x}(x) = \frac{\text{Advection time}}{\text{Eddy turnover time}} = \int_{1D_e}^{x} \frac{u'_x(\xi)}{\mathcal{L}_{ux}(\xi)\overline{U_x}(\xi)} \mathrm{d}\xi, \tag{4.1}$$

which illustrates the computation of the number of eddy turnover times undergone in the time taken for the flow to advect distance x. Note that the integration commences at $x/D_e = 1$ since neither the velocity fluctuations nor the correlation is well defined in the "top-hat" jet exit and the correlations and r.m.s. velocity fluctuations are calculated in the shear layer, where the Kelvin-Helmholtz structures reside. From the hot-wire data, the integral length scale $\mathcal{L}_{ux}$ was estimated as

$$\mathcal{L}_{ux}(x) = \overline{U_x}(x) \int_0^{\mathcal{T}} R(x,\tau)\, \mathrm{d}\tau \tag{4.2}$$

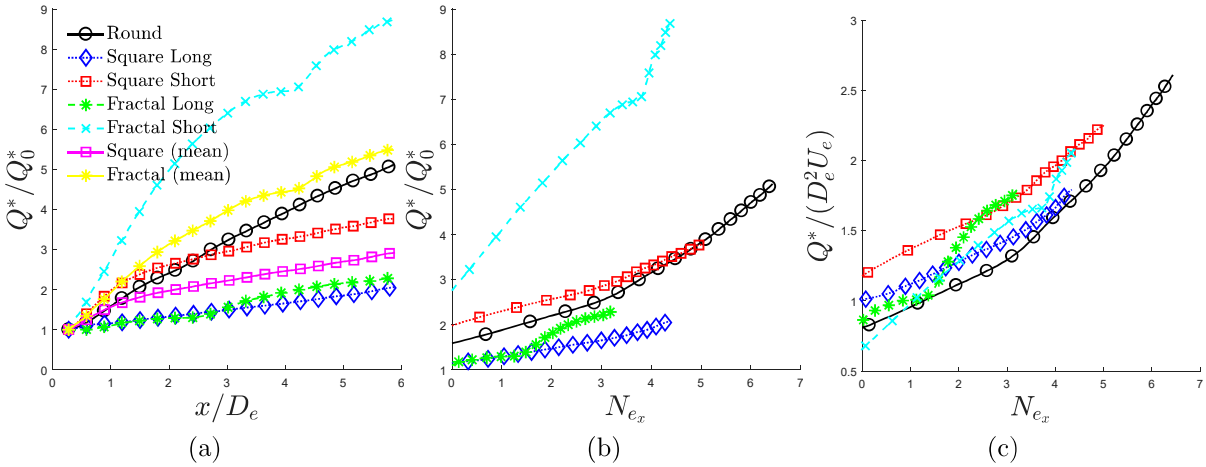
by integrating the autocorrelation of the velocity fluctuations, $R(x,\tau)$, in time-delay τ, from $\tau = 0$ to $\tau = \mathcal{T} \to \infty$

$$R(x,\tau) = \frac{\langle u_x(x,t)u_x(x,t+\tau)\rangle}{{u'_x}^2(x)}. \tag{4.3}$$

From a sensitivity analysis, it was found that $\mathcal{T} = 20\tau'$ (where τ' is the time-delay at which $R(x,\tau)$ first crosses zero) was sufficient. The autocorrelation in time was then converted into space by multiplying it by the advection velocity (i.e. the mean flow, $\overline{U_x}$) assuming Taylor's hypothesis. Regarding the choice of the location of the mean velocity for eq. (4.1), various options are available. One is the shear layer, where the integral lengthscale has been calculated, a second option is the jet centreline, whilst a third option is the characteristic jet velocity u_m later described in section 4.3. A comparison between the effect of these different velocity scales is shown in fig. 4.2a. In general, the choice of velocity appears to impact slightly the magnitude of N_{e_x}, but not the trends. Since u'_x and $\mathcal{L}_{ux}$ were taken at the shear layer in the near field, the mean velocity was taken at the same location.

The ratio N_{e_x} as a function of the streamwise distance x is evaluated at two Re_G in fig. 4.2. It is observed that the fractal jet develops the most slowly. This trend is accentuated with increasing Reynolds number, with a stark difference in development rates between the fractal jet and the round and square jets at $Re_G = 31,000$. This is to be expected, since a larger Reynolds number requires a broader range of length scales to dissipate the turbulent kinetic energy meaning that the dissipative scales become smaller and the finest details of the fractal geometry become, relatively, more significant. This indicates that at sufficiently high Reynolds number the fractal jet develops more slowly than the round and square jets, thereby delaying the development of some of the near-field turbulent properties as hypothesised when considering fig. 4.1. Comparing N_{e_x} at the major and minor axes, the latter has higher values for both noncircular jets due to the smaller integral length scale in the near field.

4.3 Evaluation of entrainment and mixing



(a) (b) (c)

Figure 4.3: Volume flux evolution in terms of x (a), N_{e_x} (b) and compensated by the initial volumetric flow rate (c) at $Re_G = 10,000$ (LPIV data). The mean value between the major and minor axes at the same streamwise location is shown in magenta and yellow. A marker is plotted every 10 points. Note that $N_{e_x} = 0$ corresponds to the streamwise location $x/D_e = 1$.

Suppressing the near-field coherence has previously proven to significantly affect the entrainment and mixing of background fluid into a jet (Brown and Roshko, 1974), and thus the jet's evolution towards a self-similar state. Entrainment may be studied through consideration of the volumetric flow rate of the jet, Q^*, as a function of x

$$Q^*(x) = 2\pi \int_0^{R_0} \overline{U_x} r \mathrm{d}r, \tag{4.4}$$

where $R_0 \to \infty$ is the location at which $\overline{U_r} = 0$. Here, due to the finite size of the experimental field of view, the location where $U_r \approx 0$ could not be reached. Hence, the integration is performed up to the radial location R_0 at which the mean radial (inwards) velocity $\overline{U_r}$ is 1% of the streamwise centreline velocity $\overline{U}_{cl}$,

$$\overline{U_r}(x, R_0) = 0.01 \overline{U}_{cl}(x), \tag{4.5}$$

which allows including a wider portion of the jet compared to the threshold used by van Reeuwijk and Craske (2015), where the integration was performed up to the point where the mean streamwise velocity $\overline{U_x}$ was 2% of the mean centreline velocity. The volume flux

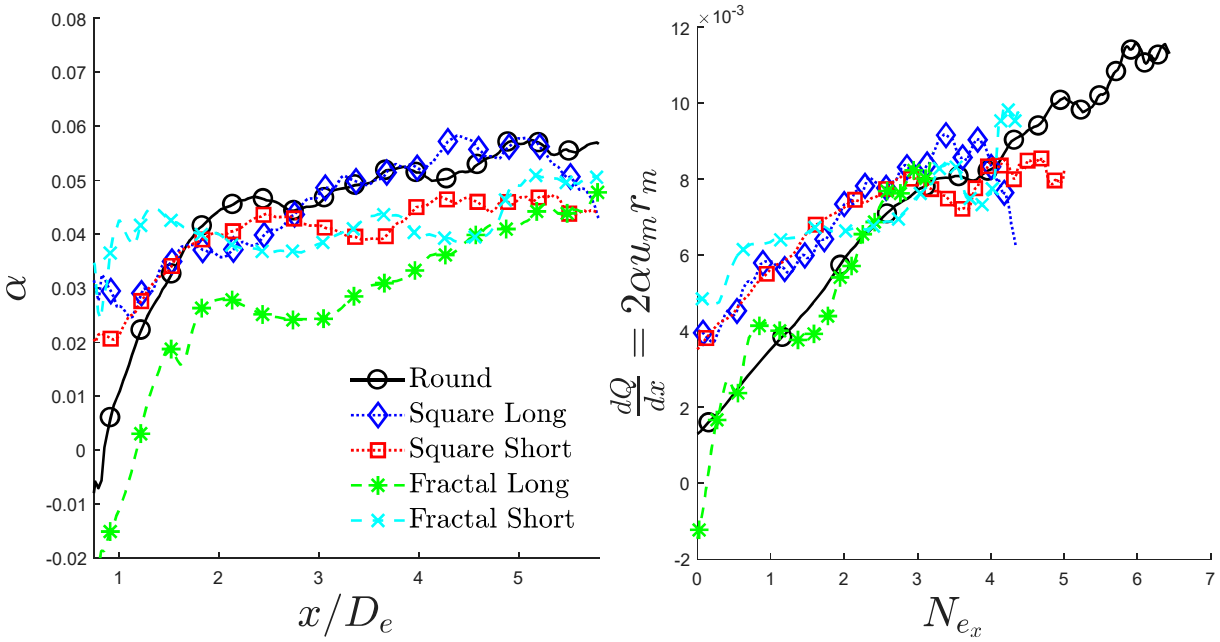


Figure 4.4: (a) Entrainment parameter α as a function of x for the various jets at $Re_G = 10,000$. (b) Streamwise spatial gradient of the volume flux as a function of N_{e_x} for the various jets (LPIV data). Note that $N_{e_x} = 0$ corresponds to the streamwise location $x/D_e = 1$. One marker is plotted every 10 data points to avoid clutter.

Q^*, compensated by its value at the jet exit Q_0^*, has been used to compare entrainment performance in various studies, including Grinstein (2001) amongst others. However, the normalised volumetric flow rate trends can be affected by the choice of the reference volumetric flow rate, since the noncircular geometries will have different values between major and minor axes depending on the aspect ratio.

It is shown that the major axis of the non-circular geometries always sustains a lower normalised volumetric flow rate than the round jet in fig. 4.3a. However, when calculating the geometrical mean between minor and major axis the fractal jet shows the highest Q^*, whilst the square jet shows the lowest. These findings are consistent with Cafiero et al. (2015), where a jet equipped with a space-filling fractal square grid (that suppressed the large-scale coherence) had a higher normalised volumetric flow rate compared to a round jet. It can be seen in fig. 4.3b and fig. 4.3c that the fractal jet has a higher normalised volumetric flow rate than both the square and round jets, whichever normalisation is chosen for Q^*, when plotted against N_{e_x} (extracted from the HW data). Fig. 4.3c suggests

that when scaled by the constant $D_e^2 U_e$ and plotted against N_{e_x} the volumetric flow rates are initially higher for the non-circular jets; however after 3-4 N_{e_x} the Q^* of the various jets seem to increase at a comparable rate. Moreover, this appears to take place between the major and minor axes of each noncircular jet as well. Hence, it is hypothesised that after an initial development region where the initial conditions play a key role, the different jets entrain fluid at the same rate, well ahead of reaching the self-similar state.

The local rate of entrainment into the jet is better examined through the streamwise spatial gradient of the volume flux Q, which differs from Q^* by a factor of π. van Reeuwijk and Craske (2015) derived a series of relationships describing the mean local entrainment dQ/dx in terms of a characteristic jet width, a characteristic jet velocity and an entrainment parameter α

$$\frac{dQ}{dx} = 2\alpha r_m u_m. \tag{4.6}$$

Here, the Richardson number Ri has been set to zero, to make the original equation valid for a pure jet.

The entrainment parameter α includes a contribution from the volume flux but also contains contributions from the production of turbulent kinetic energy and the energy flux as outlined in (4.7) and is consistent with the entrainment model of Kaminski et al. (2005).

$$\alpha = \underbrace{-\frac{\delta_m}{2\gamma_m}}_{\text{production}} + \underbrace{\frac{Q}{2M^{1/2}}\frac{d}{dx}(\ln \gamma_m)}_{\text{shape}} \tag{4.7}$$

The constituent terms of α are given in table 4.1 and the integrals are again performed up to radial location R_0 as defined in (4.5).

Fig. 4.4a shows α as a function of x and it can be seen that once the momentum flux, energy flux and turbulence production are taken into account, the suppression of the coherence due to the fractal geometry leads to a reduced entrainment parameter relative to the other jets. The initially negative α for the round and fractal jets (major axis), is primarily due to the initially decreasing energy flux for the former and due to the integrand of the turbulence production for the latter. Moreover, the entrainment parameter is an

Table 4.1: Table of terms used to calculate the entrainment parameter α

Term	Equation
Mean Volume Flux	$Q = 2\int_0^{R_0} \overline{U_x} r \mathrm{d}r$
Mean Momentum Flux	$M = 2\int_0^{R_0} \overline{U_x}^2 r \mathrm{d}r$
Characteristic jet width	$r_m = \frac{Q}{M^{1/2}}$
Characteristic jet velocity	$u_m = \frac{M}{Q}$
Mean Turbulence Production	$\delta_m = \frac{4}{u_m^3 r_m}\int_0^{R_0} \overline{u_x u_r}\frac{\partial \overline{U_x}}{\partial r} r \mathrm{d}r$
Mean Energy Flux	$\gamma_m = \frac{2}{u_m^3 r_m^2}\int_0^{R_0} \overline{U_x}^3 r \mathrm{d}r$
Entrainment parameter	$\alpha = -\frac{\delta_m}{2\gamma_m} + \frac{Q}{2M^{1/2}}\frac{d}{dx}(\ln \gamma_m)$

increasing function of x for all jets tested. van Reeuwijk and Craske (2015) show that a value of $\alpha \approxeq 0.08$ is typical for self-similar axisymmetric jets, and fig. 4.4a suggests that all jets tested are tending toward a comparable value. Fig. 4.4b shows dQ/dx, calculated according to (4.6) as a function of N_{e_x}. It can be seen that whilst α and the different jets' shape parameters u_m and r_m (not shown for brevity) vary differently from one another in terms of streamwise distance, x, once combined and scaled according to the number of eddy turnover times all three jets tend towards the same trend. Whilst there is a significant variation in the near field, where the influence of the large-scale coherence is known to be largest (Townsend, 1966), it is suggested that the suppression of the coherence by the fractal geometry may only have a small impact on the jet's evolution after $\approx 3 - 4N_{e_x}$. In fact, at $Re_G = 10,000$, all jets are found to eventually spread at the same rate, over the streamwise region probed ($x/D_e \leq 26$) as shown in fig. 4.5b, whilst at $Re_G = 3,000$, where the effect of the coherent structures is much more significant, the round jet grows at a slightly faster rate compared to the non-circular jets as shown in fig. 4.5a. This can perhaps be attributed to the greater significance of engulfment events at lower Reynolds number, due to the more dominant large-scale coherent structures in the transitional region ($\approx 3 - 4N_{e_x}$) of greater streamwise extent than for the higher Reynolds number jet. Yule (1978) shows that entrainment is dominated by engulfment in the near field of axisymmetric jets.

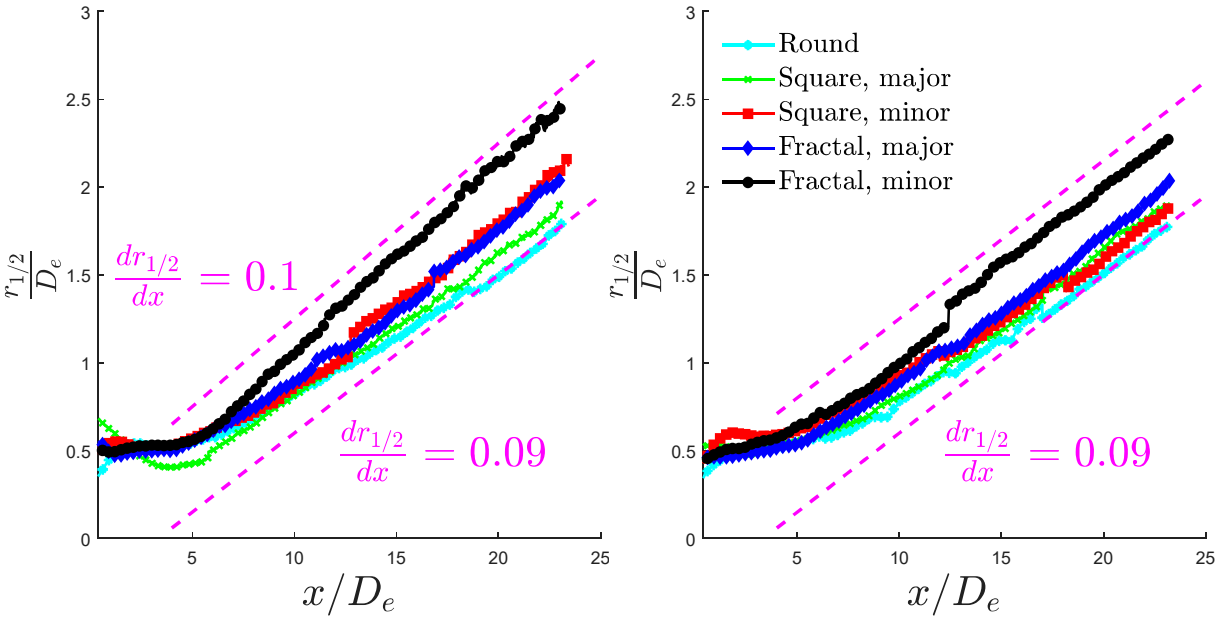


Figure 4.5: Spreading rate $dr_{1/2}/dx$ of the various jets at (a)$Re_G = 3,000$ and $Re_G = 10,000$ (Breda and Buxton, 2017). Trend lines are shown in magenta and one marker is plotted every 10 points to avoid clutter (LPIV data).

4.4 Time-averaged Momentum Equation

The development of the jets is examined in terms of the time averaged momentum equation (TAME) split into the radial (4.8) and streamwise directions (4.9), as in Chao and Sandborn (1966).

$$\overline{U_r}\frac{\partial \overline{U_r}}{\partial r} + \overline{U_x}\frac{\partial \overline{U_r}}{\partial x} + \frac{\partial \overline{u_r^2}}{\partial r} + \frac{1}{r}(\overline{u_r^2} - \overline{u_\theta^2}) + \frac{\partial \overline{u_x u_r}}{\partial x} = -\frac{1}{\rho}\frac{\partial p}{\partial r} + \nu\left(\frac{\partial^2 \overline{U_r}}{\partial r^2} + \frac{1}{r}\frac{\partial \overline{U_r}}{\partial r} - \frac{\overline{U_r}^2}{r^2} + \frac{\partial^2 \overline{U_r}}{\partial x^2}\right) \quad (4.8)$$

$$\overline{U_r}\frac{\partial \overline{U_x}}{\partial r} + \overline{U_x}\frac{\partial \overline{U_x}}{\partial x} + \frac{\partial \overline{u_x u_r}}{\partial r} + \frac{\overline{u_x u_r}}{r} + \frac{\partial \overline{u_x^2}}{\partial x} = -\frac{1}{\rho}\frac{\partial p}{\partial x} + \nu\left(\frac{\partial^2 \overline{U_x}}{\partial r^2} + \frac{1}{r}\frac{\partial \overline{U_x}}{\partial r} + \frac{\partial^2 \overline{U_x}}{\partial x^2}\right) \quad (4.9)$$

The data are taken from the same streamwise interval $(2-5D_e)$, however they are plotted in terms of number of N_{e_x} (extracted from the HW data). Three non-negligible radial

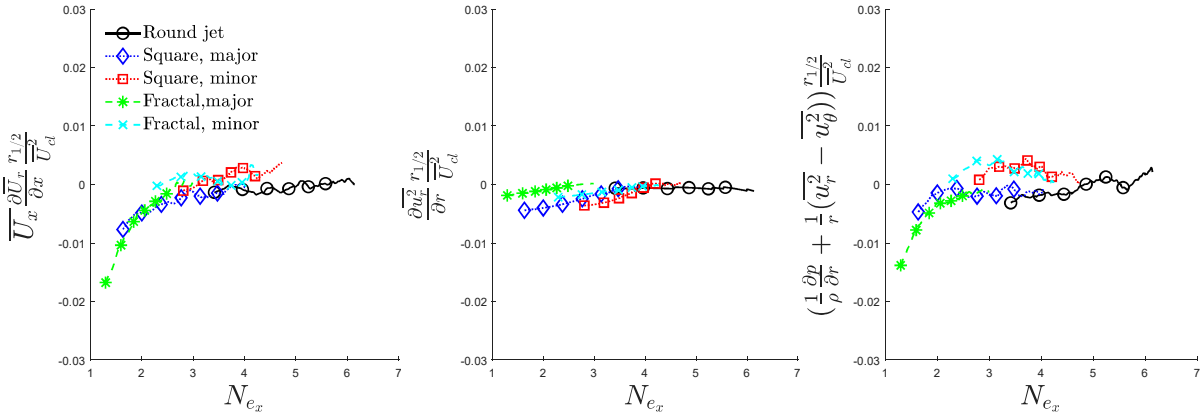


Figure 4.6: Terms of (4.8) for the various jets in the shear layer, where the near-field coherent motions reside at $Re_G = 10,000$ (HPIV data). One marker plotted every 20 points to avoid clutter. The location of peak $u'_x(x)$ is chosen to locate the shear layer.

terms in the near field only of the radial TAME (4.8) are presented in fig. 4.6. The terms $\overline{U_x}\partial\overline{U_r}/\partial x$, $\partial\overline{u_r^2}/\partial r$ and the residuals are observed to differ between the various jets only up to $N_{e_x} \simeq 3-4$, after which they follow comparable trends. Further, after an initial development the terms of the noncircular exits appear to tend to zero similarly to the round jet. This indicates that the non-circular jets transition to an axisymmetric state, in which the mean radial momentum evolves in a comparable fashion to the round (initially axisymmetric) jet. This finding mirrors that of Nedić et al. (2013a), who showed that the wakes generated by square and fractal plates also tended rapidly towards axisymmetry after an initial transition period. The role of the fluctuations is found to be minor compared to the mean velocity gradients in terms of magnitude, which are counterbalanced by the residuals (i.e. the pressure gradient). We now conclude that the streamwise distance at which this transition starts to take place scales with the distance advected for a fixed ($\simeq 4$) number of eddies to overturn. This resembles the time required for the local entrainment rate ($\partial Q/\partial x$) to adjust to a similar trend between the three jet configurations.

Clearer differences between the various jets are, however, found for the terms of the streamwise TAME (4.9) as shown in fig. 4.7 and fig. 4.8. The terms evolving radially, $\overline{u_x u_r}/r$ (fig. 4.7b) and $\overline{U_r}\partial\overline{U_x}/\partial r$ appear to be tending towards a comparable trend after

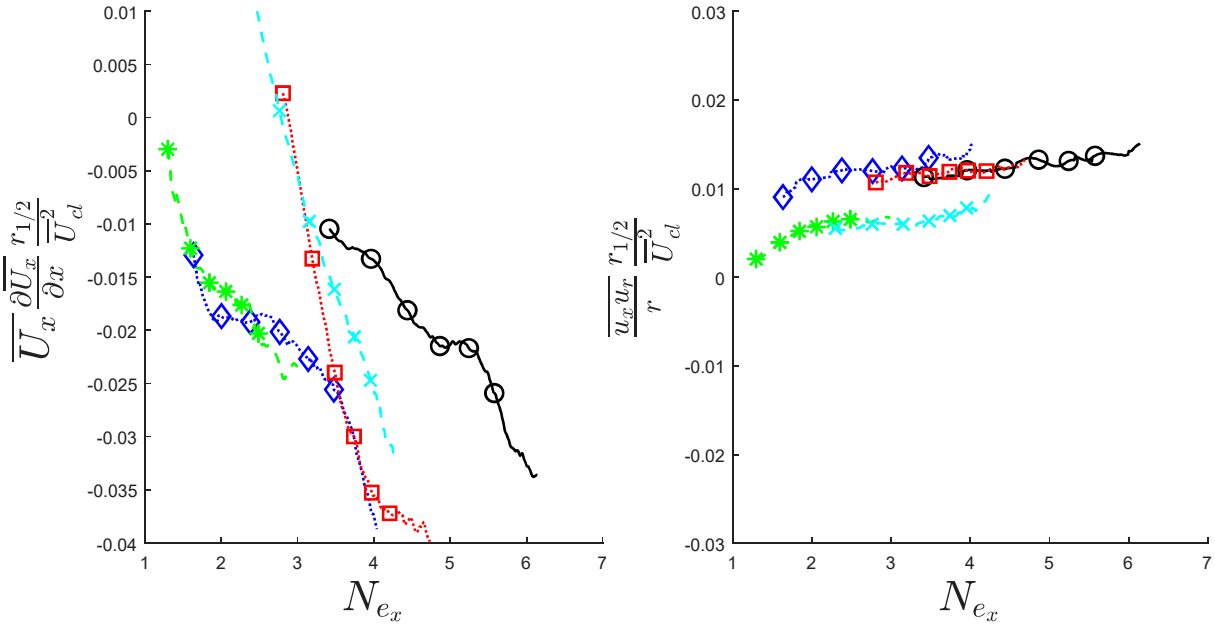


Figure 4.7: a) $\overline{U}_x \frac{\partial \overline{U}_x}{\partial x}$ along the centreline and (b) $\overline{u_x u_r}/r$ in the shear layer at $Re_G = 10,000$ (HPIV data). One marker plotted every 20 points to avoid clutter.

$N_{e_x} \gtrsim 4$. However, the region of space probed for $\overline{U_r}\partial\overline{U_x}/\partial r$ is insufficient for all of the jet configurations to reach $N_{e_x} = 4$ and hence the low-resolution PIV data was used to verify that all the jets did indeed converge to a similar trend. Since even the low-resolution PIV field of view is too small for the autocorrelation function of u_x in the x-direction to reach zero, and hence calculate $\mathcal{L}_{ux}$, a new quantity N_{e_r} is defined which is again analogous to the total number of eddies overturned in the time taken for the fluid to advect distance x. This relied upon computing a spatial autocorrelation function of u_x in the radial direction r with increment ψ

$$R_{u_x r}(x, r, \psi) = \frac{\langle u_x(x, r) u_x(x, r + \psi) \rangle}{u'_x(x, r) u'_x(x, r + \psi)}. \tag{4.10}$$

For the same reasons as previously, the correlation function was computed in the shear layer in the near field (radial location of maximal $u'_x(x)$), before transitioning to the centre line downstream of the location of maximum u'_x along the centre line. Since the two-point correlation from the PIV data is not radially symmetric at the shear layer, $\mathcal{L}_{ur}$ was calculated by averaging both sides, i.e. between the correlation in the direction of

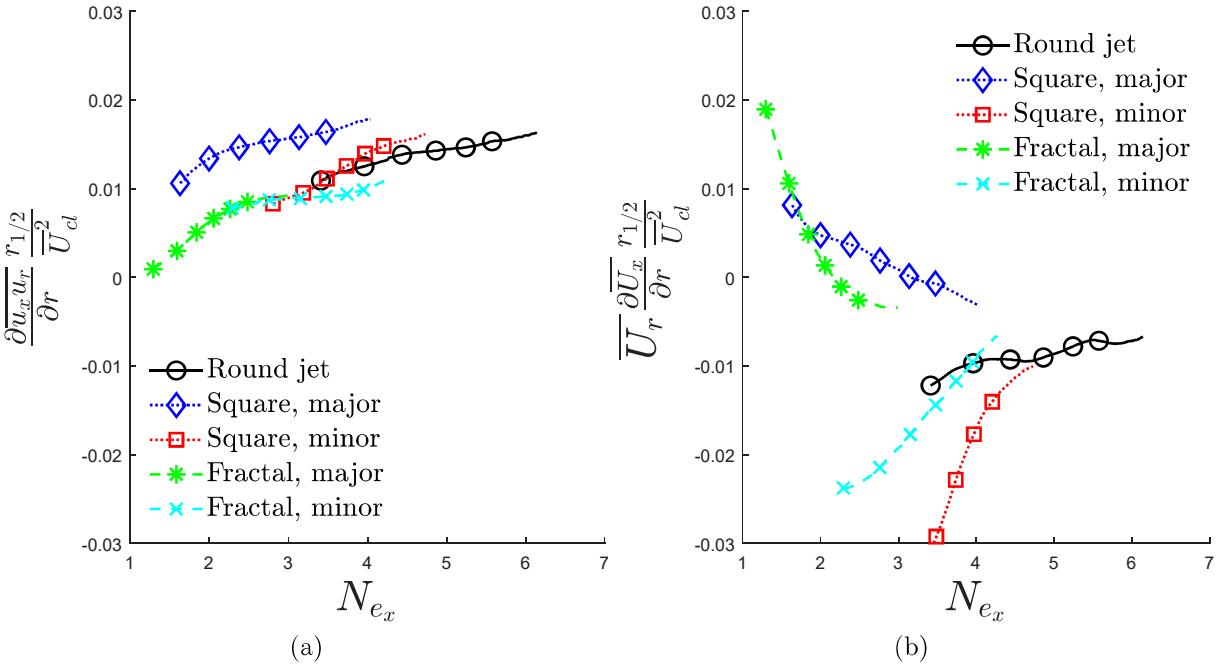


Figure 4.8: (a) $\partial(\overline{u_x u_r})/\partial r$ along the centreline and (b) $\overline{U}_r \frac{\partial \overline{U}_x}{\partial r}$ along the shear layer as a function of N_{e_x} calculated for the various jets at $Re_G = 10,000$ (HPIV data).

the jet core and in the direction of the background (co-)flow

$$\mathcal{L}_{ur}(x) = \frac{1}{2}\int_{r'_-}^{r'_+} R_{u_x r}(x,\psi)\mathrm{d}\psi. \tag{4.11}$$

Since the field of view was finite, the integration was truncated at the locations of the first zero-crossing (in either direction), $r'_\pm$ This choice, when considering a limited field of view, has been validated as the best option for PIV data by the study of Nicolaides et al. (2004). N_{e_r} could then be calculated according to

$$N_{e_r}(x) = \int_{1D_e}^{x} \frac{u'_x(\xi)}{\mathcal{L}_{ur}(\xi)\overline{U_x}(\xi)}\mathrm{d}\xi. \tag{4.12}$$

The evolution of N_{e_r} with N_{e_x} is shown in fig. 4.9b. It can be seen that N_{e_r} is a monotonically increasing function of N_{e_x} for all jets studied, giving us confidence that subsequent results presented in terms of N_{e_r} are indeed analogous to the those in terms of Ne_x.

Fig. 4.9a shows that $\overline{U_r}\partial\overline{U_x}/\partial r$ does indeed tend to the same trend (≈ 0) for all jets after a sufficient number of eddy turnover times. The major and minor axes are opposingly

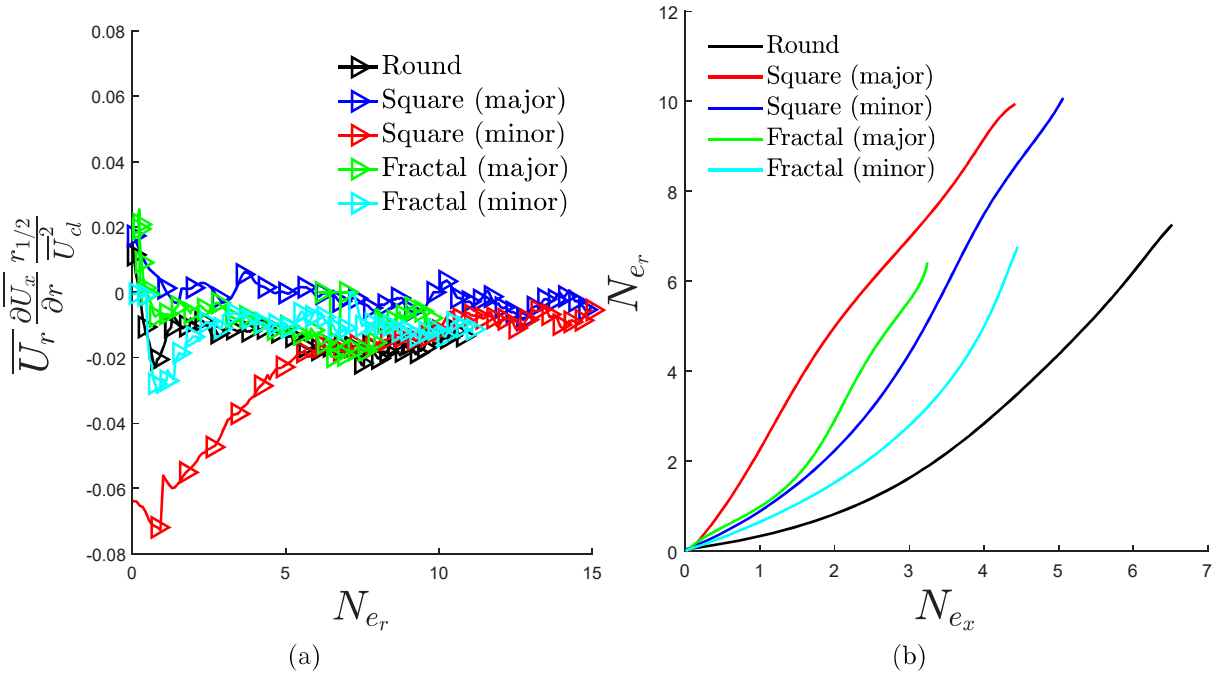


Figure 4.9: Evolution of $\overline{U_r}\partial\overline{U_x}/\partial r$ with N_{e_r} for the various jets in the shear layer at $Re_G = 10,000$ (LPIV data). One marker plotted every 20 points to avoid clutter. (b) Evolution of N_{e_r} with respect to N_{e_x}.

signed due to the initial tendency of the major axis to shrink and of the minor one to expand. This was also observed for $\overline{u_x u_r}/r$, although not shown for brevity.

Differently from the other terms, the third quantity of significance, $\overline{U_x}\partial\overline{U_x}/\partial x$ shows no such sign of converging to a common value between the three different jets and its development certainly does not scale with the number of eddy turnovers. This indicates that, despite the different geometry at the jet exit, all three jets evolve radially towards axisymmetry and do so in a time scale that depends upon a certain number of eddy turnovers (≈ 4). However, this is not found to be the case for the terms evolving in the streamwise direction x. The terms in eq. (4.9) that include gradients in the radial direction thus also tend to evolve in a similar fashion to one another (after this transitional region), regardless of the geometry at the jet exit, in order to facilitate this return to axisymmetry. The alteration of the initial conditions has the largest effect on the streamwise development of the mean flow, and not that of the velocity fluctuations. These observations are reinforced in fig. 4.8 which shows example terms from the streamwise TAME calculated along the jets' centre line as a function of N_{e_x}. The term $\overline{U_x}\partial\overline{U_x}/\partial x$ can be seen to behave differ-

ently between the various jets whilst the term $\overline{U_r}\partial\overline{U_x}/\partial r$ can be seen to collapse onto the same trend, for all of the jets tested, after $\approx 3-4$ eddy turnover times.

Based on the available literature, an order of magnitude analysis is now conducted to evaluate the expected value of some the terms of the TAME, which are non-negligible in the far field. Based on the work of Pope (2000), the following relationships are expected at the jet centreline:

$$\frac{r_{1/2}}{\overline{U}_{cl}^2}\left(\overline{U_x}\frac{\partial\overline{U_x}}{\partial x}\right) = -\frac{dr_{1/2}}{dx} \approx -0.09 \tag{4.13}$$

$$\frac{r_{1/2}}{\overline{U}_{cl}^2}\frac{\partial\overline{u_x u_r}}{\partial r} \approx 0.05 \tag{4.14}$$

$$\frac{r_{1/2}}{\overline{U}_{cl}^2}\frac{\partial\overline{u_x^2}}{\partial x} \approx -0.014 \tag{4.15}$$

Further, based on the work of Hussein et al. (1994), who measured the far field of a round jet emitted by a nozzle, it was derived from the self-similar profiles that at the shear layer:

$$\frac{r_{1/2}}{\overline{U}_{cl}^2}\frac{\overline{u_x u_r}}{r} \approx 0.03. \tag{4.16}$$

Finally, an estimate for $\overline{U_r}\partial\overline{U_x}/\partial r$ at the shear layer can be found by starting from the definition of a self-similar profile $f(\varrho)$ based on the constant α and the compensated radial distance ϱ:

$$\varrho = \frac{r}{X - X_0} \tag{4.17}$$

$$\alpha = \frac{\sqrt{2}-1}{dr_{1/2}/dx} \tag{4.18}$$

$$f(\varrho) = (1+\alpha\varrho^2)^{-2}. \tag{4.19}$$

Based on the definition of $r_{1/2}$ and after some manipulation, the following relationships can be derived:

$$\frac{r_{1/2}}{\overline{U}_{cl}}\frac{\partial\overline{U_x}}{\partial r} = -\frac{dr_{1/2}}{dx}\frac{-4\alpha\varrho}{(1+\alpha\varrho^2)^3}. \tag{4.20}$$

Based on the self-similar profile of $\overline{U_r}$(Hussein et al., 1994), it can be estimated that at

the shear layer:

$$\frac{r_{1/2}}{\overline{U}_{cl}^2}\overline{U_r}\frac{\partial\overline{U_x}}{\partial r} \approx -0.012. \tag{4.21}$$

Other non-negligible terms throughout the entire development of the jet, up to a distance of $x/D_e = 26$, are the pressure terms which, together to u_θ, could not be computed directly from the 2D planar PIV data and could thus only be derived from the residual of the balance of the various terms. The remaining terms of the TAME equations were found to be negligible.

In order to study the trends of the quantities described above in the near field, first the "far field" between $x/D_e = 23 - 26$, where such trends are expected, is examined. As shown

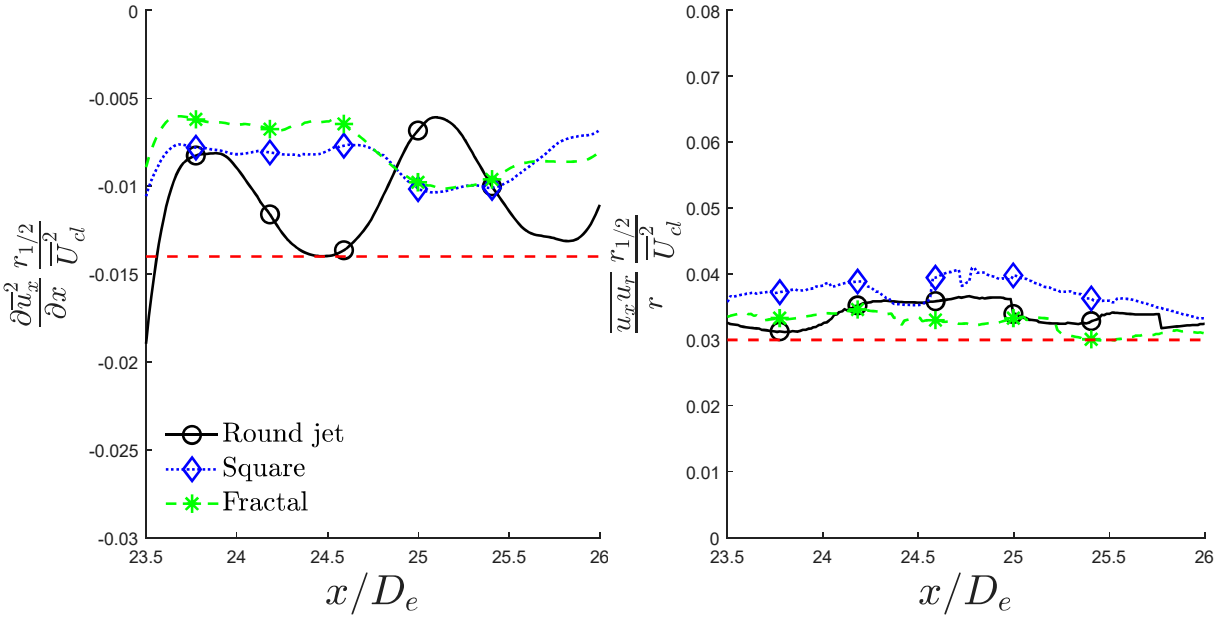
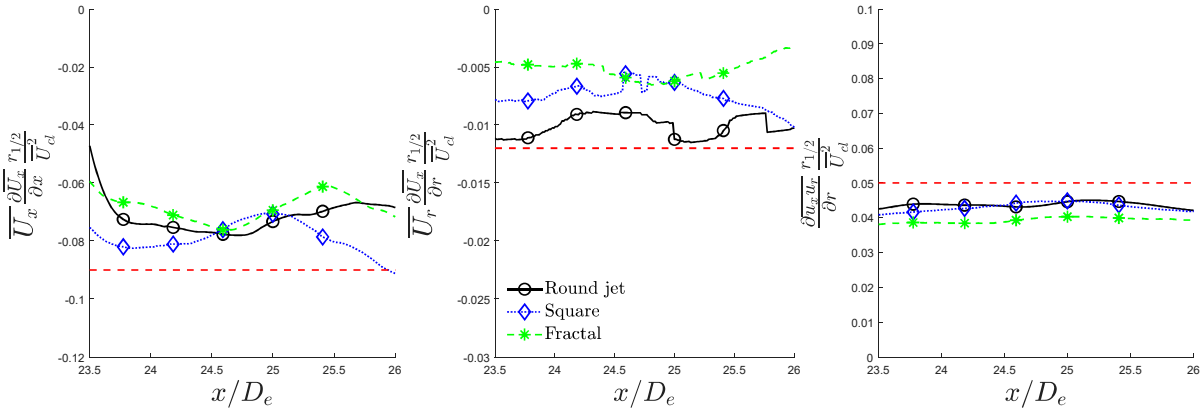


Figure 4.10: Variation of (a) $\partial\overline{u_x^2}/\partial x$ and of (b) $\overline{u_x u_r}/r$. The expected far-field trend is shown by a red dashed line. (HPIV data, $Re_G = 10,000$)

in fig. 4.10, $\partial\overline{u_x^2}/\partial x$ and $\overline{u_x u_r}/r$ are approaching the trends expected in the "far field". The same behaviour is found in fig. 4.11, where $\overline{U_x}\partial\overline{U_x}/\partial x$, $\overline{U_r}\partial\overline{U_x}/\partial r$ and $\partial\overline{u_x u_r}/\partial r$ are also approaching their "far-field" trends, however it is suggested that $x/D_e = 26$ is not enough far away from the jet exit for the turbulent flow to become self-similar at all scales, even though the same "far-field" trends are being approached by all jets, independently of their initial conditions.



(a) (b) (c)

Figure 4.11: Variation of (a) $\overline{U_x}\partial\overline{U_x}/\partial x$, (b) $\overline{U_r}\partial\overline{U_x}/\partial r$ and (c) $\partial\overline{u_x u_r}/\partial r$. The expected far-field trend is shown by a red dashed line (HPIV data and $Re_G = 10,000$).

Having looked at the trends reached at $x/D_e = 26$, now the near field is examined, to evaluate how an axisymmetric jet evolves to such trends. Neglecting the pressure gradient, which is inferred from the residual of the balance of terms, the magnitude of some of the terms in the near field is compared to their far-field prediction. As discussed, $\overline{U_x}(\partial U_x/\partial x)$ is expected to vary as the spreading rate of the jet in the far field, however near the jet exit (fig. 4.7a) this term does not yet reach $dr_{1/2}/dx$, but values around -0.04. This is to expected, since the gradient of the mean velocity will be lower at this location due to the fact that the jet still has a potential core (where the streamwise velocity will be approximately constant) and a low $r_{1/2}$ (since the jet is just starting to spread). This argument also applies to $\partial u_x^2/\partial x$, which is found to be approximately 10% of the predicted "far field " value. The term $\overline{u_x u_r}/r$ appears to approach 0.01 at the shear layer (fig. 4.7b), whilst a value of 0.03 is expected in the far field. This is due to the fact the jet is in a state of turbulent production; hence the fluctuations still need to grow with respect to the centreline velocity. Moreover, $r_{1/2}$ is still relatively small whilst $\overline{U}_{cl}$ is relatively high since the region probed is close to the jet exit. The same argument relates to $\partial(\overline{u_x u_r})/\partial r$, which is found to approach 0.02 rather than 0.05 (fig. 4.8a). Finally, $\overline{U_r}\partial\overline{U_x}/\partial r$ is evaluated along the shear layer (fig. 4.8b). It is found that only the round jet is close to the predicted "far-field" value of -0.012. The noncircular jets, imaged across the major axes, initially show a positive decreasing trend since, due to axis-switching, the radial velocity is pointing

towards the jet centre. The opposite takes place for the noncircular jets imaged across the minor axes, which initially show a very high magnitude, which then decays towards the value of the round jet.

4.5 Self-similarity and microscales

It was shown that despite the fractal geometry strongly influencing the coherence in the near field of the jet, and subsequently the entrainment and mixing of background fluid into the turbulent stream, all three jets have a tendency to evolve to an axisymmetric mean state. Indeed for at least the past century it has been assumed that such turbulent shear flows will evolve to a self-similar state with many researchers, since the work of Townsend (1976), stating that these flows achieve a self-similar state by becoming asymptotically independent of their initial conditions. However, more recently George (1989) has argued that there is a link between the self-similar state of a flow and its coherence which naturally leads to an examination of the evolution towards self-similarity for the three jets at issue.

Self-similarity requires normalisation of the jet's one-point statistical profiles with a relevant flow statistic and length scale. Let's, as an example, consider the streamwise mean velocity profile at a given x location, $\overline{U_x}(x,r)$. "Classically" one would choose the mean centre-line velocity $\overline{U}_{cl}$ and the jet half width $r_{1/2}$, defined as

$$\overline{U_x}(x,r_{1/2}) = 0.5\overline{U}_{cl}(x). \tag{4.22}$$

The subsequent analysis follows from George (1989) and the reader is referred to the original work for the full set of equations. The following self-preserving forms of some

important terms of the turbulent kinetic energy equation are written as follows:

$$\hat{r} = r/r_{1/2}(x) \tag{4.23}$$

$$\overline{U_x} = \overline{U}_{cl}(x) f(\hat{r}) \tag{4.24}$$

$$-\overline{u_x u_r} = R_s(x) g_{12}(\hat{r}) \tag{4.25}$$

$$\overline{q^2} = K_s(x) k(\hat{r}) \tag{4.26}$$

$$-(\overline{pu_r} + \frac{1}{2}\overline{q^2 u_r}) = T_s(x) t(\hat{r}) \tag{4.27}$$

$$\varepsilon = D_s(x) e(\hat{r}). \tag{4.28}$$

Here $\overline{q^2}$ is the turbulent kinetic energy per unit mass, p is the pressure and K_s, T_s and D_s are the normalisation scales (along the centreline) for turbulent kinetic energy, third order moments and dissipation rate analogous to $\overline{U}_{cl}$ for the mean velocity.

The turbulent kinetic energy equation, reduced to second order, may be stated as

$$\left[\overline{U_x}\frac{\partial \overline{q^2}}{\partial x}\right] + \overline{U_r}\frac{\partial \overline{q^2}}{\partial r} = -\left[\frac{1}{r}\frac{\partial}{\partial r} r(\overline{pu_r} + \overline{q^2 u_r})\right] - \frac{\partial}{\partial x}(\overline{pu_x} + \overline{q^2 u_x}) - \left[\overline{u_x u_r}\frac{\partial \overline{U_x}}{\partial r}\right] - \overline{u_x^2}\frac{\partial \overline{U_x}}{\partial x} - \overline{u_r^2}\frac{\partial \overline{U_r}}{\partial r} - [\varepsilon]\,. \tag{4.29}$$

Only the terms in square brackets are considered in the following analysis, whilst the others are neglected. The self-similar forms are now substituted into the turbulent kinetic energy equation yielding

$$[\overline{U}_{cl} K_s'] fk - \left[\overline{U}_{cl}\frac{K_s}{r_{1/2}}\frac{dr_{1/2}}{dx}\right]\hat{r} f k' = \left[\frac{T_s}{r_{1/2}}\right]\frac{(\hat{r}t)'}{\hat{r}} + \left[R_s\frac{\overline{U}_{cl}}{r_{1/2}}\right] g_{1/2} f' - [D_s] e. \tag{4.30}$$

Dividing through by $K_s \overline{U}_{cl}/r_{1/2}$ it is found that

$$\left[\frac{r_{1/2} K_s'}{K_s}\right] fk - \left[\frac{dr_{1/2}}{dx}\right]\hat{r} f k' = \left[\frac{T_s}{K_s \overline{U}_{cl}}\right]\frac{(\hat{r}t)'}{\hat{r}} + \left[\frac{R_s}{K_s}\right] g_{12} f' - \left[\frac{D_s r_{1/2}}{K_s \overline{U}_{cl}}\right] e. \tag{4.31}$$

In order to have a self-similar form, all the terms in the square brackets must have the

same x-dependence. In particular

$$\frac{dr_{1/2}}{dx} \sim \frac{r_{1/2}K_s'}{K_s}. \tag{4.32}$$

Now, George (1989) used the constant momentum flux, M_0, for an axisymmetric jet (Hussein et al. (1994)) to link $\overline{U}_{cl}$ to $r_{1/2}$ via

$$\overline{U}_{cl} = BM_0^{1/2}r_{1/2}^{-1} \tag{4.33}$$

i.e. $\overline{U}_{cl} \sim r_{1/2}^{-1}$. In fact, the constant momentum flux in the jet requires (George, 1989)

$$\overline{U}_{cl} \sim x^a \quad r_{1/2} \sim x^b \tag{4.34}$$

in which $a = -1$ and $b = 1$ (as widely reported in Tennekes and Lumley (1972)). Under the further assumption that $K_s \sim \overline{U}_{cl}{}^2$ it is derived that

$$K_s \sim \overline{U}_{cl}^2 \sim r_{1/2}^{-2}. \tag{4.35}$$

We may now re-write (4.32) as

$$\frac{dr_{1/2}}{dx} \sim \frac{r_{1/2}K_s'}{K_s} \sim \frac{r_{1/2}r_{1/2}^{-3}}{r_{1/2}^{-2}} \sim \text{constant}. \tag{4.36}$$

(4.36) shows that the spreading rate of the jet must be a constant and since self-similarity requires that all the terms in square brackets of (4.31) have the same x-dependence it is inferred that

$$\frac{dr_{1/2}}{dx} \sim \frac{D_s r_{1/2}}{K_s\overline{U}_{cl}} \sim \text{constant}. \tag{4.37}$$

Now, a further assumption is adopted from George (1989) to go alongside the assumption that $K_s \sim \overline{U}_{cl}{}^2$, namely

$$\mathcal{L}_{ur} \sim r_{1/2}. \tag{4.38}$$

If these assumptions are inserted into (4.37), it is found that

$$\frac{D_s r_{1/2}}{K_s \overline{U}_{cl}} = \frac{\varepsilon \mathcal{L}}{q^3} = \text{constant} \tag{4.39}$$

i.e. $C_\varepsilon = \text{constant}$. Note that this constancy of C_ε depends upon three assumptions

$$\overline{U}_{cl}^2 \sim K_s \tag{4.40}$$

$$\mathcal{L}_{ur} \sim r_{1/2} \tag{4.41}$$

$$\varepsilon = D_s(x) e(\hat{r}). \tag{4.42}$$

If assumptions (4.40), (4.41) and (4.42) are observed to hold then it may be predicted the x-dependence of the dissipation using (4.34) and (4.35) as

$$D_s = \varepsilon \sim \frac{K_s \overline{U}_{cl}}{r_{1/2}} \sim x^{-4}. \tag{4.43}$$

Note that if (4.42) is observed to be valid but (4.40) and (4.41) are not valid then the definition of C_ε in (1.1) may be used to instead write

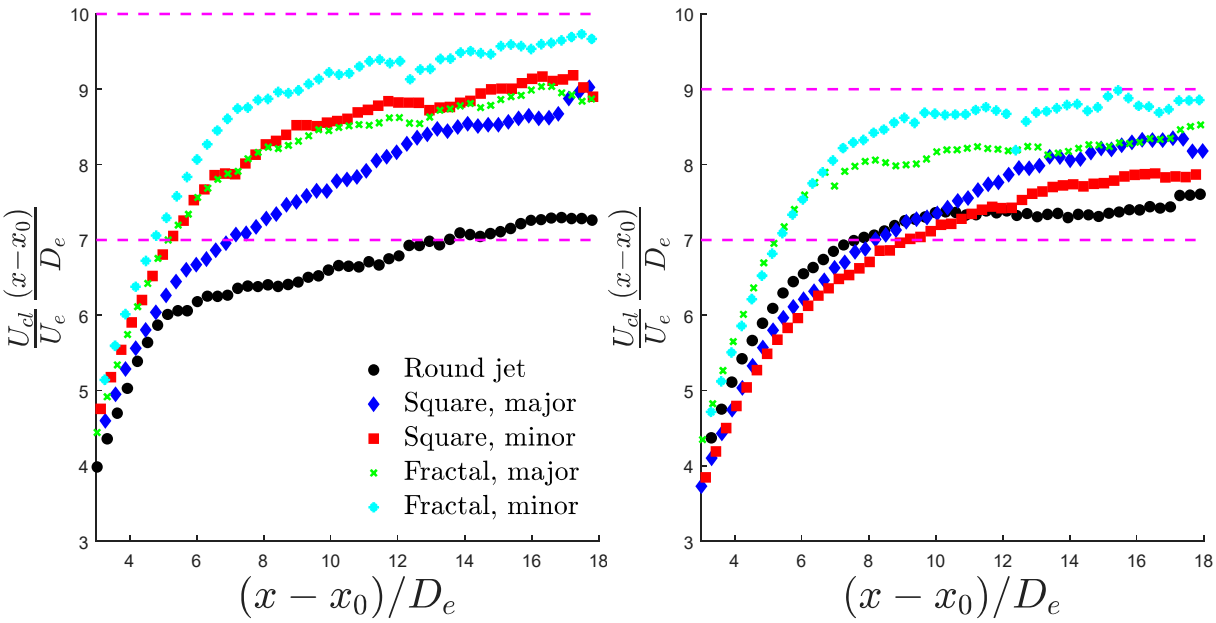
$$\text{constant} = \frac{D_s r_{1/2}}{K_s \overline{U}_{cl}} \sim C_\varepsilon \frac{q}{\overline{U}_{cl}} \frac{r_{1/2}}{\mathcal{L}} \tag{4.44}$$

in which case it is possible that $C_\varepsilon \neq$ constant if the other two ratios in (4.44) vary spatially. Note that if only some of the terms in (4.31) vary in an identical fashion in x, i.e. $\overline{U}_{cl}$ or R_s, but not others then it would be possible for the jet to appear self-similar (in a less restrictive sense, i.e. the mean velocity profiles or Reynolds stress profiles appear self-similar whilst the dissipation does not) whilst $C_\varepsilon \neq$ constant. Given the seemingly ubiquitous nature of non-equilibrium dissipation in a multitude of turbulent shear flows, this section of the chapter will be used to seek such a less-restrictive weakly self-similar region of the flow in the explored domain $x/D_e \lesssim 26$.

First, the evolution of the jet centreline velocity for all three different jets is considered at both $Re_G = 3,000$ and $Re_G = 10,000$ in fig. 4.12, where $\overline{U}_{cl}$ is premultiplied by x so

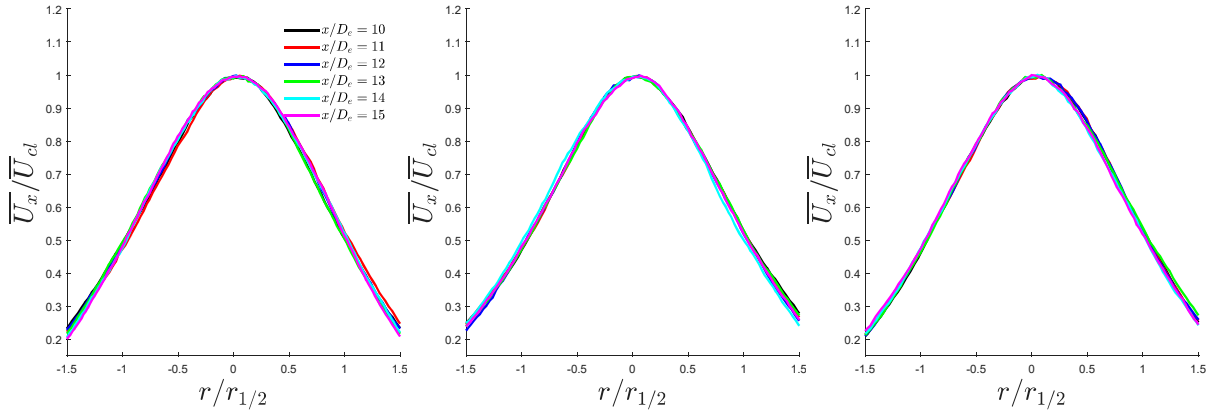
that a self-similar behaviour will be identified by a straight horizontal line. In the figure, the streamwise distance accounts for the location of the jet's virtual origin x_0 since, as discussed by Hunt and Kaye (2001), it proved to allow a better modelling of the behaviour of plumes under the assumption of a point-source. Fig. 4.12 verifies that the exponent $a \to -1$ with increasing x, as required by (4.34) for a jet approaching a self-similar state. As discussed previously, at the lower Reynolds number, the round jet shows a slightly higher spreading rate than the fractal jet, as shown in fig. 4.5. At the higher Reynolds number the spreading rate is comparable between the jets, however due to the different location of the virtual origin (if one assumes the jet to emanate from a point source of momentum) the round jet is always wider in the far field than the fractal jet, due to their different state of coherence in the near field. Thus, at a sufficiently high Re_G, it can be seen that the jet's spreading rate reaches a constant value. It may be argued that at this $Re_G > Re_{G,crit.}$ in a sense the jets' large scale properties have become "memoryless" of the initial conditions after a certain number of eddies have been overturned (N_{e_x}), suggesting that at high enough Reynolds number the spreading rate of the jet is independent of the initial conditions, as hypothesised by Townsend (1976). At $Re_G = 3,000$, the higher spreading rate for the round jet does not contrast with $a \to -1$ and $b \to 1$. In fact, as suggested by George (1989) and Wygnanski et al. (1986), different growth rates can coexist with the same self-similar power laws if one considers self-similarity as a multi-scale phenomenon. Therefore, despite the different exit geometries leading to different spreading rates, this does not translate into different scaling exponents.

It is now necessary to determine the correct scaling quantities for the single-point statistics and at which downstream locations the mean momentum/Reynolds stress profiles become self-similar. In order to do so, the radial profiles of the mean velocity and of the Reynolds stresses compensated by a specific flow quantity are examined for the three jets. As previously suggested by the approximately constant centreline velocity in fig. 4.12 and by the radial profiles of $\overline{U_x}$ in fig. 4.13, the streamwise centreline velocity reaches self-similarity at approximately $x/D_e = 12$. Regarding the Reynolds stresses, two approaches are followed to evaluate their self-preservation: the "classical" one (i.e. normalising the



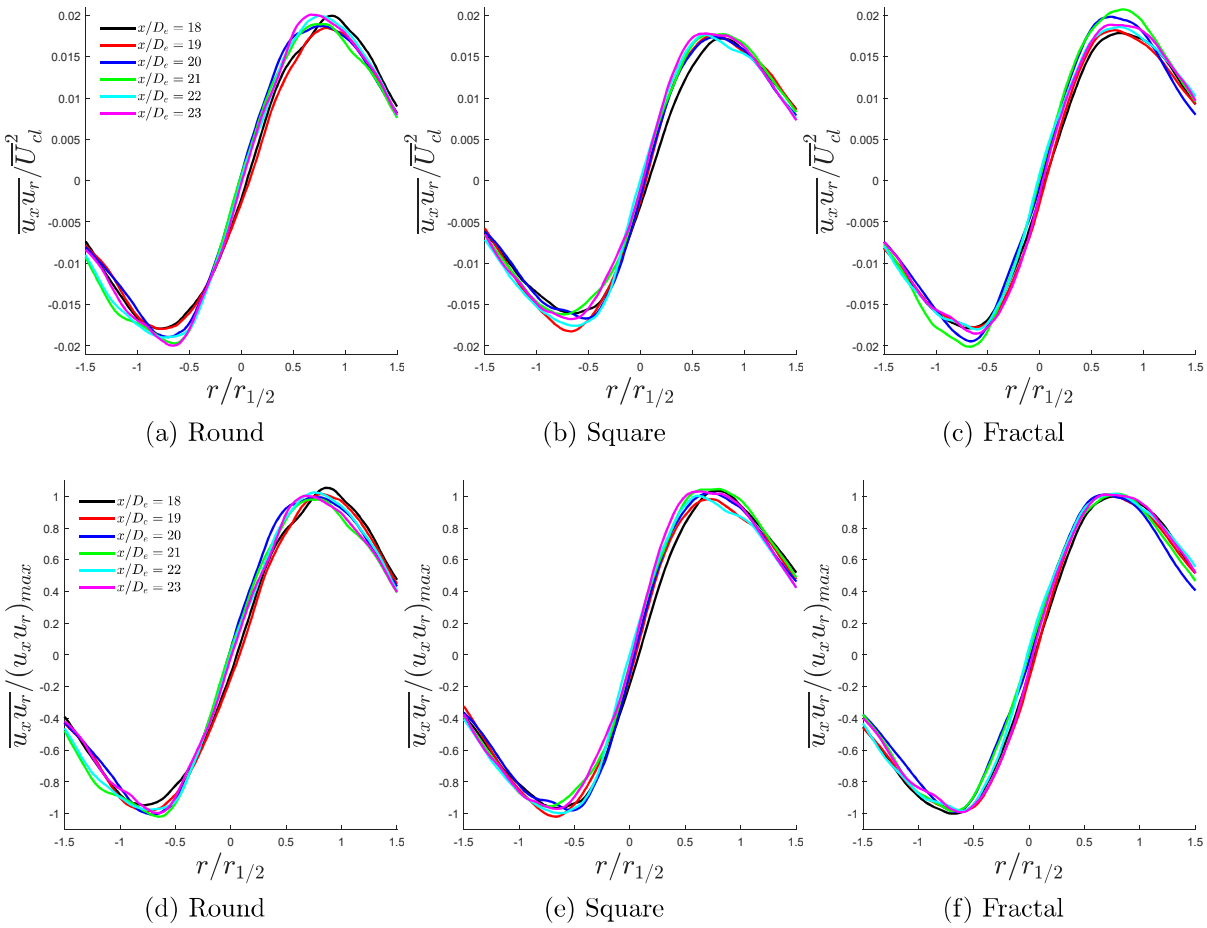
(a) $Re_G = 3,000$ (b) $Re_G = 10,000$

Figure 4.12: Centreline mean streamwise velocity as a function of x (LPIV data). The velocity is multiplied by x so that the self-similar state will be shown by a constant horizontal trend. Only 10% of the points are shown to avoid clutter.



(a) Round (b) Square (c) Fractal

Figure 4.13: Radial profiles of $\overline{U_x}$ at various streamwise locations and at $Re_G = 10,000$ (LPIV data), normalised by centreline value.



(a) Round (b) Square (c) Fractal

(d) Round (e) Square (f) Fractal

Figure 4.14: Radial profiles of $\overline{u_x u_r}$ at various streamwise locations and at $Re_G = 10,000$ (LPIV data), normalised by the centreline velocity (top) and by the a local quantity (bottom).

profiles by the mean centre-line velocity $\overline{U}_{cl}$) and a "local" one (i.e. normalising the profiles by a local value of the Reynolds stress). In fact, as shown by Dairay et al. (2015), the Reynolds stresses of an axisymmetric wake collapsed to the same self-similar profile earlier if normalised by a local quantity than if normalised by the classical method (centre-line velocity deficit) due to flow anisotropy. Therefore, $(\overline{u_x u_r})_{max}$ is defined as simply the arithmetic mean of the magnitude of the two peak values within the Reynolds stress profiles of the axisymmetric jets.

As shown in fig. 4.14 the radial profiles of $\overline{u_x u_r}$ are found to be self-similar from $x/D_e \gtrsim 19$ when collapsed with local quantities and later around $x/D_e \gtrsim 21$ in terms of $\overline{U}_{cl}^2$. Self-similarity in the strictest sense is only achieved when the ratio between $(\overline{u_x u_r})_{max}$ and $\overline{U}_{cl}^2$ becomes constant, however this does not occur in the region of the flow studied. We thus conclude that the argument of Dairay et al. (2015) is found applicable to axisymmetric jets in addition to axisymmetric wakes. This is the explanation for using the "local" approach to normalising the Reynolds stress profiles in (4.25).

Having established that all of the jets reach a self-similar state (at least in terms of the mean velocity and Reynolds stress profiles) and that the scaling exponents a and b of (4.34) are those predicted according to the analysis of George (1989) it is now examined whether the assumptions (4.40) and (4.41) hold. Fig. 4.15a shows the ratio $K_s/\overline{U}_{cl}^2$, whilst fig. 4.15b shows the ratio $\mathcal{L}_{ur}/r_{1/2}$ in the region $23.5 \leq x/D_e \leq 26$. Both ratios remain constant (to within experimental uncertainty) over the region of space examined and thus verify assumptions (4.40) and (4.41) introduced previously. It is interesting to note that in both figures, but more so in fig. 4.15b, the round and square jets are closely grouped with one another whilst the fractal jet appears offset from the other two. In particular the ratio $\mathcal{L}_{ur}/r_{1/2}$ is larger for the fractal jet, which is due to the different state of coherence in the near field.

Now, the dissipation in this far-field region of the various jets is directly considered. The calculation of this quantity has been done in different ways due to the lack of 3-dimensional

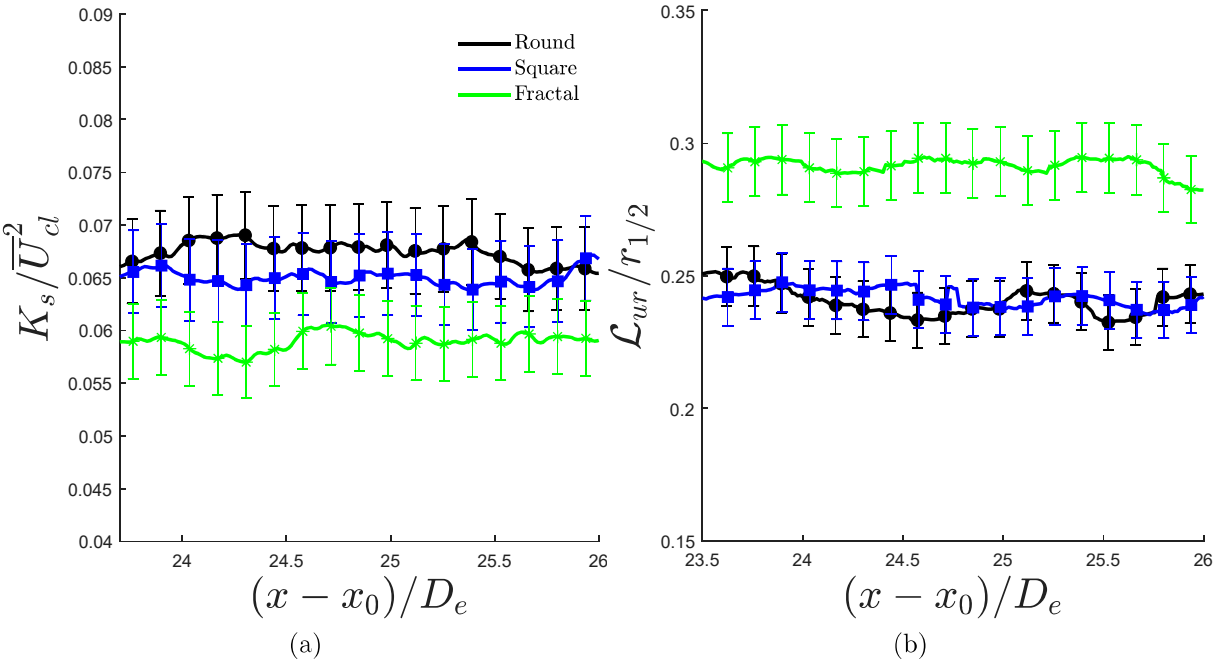


Figure 4.15: (a) Dissipation and (b) $r_{1/2}/K_s\overline{U}_{cl}$ as a function of x for the far fields of the various jets at $Re_G = 10,000$ (HPIV data).

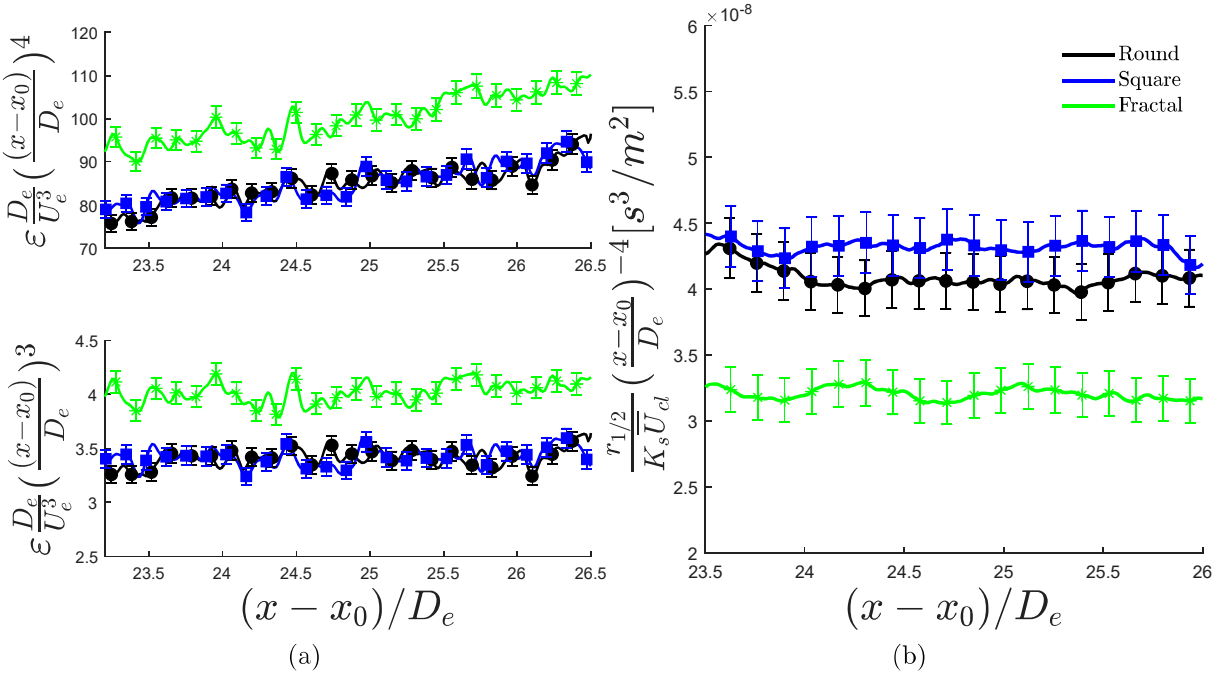


Figure 4.16: (a) Dissipation premultiplied by $(x - x_0/D_e)^4$ (top), premultiplied by $(x - x_0/D_e)^3$ (bottom) and (b) $r_{1/2}/K_s\overline{U}_{cl}$ as a function of x for the far fields of the various jets at $Re_G = 10,000$ (HPIV data).

data for the complete equation

$$\varepsilon = \nu\left[\left\langle \frac{\partial u_i}{\partial x_j}\frac{\partial u_i}{\partial x_j}\right\rangle + \left\langle \frac{\partial u_i}{\partial x_j}\frac{\partial u_j}{\partial x_i}\right\rangle\right]. \tag{4.45}$$

The assumption of local isotropy has often been used to significantly simplify eq. (4.45)

$$\varepsilon_{isotropic} = 15\nu\left\langle \left(\frac{\partial u_x}{\partial x}\right)^2\right\rangle. \tag{4.46}$$

However, this assumption has often not been found applicable in laboratory experiments and it is usually only applied to very high-Reynolds-number-flows. As discussed by George and Hussein (1991), the ratios between the velocity gradients K_1 and K_3 should be as follows

$$K_1 = 2\left\langle \left(\frac{\partial u_x}{\partial x}\right)^2\right\rangle \Big/ \left\langle \left(\frac{\partial u_r}{\partial x}\right)^2\right\rangle = 1 \tag{4.47}$$

$$K_3 = 2\left\langle \left(\frac{\partial u_x}{\partial x}\right)^2\right\rangle \Big/ \left\langle \left(\frac{\partial u_x}{\partial r}\right)^2\right\rangle = 1. \tag{4.48}$$

if the flow was truly isotropic. In general, values of $K_1 \approx 1.6$ and $K_3 \approx 1.4$ were found, indicating the isotropic assumption would not be applicable to this work. A more rigorous approach has been done by Burattini et al. (2005a), who derived an expression for dissipation for homogeneous flows that suited their cross hot-wire measurements

$$\varepsilon_{homogeneous} = 3\nu\left[\left\langle \left(\frac{\partial u_x}{\partial x}\right)^2\right\rangle + 2\left\langle \left(\frac{\partial u_r}{\partial x}\right)^2\right\rangle\right]. \tag{4.49}$$

However this expression still relies on the strong assumption that the statistics of the field are independent of the location of the origin in space (George and Hussein, 1991). An alternative way of calculating dissipation was discussed by George and Hussein (1991), assuming local axisymmetry (i.e the statistical measures have rotational symmetry around the streamwise axis x, which is applicable to this case since the jet is axisymmetric)

$$\varepsilon = \nu\left[-\left\langle \left(\frac{\partial u_x}{\partial x}\right)^2\right\rangle + 2\left\langle \left(\frac{\partial u_x}{\partial r}\right)^2\right\rangle + 2\left\langle \left(\frac{\partial u_r}{\partial x}\right)^2\right\rangle + 8\left\langle \left(\frac{\partial u_r}{\partial r}\right)^2\right\rangle\right]. \tag{4.50}$$

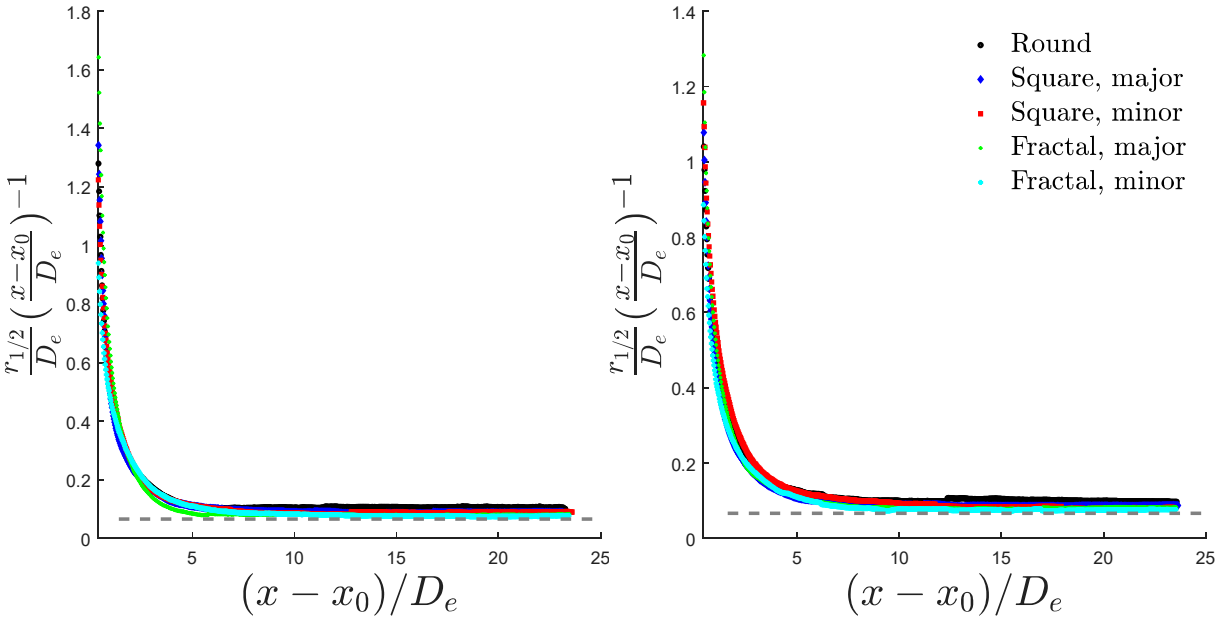
The reader is referred to the original work of George and Hussein (1991) for the complete derivation of (4.50). Compared to eq. (4.49), the assumption of local axisymmetry is applicable since both mean velocity and Reynolds stresses have reached an axisymmetric self-preserving state. An alternative form of (4.50) was used by Ganapathisubramani et al. (2007) to estimate the dissipation in the far field of an axisymmetric turbulent jet, of similar dimensions and Re_G to ours. The authors found their estimate was within 5% of the value ε calculated using all nine components of the velocity gradient tensor determined in their time-resolved stereoscopic PIV measurements. The latter quantity was shown to scale with one calculated assuming local isotropy, ε_{iso}, even though the authors found that ε_{iso} was an underestimate of ε_{3D}.

Due to the inherent noise present in the measurements of the velocity gradients, the locally axisymmetric dissipation estimate was corrected using the method of Tanaka and Eaton (2007). The authors calculated the dissipation rate from a coarser stencil ($\varepsilon_{2\Delta h}$) and compared it to their fully resolved measurements ($\varepsilon_{\Delta h}$) as

$$\varepsilon = \frac{4\varepsilon_{2\Delta h} - \varepsilon_{\Delta h}}{3}, \tag{4.51}$$

which allowed correcting for errors attributed to the sub-pixel discrimination algorithm in the PIV processing. This correction led to a spatial resolution in this region which was always $< 3.7\eta$, usually considered to be sufficient to resolve dissipation in turbulent flows (Worth et al., 2010; Buxton et al., 2011a).

Premultiplying the plot in fig. 4.16a and following the argument of Hunt and Kaye (2001), shows that the dissipation does not follow a classical scaling $\varepsilon \sim x^{-4}$ required by (4.43) (fig. 4.16a), but $\varepsilon \sim x^{\alpha}$, where $\alpha \simeq -3$ for all three different jets within experimental uncertainty. Despite the distance sampled only being approximately $4D_e$ growing pre-multiplied dissipation has been found in previous studies too, a short summary of which is reported in section 4.6. Fig. 4.16b shows the x-dependence of $r_{1/2}/K_s\overline{U}_{cl}$, which is the grouping that normalises D_s (i.e. ε) in (4.37), pre-multiplied by x^{-4}. Since assumptions (4.40) and (4.41) have been experimentally verified in fig. 4.15a and fig. 4.15b respectively,



(a) $Re_G = 3,000$ (b) $Re_G = 10,000$

Figure 4.17: Jet half-width premultiplied by $(x/D_e)^{-1}$ so that the self-similar state will be shown by a constant horizontal line (LPIV data).

and since it was verified that $\overline{U}_{cl} \sim x^{-1}$ in fig. 4.12 and $r_{1/2} \sim x$ (fig. 4.17), it is natural to observe the horizontal line for all three jets. Note also that the round and square jets are grouped together whilst the fractal jet is alone, which is another indication of the effects of the suppression of the coherent structures in the near field. We therefore conclude that the rate of dissipation is not behaving in a way that is expected from the "classical" analysis. The fact that the assumptions (4.40) and (4.41) are observed to hold whilst ε does not vary in x in the same fashion as $r_{1/2}/K_s\overline{U}_{cl}$ shows that assumption (4.42) is in fact violated. Hence, this particular region of the jet ($23.5 \leq x/D_e \leq 26$) exhibits self-similarity for the mean velocity and Reynolds stress profiles but not for the dissipation rate. As discussed previously, under such circumstances it is possible to observe $C_\varepsilon(x) \neq$ constant behaviour.

(1.1) defines the dissipation coefficient using $q^3 \equiv \overline{q^2}^{3/2}$ and $\mathcal{L}$. For the aforementioned reasons it is chosen to use $\mathcal{L}_{ur}$ from the HPIV data. We do not have access to all three components of the fluctuating velocity and hence it is not possible to directly compute $q \equiv \overline{q^2}^{1/2}$. Instead, due to axisymmetry, it is assumed that the r.m.s. of the radial component of the fluctuating velocity normal to u_x and u_r, $u'_\theta = u'_r$ and hence estimate q

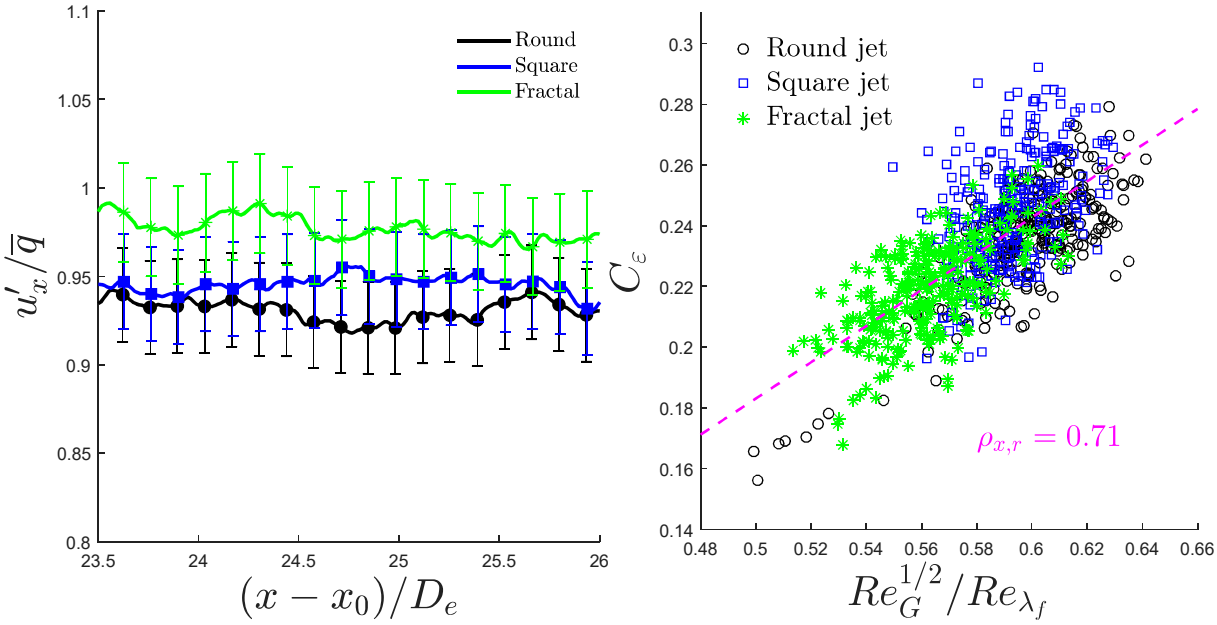


Figure 4.18: (a) u'_x/q as a function of x and (b) C_ε (from the corrected ε) as a function of $Re_G^{1/2}/Re_{\lambda_f}$ for the various jets in the region $23.5 \leq x/D_e \leq 26$ at $Re_G = 10,000$ (HPIV data).

via $\overline{q^2} = \overline{u_x^2 + 2u_r^2}$. We subsequently plot the ratio u'_x/q as a function of x in fig. 4.18a and observe that it remains constant over the region studied for all three jets. To avoid the assumption $u'_\theta = u'_r$, and so that a dissipation coefficient from the hot-wire data (in which only one component of fluctuating velocity is available) may be computed, the dissipation coefficient is derived as

$$C_{\varepsilon_{PIV}} \equiv \frac{\varepsilon \mathcal{L}_{ur}}{{u'_x}^3}. \tag{4.52}$$

Fig. 4.18b shows the dissipation coefficient, as defined in (4.52), plotted against $Re_{\lambda_f}^{-1}$ for all three jets for which the global Reynolds number $Re_G = 10,000$. Each point on the graph corresponds to a streamwise location in the region $23.5 \leq x/D_e \leq 26$. For a self-similar jet under classical"dissipation", Re_{λ_f} = constant. Hence, it is expected that plotting C_ε against $Re_G^{1/2}/Re_{\lambda_f}$ for a single Re_G, a constant point value should be approximated. However, it can be seen that Re_{λ_f} varies in space and the dissipation coefficient is found to scale in a linear fashion with $Re_{\lambda_f}^{-1}$, as might be expected if the non-equilibrium dissipation law is found to hold over this region of the flow. Despite the well-known difficulty in experimentally measuring dissipation a straight line may be

fitted to the data with a correlation coefficient of $\rho_{x,r} \approx 0.71$, giving confidence that the measurements are not effectively a single point value. From the following property of the Taylor microscale

$$\lambda_f^2 \sim \nu \frac{{u'_x}^2}{\varepsilon}, \tag{4.53}$$

it is found that the consequence of assuming that both the dissipation profile is self-similar, i.e. $\varepsilon \sim x^{-4}$, and $u' \sim \overline{U}_{cl} \sim x^{-1}$ is that $\lambda_f \sim x$. As a result it is derived that $Re_{\lambda_f} = u'_x \lambda_f / \nu =$ constant in the self-similar region of axisymmetric jets, as widely reported in Tennekes and Lumley (1972) for axisymmetric jets. The consequence of $\varepsilon \sim x^{\alpha}$, where $\alpha \neq 4$ is thus that Re_{λ_f} must vary in space and it is shown from fig. 4.18b that C_ε varies as an inverse function of Re_{λ_f}.

In order to verify that this is indeed non-equilibrium dissipation of the form $C_\varepsilon \sim Re_G^{1/2}/Re_{\lambda_f}$ it is necessary to similarly vary the global Reynolds Re_G. Due to the difficulty of making accurate measurements in the far field of the jet flow, where $\overline{U}_{cl}$ is significantly smaller than at the jet exit, and the necessity that $Re_{\lambda_f} \gtrsim 140$ ($Re_{\lambda_g} \gtrsim 100$) in order to observe non-equilibrium dissipation effects (Goto and Vassilicos, 2015) a final set of experiments was carried out at $Re_G = 31,000$ via hot-wire anemometry for comparison to the hot-wire data at $Re_G = 10,000$. In comparison to the near field a slightly different methodology had to be used to calculate the integral length scale, $\mathcal{L}_{ux}$. In fact, at $Re_G = 10,000$ the flow velocity was $\leq 3\,\mathrm{m/s}$ and this low speed was found very difficult to be captured by hot-wire anemometry. Hence, an exponential fit, fitted to the velocity fluctuation autocorrelation in the region $0.4 \leq R(\tau) \leq 0.8$, was used to estimate the correlation $R(\tau) \leq 0.4$ and this was appended to the empirical $R(\tau)$ from the original hot-wire data. The integral length scale was subsequently computed by integrating this compound function $\tilde{R}(\tau)$ between 0 and ∞ and converting time into space via Taylor's hypothesis in which $\overline{U}(x,r)$ was assumed to be the correct advection velocity. At $Re_G = 31,000$, this problem did not occur, however for consistency an exponential function was fitted to $R(\tau)$ in an identical manner.

ε was calculated assuming local isotropy (since only one velocity component was available).

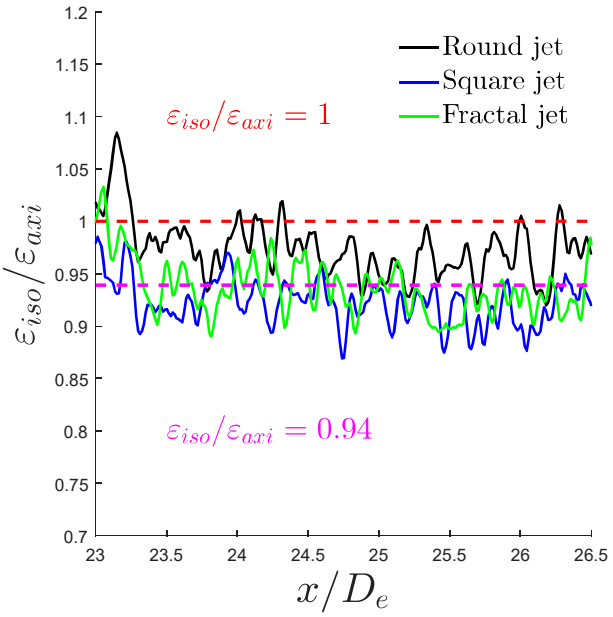


Figure 4.19: Ratio between dissipation calculated assuming local isotropy ε_{iso} and assuming local axisymmetry ε_{axi} at $Re_G = 10,000$ at the jet centreline (HPIV data).

The ratio between the dissipation rate estimated assuming local isotropy and estimated assuming local axisymmetry, $\varepsilon_{iso}/\varepsilon_{axi}$, from the high resolution PIV data is plotted in fig. 4.19. It can be seen that the assumption of local isotropy leads to an underestimate of the dissipation rate in comparison to the assumption of local axisymmetry with an average value of the ratio $\varepsilon_{iso}/\varepsilon_{axi} = 0.94$. However, the ratio is roughly constant for all jets over the region sampled giving confidence that the behaviour of the dissipation may be captured by making the assumption of local isotropy and applying it to the hot-wire data. Moreover, comparable scalings for fig. 4.16a and fig. 4.18b were found under this assumption but not shown for brevity. The longitudinal Taylor lengthscale was calculated directly as $\lambda_f = \sqrt{2}u'/\sqrt{\left\langle \left(\frac{\partial u}{\partial x}\right)^2 \right\rangle}$.

The results of fig. 4.20, where ε was calculated assuming local isotropy, show that C_ε is an increasing function of $Re_G^{1/2}$ as well as $Re_{\lambda_f}^{-1}$ indicating the presence of non-equilibrium dissipation for all three jets studied. The fractal jet, being the fastest in the far field, has a lower uncertainty and shows the best collapse to the trend line computed from the two values of Re_G. This is concurrent with a fully turbulent flow, as shown in fig. 4.21, where the one-dimensional energy spectrum, E_{11}, has been pre-multiplied so that the $f^{-5/3}$ power law is shown by a constant horizontal line. This finding is consistent with the

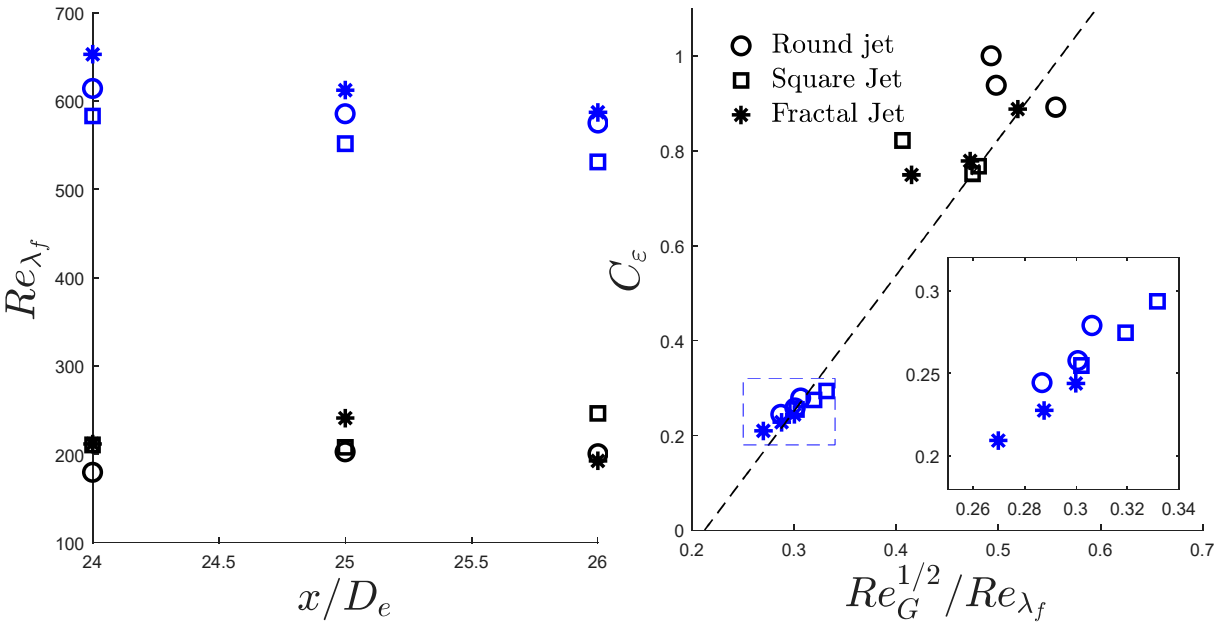
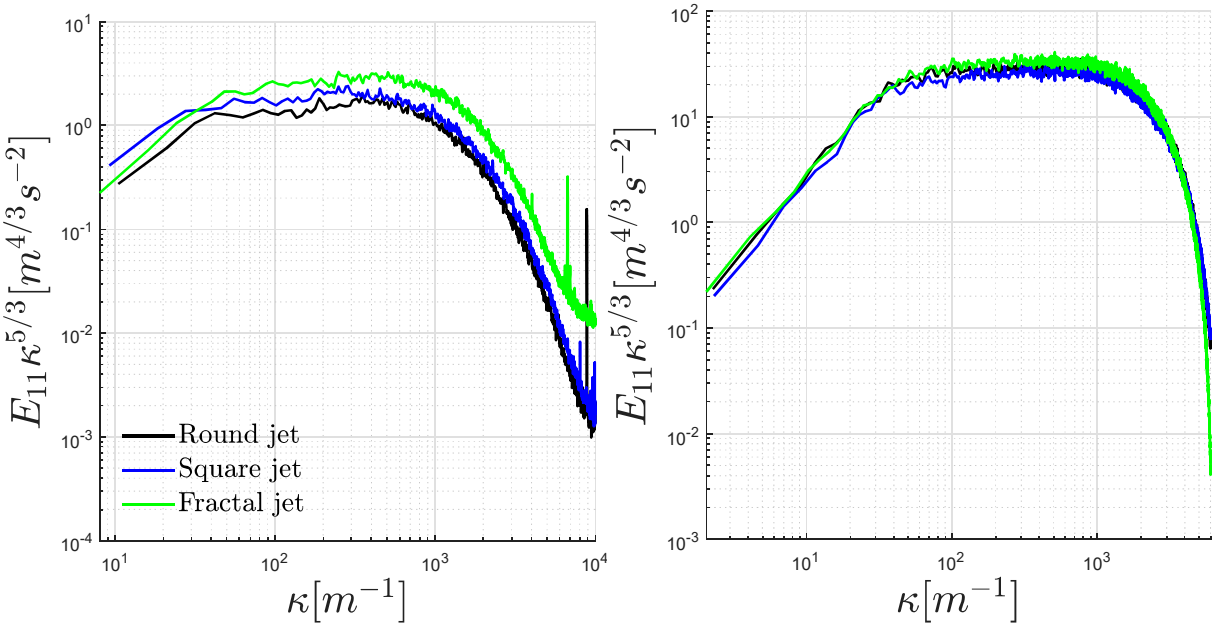


Figure 4.20: Re_{λ_f} and C_ε at $Re_G = 10,000$ (black) and $Re_G = 31,000$ (blue) (HW data).

work of Dairay et al. (2015), who found "local" self-similar scalings and non-equilibrium dissipation in the same region of a turbulent shear flow. The gradient of the two C_ε plots, calculated from the hot-wire and PIV data, is not expected to be the same since the ratio $\mathcal{L}_{ux}/\mathcal{L}_{ur} \neq 1$ (Pope (2000)) and is a nonlinear function of x.

Further experimental evidence of non-equilibrium dissipation were subsequently sought in previous works, where the authors may not have been aware of it. Therefore, C_ε was calculated from the work of Mi and Nathan (2010). The original authors calculated the integral lengthscale $\mathcal{L}$ from the autocorrelation (in time delay) of the streamwise velocity fluctuations (deriving the integral time scale), truncating it at the first zero-crossing, and converted it to space using Taylor's frozen turbulence hypothesis. The dissipation rate was calculated assuming the flow was locally isotropic as in eq. (4.46). As shown by reproducing their data, Re_{λ_f} is initially decreasing, however it becomes approximately constant from $x/D_e = 25$, in fig. 4.22a. Concurrently, C_ε is initially increasing (i.e. non-equilibrium dissipation), however around $C_\varepsilon = 0.65$ a different trend is found. Therefore, non-equilibrium dissipation is found for a wide variety of noncircular exit geometries, suggesting it may be a universal feature for axisymmetric jets too. Further comments are



(a) $Re_G = 10,000$ (b) $Re_G = 31,000$

Figure 4.21: Premultiplied energy spectra a $x/D_e = 25$ at jet centre-line, (HW data).

given in section 4.6. The presence of this novel dissipation law does not however conflict with the previous findings suggesting that $\varepsilon \sim x^{-4}$. In fact, as shown by Hearst and Lavoie (2014), the dissipation constant for a grid-generated flow would initially grow (non-equilibrium dissipation), however at a certain distance downstream C_ε would transition to a constant value ("classical" disipation law). Therefore, it is possible that further downstream of the jet exit a constant C_ε may be found.

To summarise, in a region of the flow of the jets, which from now on is defined as the "weakly self-similar region", the mean velocity and Reynolds stress profiles were observed to be self-similar. Evidence that the dissipation in this far-field region is behaving in a non-equilibrium manner are presented, but this presence of non-equilibrium dissipation is shown only through the microscales of the flow, whilst the large-scale spreading rate etc. shows the behaviour predicted by the "classical" theories. This is likely due to the particular flow considered. Axisymmetric jets are, to first order, known to have a constant momentum flux at each streamwise location x which is equal to the rate at which momentum is added at the source (Hussein et al., 1994), leading to equivalent predictions for the scalings of $\overline{U}_{cl}$ and $r_{1/2}$ as in (4.34) regardless of which dissipation

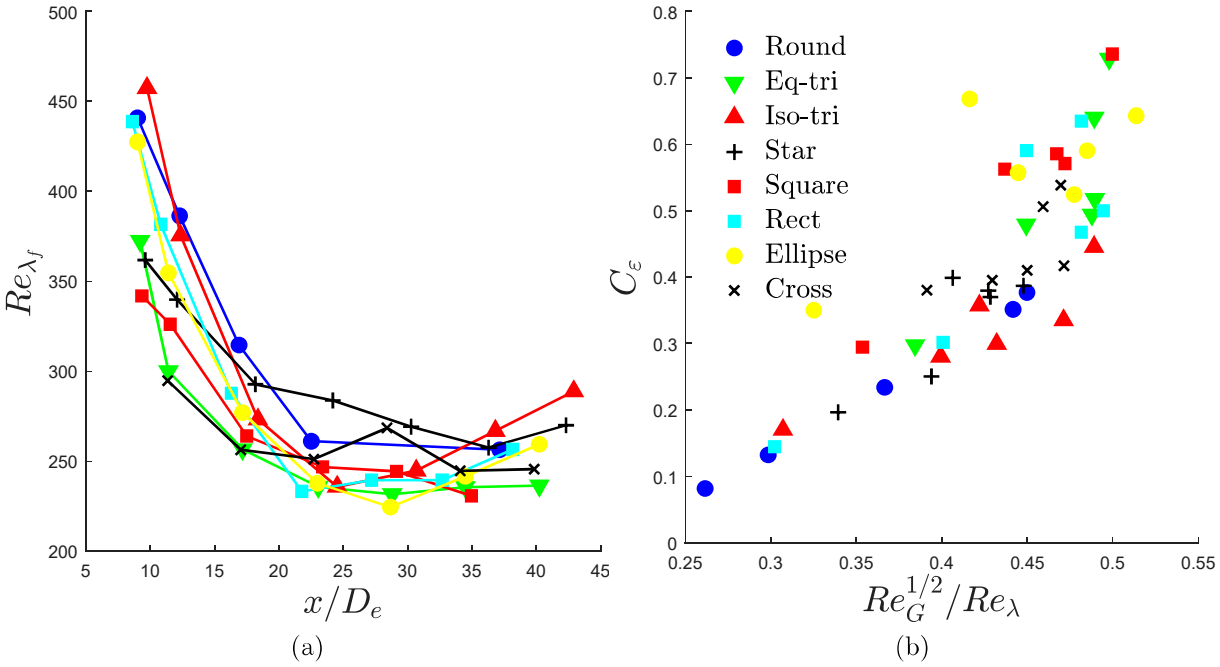


Figure 4.22: (a) Variation of Re_{λ_f} with streamwise distance for an axisymmetric jet. (b) Variation of dissipation constant. Data reproduced from the work of Mi and Nathan (2010) for axisymmetric round jets emitted from orifices at $Re_G = 13,000$ (based on the current definition of D_e) and acquired with a hot-wire.

law is used. In previous shear flows where non-equilibrium dissipation has been observed, axisymmetric wakes, this is not the case and the presence of non-equilibrium dissipation has been marked by novel large scale exponents for the velocity deficit and wake width as a power law function of x (Nedić et al., 2013b; Dairay et al., 2015; Obligado et al., 2016). Moreover, non-equilibrium dissipation was found irrespectively of the initial conditions since it is present for all three jet types, with different states of coherence in the near field. It is worth noting that the study of Hearst and Lavoie (2014) observed non-equilibrium dissipation for the flow downstream of their repeating fractal element grid but found that $C_\varepsilon(x)$ transitioned back to the "classical" $C_\varepsilon(x) =$ constant far-away from the grid, which may be true for an axisymmetric jet as well. Through violation of assumption (4.42) it is shown that whilst the mean momentum and Reynolds stresses are in a self-similar state the dissipation is not, and this dynamical mismatch between the large-scale turbulent properties and the microscales allows for the possibility of the dissipation being out of equilibrium. This suggests that an axisymmetric jet may eventually return to $C_\varepsilon =$ constant and the classical $\varepsilon \sim x^{-4}$, but this distance was not reached in the

present experiments. This point was confirmed whilst reproducing the work of Mi and Nathan (2010), where non-equilibrium dissipation was found too and $C_\varepsilon \approx$ constant further downstream. Now, a brief discussion on the classical dissipation and its previous experimental evidence is presented.

4.6 Previous works on $\varepsilon \sim x^{-4}$

Various studies, George (1989) and Thiesset et al. (2014) amongst others, have analytically demonstrated that complete self-preservation of a turbulent axisymmetric jet will lead to:

$$\varepsilon \sim x^{-4} \tag{4.54}$$

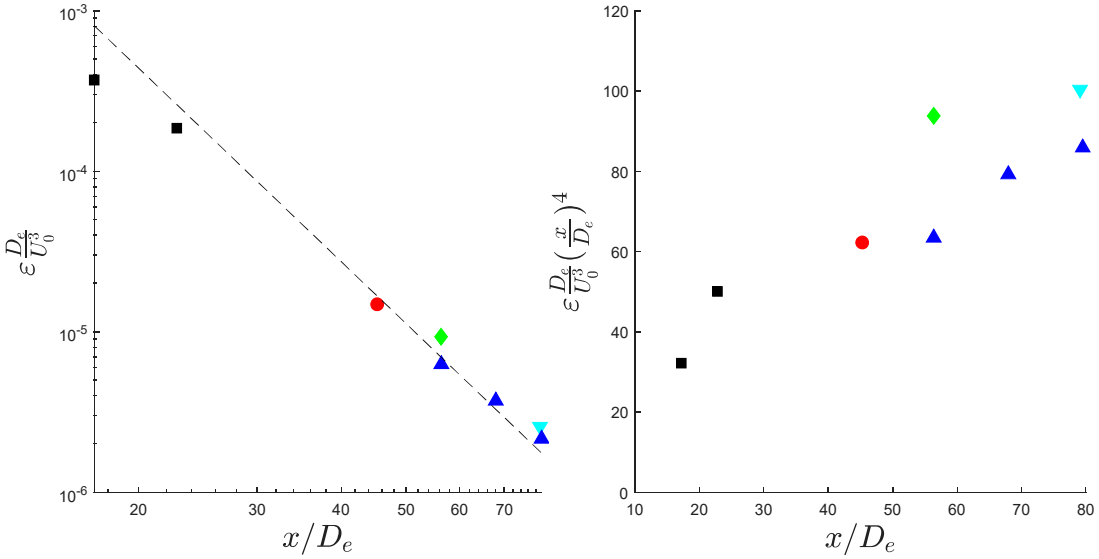
However, its experimental validation has posed significant issues to researchers, which can be grouped into the following two categories:

- Initial conditions.
- Spatial resolution.

We will now examine each of these issues.

4.6.1 Initial conditions

This work has discussed the importance of the initial conditions in determining the rate of evolution of an axisymmetric turbulent jet. It has been found that exit geometry and Re_G influence the development of the eddy turnover time parameter N_{e_x}. Therefore, when considering different initial conditions, each case should be treated separately since they may be markedly different. An example where this was not done is in fig. 4.23. In fig. 4.23a, the data published by Friehe et al. (1972) are reproduced in a similar manner to the original work. Despite fitting a line of best fit on a logarithmic scale seeming to



(a) Log plot as in the original work

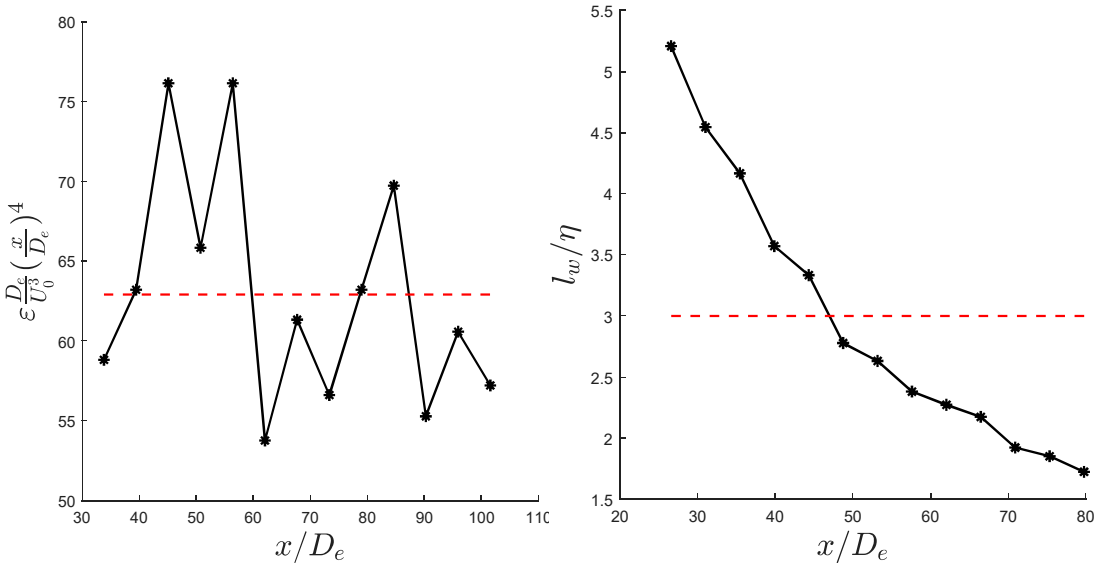
(b) Premultiplied

Figure 4.23: Reproduction of *Figure 2* from Friehe et al. (1972). The markers represent the following data: ■ unpublished work of LaRue and Friehe (1971) ($Re_G = 18,000$), ● Friehe et al. (1972) ($Re_G = 106,000$), ♦ Gibson (1963) ($Re_G = 440,000$), ▲ ($Re_G = 330,000$) and ▼ ($Re_G = 514,000$) from a private communication with F. H. Champagne (1971). Please note the round jet diameter in the original works D was converted to the equivalent diameter as in the current work. The variable U_0 represent the jet exit velocity in the experiments.

be a reasonable approach (and it has been widely done in previous literature), fig. 4.23b shows the same data points premultiplied by $(x/D_e)^4$. If eq. (4.54) holds, the data points would fall on a flat horizontal line. As shown, the trend is actually increasing with x and one may fit a different trend line between the different experiments (i.e. the different initial conditions) considered. The Reynolds number here ranged from 18,000 to 514,000, therefore the development of N_{e_x} of the jets may be significantly different and hence the location and the extent of any weakly self-similar region will also be different. Moreover, the spatial resolution of the data points (●) measured by Friehe et al. (1972) was above 8η (based on the length of their platinum-plated tungsten hot-wire). The importance of this point is covered in the next section.

4.6.2 Spatial resolution

Two recent studies (Buxton et al., 2011a; Worth et al., 2010) have suggested a spatial resolution of at least 3η is needed to adequately capture the small-scale behaviour of a flow. This has proven to be challenging to achieve with both hot-wire and PIV, due to the limitation of the experimental apparatus and due to the decrease of η with increasing Re_G. Burattini et al. (2005b), achieved an adequate spatial resolution, however the scatter in the premultiplied dissipation in fig. 4.24 does not permit concluding if the flow is completely self-preserving across the whole experiment or if between 30 and 45 D_e there is a region of weakly self-similar flow. Problems with spatial resolution were encountered



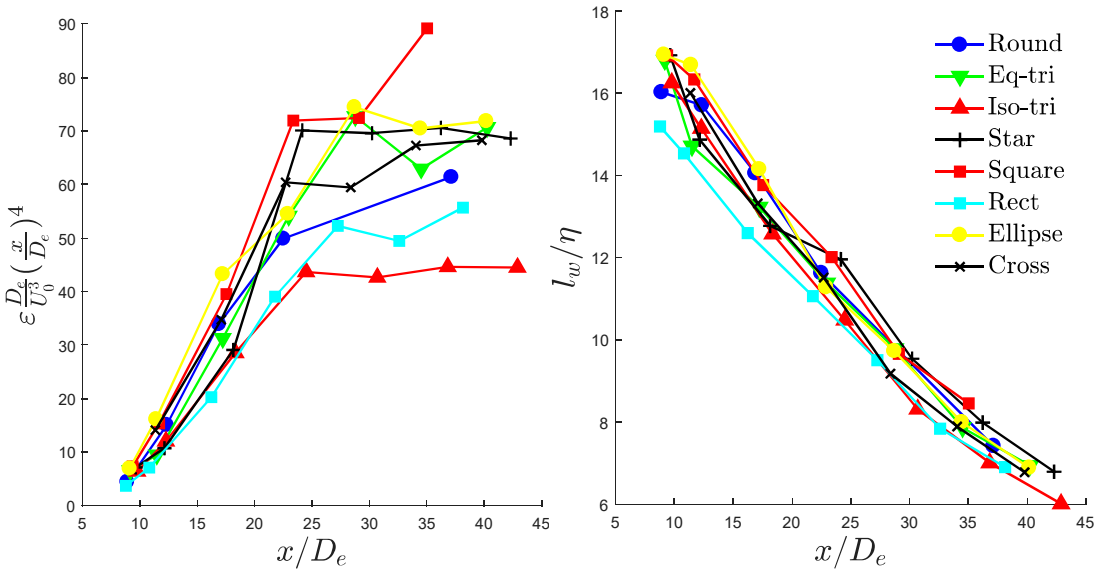
(a) Premultiplied dissipation

(b) Hot-wire spatial resolution

Figure 4.24: Data from the work of Burattini et al. (2005b) acquired with a hot-wire and at $Re_G = 115,000$. Jet emitted from a round nozzle. Dissipation was estimated converting the Kolmogorov length scale reported in Table IV into dissipation as $\varepsilon = \nu^3/\eta^4$. The variable l_w represents the hot-wire length and the round jet diameter is rescaled in terms of equivalent diameter D_e.

by Mi and Nathan (2010), as shown in fig. 4.25b. Despite that, the authors managed to measure a region of self-preserving dissipation for some of the jets as shown by the flat horizontal in fig. 4.25a, whilst the round jet appears to be growing and is therefore still in a weakly self-preserving state. This again reveals the importance of the initial conditions in affecting the evolution of the jet. These findings suggest that for a jet emitted from an

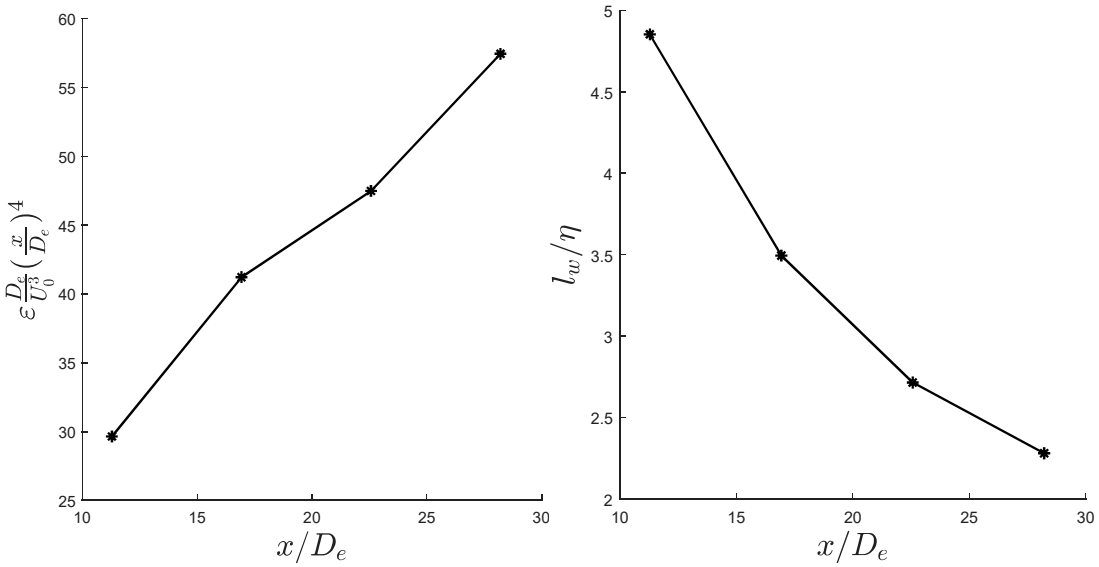
orifice the transition from weakly to completely self-similar will start somewhere between $x/D_e = 25-30$, even though a strong influence is played by the initial conditions. Sadeghi



(a) Premultiplied (b) Spatial Resolution

Figure 4.25: Data from Mi and Nathan (2010), acquired with hot-wire and at $Re_G = 13,000$. Jet emitted from sharp orifices. Dissipation is calculated from *Figure 11c* of the original work. Please note the round jet diameter D has been converted to the equivalent diameter D_e of this work.

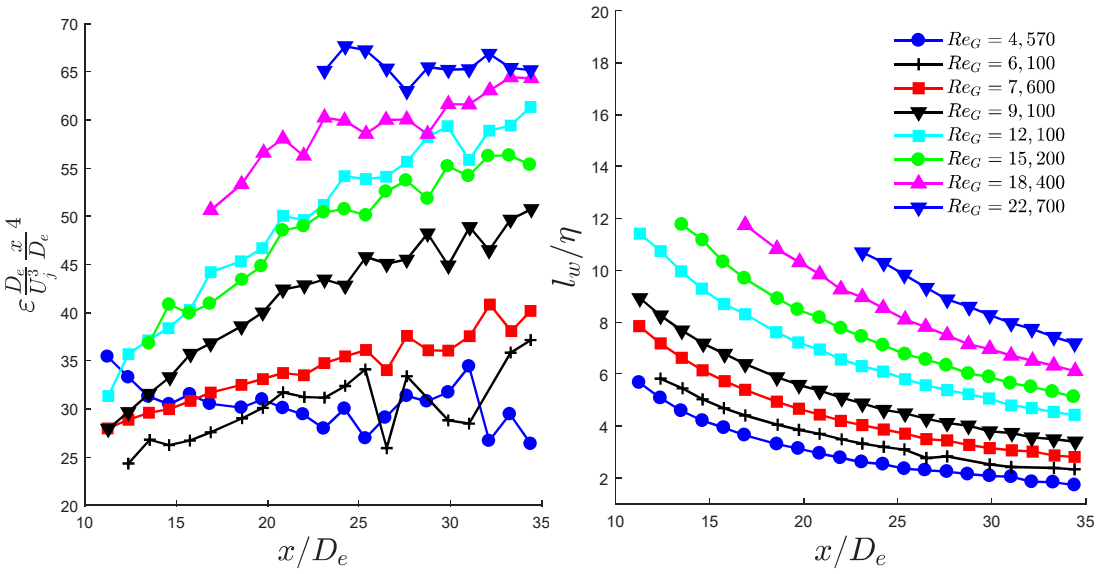
et al. (2015) looked into a similar streamwise region for a jet emitted by a round nozzle, which usually have a lower mixing and therefore a slower development compared to their orifice counterparts. Again, as shown in fig. 4.26, it is shown that up to $x/D_e = 30$ the flow has not reached complete self-preservation, but it appears it may be in a weakly self-similar state. The spatial resolution of this study was also close to 3η. Certainly the choice of high Reynolds numbers reduces the chances of actually resolving dissipation and a clear example is given by Mi et al. (2013), where a jet emitted by a round nozzle is studied between $Re_G = 4,570$ and 22,700. As shown in fig. 4.27b, the spatial resolution progressively worsens at increasing Reynolds number. This is due to the fact that at high Re_G, the energy of the flow is redistributed across a wider range of scales, leading to a smaller η and therefore to a coarser relative spatial resolution. In fig. 4.27a, the premultiplied dissipation is again found to be increasing up to $x/D_e = 35$ at all Reynolds numbers, apart from $Re_G = 22,700$, which also has the worst spatial resolution.



(a) Premultiplied (b) Spatial Resolution

Figure 4.26: Data of *homogeneous* dissipation (eq. (4.49)) from *Table 1* of Sadeghi et al. (2015), acquired with a cross-wire probe and at $Re_G = 44,000$. Jet emitted from a round nozzle. The diameter has been converted to equivalent diameter, as stated in the current paper.

Concluding, this section has examined the effect of initial conditions and spatial resolution on the estimate of the dissipation rate. These need to be accounted for when evaluating the microscales of a flow, which could be mistaken to be completely self-similar (especially if considered on a logarithmic scale). Despite these differences in the initial conditions and spatial resolution, quite a few of the previous studies mentioned point to the existence of the weakly self-similar region in the same area studied, even if not explicitly pointed out by the authors.



(a) Premultiplied (b) Spatial Resolution

Figure 4.27: Reproduction of *Figure 14* from the work of Mi et al. (2013) (the Kolmogorov scale was then converted into dissipation). The data are acquired with a hot-wire and the jet was emitted by a smooth nozzle. Please note both round jet diameter D and Reynolds number have been rescaled with the equivalent diameter D_e, as the present work.

Chapter 5

The evolution of the small-scale properties and the behaviour of the TNTI at different streamwise locations

Having established the influence of the exit geometries on coherent structures, entrainment, mixing and having discussed the weakly self-similar behaviour, the development of the turbulent-non turbulent interface (TNTI) is now examined for round and fractal jets since its behaviour and dynamics are crucial in determining the entrainment into the jet. This is done by evaluating the properties of the TNTI at three different streamwise locations:

- $x/D_e = 2$: here the jets are in a state of development. The first Kelvin-Helmholtz vortex rings have already developed and the turbulent kinetic energy is in a production phase, where the velocity fluctuations increase with streamwise distance x.

- $x/D_e = 10$: both round and fractal jet have passed the peak of turbulent kinetic

energy.

- $x/D_e = 25$: mean velocity and Reynolds stresses are self-similar.

Moreover, in the past some of the microscales' properties of various flows have been found universal, as mentioned in chapter 1. Therefore, the microscales of the flow will also be characterised through the velocity gradients, to verify how the microscale structure of the jets evolve in space and from the edge of the TNTI into the turbulent bulk of the jet. The latter is necessary to gain a deeper understanding of the entrainment mechanism and how quiescent irrotational flow acquires vorticity.

5.1 Detection of the TNTI

In chapter 1, the importance of the TNTI in the entrainment of irrotational fluid into the turbulent stream was described. Studying this interface has posed significant challenges due to its small thickness and due to the difficulty in establishing a reliable criteria for its detection. Usually, the best way to detect it is to choose a quantity that has a steep gradient across the TNTI, since the flow will change from irrotational to turbulent (i.e. rotational). According to this definition one may simply set a threshold based on the enstrophy $\Omega^2 > 0$. However, experimental/numerical noise, weak turbulence in the background, etc make this criteria not always effective. Therefore, various authors in the past have tested various threshold-based detection systems to find one which was relatively insensitive to the threshold chosen and which made the study of the TNTI reliable.

Now, various detection systems are analysed. The vorticity is split into its mean and fluctuating component as follows:

$$\Omega = \overline{\omega} + \omega. \tag{5.1}$$

Bisset et al. (2002) estimated the location of the TNTI from their DNS data for a wake generated by a flat plate based on a vorticity threshold Ω_{th} calculated from the centre-

plane velocity deficit U_0 and the wake half-width b:

$$\Omega_{th} = 0.7\frac{U_0}{b}, \tag{5.2}$$

Mathew and Basu (2002), modelling a round jet in DNS, and da Silva and Taveira (2010), for a DNS of homogeneous shear free turbulence, also used a threshold based on the r.m.s. of the mean vorticity fluctuations ω':

$$\Omega_{th} = 20\omega', \tag{5.3}$$

Anand et al. (2009) reviewed some of the most used criteria proposing one for an axisymmetric jet where the full vorticity vector is evaluated in terms of the mean streamwise velocity and of the distance b_e (defined as the distance between the centre of the jet and the location where the flow's streamwise velocity is equal to $\overline{U}_{cl}\, e^{-1}$)

$$\overline{U_x}(x, b_e) = \frac{1}{e}\overline{U}_{cl}(x) \tag{5.4}$$

$$\frac{\Omega b_e}{\overline{U_x}} > 0.1, \tag{5.5}$$

and one where only the azimuthal component of vorticity Ω_θ is available, which is evaluated with the instantaneous and mean streamwise velocity

$$\frac{U_x}{(|\Omega_\theta| b_e \overline{U_x})^{1/2}} < 0.03. \tag{5.6}$$

Holzner and Lüthi (2011) proposed a different threshold for their study on the viscous super layer (VSL) of a turbulent flow generated by an oscillating grid using both DNS and particle tracking velocimetry (PTV), who set a vorticity threshold of 5% of the mean vorticity

$$\Omega_{th} = 0.05\overline{\omega}. \tag{5.7}$$

A similar methodology was used by Wolf et al. (2013) for their 3D-PTV and DNS study, who set the threshold to 2%. Chauhan et al. (2014a) and da Silva et al. (2014b) proposed

a threshold based on the local turbulent kinetic energy q^2, which had to be greater than a certain threshold either in a 3×3 box of data points (the former) of point-by-point (the latter). However, this may be not the best approach since, as pointed out by Kwon et al. (2016), there may be non-turbulent regions of the flow with high velocity fluctuations and therefore kinetic energy. Finally, da Silva et al. (2014b) and Zhou and Vassilicos (2017) proposed a method of evaluating the size of the volume (the former) or of the area (the latter) of regions of vorticity greater than a certain threshold value. Plotting the size of the area against the vorticity threshold chosen, it will be noticed that increasing the threshold of Ω_{th} at some point the area (or volume) will suddenly show a plateau, suggesting the turbulent zone has been entered due to the fact vorticity increases sharply at the interface (whilst the area does not vary as much). An example is shown in fig. 5.1. This method

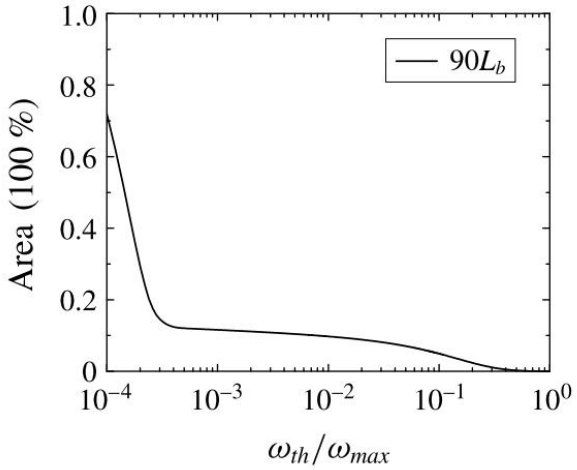
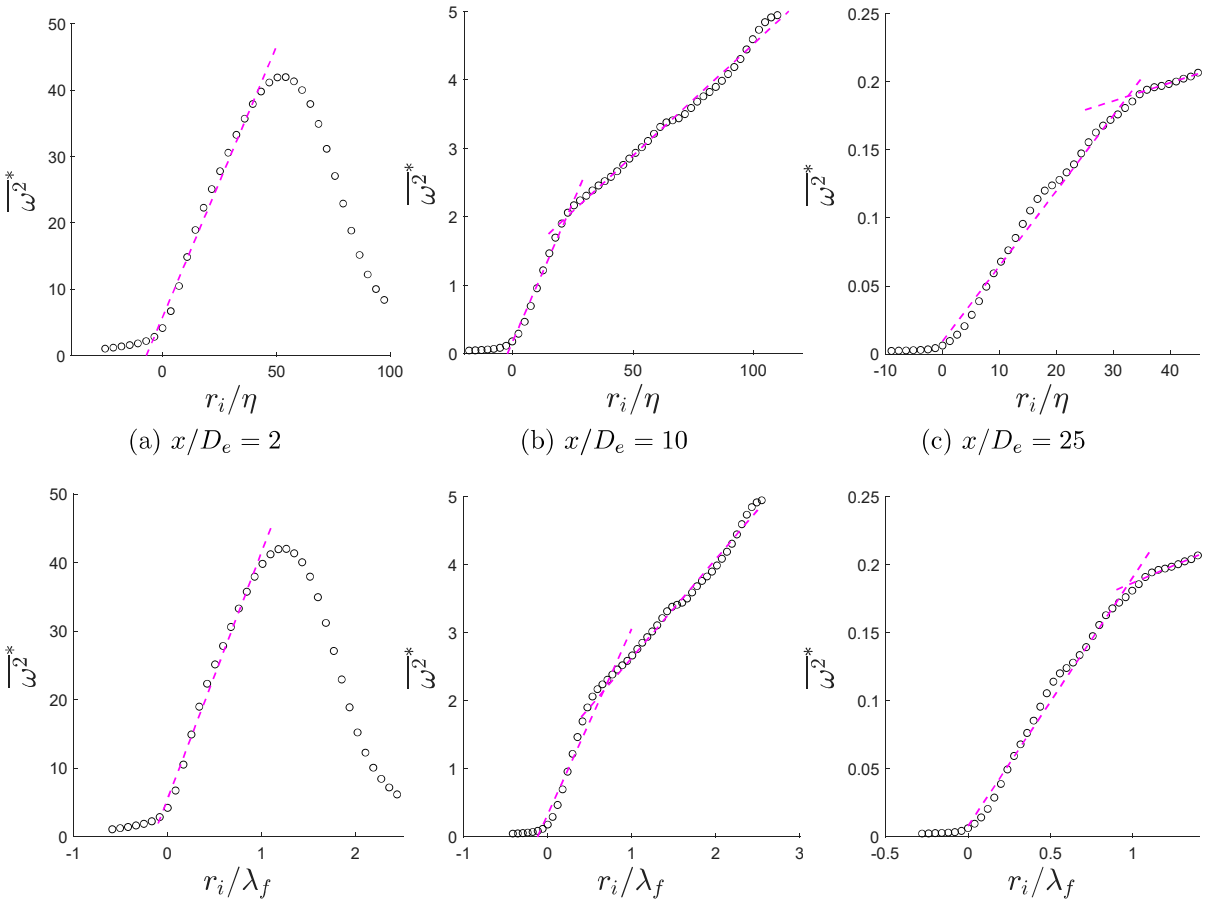


Figure 5.1: Example of threshold detection based on the turbulent area. Figure reproduced from Zhou and Vassilicos (2017) with the permission of the Journal of Fluid Mechanics.

has been used for DNS data and may therefore not be applicable for experimental works, where the underlying noise in calculating the vorticity vector may make the jump where the turbulent volume (or area) sharply increases less steep, as in fig. 5.1. In summary, the works above suggested that the most reliable threshold for an experimental work should be based on vorticity (or enstrophy), since the quiescent fluid will have zero vorticity (or will appear weakly vortical due to experimental/numerical noise).

Therefore, this approach is followed for the present study. A certain threshold (discussed



(a) $x/D_e = 2$ (b) $x/D_e = 10$ (c) $x/D_e = 25$

(d) $x/D_e = 2$ (e) $x/D_e = 10$ (f) $x/D_e = 25$

Figure 5.2: $\overline{\omega^2}^*$ at various streamwise locations for the round jet, compensated by the mean bulk η (a, b, c) and λ_f (d, e, f). The change of growth rate are shown with the dashed magenta lines (TPIV data and $Re_G = 10,000$).

later in the paragraph) of the square root of enstrophy was selected and the radial distance r from the jet centre was converted into distance r_i from the TNTI, where $r_i = 0$ corresponds to where the TNTI is detected and positive r_i is in the direction of the turbulent bulk. The conditional mean enstrophy $\overline{\omega^2}^*$ (i.e. conditioned to the distance from $r_i = 0$) is premultiplied by equivalent diameter and velocity

$$\overline{\omega^2}^* = \overline{\omega^2}\left(\frac{D_e}{U_e}\right)^2, \tag{5.8}$$

and then plotted in fig. 5.2a. As shown, the threshold chosen captures the point where $\overline{\omega^2}^*$ sharply increases across the TNTI, whilst for $r_i < 0$ the enstrophy is approximately zero. The threshold had to be adjusted for the three different streamwise locations studied,

since the coflow would slow down moving up vertically from the jet exit, showing as a consequence a reduced background vorticity. The values chosen were $\Omega^* \geq 1.91$ for $x/D_e = 2$, $\Omega^* \geq 0.40$ for $x/D_e = 10$ and $\Omega^* \geq 0.08$ for $x/D_e = 25$. As shown in fig. 5.2, these thresholds allow being above the background weakly vortical flow. In Bisset et al. (2002), it was shown that for a fully developed turbulent wake $\overline{\omega}$ would be close to zero in the non-turbulent zone. It would then sharply increase across the TNTI and finally it would have a different and slower growth rate inside the wake. In figs. 5.2a to 5.2c, two different behaviours can be identified as expected. It is also shown that, due to experimental noise, a threshold $\Omega > 0$ is needed to distinguish between the jet and the background fluid. Moreover, comparing figs. 5.2a to 5.2c (r_i compensated by η) with figs. 5.2d to 5.2f (r_i compensated by λ_f), it is found that the TNTI's thickness appears to scale with λ_f rather than η. In fact, at $x/D_e = 2$, the TNTI has a thickness of $\approx 1.2\lambda_f$, at $x/D_e = 10$ of $\approx 0.7\lambda_f$ and of $\approx \lambda_f$ at $x/D_e = 25$. Moreover, at $x/D_e = 2$, the TNTI of the fractal jet appears to have a thickness of $\approx 0.6\lambda_f$, which is almost half of the one of the round jet. This suggests that in the near field, the coherent structures present for the round jet alter the development of the TNTI, increasing the thickness of the outer TNTI, between the jet and the background fluid, whilst the one between the jet and the core appears to have a comparable thickness between round and fractal jet (fig. 5.3). Once the jet's shear layers meet and the core is absorbed, the TNTI's thickness is initially less than a Taylor lengthscale but then evolves towards $\approx \lambda_f$ once the turbulent flow is fully developed in the weakly self-similar region ($x/D_e = 25$). The point of the TNTI scaling with λ_f, despite being in agreement with previous literature, contrasts with a recent work of Silva et al. (2018) for a planar jet, who suggested a TNTI's thickness of 17η. Further remarks are given in section 5.6.

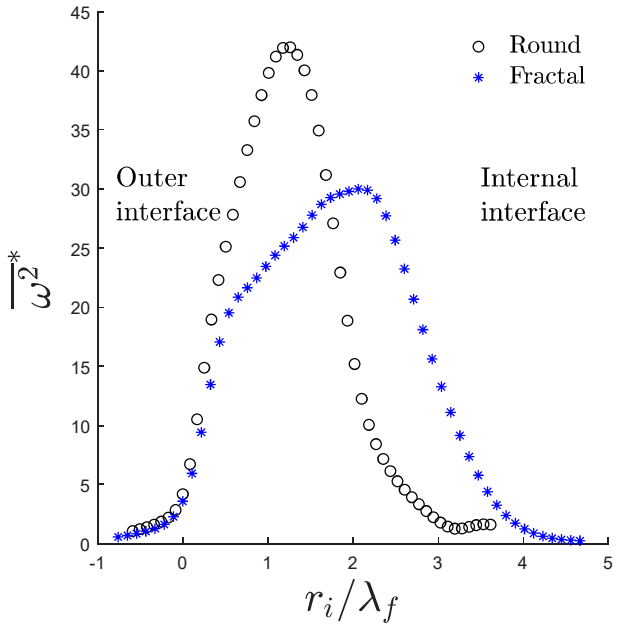


Figure 5.3: Mean conditional interface for round and fractal jet at $x/D_e = 2$ (TPIV data, $Re_G = 10,000$).

5.2 Properties of TNTI

As discussed in chapter 3, the fractal geometry considered in this thesis has been found to break-up the coherent structures, leading to a reduction of entrainment and mixing. It is hypothesised therefore that the different coherent structures may affect the wrinkling of the interfaces and its distance from the jet centre $\hat{r}$. The analysis focuses on different types of TNTI. At $x/D_e = 2$, two interfaces are present: the *outer interface* (OTNTI), between the jet and the quiescent background flow, and the *inner interface* (ITNTI)[1], between the laminar potential core and the turbulent part of the jet. The tortuosity is calculated for the ITNTI only, since the field of view was not big enough to always capture the complete OTNTI. This was estimated as a function of the averaged interface length L_{TNTI} across all time steps and the average radial distance $\overline{\hat{r}}$ of the TNTI from the jet centre:

$$tortuosity = \frac{L_{TNTI}}{2\pi\overline{\hat{r}}}. \tag{5.9}$$

[1]Note that at $x/D_e = 10$ and $x/D_e = 25$, the terminology TNTI refers to the outer interface of the jet since it is the only one present.

It is found that the round jet has a tortuosity of $1.49 \pm 0.5\%$, whilst the fractal jet of $1.40 \pm 0.5\%$. Hence, this hints that the break-up of the coherent structures may reduce the wrinkling and the tortuosity that can be achieved by the TNTI. In order to further investigate this, the probability density function (p.d.f.) of $\hat{r}$ is examined. As shown in fig. 5.5a, the round jet has wider pdfs at both ITNTI and OTNTI. However, it is unclear if this is due to the suppression of the large scale structures or simply due to the different exit geometry influencing the mean interface shape. As shown in fig. 5.4, both

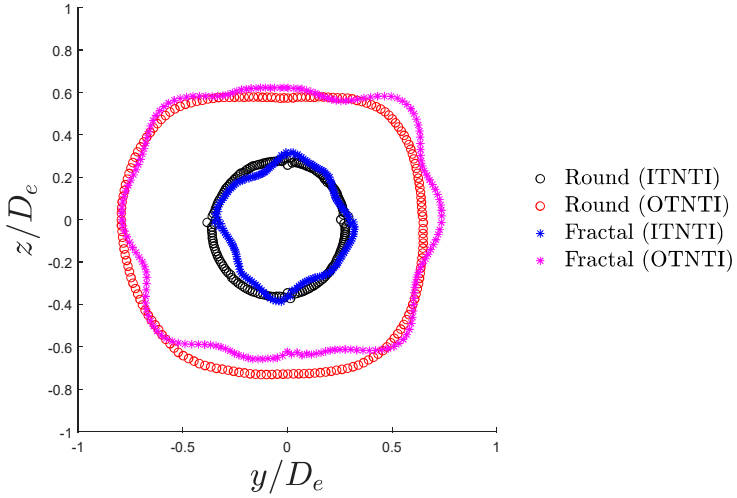


Figure 5.4: $\overline{\hat{r}}(\theta)$ for round and fractal jet at $x/D_e = 2$. (TPIV data and $Re_G = 10,000$)

the ITNTI and the OTNTI of the fractal jet having a noncircular shape resembling the exit geometry, hence the radial fluctuations based on a single mean value for $\hat{r}$ may not be actually influenced by the exit geometry. Therefore, in order to evaluate the fluctuations of $\hat{r}$, a different mean $\overline{\hat{r}}(\theta)$ was calculated every 2°, to account for the different shape of the two TNTIs. The pdf of the fluctuations of $\hat{r}$ is examined in fig. 5.5b, where the abscissa has been re-ordered so that when it is positive the TNTI is moving towards the turbulent zone, whist when negative towards the non-turbulent zone. It is found that the OTNTI and ITNTI of both jets have a comparable positive tail of the pdf, suggesting therefore that the movement towards the turbulent zone is not affected by the break-up of the coherent structures. On the negative side of the pdf, the OTNTI appears to have a larger tail compared to the ITNTI. Small differences are found on the ITNTI between the two jets, where the round jet has a larger negative tail indicating it is fluctuating more with respect to $\overline{\hat{r}}(\theta)$ due to the influence of the large coherent structures. However,

no appreciable differences are found on the negative side of the OTNTI of round and fractal jets, suggesting therefore it is insensitive to the state of the coherent structures.

Now, the effect of exit geometry and coherent structures on the velocity fluctuations is

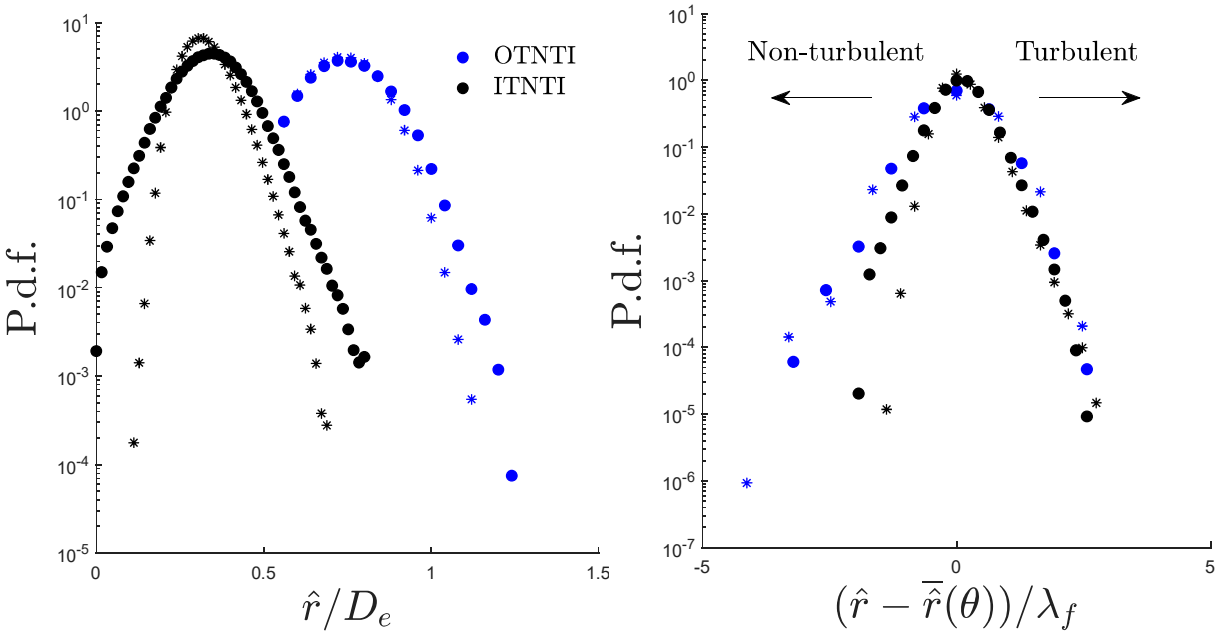
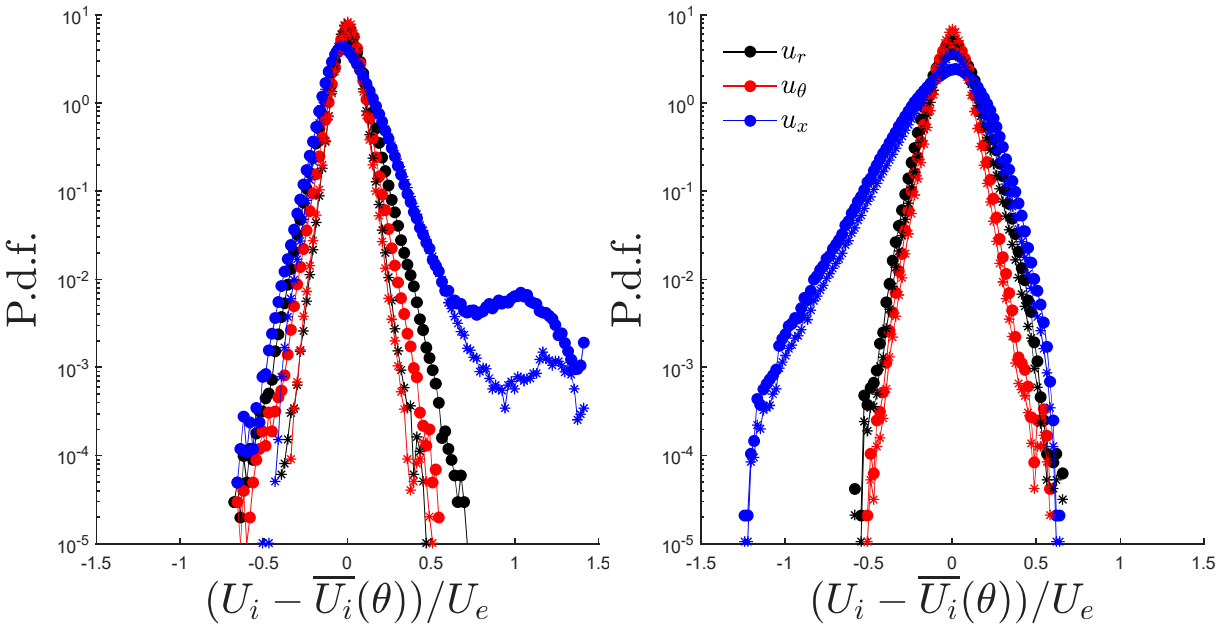


Figure 5.5: (a) P.d.f. of $\hat{r}$ for round ($\circ$) and fractal ($*$) jet. (b) P.d.f. of fluctuations of the TNTI based on the angular mean radial distance (same legend applied). Here the abscissa has been oriented so that positive represents the turbulent zone, whilst negative represents non-turbulent areas (either in the jet core or in the quiescent background). TPIV data at $x/D_e = 2$ and $Re_G = 10,000$.

examined. As before, a local mean velocity $\overline{U_i}(\theta)$ is calculated every 2° to account for the different shape of the exit perimeters. As shown in fig. 5.6b, at the OTNTI the two jets have comparable velocity fluctuations. At the ITNTI, similar pdfs are found for the streamwise velocity fluctuations u_x, where the only difference is on the right-hand tail, which suddenly becomes approximately constant suggesting the potential core has been entered. Moreover, the pdfs of the round jet are wider compared to the ones of the fractal jet for u_r and u_θ.

In chapter 3, it was suggested that the break-up of the coherent structures produced a thinner shear layer that coalesced further downstream for the fractal jet, influencing the two-point correlations of the velocity fluctuations. This finding is here confirmed, however it is shown that the fractal orifice primarily affects the fluctuations at the ITNTI, whilst



(a) ITNTI (b) OTNTI

Figure 5.6: P.d.f. of velocity fluctuations at the interface based on the mean interface velocity at the inner and outer interface for round ($\circ$) and fractal jet ($*$). ($x/D_e = 2$, $Re_G = 10,000$).

they remain comparable at the OTNTI to the round jet. Further downstream, comparable pdfs are found between the two jets for both $(\hat{r} - \overline{\hat{r}}(\theta))$ and $(U_i - \overline{U_i}(\theta))$.

Having discussed the radial position of, and velocity fluctuations at the interface, now its evolution in terms of its fractal dimension is examined.

5.3 Fractal dimension of the TNTI

Since the work of Sreenivasan and Meneveau (1986), it has been believed that the the area of a turbulent surface S of a TNTI would follow a power-law in the form $S \sim \Delta^{2-D_f}$, where D_f is the three-dimensional fractal dimension and Δ is the side length of a cube. As discussed by Mistry et al. (2018), invoking Reynolds similarity hypothesis and Kolmogorov scalings leads to a prediction of $D_f = 2 + 1/3$. Various computational and experimental works have attempted to verify this hypothesis, however strong limitations were posed by the spatial resolution and by the dimensions available (2D or 3D). Therefore, rather than evaluating the area of the TNTI, the "fractality" of its length was tested to check it

would follow a power law. A popular method to verify this has been the "box counting" technique (Mandelbrot, 1982; Sreenivasan et al., 1989; Mistry et al., 2016; Zhou and Vassilicos, 2017). This technique consists in covering the field of view with squares of the same size and counting how many of them contains the TNTI. An example of the procedure is given in fig. 5.7. Varying the box size B_s and counting each time the number

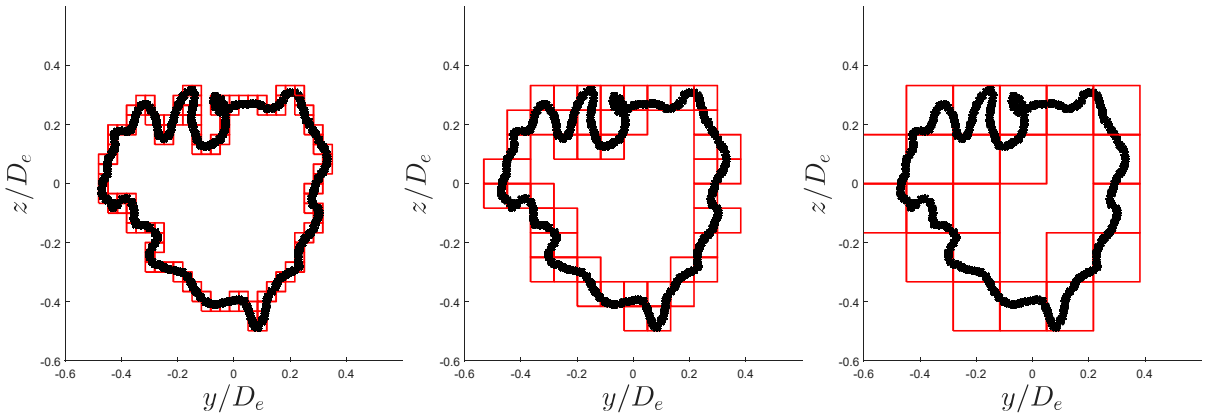
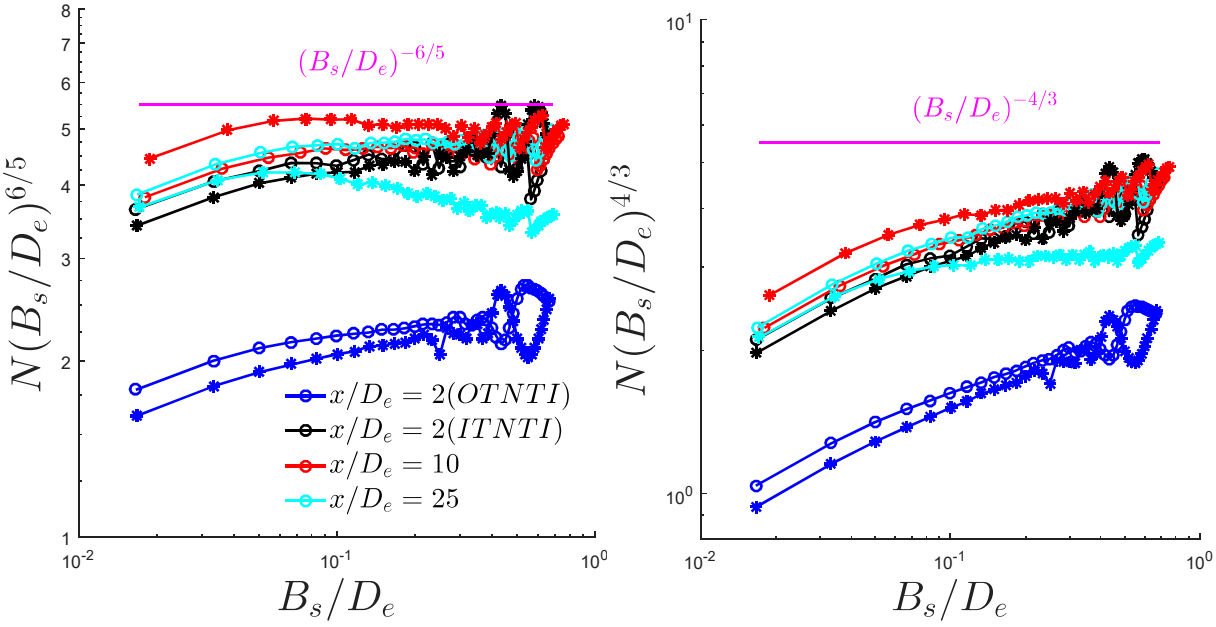


Figure 5.7: ITNTI of the round jet from a single time step at $x/D_e = 2$ with varying box size: (a) $B_s = 0.03D_e$, (b) $B_s = 0.08D_e$ and (c) $B_s = 0.16D_e$. The boxes containing the TNTI are shown in red. (TPIV data and $Re_G = 10,000$)

N of boxes containing the TNTI, it should be found that there is a power law in the form $N \sim B_s^m$. The exponent m is related to the fractal dimension as $D_f = 1 - m$. Therefore, if a Kolmogorov scaling were to be found it would be expected that $m = -4/3$. The box-counting technique was applied to the present data at various streamwise locations to probe the evolution of the TNTI further downstream. In order to test if they follow the Kolmogorov scaling, they are premultiplied so that if a specific scaling was followed, the data would lie on a straight horizontal line.

The data indicates that the TNTI follows a power law at all streamwise locations, however it does not seem to follow a Kolmogorov scaling. As shown in fig. 5.8, the interfaces premultiplied by $(B_s/D_e)^{-6/5}$ in fig. 5.8a appears to follow a $-6/5$ scaling rather than the $-4/3$ Kolmogorov scaling, as shown in fig. 5.8b. Only the fractal jet at $x/D_e = 25$ appears to start approaching the Kolmogorov scaling, whilst the round jet does not. This may be linked to a different state of development of the TNTI at this stage, however more



(a) Non-equilibrium scaling

(b) Kolmogorov scaling

Figure 5.8: Box counting of different interfaces at various streamwise locations for round ($\circ$) and fractal ($*$) jets (TPIV data ad $Re_G = 10,000$).

streamwise locations would need to be probed to confirm this. The $-6/5$ scaling has been previously discussed by Zhou and Vassilicos (2017), who completed 3D DNS simulations, looking at the TNTI in 2D planes normal to the mean flow direction of an axisymmetric wake at various streamwise locations. The authors linked the -6/5 scaling to the presence of the non-equilibrium dissipation. However, in the present study a Kolmogorov scaling was found for the fractal jet at $x/D_e = 25$ despite non-equilibrium dissipation being measured for this jet at this location, as discussed in chapter 4. Therefore, further streamwise locations are needed in order to unveil the transition from a $-6/5$ to a Kolmogorov scaling and which phenomena are determining it. The present findings differ from the results of Mistry et al. (2018), who investigated the scaling of the TNTI in the streamwise direction for an axisymmetric jet emitted by a round nozzle. The authors found that up to $x/D_e = 5$, the TNTI would have a 2D fractal dimension lower than 4/3 up to $x/D_e = 5$ and then it would be approximately 4/3 (hence a Kolmogorov scaling) from there up to $x/D_e = 73$ ($x/D = 65$ in the original work where D is simply defined as the round jet diameter), where the jet was self-similar. The authors investigated the jet acquiring the data across planes normal to the jet exit rather than in parallel as in the present thesis.

On one side, it may be argued that it is more accurate to count the boxes in a $r-\theta$ plane at a specific streamwise location rather than counting them in the streamwise direction where the scaling may vary spatially. On the other hand, as discussed in chapter 3, the terms of the momentum equation for a jet tended rapidly to axisymmetry in the radial direction, whilst they took much longer for the streamwise terms. This picture may point to different radial and streamwise evolution of the fractal scaling, which will become the same both radially and streamwise only when the jet is fully self-similar.

Overall, despite the different state of the coherent structures, the jet appears to have a comparable behaviour and fractal scalings of the TNTI. Therefore, the state of the micro structure of the jet is now examined to better understand its evolution.

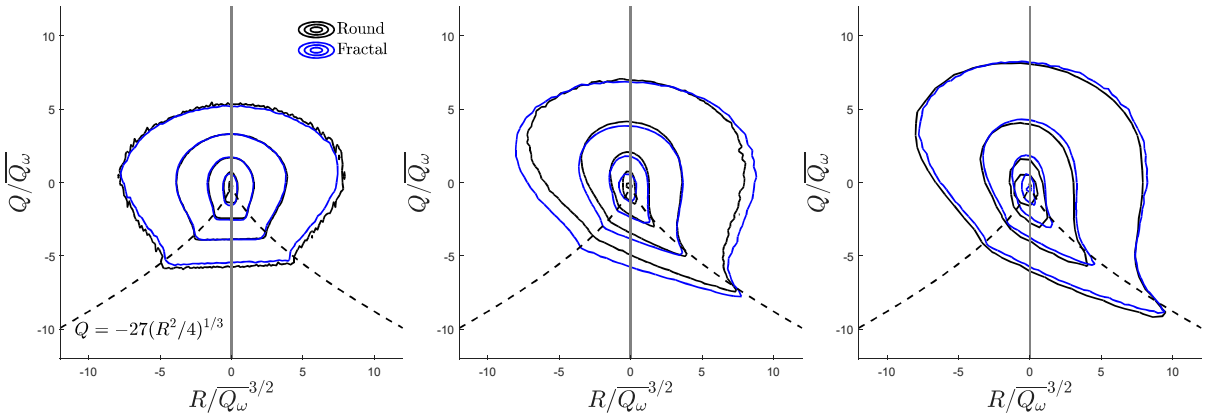
5.4 State of the microscales of the jet

Having shown the evolution of the TNTI from $x/D_e = 2$ to $x/D_e = 25$, it is now investigated how the jet's small-scale structure evolves with x.

5.4.1 Unfolding of the jpdf of Q and R

As discussed in chapter 1, the smallest scales of the flow have been thought to be isotropic and statistically homogeneous and in fully developed turbulence the joint probability density function (jpdf) of Q and R have been found to have the so-called "tear-drop" shape. However, Buxton et al. (2017) found this shape also in the turbulence production region and just after the peak of turbulence production for a wake generated by a high-aspect-ratio square cylinder, arguing that the tear-drop shaped jpdf may be a signature of turbulent flows in general. This work followed previous findings from Gomes-Fernandes et al. (2014). The authors investigated the evolution of the microscales of a grid-generated flow measuring in the middle of the turbulence production region ($x/x_*^{\text{peak}} = 0.57$, where x_*^{peak} was the distance of the peak of turbulence kinetic energy production from the grid),

at the peak and far downstream in the turbulence decay region. They found that the jpdf of Q and R would unfold in its tear-drop shape from the first station moving downstream. Moreover, they noted that even at the station closest to the grid, there already was a slightly greater percentage of events associated with excess of strain production over enstrophy production ($R > 0$), which increased moving further downstream, i.e. a developing Viellefosse tail. Therefore, these two works suggested that the tear-drop shape would start developing very close to the point where the flow is generated, even where the effect of the coherent structures was still present. Hence, it is now examined if a similar evolution takes place in the axisymmetric jets at issue. The region of the flow studied is the bulk of the turbulent flow, where $\Omega^* >$ threshold as discussed in section 5.1. Despite the spatial resolution not being sufficient to resolve the Kolmogorov scale in the near field, Buxton (2015) showed that a mix of inertial and dissipative scales is needed to recover the tear-drop shape. Hence, the current spatial resolution is sufficient to study some structural aspects of the small-scale behaviour of the flow. In fig. 5.9, the evolution



(a) $x/D_e = 2$ (b) $x/D_e = 10$ (c) $x/D_e = 25$

Figure 5.9: Jpdf of Q and R for the round and fractal jet (TPIV data and $Re_G = 10,000$). Isocontours range from 10^{-4} to 10^0. The regions of positive and negative D (the discriminant of the velocity gradient tensor) are separated by a black dashed line. (TPIV data, $Re_G = 10,000$)

of the of the jpdf of Q and R is examined. At the station farthest downstream, a fully developed tear drop shape is found. A similar shape, where however the Viellefosse tail is still developing, is found at $x/D_e = 10$, as shown in fig. 5.9b. Despite the effect of the initial conditions still "being felt" by the flow, the tear drop was found even in the

turbulence production region of a wake generated by a square cylinder (Buxton et al., 2017). At $x/D_e = 25$, as shown in fig. 5.9c, the tear-drop shape appears in a fully-developed state as expected since the turbulence is fully developed (even though not fully self-similar) as discussed in chapter 4. In fig. 5.9a a differently shaped jpdf is found at $x/D_e = 2$, with a close balance between events of $R > 0$ and $R < 0$. The potential effect of experimental noise at this station was investigated since, as discussed by Buxton et al. (2011a), this jpdf can be highly susceptible to it. As discussed in chapter 2, a divergence correction scheme (DCS) was applied to keep the divergence error $|\partial u_i/\partial x_i \leq 10s^{-1}|$. In order to test the level of noise on this jpdf, a further restricting condition was set so that $|\partial u_i/\partial x_i \leq 1s^{-1}|$, however the same shaped jpdf was found, giving confidence noise was not affecting it. A similar type of jpdf as in fig. 5.9a was found by Chertkov et al. (1999), for a flow where the real velocity field was replaced by a random Gaussian one (hence of reduced intermittency) with the same velocity spectrum. In general, when a "classical" tear-drop shape is present, in regions where strain dominates over rotation ($Q < 0$) strain production usually exceeds enstrophy production ($R > 0$), whilst in regions where rotation dominates ($Q > 0$) it is more likely that $R < 0$. Gomes-Fernandes et al. (2014) found such characteristics even in the middle of the turbulence production region of their grid-generated flow, however this is not the case for the current experiment, where data were acquired earlier than $x/x_*^{\text{peak}} = 0.57$. At $x/D_e = 2$, the jpdf is approximately symmetrical and there is no trace of the so-called Viellefosse tail. Moreover, it is found that there is an approximately equal balance between events where strain production exceeds enstrophy production and vice-versa. Therefore, it may be postulated that at the start of the turbulence production region of a jet, the flow does not have a classical tear-drop shaped jpdf since the flow is not yet fully turbulent, but rather there is a balance between strain production and enstrophy production dominated events. This differs from the grid flow of Gomes-Fernandes et al. (2014), where the separated flow is immediately turbulent. Later on, when the jet is also fully turbulent, the jpdf of $Q - R$ evolves towards tear-drop shape, as shown at $x/D_e = 10$ and $x/D_e = 25$.

Now, the analysis is focused on the behaviour of the flow at $x/D_e = 2$, which may be in a

way better understood by considering previous studies on the restricted Euler equation. Cantwell (1992) verified that the trajectories through time of the invariants of the velocity gradient tensor predicted by such an equation would have a likely symmetrical behaviour if the pressure Hessian Π_{ij},

$$\Pi_{ij} = -\left(\frac{\partial^2 p}{\partial x_i \partial x_j} - \frac{\partial^2 p}{\partial x_k \partial x_k}\frac{\delta_{ij}}{3}\right) + \nu\frac{\partial^2 A_{ij}}{\partial x_k \partial x_k} \tag{5.10}$$

involving non-local pressure (p) distribution, viscous, dissipative effects on the velocity gradient tensor A_{ij} and the Kronecker delta δ_{ij}, was assumed to be diagonal ($\Pi_{ij} = 0 \; \forall \; i \neq j$). Despite the author discussing the trajectories of the invariants of the velocity gradient tensor rather than the jpdf, the former may still give an indication of the behaviour of the latter (as discussed by Cheng and Cantwell (1996)). Hence, it may be expected that the jpdf of Q and R will be symmetrical with respect to R as are its trajectories. In addition, Wilczek and Meneveau (2014) confirmed the intimate interactions between the non-local pressure and dissipative events that take place in real flows, suggesting the assumption $\Pi_{ij} = 0$ does not work in regions where $s_{ij}s_{ij}$ (which is proportional to dissipation) is intermittent. Hence, the p.d.f. of the latter quantity is examined at the three streamwise locations. As shown in fig. 5.10, there is an increasing intermittency of $s_{ij}s_{ij}$ moving further downstream. At $x/D_e = 2$ the intermittency is the lowest, which, together with fig. 5.9a, fits with the model of Chertkov et al. (1999) for a "Gaussian" velocity gradient tensor. Moreover, the increasing intermittency indicates that the non-diagonal part of Π_{ij} becomes increasingly important in comparison to the diagonal one at $x/D_e = 10$ and $x/D_e = 25$. At $x/D_e = 2$, the coherent motions may contribute strongly to the pressure Hessian, however the present findings may suggest that this is mainly across its diagonal part making the non-diagonal part negligible in comparison, so that the jpdf of Q and R appears symmetrical as if $\Pi_{ij} = 0$. In this case the restricted Euler equation may be a good model of the flow behaviour. Once the coherent motions have decayed, the diagonal and non-diagonal parts may be of the same order of magnitude and therefore $\Pi_{ij} = 0$ is not a valid assumption any more to model the invariants of the velocity gradient tensor and in fact the jpdf of Q and R is not symmetric any more.

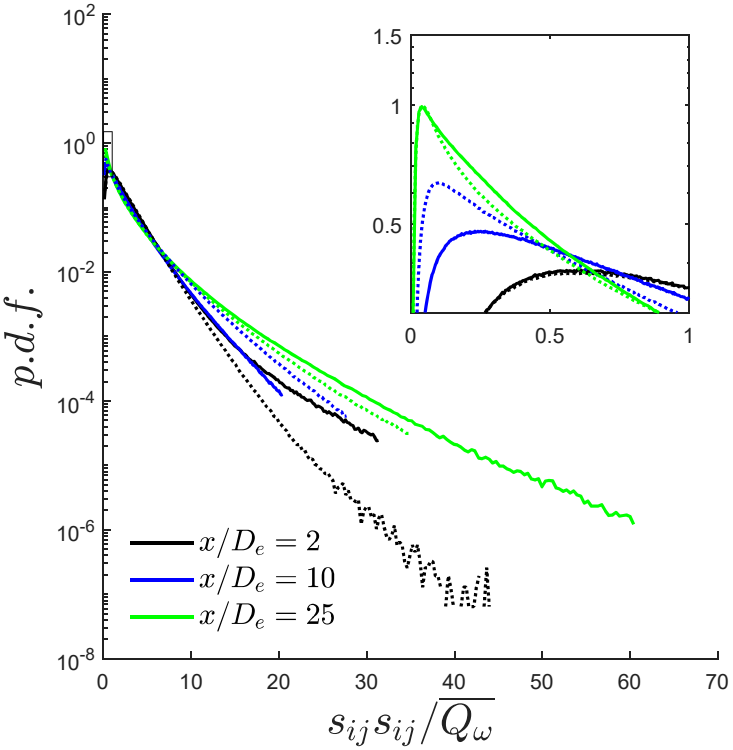


Figure 5.10: P.d.f. of $s_{ij}s_{ij}$ for round jet (-) and fractal jet (- -) a various streamwise locations. An insert with a close up of the peaks of the pdf is added.

5.4.2 Evolution of enstrophy and strain production

As discussed by Buxton et al. (2011b), Q and R can be interpreted as *local departures from homogeneity with regards to strain/rotation and strain/rotation amplification rates respectively*. Having already discussed the evolution of $s_{ij}s_{ij}$, the analysis is now focused on the evolution $-s_{ij}s_{jk}s_{ki}$ and $\omega_i s_{ij}\omega_j$, the inviscid source/sink terms for the evolution of strain and rotation respectively. In fig. 5.11b, the strain production/destruction is analysed. The pdfs at the three streamwise locations indicate that at $x/D_e = 2$ strain destruction is favoured with respect to strain production. However, the flow then develops indicating a prevalence of strain production ($-s_{ij}s_{jk}s_{ki}$) further downstream of the jet exit with an amplification of $-s_{ij}s_{jk}s_{ki}$ at the farthest location. The same behaviour was found by Gomes-Fernandes et al. (2014), who showed an increasing tendency for positive strain self-amplification ($-s_{ij}s_{jk}s_{ki}$) moving further away from their space-filling fractal-square grid. Positive strain self amplification was also already present in their turbulent production region.

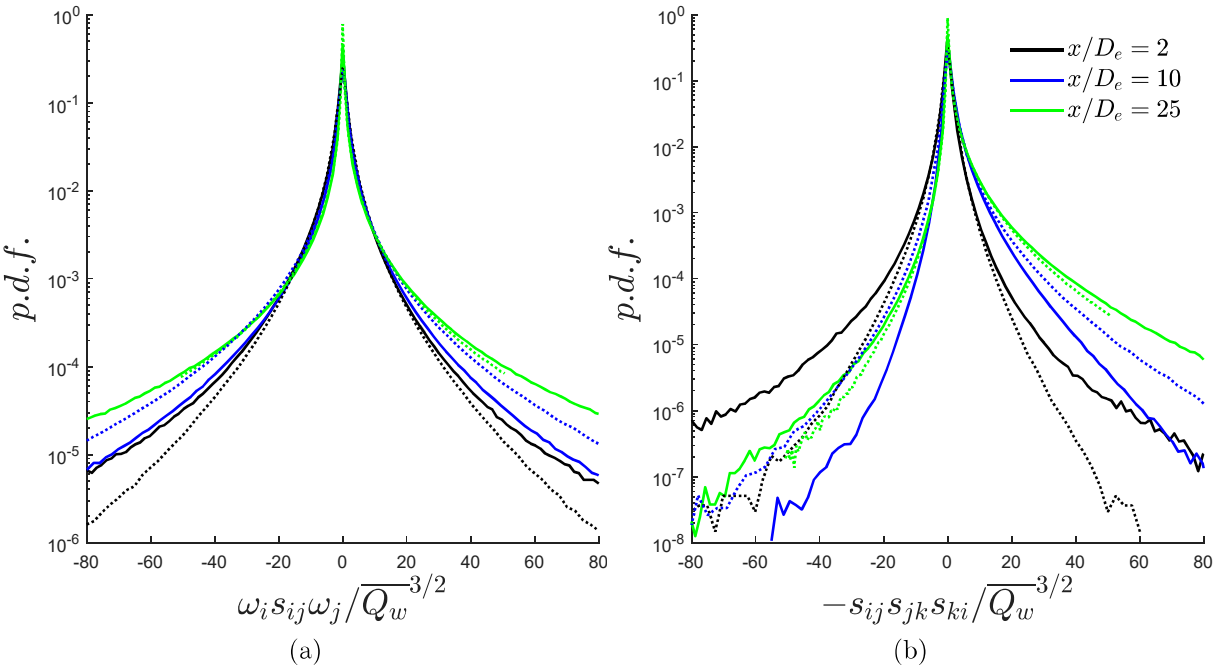


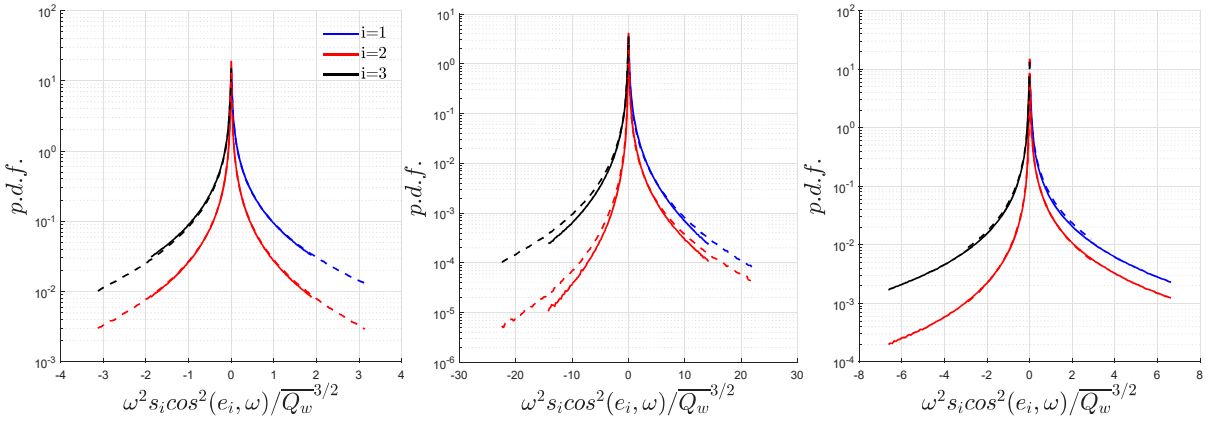
Figure 5.11: P.d.f. of enstrophy and strain for round jet (-) and fractal jet (- -). (TPIV data at $Re_G = 10,000$)

Another term of interest is the vortex stretching term $\omega_i s_{ij} \omega_j$. As discussed by Taylor (1938), this term is responsible for allowing the flow's energy to be transferred inertially from the large to the small scales. On average $\langle \omega_i s_{ij} \omega_j \rangle > 0$, indicating therefore that vortex stretching is favoured over compression, and this has been verified in a wide range of flows (Tsinober et al. (1992) amongst others). At $x/D_e = 10$ and $x/D_e = 25$, the ensemble average of $\omega_i s_{ij} \omega_j$ is positive for both jets, in accordance with previous literature. This is also shown in fig. 5.11a, where the pdf indicates a slight skewness towards the positive side. However, at $x/D_e = 2$ $\langle \omega_i s_{ij} \omega_j \rangle$ is negative for both jets, indicating a predominance of vortex compression over stretching.

5.4.3 Strain-vorticity coupling

This point is further studied by considering the eigenvectors of the strain-rate tensor s_{ij} in fig. 5.12. In fact, as discussed by Betchov (1956), the vortex stretching can be rewritten as $\omega_i s_{ij} \omega_j = \omega^2 s_i (\boldsymbol{e_i} \cdot \boldsymbol{\omega})^2$, where s_i are the eigenvalues of the strain-rate tensor, $\boldsymbol{e_i}$ are the corresponding eigenvectors, $\boldsymbol{\omega}$ a unit vector indicating the direction of the vorticity vector

and summation over index i is implicit. Here, s_3 represents the compressive eigenvalue (always negative), s_1 the extensive one (always positive) and s_2 the intermediate one (either positive or negative). These eigenvalues can be ordered as $s_1 \geq s_2 \geq s_3$ and for an incompressible flow $\sum_{i=1}^{3} s_i = 0$. As shown in fig. 5.12a, the symmetrical pdf of $\omega_i s_{ij} \omega_j$ is con-

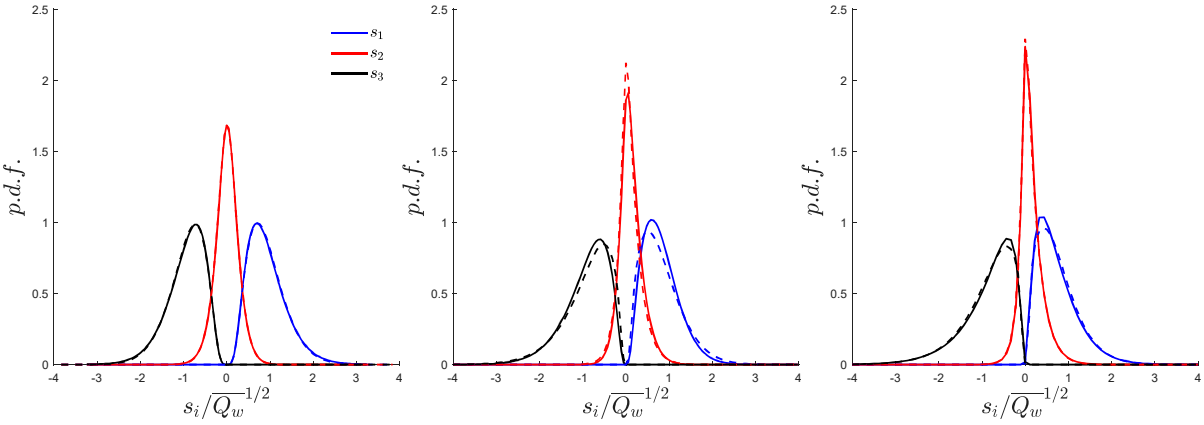


(a) $x/D_e = 2$ (b) $x/D_e = 10$ (c) $x/D_e = 25$

Figure 5.12: Pdf of the spatial evolution of $\omega^2 s_i \cos^2(\boldsymbol{e_i}, \boldsymbol{\omega})$ for round jet (-) and fractal jet (- -). TPIV data at $Re_G = 10,000$.

firmed at $x/D_e = 2$. At $x/D_e = 10$, $\omega^2 s_1 \cos^2(\boldsymbol{e_1}, \boldsymbol{\omega})$ and $\omega^2 s_3 \cos^2(\boldsymbol{e_3}, \boldsymbol{\omega})$ have an almost symmetrical pdf, whilst $\omega^2 s_2 \cos^2(\boldsymbol{e_2}, \boldsymbol{\omega})$ has a clear skewness for vortex stretching which persists up to $x/D_e = 25$. At this station, the pdfs of $\omega^2 s_1 \cos^2(\boldsymbol{e_1}, \boldsymbol{\omega})$ and $\omega^2 s_3 \cos^2(\boldsymbol{e_3}, \boldsymbol{\omega})$ are again similar,even though $\omega^2 s_3 \cos^2(\boldsymbol{e_3}, \boldsymbol{\omega})$ appears to be slightly more intermittent, whilst the clear skewness of $\omega^2 s_2 \cos^2(\boldsymbol{e_2}, \boldsymbol{\omega})$ points to the importance of the intermediate eigenvalue s_2 in the process of vortex stretching. The findings in fig. 5.12 show some similarities to the evolution of vortex stretching studied by Gomes-Fernandes et al. (2014). The authors found that, up to the turbulence production peak, $\omega^2 s_i \cos^2(\boldsymbol{e_i}, \boldsymbol{\omega})$ displayed symmetrical pdfs, whilst in the decay region $\omega^2 s_2 \cos^2(\boldsymbol{e_2}, \boldsymbol{\omega})$ would show a clear skewness towards positive values. However, differently from the present study, the authors found that $\omega^2 s_1 \cos^2(\boldsymbol{e_1}, \boldsymbol{\omega})$ would have a wider pdf compared to $\omega^2 s_3 \cos^2(\boldsymbol{e_3}, \boldsymbol{\omega})$, suggesting the behaviour of $\omega^2 s_i \cos^2(\boldsymbol{e_i}, \boldsymbol{\omega})$ might be intimately related to the particular flow studied.

Now, the constituent parts of $\omega^2 s_i \cos^2(\boldsymbol{e_i}, \boldsymbol{\omega})$ are examined, starting from the pdfs of s_i. As shown in fig. 5.13a, at $x/D_e = 2$ there is a symmetrical distribution between s_1 and s_3 and between the positive and negative side of the pdf of s_2. The previously observed

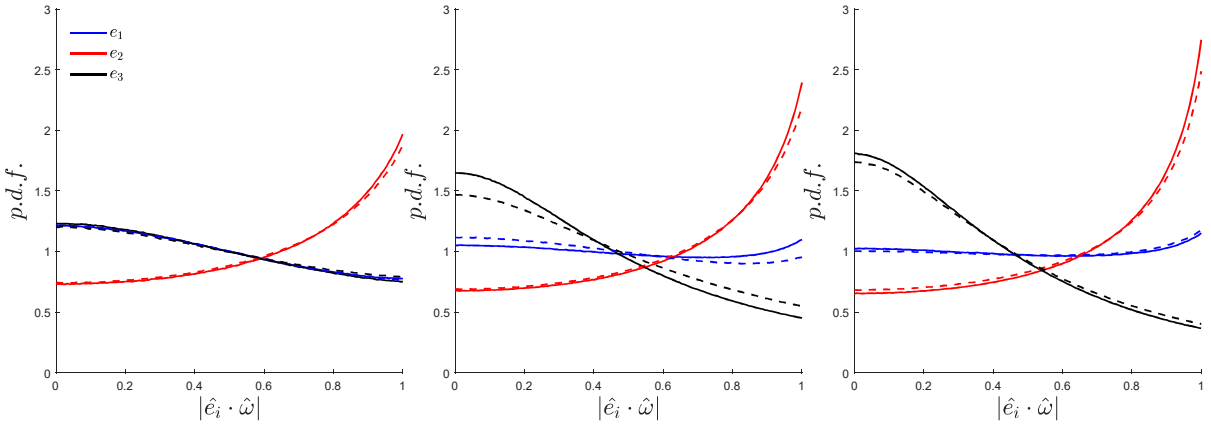


(a) $x/D_e = 2$ (b) $x/D_e = 10$ (c) $x/D_e = 25$

Figure 5.13: Pdf of the eigenvalues s_i for round jet (-) and fractal jet (- -). TPIV data and $Re_G = 10,000$.

symmetry in vortex stretching and compression translates to the extensive, compressive and intermediate strain-rate eigenvalues as well. Gomes-Fernandes et al. (2014) identified a similar behaviour in the turbulence production region of their grid generated flow. This symmetry between the pdfs of s_1 and s_3 persisted up to the peak of turbulence production, where, however, the pdf of s_2 showed a skewness towards the positive side. Further downstream, as shown in fig. 5.13b and fig. 5.13c, there is a greater tendency towards positive values of s_i for both it extensive and intermediate counterparts, concurrently to vortex stretching and strain production. The pdf of s_1 is found to be more intermittent with respect to s_3, a behaviour that was found by Gomes-Fernandes et al. (2014) as well. Comparing the round and fractal jets, similar trends are found and at $x/D_e = 2$ the pdfs of the two jets are even superimposed. At $x/D_e = 10$ and $x/D_e = 25$, small differences in the peak value and in the width of the pdfs are found, which may be linked to the different evolution in terms of eddy turnover time discussed in chapter 4.

The analysis on $\omega^2 s_i \cos^2(\boldsymbol{e_i}, \boldsymbol{\omega})$ is concluded by investigating the pdf of the alignments $|\hat{\boldsymbol{e}}_{\boldsymbol{i}} \cdot \hat{\boldsymbol{\omega}}|$. As shown in fig. 5.14b and fig. 5.14c, the pdfs show a comparable behaviour of the alignments at $x/D_e = 10$ and $x/D_e = 25$. The extensive eigenvector $\boldsymbol{e_1}$ shows a random alignment with the vorticity vector. The intermediate eigenvector $\boldsymbol{e_2}$ shows a clear preferential parallel alignment with the vorticity vector, whilst $\boldsymbol{e_3}$ tends to be perpendicular to it. A similar behaviour of the three alignments was found for an axisymmetric jet (Bux-



(a) $x/D_e = 2$ (b) $x/D_e = 10$ (c) $x/D_e = 25$

Figure 5.14: Pdf of the spatial evolution of the alignment of the vorticity vector with the eigenvectors of the strain-rate tensor for the round jet (-) and the fractal jet (- -). (TPIV data and $Re_G = 10,000$).

ton and Ganapathisubramani, 2010) at $x/D_e = 36$ and in the turbulence decay region of a variety of other flows (Ashurst et al., 1987; Gomes-Fernandes et al., 2014; Fiscaletti et al., 2016a). Between the two stations investigated, the intermediate eigenvector tends to increase its parallel alignment moving further downstream, whilst the compressive one becomes increasingly perpendicular. The behaviour of the extensive eigenvector appears to be unaltered. Overall, the round and fractal jets appear to behave in a similar manner at all streamwise locations studied. At $x/D_e = 2$, the plots are almost superimposed suggesting the state of the coherent structures does not affect the alignment $|\hat{\boldsymbol{e}}_{\boldsymbol{i}} \cdot \hat{\boldsymbol{\omega}}|$.

At $x/D_e = 2$, a markedly different behaviour is found compared to the other streamwise locations, as shown in fig. 5.14a. Despite the intermediate eigenvector maintaining a preferential parallel alignment with the vorticity vector and the compressive one remaining perpendicularly aligned, $\boldsymbol{e_1}$ shows a slight preference for perpendicular alignment and is almost superimposed to $\boldsymbol{e_3}$. Gomes-Fernandes et al. (2014) found a slight tendency of $\boldsymbol{e_3}$ to be in parallel alignment with the vorticity vector in the turbulence production region and at the peak for their grid generated flow, however this effect was not as marked as in the present case.

In section 5.4.1, the role of Π_{ij} in the restricted Euler equation was discussed for the $Q-R$ space. However, its role is also intimately linked to the alignment between the eigenvector

of the strain rate tensor and to the vorticity vector. Hamlington et al. (2008) showed that strain rate and vorticity are linked by a non-linear coupling, where the non-locality of the vorticity and of the strain rate co-evolution involves Π_{ij} (Nomura and Post, 1998; Ohkitani and Kishiba, 1995). Hamlington et al. (2008) further discusses the alignment of the vorticity vector with the *non-local* (background) strain and with the *local* one induced by the vorticity within it. Using a Biot-Savart integration to study the effect of both types of strain on their DNS data, the authors found that, for the *non-local* strain, $\boldsymbol{e_1}$ and $\boldsymbol{e_2}$ had a clear preference for parallel alignment, whilst $\boldsymbol{e_3}$ was perpendicular to the vorticity vector. The most interesting result, was the alignment of the *local strain field*. In fact, $\boldsymbol{e_2}$ had a clear preference for parallel alignment, whilst $\boldsymbol{e_1}$ and $\boldsymbol{e_3}$ were almost superimposed with a preference for perpendicular alignment, like in the present study at $x/D_e = 2$. Since the nonlocality of the strain field involves Π_{ij}, the study of Hamlington et al. (2008) suggests that at $x/D_e = 2$, the effect of the non-diagonal part of the pressure Hessian may be negligible and in fact the alignments of $\boldsymbol{e_i}$ with $\boldsymbol{\omega}$ behave like if the strain field was *local* only, which is expected due to the dominance of the coherent structures in the near field. This conclusion confirms the previous hypothesis that at $x/D_e = 2$, Π_{ij} acts like if it was diagonal.

Now, it remains to be understood what causes the pressure-viscous stress field represented by Π_{ij} to be approximately diagonal at $x/D_e = 2$ (where the flow is less intermittent and dominated by the coherent structures) and how it evolves to the other locations probed. Certainly, near the jet exit, the evolution of the strain field is somewhat constrained by the presence of the potential core, where the ITNTI and the OTNTI act like barriers to the development of the vortical structures. We may thus define a characteristic lengthscale separating OTNTI and ITNTI as $\mathcal{L}_\omega = \hat{r}_{OTNTI} - \hat{r}_{ITNTI}$, or simply the difference between the mean radius of the OTNTI and of the ITNTI. It is hypothesised that $\mathcal{L}_\omega$ may constrain the evolution of the turbulent structures, since $\mathcal{L}_\omega < 2.8\lambda_f$ $(4\lambda_g)$. In fact, Ishihara et al. (2013) hypothesised in their DNS work on homogeneous turbulence that thin layers of thickness $2.8\lambda_f$ $(4\lambda_g)$ exists, which consists of clusters of strong vortex tubes which largely contributes to the mean dissipation rate. Elsinga et al. (2017) confirmed these findings

for homogeneous turbulence (DNS) suggesting that the non-local strain width was $2.8\lambda_f$ ($4\lambda_g$) and that the local strain scaled with η. In the present study, it was found that $\overline{\mathcal{L}_\omega} \approx 1.8\lambda_f$ for the round jet and $\overline{\mathcal{L}_\omega} \approx 2.4\lambda_f$ for the fractal one. Now, it was just shown at $x/D_e = 2$ that the bulk turbulent flow behaves like if only local strain was present. Since $\overline{\mathcal{L}_\omega}$ is less than $2.8\lambda_f$ for both jets, this may suggest that the physical space is not sufficient for the non-local strain to develop, hindering vortex stretching. Later on, when the shear layer meets and the ITNTI is absorbed into the turbulent bulk, the strain has all the physical space necessary to evolve towards its non-local state. A schematic is shown in figs. 5.15a and 5.15b. The round and fractal jets have a comparable pdf of the fluctuations of $\overline{\mathcal{L}_\omega}$, where the positive side of the pdf is wider than the negative one. In general, the pdf of the fractal jet is only marginally wider than the one of the round jet as shown in fig. 5.15c, suggesting that the break-up of the coherent structures does not significantly alter the behaviour of $\mathcal{L}_\omega$.

Summarising, it was found that the presence of two interfaces inhibits the transition from local to nonlocal strain, which is shown by the alignment of $\boldsymbol{e_i}$ with $\boldsymbol{\omega}$. This is evidenced by the jpdf of Q and R and by the alignments of $\boldsymbol{e_i}$ with $\boldsymbol{\omega}$, which resembles a state of the pressure Hessian as if it was diagonal only.

5.4.4 Scale-dependence of alignments $|\hat{\boldsymbol{e}}_i \cdot \hat{\boldsymbol{\omega}}|$

In this section the scale-dependence of the alignments $|\hat{\boldsymbol{e}}_i \cdot \hat{\boldsymbol{\omega}}|$ is examined. Buxton et al. (2011b) previously investigated this topic in the self-similar region of a planar mixing layer (DNS). The authors analysed the data from two quadrants of the $Q - R$ space, specifically quadrant I ($D > 0$ and $R > 0$) and IV ($D > 0$ and $R < 0$). The data were then mean filtered at windows of dimension ranging between 2.5η and 25η. Analysing e_1 (which determines if enstrophy is amplified or attenuated), the authors found that enstrophy attenuation was scale independent (quadrant I), whilst enstrophy amplification was scale dependent and driven by large inertial scale structures (quadrant IV). In this study, the scale dependence is analysed by applying a mean filter to the whole data with a

window size of 3×3, 5×5 and 7×7 vectors (converted in the plots in terms of their mean bulk η). Moreover, the pdfs are conditioned to enstrophy production ($\omega_i s_{ij} \omega_j > 0$) and enstrophy destruction ($\omega_i s_{ij} \omega_j < 0$). In fact, Buxton and Ganapathisubramani (2010), studying an axisymmetric jet in the far field, found that, despite the alignment of $\boldsymbol{e_1}$ and $\boldsymbol{\omega}$ was arbitrary on average, the two vectors aligned in parallel led to enstrophy production whilst when they were aligned perpendicularly to enstrophy destruction.

An initial analysis shows that the baseline and the 3×3 vectors filter are superimposed due to the 75% overlap in the TPIV cross-correlation algorithm, as indicated in figs. 5.16 to 5.18. At $x/D_e = 2$, a strong scale dependence for all three alignments is found for both round and fractal, as shown in figs. 5.16a to 5.16d. In general, the parallel alignment of $\boldsymbol{e_2}$ with $\boldsymbol{\omega}$ appears to reduce with increasing scale size, whilst the opposite takes place for $\boldsymbol{e_3}$. The extensive eigenvector $\boldsymbol{e_1}$ appears to increase its perpendicular alignment with increasing scale. Moreover, differently from the findings of Buxton and Ganapathisubramani (2010), at this station $\boldsymbol{e_1}$ always appears to have a tendency for perpendicular alignment, leading to both enstrophy production and destruction. At $x/D_e = 10$ and $x/D_e = 25$, the intermediate and compressive eigenvectors' alignment appear to be highly scale dependent, where the former reduces its parallel alignment with increasing scale size whilst the latter reduces its perpendicular alignment, as shown in figs. 5.17 and 5.18. The extensive eigenvector $\boldsymbol{e_1}$ appears to be scale independent, at least for the points aligned perpendicularly with the vorticity vector, whilst small variations are found for the points aligned in parallel for both round and fractal jets. These findings partly agree with the work of Buxton et al. (2011b), who established that for a mixing layer enstrophy amplification was scale dependent whilst enstrophy attenuation was scale independent. Moreover, at these two locations when $\boldsymbol{e_1}$ is aligned in parallel enstrophy is produced, whilst when $\boldsymbol{e_1}$ is aligned perpendicularly to $\boldsymbol{\omega}$ enstrophy is destroyed, confirming the findings of Buxton and Ganapathisubramani (2010) for an axisymmetric jet. Moreover, Fiscaletti et al. (2016b), studying a planar turbulent mixing layer, suggested that the alignment tendencies were affected by the large-scale velocity-gradient fluctuations, which explains the changes of the pdf of the alignments at different filter lengths.

A last characterisation of $|\hat{\boldsymbol{e}}_{\boldsymbol{i}} \cdot \hat{\boldsymbol{\omega}}|$ is done by evaluating regions of high swirling, which have been shown before to be structured into worms. As discussed by Zhou et al. (1999), in order to distinguish between swirling and straining regions, the discriminant D of the characteristic equation for the eigenvalues of the velocity gradient tensor (as previously discussed in chapter 1)

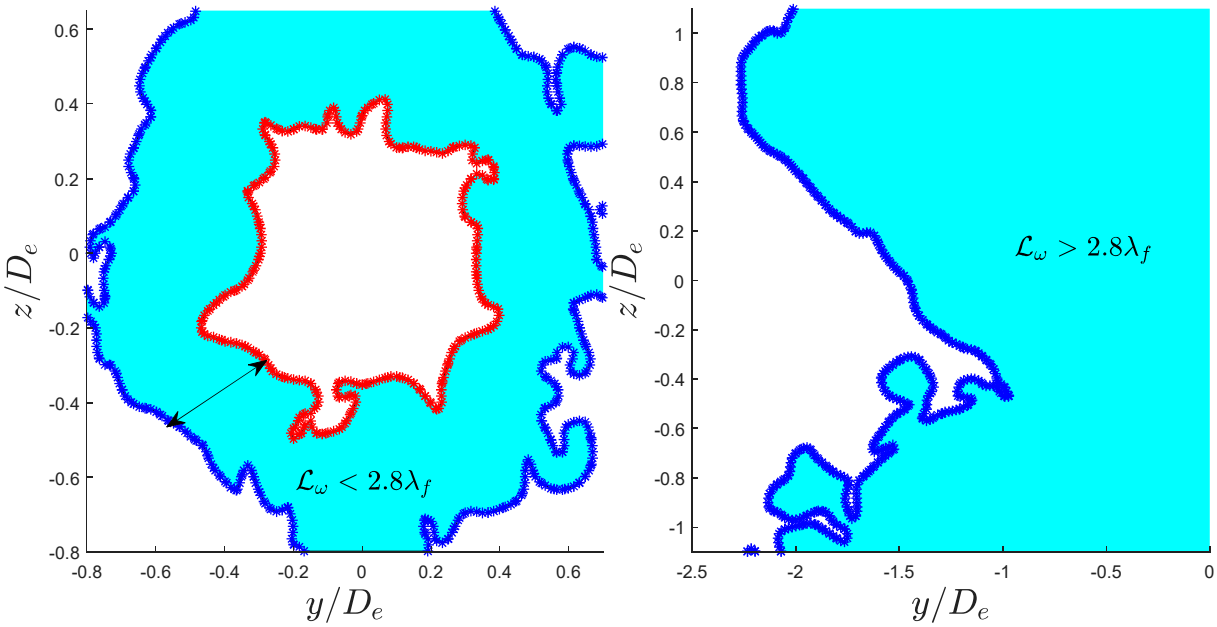
$$\xi^3 + P\xi^2 + Q\xi + R = 0, \tag{5.11}$$

is considered. When D is positive (Zhou et al., 1999; Buxton and Ganapathisubramani, 2010), there is one real and a pair of complex conjugate eigenvalues

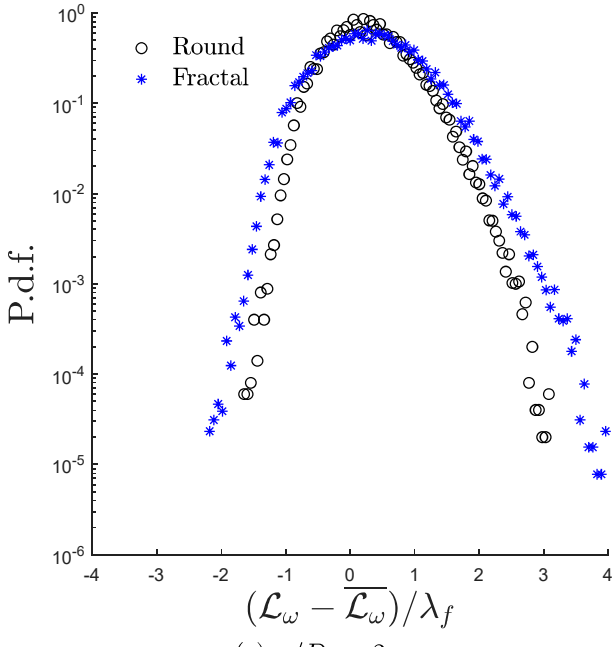
$$\lambda = \lambda_r,\ \lambda_{cr} \pm i\lambda_{ci}, \tag{5.12}$$

the streamlines of the flow are locally swirling and a measure of its intensity is given by $\lambda_{ci} = \sqrt{D}$. If the flow is straining only (no swirling), D is negative and $\lambda_{ci} = 0$. Buxton and Ganapathisubramani (2009, 2010) studied the alignment $|\hat{\boldsymbol{e}}_{\boldsymbol{i}} \cdot \hat{\boldsymbol{\omega}}|$ for an axisymmetric jet in the far field. They found that in straining only regions ($\lambda_{ci} = 0$) the pdfs of the alignment had greater peaks compared to their swirling counterpart ($\lambda_{ci} > 0$), suggesting $\boldsymbol{\omega}$ had a greater preponderance of aligning in parallel with $\boldsymbol{e_2}$ and perpendicularly to $\boldsymbol{e_3}$. Fiscaletti et al. (2016b) examined for a planar mixing layer regions of intense swirling $\lambda_{ci} > 3.5\lambda'_{ci}$, where λ'_{ci} is the root-mean-square of the swirling strength in regions where $\lambda_{ci} > 0$. The authors found that in general the preferential alignment $|\hat{\boldsymbol{e}}_{\boldsymbol{i}} \cdot \hat{\boldsymbol{\omega}}|$ were maintained compared to the bulk flow, with the preferential parallel alignment of $\boldsymbol{\omega}$ with $\boldsymbol{e_2}$ and the perpendicular alignment with $\boldsymbol{e_3}$ exaggerated for the intense swirling case. The same analysis for intense swirling regions is conducted for the present jets. At $x/D_e = 10$ (figs. 5.19c and 5.19d) and $x/D_e = 25$ (figs. 5.19e and 5.19f) the parallel alignment of $\boldsymbol{\omega}$ with $\boldsymbol{e_2}$ and the perpendicular one with $\boldsymbol{e_3}$ are exaggerated in the intense swirling regions with respect to the mean turbulent bulk for both the round and fractal jet. The alignment of $\boldsymbol{\omega}$ with $\boldsymbol{e_1}$, which is arbitrary in the mean bulk, appears to show a preference for parallel alignment for the intense swirling case, which was linked before to enstrophy production. Hence, this confirms the findings of Buxton and Ganapathisubramani

(2010), who suggested the highest enstrophy production rates would be in the intense swirling regions. At $x/D_e = 2$ (figs. 5.19a and 5.19b), despite the intense swirling regions representing $\approx 30\%$ of the total volume investigated, there appears not to be significant differences between the mean bulk turbulent flow and its intense swirling part. This is consistent with the idea that the two interfaces are constraining the turbulent flow and hindering the development of turbulent structures and vortex stretching.

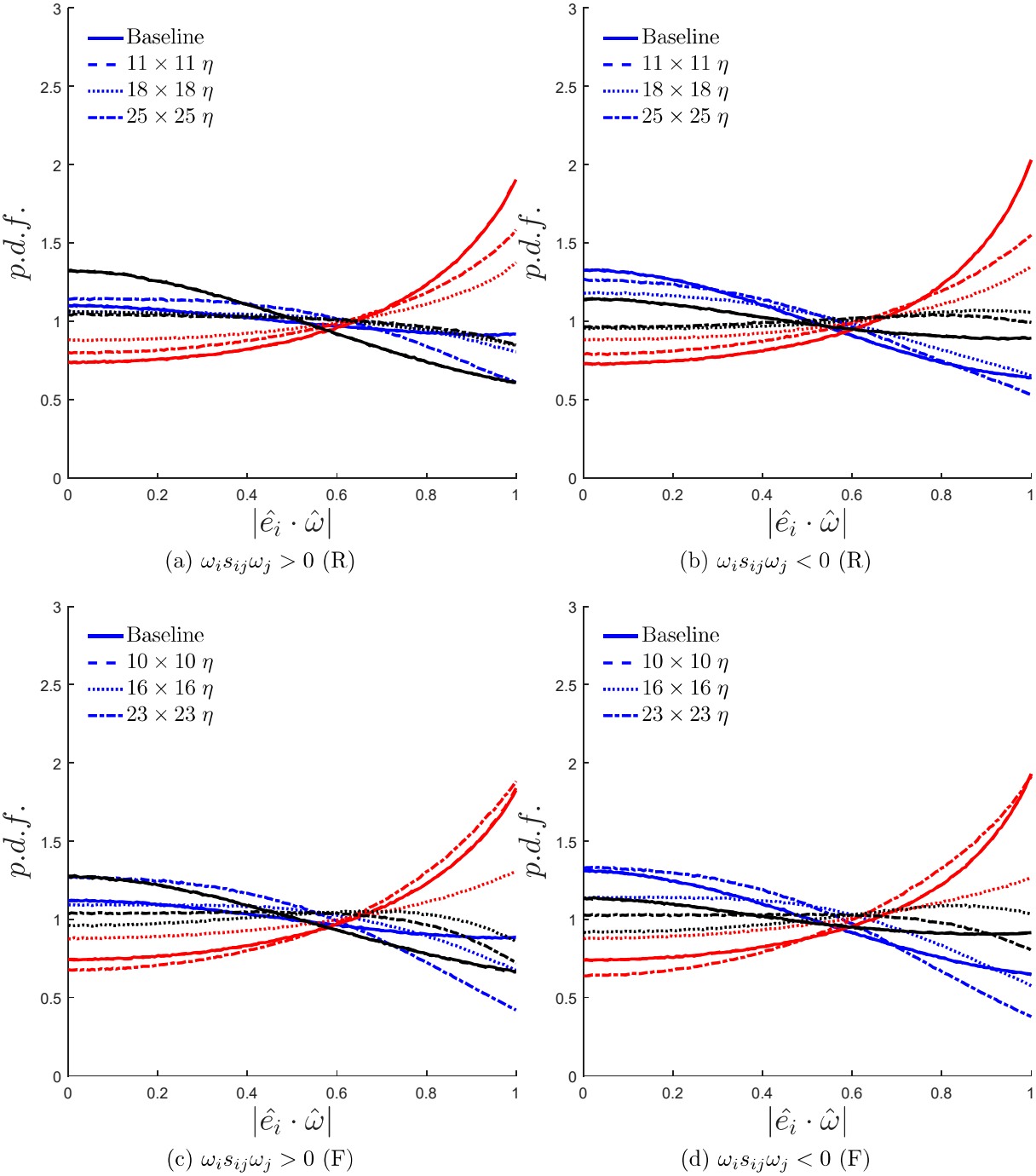


(a) $x/D_e = 2$ (b) $x/D_e = 10$



(c) $x/D_e = 2$

Figure 5.15: Example of turbulent lengthscales (a) constrained between the OTNTI and the ITNTI and (b) unconstrained (Round jet, TPIV data and $Re_G = 10,000$). The turbulent area is shaded in light blue. (c) Pdf of the fluctuations of $\mathcal{L}_\omega$ with respect to its mean $\overline{\mathcal{L}_\omega}$.



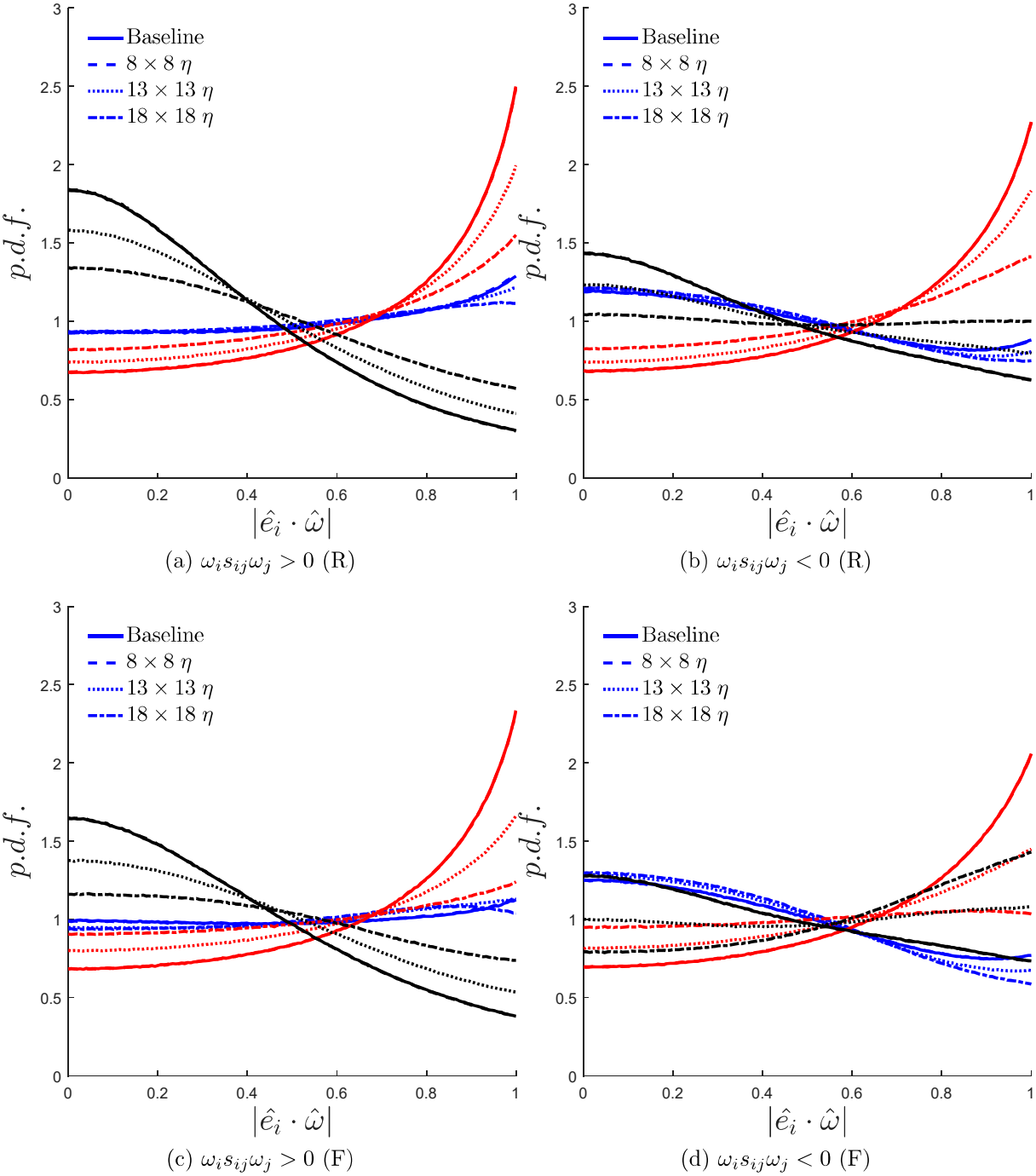
(a) $\omega_i s_{ij} \omega_j > 0$ (R)

(b) $\omega_i s_{ij} \omega_j < 0$ (R)

(c) $\omega_i s_{ij} \omega_j > 0$ (F)

(d) $\omega_i s_{ij} \omega_j < 0$ (F)

Figure 5.16: Alignment between the eigenvectors $\boldsymbol{e_i}$ of the strain rate and the vorticity unit vector $\boldsymbol{\omega}$ at $x/D_e = 2$. Round jet (R) at the top and fractal jet (F) at the bottom. The colour scheme represents $|\hat{\boldsymbol{e_1}} \cdot \hat{\boldsymbol{\omega}}|$, $|\hat{\boldsymbol{e_2}} \cdot \hat{\boldsymbol{\omega}}|$ and $|\hat{\boldsymbol{e_3}} \cdot \hat{\boldsymbol{\omega}}|$. (TPIV data and $Re_G = 10,000$)



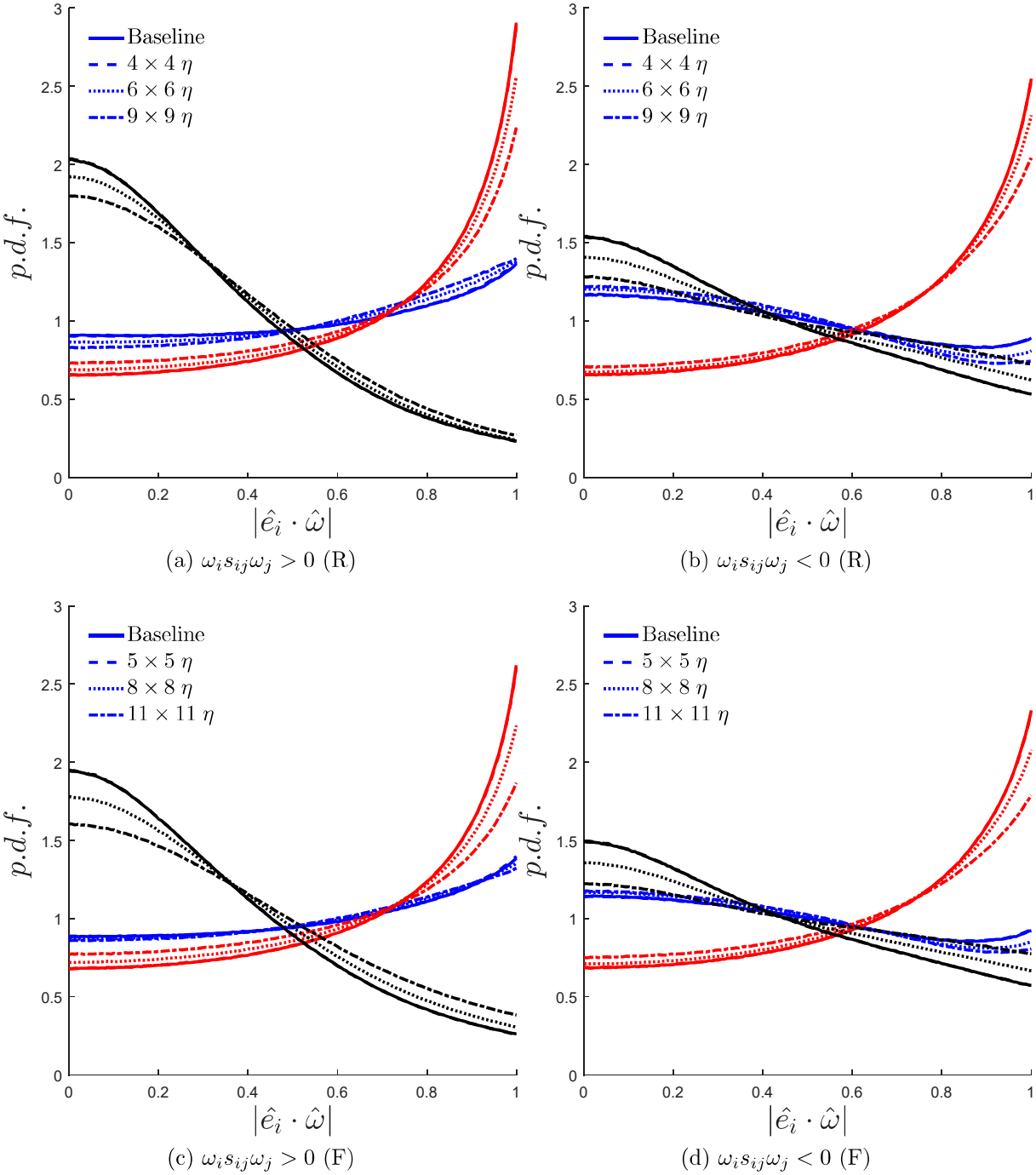
(a) $\omega_i s_{ij} \omega_j > 0$ (R)

(b) $\omega_i s_{ij} \omega_j < 0$ (R)

(c) $\omega_i s_{ij} \omega_j > 0$ (F)

(d) $\omega_i s_{ij} \omega_j < 0$ (F)

Figure 5.17: Alignment between the eigenvectors $\boldsymbol{e_i}$ of the strain rate and the vorticity unit vector $\boldsymbol{\omega}$ at $x/D_e = 10$. Round jet (R) at the top and fractal jet (F) at the bottom. The colour scheme represents $|\hat{\boldsymbol{e_1}} \cdot \hat{\boldsymbol{\omega}}|$, $|\hat{\boldsymbol{e_2}} \cdot \hat{\boldsymbol{\omega}}|$ and $|\hat{\boldsymbol{e_3}} \cdot \hat{\boldsymbol{\omega}}|$. (TPIV data and $Re_G = 10,000$)



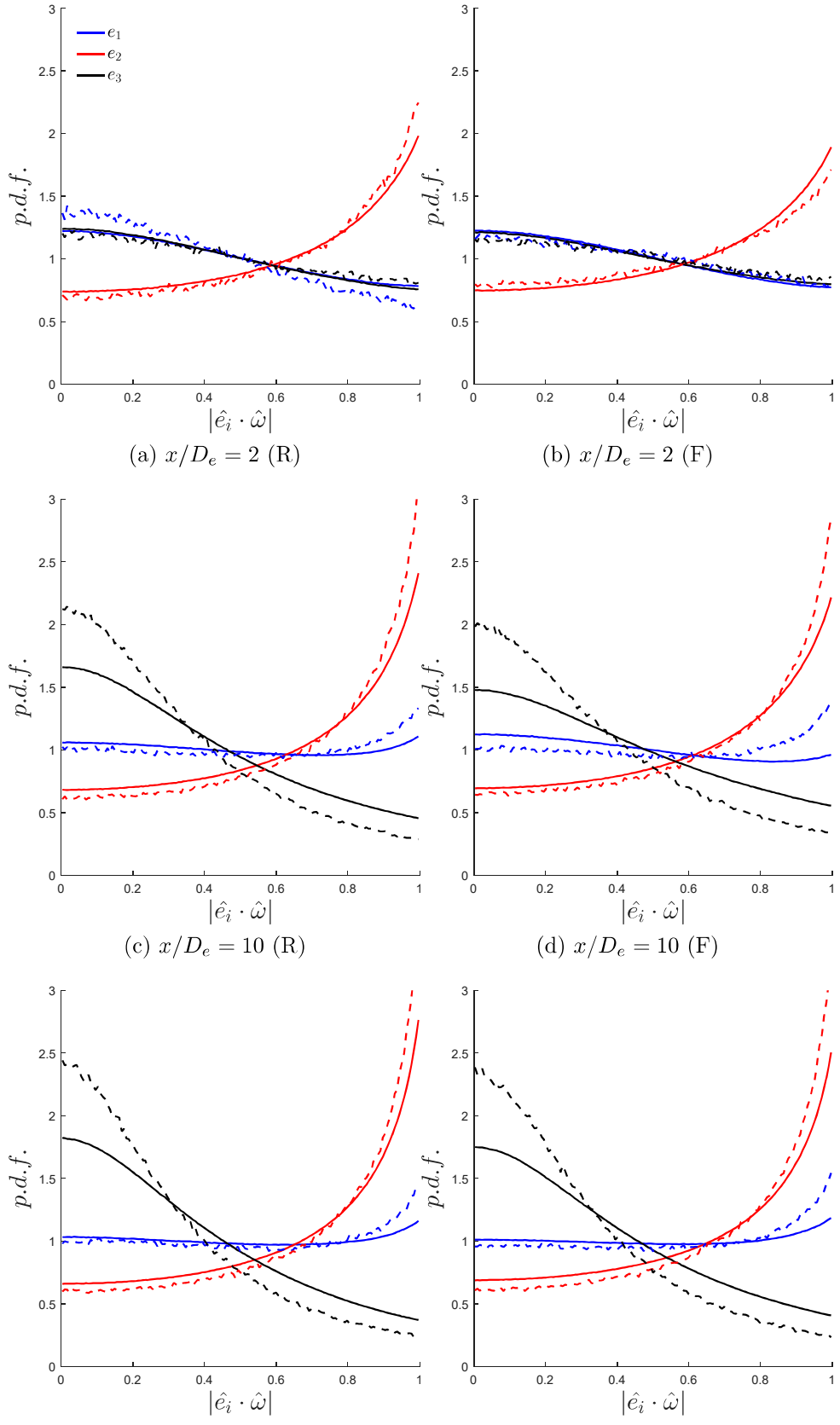
(a) $\omega_i s_{ij} \omega_j > 0$ (R)

(b) $\omega_i s_{ij} \omega_j < 0$ (R)

(c) $\omega_i s_{ij} \omega_j > 0$ (F)

(d) $\omega_i s_{ij} \omega_j < 0$ (F)

Figure 5.18: Alignment between the eigenvectors $\boldsymbol{e_i}$ of the strain rate and the vorticity unit vector $\boldsymbol{\omega}$ at $x/D_e = 25$. Round jet (R) at the top and fractal jet (F) at the bottom. The colour scheme represents $|\hat{\boldsymbol{e_1}} \cdot \hat{\boldsymbol{\omega}}|$, $|\hat{\boldsymbol{e_2}} \cdot \hat{\boldsymbol{\omega}}|$ and $|\hat{\boldsymbol{e_3}} \cdot \hat{\boldsymbol{\omega}}|$. (TPIV data and $Re_G = 10,000$)



(a) $x/D_e = 2$ (R) (b) $x/D_e = 2$ (F)

(c) $x/D_e = 10$ (R) (d) $x/D_e = 10$ (F)

(e) $x/D_e = 25$ (R) (f) $x/D_e = 25$ (F)

Figure 5.19: Pdf of the alignment $|\hat{\boldsymbol{e}}_{\boldsymbol{i}} \cdot \hat{\boldsymbol{\omega}}|$ from the turbulent bulk (-) and from regions of intense swirling $\lambda_{ci} > 3.5\lambda'_{ci}$ (- -) (TPIV data, $Re_G = 10,000$).

5.4.5 Concluding remarks on the alignment $|\hat{e_i} \cdot \hat{\omega}|$

Having investigated the spatial evolution of the alignment $|\hat{\boldsymbol{e_i}} \cdot \hat{\boldsymbol{\omega}}|$ of the vorticity vector with the eigenvector of the strain-rate tensor, now the influence of the angle of alignment $\iota = \arccos(|\hat{\boldsymbol{e_i}} \cdot \hat{\boldsymbol{\omega}}|)$ is investigated, to verify how the changing angle affects dissipation, enstrophy and strain production/destruction. This is done by calculating the pdfs of $s_{ij}s_{ij}$, $s_{ij}s_{jk}s_{ki}$ and of $\omega_i s_{ij}\omega_j$, conditioned to a specific range of angles of the alignment of $\boldsymbol{e_1}$, $\boldsymbol{e_2}$ and $\boldsymbol{e_3}$. An interval of 10° is chosen for each pdf.

The evolution of $s_{ij}s_{ij}$ is shown in fig. 5.20. It is found the role played by the alignment of $\boldsymbol{e_2}$ remains the same across the three volumes interrogated. Increasing the angle of alignment of $\boldsymbol{e_2}$ with $\hat{\omega}$, $s_{ij}s_{ij}$ has an increasingly intermittent behaviour as shown in figs. 5.20d to 5.20f. However, since $\boldsymbol{e_2}$ has a higherer tendency of alignment with $\boldsymbol{\omega}$, this may imply this alignment is not the main driver of the increasing intermittency of $s_{ij}s_{ij}$ moving further downstream. Analysing $\boldsymbol{e_1}$, it found that at $x/D_e = 2$ it counterbalances the behaviour of $\boldsymbol{e_2}$ showing an increasing intermittency together with an alignment between $\boldsymbol{e_2}$ and $\boldsymbol{\omega}$, as shown in fig. 5.20a. However, at $x/D_e = 10$ and $x/D_e = 25$ the pdf remains approximately the same (figs. 5.20b and 5.20c). The opposite takes place for the alignment of $\boldsymbol{e_3}$. At $x/D_e = 2$, the pdf of $s_{ij}s_{ij}$ is approximately the same across the range of angles studied (fig. 5.20g), however it becomes less intermittent the more $\boldsymbol{e_3}$ becomes aligned in parallel with $\hat{\omega}$ (figs. 5.20h and 5.20i). Therefore, it is found that $\boldsymbol{e_2}$ maintains the same behaviour at all streamwise locations and it is counterbalanced by $\boldsymbol{e_1}$ near the jet exit and by $\boldsymbol{e_3}$ further away from it. This is somewhat surprising, since despite $\boldsymbol{e_3}$ and $\boldsymbol{e_2}$ having an opposite tendency of alignment across all regions studied, at $x/D_e = 2$ $\boldsymbol{e_2}$ is counterbalanced by $\boldsymbol{e_1}$ instead, which is found to have the same tendency of parallel alignment with $\boldsymbol{e_3}$.

Now, the same analysis is carried on in fig. 5.21 for $-s_{ij}s_{jk}s_{ki}$. It is found that the alignment of $\boldsymbol{e_3}$ with $\boldsymbol{\omega}$ is responsible for characterising the intermittency of the strain destruction. In fact, the positive tail of the pdf (figs. 5.21a to 5.21c) becomes less intermittent with increasing angle, whilst the negative tail (strain production) remains

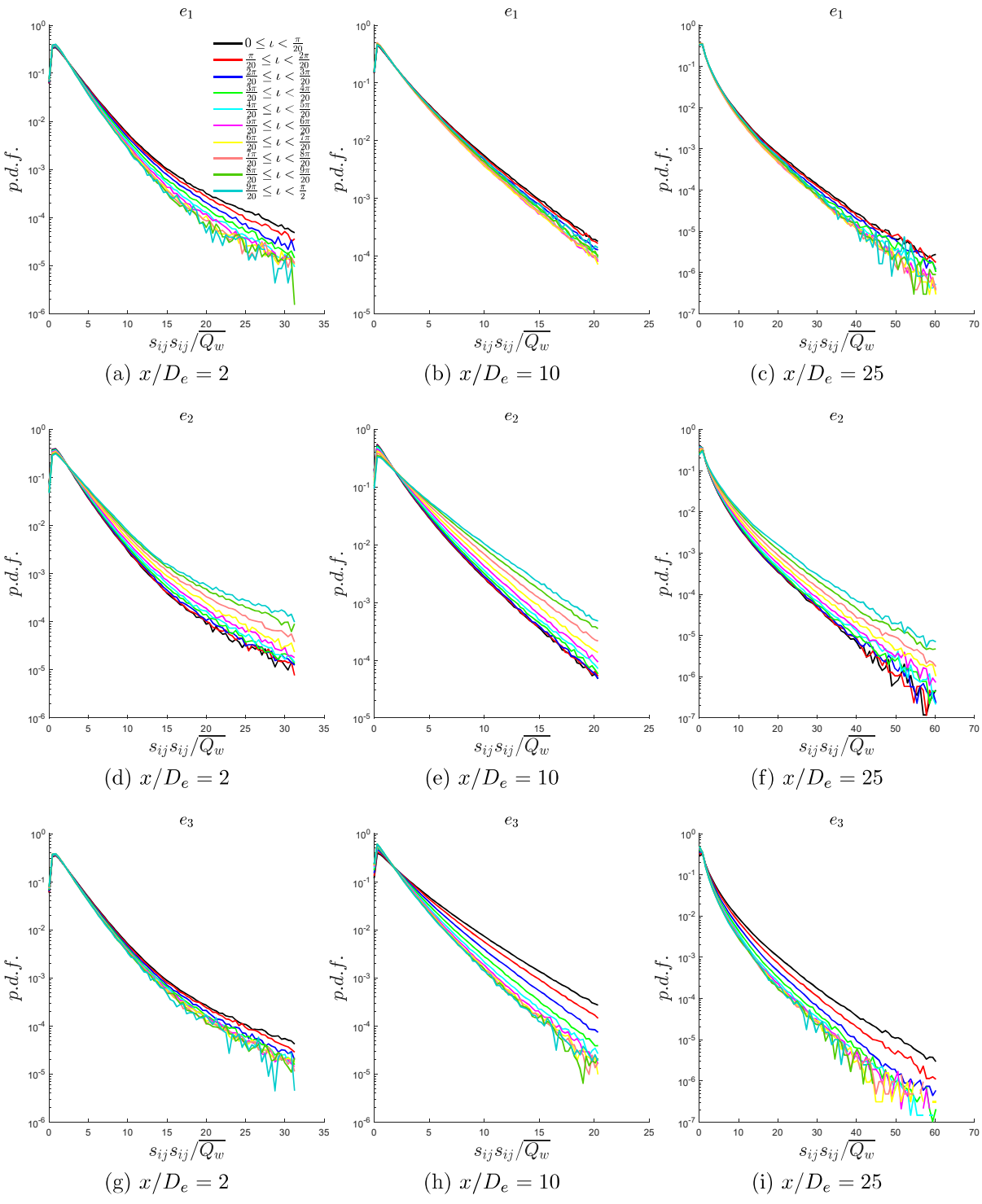
approximately the same. The other two eigenvectors $\boldsymbol{e_2}$ and $\boldsymbol{e_3}$ appear not to affect the strain destruction, since the tails remain the same across all angles studied. Instead, they show an opposite behaviour concerning strain production. At increasing alignment of $\boldsymbol{e_2}$ with $\boldsymbol{\omega}$, the intermittency of the strain production increases (figs. 5.21d to 5.21f), which is counterbalanced by the opposite behaviour of the alingment between $\boldsymbol{e_3}$ and $\boldsymbol{\omega}$ (figs. 5.21g, 5.21g and 5.21i). The data presented in figs. 5.20 and 5.21 are presented for the round jet only for brevity, but the same behaviour is found for the fractal jet as well.

Now, the behaviour of $\omega_i s_{ij} \omega_j$ is examined in fig. 5.22. The intermediate eigenvector shows an opposite behaviour compared to the other two. At increasing angle, the pdf of $\omega_i s_{ij} \omega_j$ conditioned with $\boldsymbol{e_2}$ shows increasing intermittency (figs. 5.22d to 5.22f). Regarding the other two eigenvectors, $\boldsymbol{e_1}$ shows a decreasing intermittency with increasing ι (figs. 5.22a to 5.22c). However, at $x/D_e = 25$ greater changes appear to take place mainly on the negative tail of the pdf (fig. 5.22c). This is counterbalanced by the behaviour of $\boldsymbol{e_3}$, which shows changes mainly on the positive side of the tail (fig. 5.22i), whilst the trends are comparable on the negative side. Therefore, it appears that the behaviour of $\boldsymbol{e_2}$ is alternatively balanced by $\boldsymbol{e_1}$ (mainly on the negative side) and $\boldsymbol{e_3}$ (mainly on the positive one).

Summarising, it is shown that an increasing angle of alignment of the extensive eigenvector $\boldsymbol{e_1}$ is responsible for reducing the intermittency of $s_{ij}s_{ij}$ at all three streamwise locations studied. Moreover, it also reduces the intermittency of the strain destruction and of both enstrophy production and destruction. It appears however to not affect strain production. Differently, an increasing angle of alignment of the intermediate eigenvector $\boldsymbol{e_2}$ appears to increase the intermittency of $s_{ij}s_{ij}$ at all three streamwise locations. Moreover, it is found to substantially increase the intermittency of the strain production, whilst strain destruction appears to be affected only at $x/D_e = 2$, whilst it remains comparable at the other streamwise stations. Further, the angle of $\boldsymbol{e_2}$ appears to increase the intermittency of both enstrophy production and destruction. Finally, an increasing angle of alignment of the compressive eigenvector $\boldsymbol{e_3}$ appears to reduce the intermittency of $s_{ij}s_{ij}$ at all three streamwise locations. The same takes place for strain production, however strain destruc-

tion appears to be unaffected by this angle. Similarly, it reduces the intermittency of enstrophy production at $x/D_e = 10$ and $x/D_e = 25$, whilst it marginally affects enstrophy destruction. At $x/D_e = 2$, both enstrophy production and destruction appears to be marginally affected, suggesting that at this location where the flow is constrained by the two TNTIs the alignment between $\boldsymbol{e_3}$ and $\boldsymbol{\omega}$ contributes in approximately equal manner across all angles to enstrophy production. Later on, where the flow has space to develop, at a decreasing ι will correspond a higher enstrophy production.

Having discussed various properties of the alignments between $\boldsymbol{e_i}$ and $\boldsymbol{\omega}$, now a further insight into the microstructure of the turbulent fluid is sought.

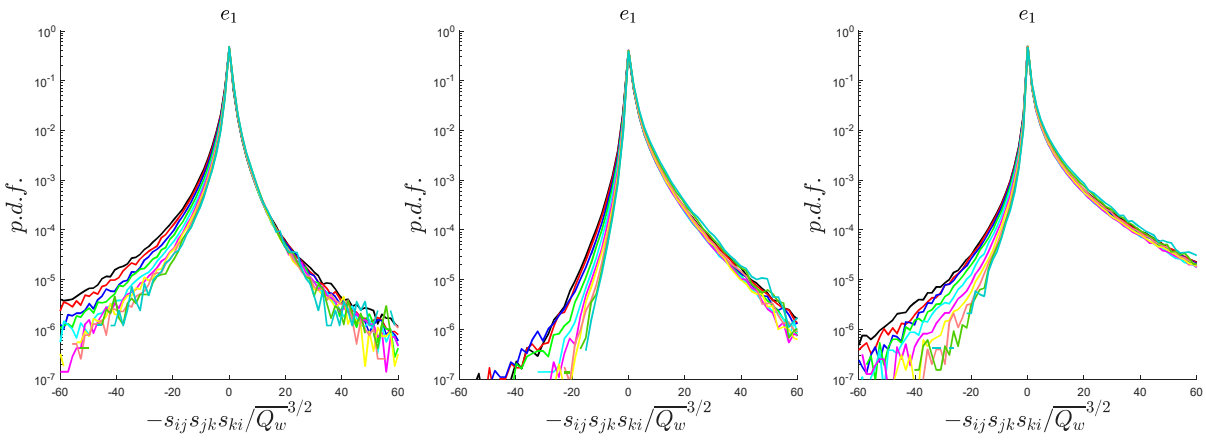


(a) $x/D_e = 2$ (b) $x/D_e = 10$ (c) $x/D_e = 25$

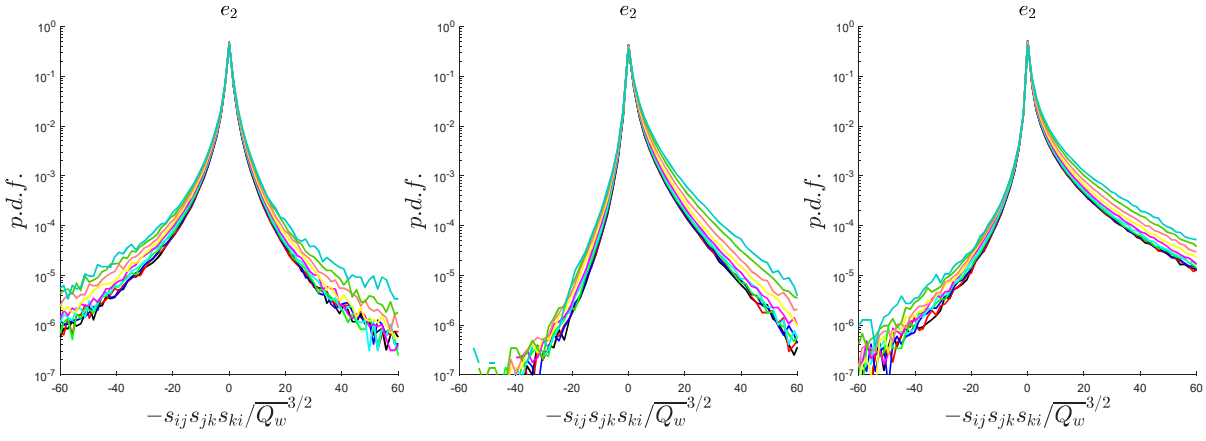
(d) $x/D_e = 2$ (e) $x/D_e = 10$ (f) $x/D_e = 25$

(g) $x/D_e = 2$ (h) $x/D_e = 10$ (i) $x/D_e = 25$

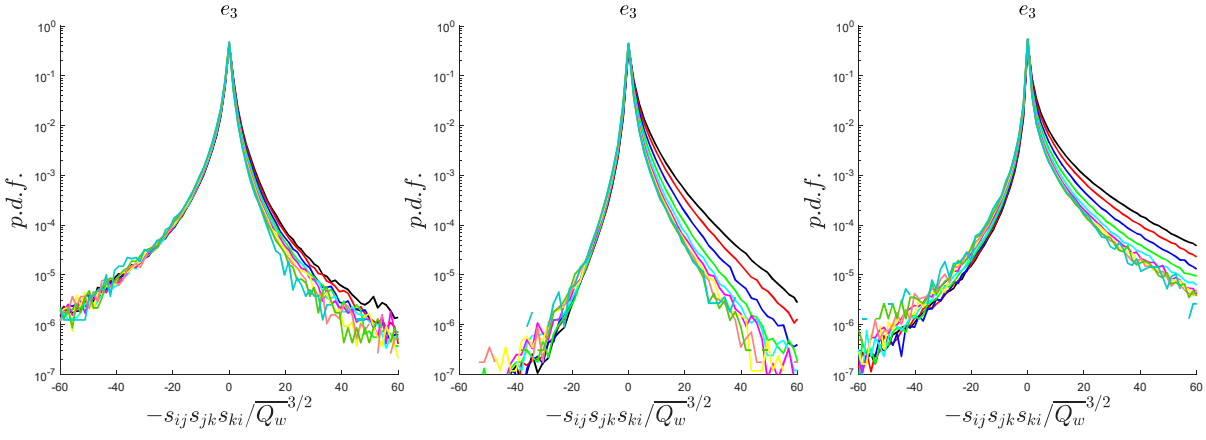
Figure 5.20: Pdfs of $s_{ij}s_{ij}$ for the round jet conditioned to various angles of alignment. (TPIV data, $Re_G = 10,000$).



(a) $x/D_e = 2$ (b) $x/D_e = 10$ (c) $x/D_e = 25$

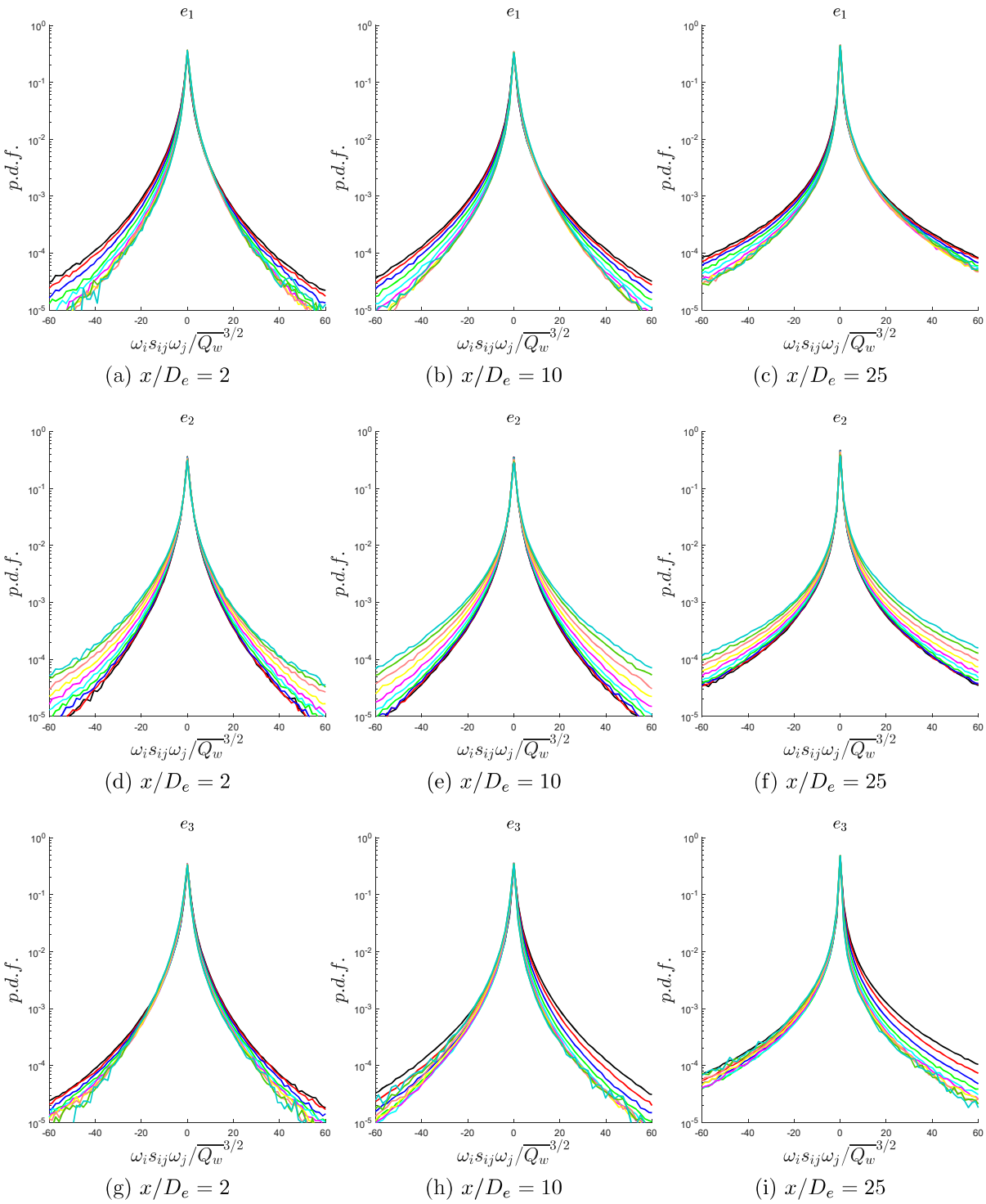


(d) $x/D_e = 2$ (e) $x/D_e = 10$ (f) $x/D_e = 25$



(g) $x/D_e = 2$ (h) $x/D_e = 10$ (i) $x/D_e = 25$

Figure 5.21: Pdfs of $s_{ij}s_{jk}s_{ki}$ for the round jet conditioned to various angles of alignment. (TPIV data, $Re_G = 10,000$). Legend as in fig. 5.20.



(a) $x/D_e = 2$ (b) $x/D_e = 10$ (c) $x/D_e = 25$

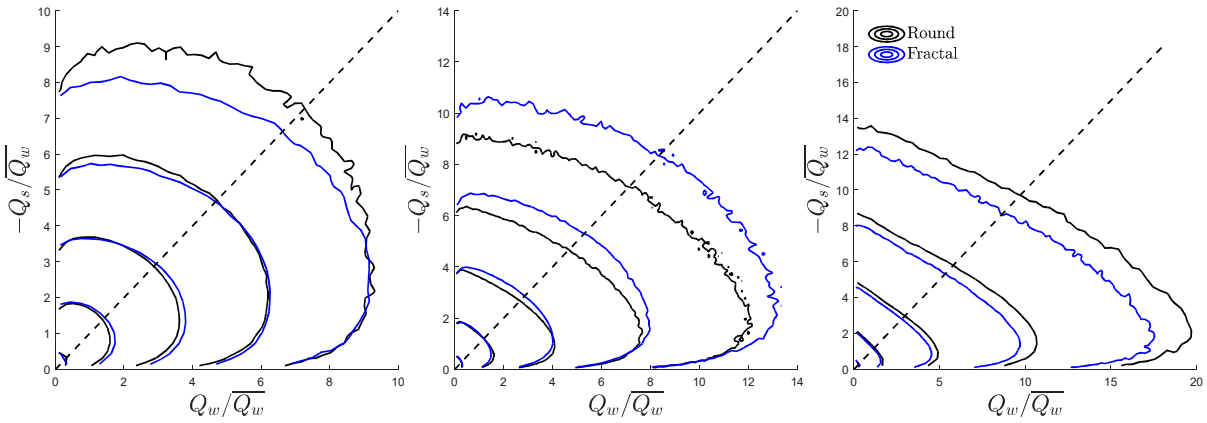
(d) $x/D_e = 2$ (e) $x/D_e = 10$ (f) $x/D_e = 25$

(g) $x/D_e = 2$ (h) $x/D_e = 10$ (i) $x/D_e = 25$

Figure 5.22: Pdfs of $\omega_i s_{jk} \omega_j$ for the round jet conditioned to various angles of alignment. (TPIV data, $Re_G = 10,000$). Legend as in fig. 5.20.

5.4.6 Evolution of the symmetric and skew-symmetric parts of the $Q - R$ invariants

The microstructure of the flow is examined by studying the symmetric and skew-symmetric parts of the invariants. In fig. 5.23, the jpdf of $-Q_s$ and Q_ω is examined. The axis $-Q_s$



(a) $x/D_e = 2$ (b) $x/D_e = 10$ (c) $x/D_e = 25$

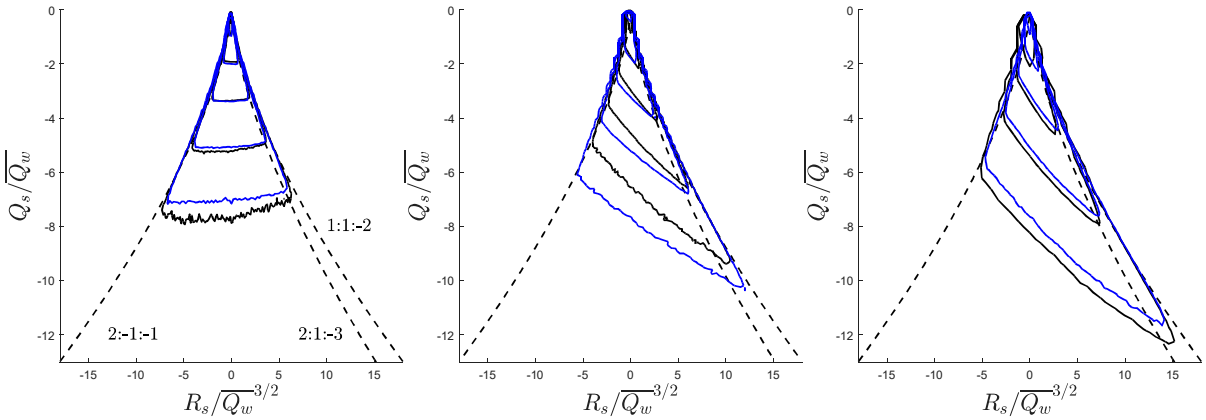
Figure 5.23: Jpdf of Q_ω and Q_s for round and fractal jet (TPIV data and $Re_G = 10,000$). Isocontours range from 10^{-4} to 10^0.

represents points with a locally high rate of (irrotational) dissipation of turbulent kinetic energy arranged in sheet-like structures (Ganapathisubramani et al., 2008; Buxton et al., 2017). The axis Q_ω represents instead the points associated with high enstrophy and arranged in tube-like structures (Jiménez et al., 1993). At the 45° line there is a balance of enstrophy and dissipation, where points are arranged in vortex sheets. As shown in fig. 5.23a, at $x/D_e = 2$ there is an approximately equal percentage of points distributed near the vertical axis, the horizontal axis and near the 45° line, suggesting a close balance between irrotational dissipation (along the $-Q_s$ axis), vortex tubes and vortex sheets. Passing the turbulence production region at $x/D_e = 10$ (fig. 5.23b), the most frequent events approach the $-Q_s$ axis, however this time the extreme events take place about the Q_ω axis. This indicates that regions of high Q_ω are associated with solid body rotation and little dissipation (da Silva and Pereira, 2008). The same behaviour is found at $x/D_e = 25$ (fig. 5.23c) as well, where an even greater amount of intense events is aligned with the $-Q_s$ axis. A similar behaviour was found by Ooi et al. (1999) for homogeneous

isotropic turbulence and by Chong et al. (1998) in the wake region of a boundary layer (DNS). Therefore, it appears that near the jet exit various types of vortical structures coexist in a similar percentage, whilst moving further downstream there is a preference for frequent events to be linked to irrotational dissipation and for extreme events to take place as vortex tubes.

This evolution is not universal between turbulent flows. For example, Blackburn et al. (1996) found a larger peak value at $-Q_s$ compared to Q_ω in the log-law region and wake region of a turbulent channel flow, indicating the extreme events would more often be linked to irrotational dissipation (along the $-Q_s$ axis). Gomes-Fernandes et al. (2014) found instead an equal distribution of points at the $-Q_s$ and Q_ω axes in their spatially-developing grid-generated flow at all locations studied. Hence, the evolution of the $-Q_s - Q_\omega$ space, and hence the fine-scale topology of the flows, appears to vary based on the type of flow studied.

Now the Q_s-R_s jpdf is examined in fig. 5.24 to analyse the local deformation of the turbulent flow. The dashed line indicates various triples of the eigenvalues of the rate of strain tensor which are linked to R_s as $R_s = -s_1 s_2 s_3$. As before, s_1 is the extensive eigenvalue, s_2 is the intermediate one and s_3 is the compressive one. In their works, various



(a) $x/D_e = 2$ (b) $x/D_e = 10$ (c) $x/D_e = 25$

Figure 5.24: Jpdf of Q_s and R_s for round and fractal jet (TPIV data and $Re_G = 10,000$). Isocontours range from 10^{-4} to 10^0. In (a), the eigenvalues $s_1 : s_2 : s_3$ corresponding to each dashed line are shown. Legend as in fig. 5.23.

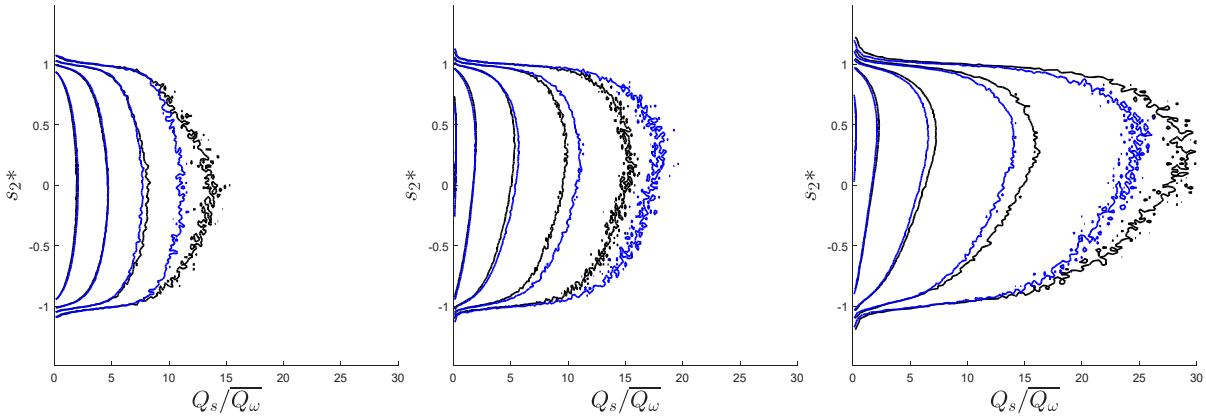
authors suggested that the majority of events for a turbulent flow tends to align to regions

corresponding to the triplets in the ratio $3:1:-4$ or $2:1:-3$ (da Silva and Pereira, 2008; Ooi et al., 1999; Soria et al., 1994; Blackburn et al., 1996; Ashurst et al., 1987). da Silva and Pereira (2008) found that for their turbulent plane jet (DNS), the most frequent (and lower $|Q_s|$) events tended to have a ratio between their eigenvalues of $2:1:-3$, whilst the high strain regions (higher $|Q_s|$) of $1:1:-2$. This latter behaviour was found by Gomes-Fernandes et al. (2014) as well for all the stations probed in their grid-generated flow. At $x/D_e = 10$ and $x/D_e = 25$, the present round and fractal jets appear to behave in the same manner found by da Silva and Pereira (2008), where for the most frequent events the ratio between the eigenvalues is $2:1:-3$, whilst for the high-strain regions of $1:1:-2$. A different behaviour is however found at $x/D_e = 2$ in fig. 5.24a. It appears that high strain regions are slightly more concurrent with strain destruction ($R_s < 0$) than strain production ($R_s > 0$). Therefore, it appears that close to the jet exit the high strain regions have no preference towards strain production/destruction, whilst further away from the jet exit a clear tendency towards $R_s > 0$ is found, as in previous studies and as suggested by the distribution of the eigenvalues in the pdfs in fig. 5.13.

Having discussed the flow topology of the jet, now its relationship with s_2, intimately related to vortex stretching Betchov (1956), is further examined. As discussed by Gomes-Fernandes et al. (2014), *if s_2 is positive, there are two stretching directions and the flow behaves locally like a jet parallel to e_3 and impinging on a wall on the e_1e_2 plane (sheet-forming structures). If s_2 is negative, the flow behaves locally as if entering a contraction cone (tube-like structures).* In fig. 5.13, it was found that from $x/D_e = 10$ onwards s_2 had a positive skewness (tube-like forming). This strain-rate is further studied considering the normalised second eigenvalue s_2^* (Ashurst et al., 1987) as

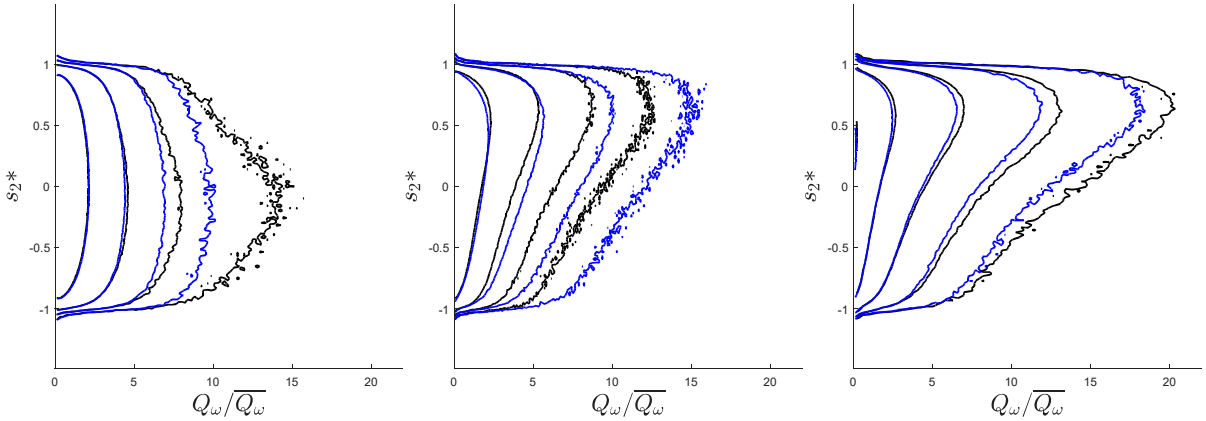
$$s_2^* = \frac{\sqrt{6}s_2}{\sqrt{s_1^2 + s_2^2 + s_3^2}}. \tag{5.13}$$

In fig. 5.25 and fig. 5.26 the relationship between s_2^* and areas where Q_s and Q_ω are large is examined. As shown in fig. 5.25a and fig. 5.26a, at $x/D_e = 2$ for regions of high strain and rotation $s_2^* \approx 0$ and the jpdfs show symmetry for positive and negative values of s_2^*.



(a) $x/D_e = 2$ (b) $x/D_e = 10$ (c) $x/D_e = 25$

Figure 5.25: Jpdf of s_2^* and Q_s for round and fractal jet (TPIV data and $Re_G = 10,000$). Isocontours range from 10^{-4} to 10^0. Legend as in fig. 5.23.



(a) $x/D_e = 2$ (b) $x/D_e = 10$ (c) $x/D_e = 25$

Figure 5.26: Jpdf of s_2^* and Q_ω for round and fractal jet (TPIV data and $Re_G = 10,000$). Isocontours range from 10^{-4} to 10^0. Legend as in fig. 5.23.

Therefore, it appears that at this location the flow has no preference for tube- or sheet-like forming tendency. A similar finding regarding the relationship between Q_ω and s_2^* was found by Gomes-Fernandes et al. (2014) at the peak of turbulence production for a grid-generated flow. However, the authors found that s_2^* was skewed towards positive values when associated with large straining events. This tendency was increased in the turbulence decay region, where the areas of high rotation were also associated with positive s_2^*. This behaviour is confirmed in figs. 5.25b, 5.25c, 5.26b and 5.26c, where s_2^* has a tendency to be positive between 0.5 and 1 concurrently to both regions of high strain and enstrophy. Therefore, the present findings, together with the work of Gomes-Fernandes et al. (2014), suggest s_2^* has no preference towards positive or negative values until approximately the

peak of turbulence production, after which it has an increasing skewness towards positive values and hence vortex stretching.

So far, the jet's turbulent properties have been studied within the whole turbulent bulk. Now, their evolution from the interface towards the jet's centre is investigated to study how they evolve and how they differ from the mean bulk properties. This is initially done by looking at the evolution of the jet's microscales from the TNTI towards the turbulent bulk.

5.5 Evolution of jet's lengthscales from the TNTI into the turbulent bulk

In early studies, Corrsin and Kistler (1954) suggested that the thickness of the TNTI scaled with a viscous lengthscale (often assumed to be the Kolmogorov lengthscale η). This point was later challenged by Bisset et al. (2002); Westerweel et al. (2005) who suggested the TNTI would scale with the Taylor lengthscale instead. However, the literature has not covered in which regions of the turbulent fluid these two lengthscales should be calculated. Often, an average value of these two lengthscales has been calculated in the turbulent bulk, however it was not established how these lengthscales vary locally from the TNTI into the turbulent bulk.

Therefore, now the evolution of η and λ_f is examined "locally", to verify how they change and if new local lengthscales better represent the thickness of the TNTI. To do so, the two local scales $\hat{\lambda_f}$ and $\hat{\eta}$ are calculated at the interface location first and then in "slices" of thickness $5\,\eta$ at various distances away from the TNTI in the following way: $0\,\eta$, $0-5\,\eta$, $5-10\,\eta$, $10-15\,\eta$ and so on. Only the data points which are above the vorticity threshold previously discussed are included in the calculation.The findings are also evaluated in terms of the mean ratio between bulk λ_f and η to verify if the local quantities vary across the TNTI only or not. The ratio for the two jets at various streamwise distances is shown

in fig. 5.27.

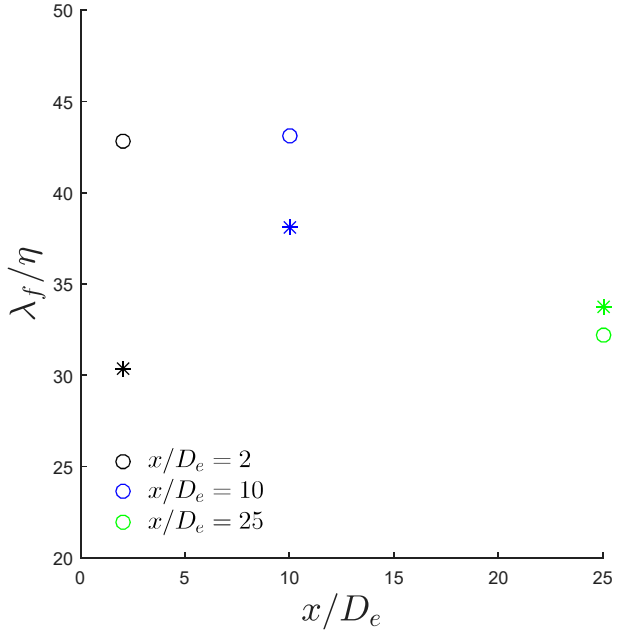


Figure 5.27: Evolution of of the ratio between bulk λ_f and η for round ($\circ$) and fractal jet ($*$) ($Re_G = 10,000$, TPIV data).

As shown in fig. 5.28, both $\hat{\lambda_f}$ and $\hat{\eta}$ vary significantly from the TNTI towards the turbulent bulk. The greatest ratio between both lengthscales and their mean bulk value is at the interface. At the three streamwise locations, $\hat{\lambda_f}$ appears to evolve up to a distance of λ_f away from the interface, after which it reaches a plateau. This would therefore suggest that the lengthscales evolve inside the TNTI of thickness λ_f, however they do not vary any more once the turbulent bulk is reached. The local $\hat{\eta}$ appears to take slightly longer to reach a plateau compared to $\hat{\lambda_f}$, even though the most rapid changes takes place again in a distance of λ_f.

Examining the relationship between the local length scales, the ratio between these two scales changes based on the streamwise location and in general it increases from the TNTI moving towards the turbulent bulk as shown in fig. 5.29a. At $r_i \approx 30 - 40\,\eta$, this ratio decreases for the ITNTI and the OTNTI at $x/D_e = 2$, however this could be due to the fact that the points furthest away from one interface are approaching the other one. This is also reflected in fig. 5.29b, where the evolution of the local Taylor Reynolds number is examined. This is calculated as $Re_{\hat{\lambda_f}} = \hat{u_x'}\hat{\lambda_f}/\nu$, where $\hat{u_x'}$ is the root-mean-square

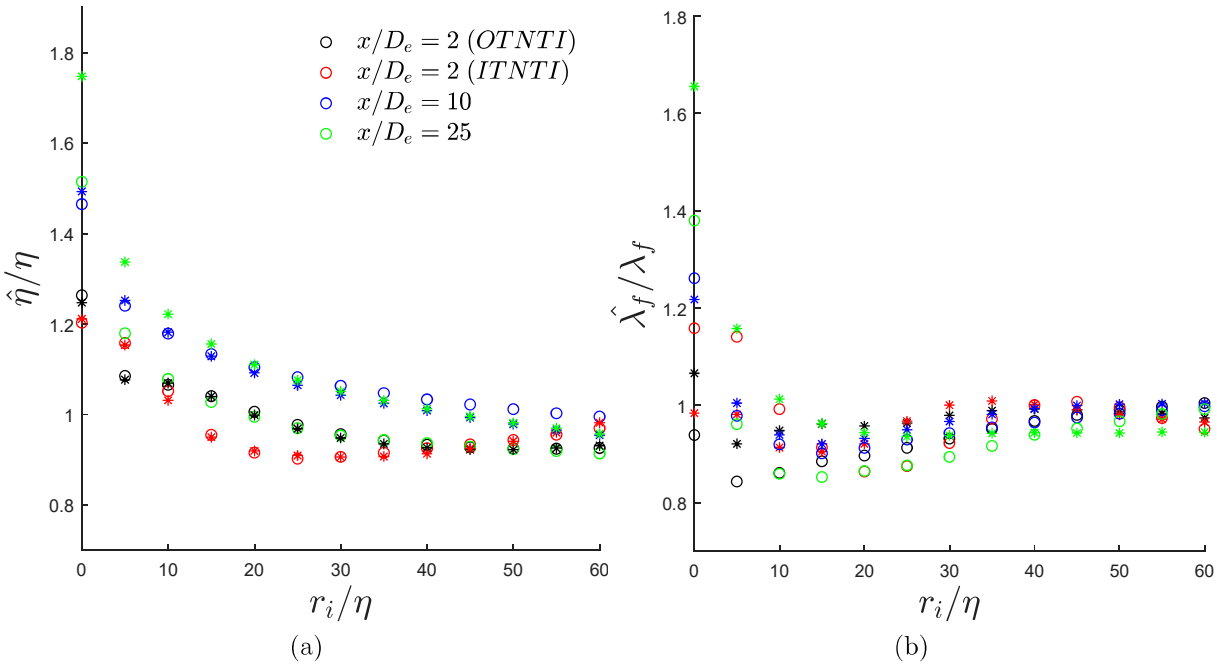


Figure 5.28: Evolution of (a) local Kolmogorov and of (b) local Taylor lengthscale for round ($\circ$) and fractal jet ($*$) ($Re_G = 10,000$, TPIV data).

of the streamwise velocity fluctuations calculated in the same region as $\hat{\lambda_f}$. As shown, $Re_{\hat{\lambda_f}}$ increases with increasing distance from the TNTI, reflecting the behaviour of $\hat{\lambda_f}/\hat{\eta}$. This shows that there is a significant scale evolution from the TNTI moving towards the turbulent bulk and that choosing the mean bulk value to describe the state of a turbulent flow may not be representative.

Now the reason for such evolution is examined. The TNTI separates the non-turbulent fluid from the turbulent one, acting like a "barrier" between the two types of flow. It may thus be hypothesised that the TNTI has a similar role to a wall in a turbulent boundary layer, which would lead to an increase of the small-scale anisotropy of the flow near the TNTI. Hence, this would affect the velocity gradients and as a consequence ε, λ_f and η, since the interface normal direction, similarly to the wall-normal direction of a turbulent boundary layer, is highly anisotropic. Bechlars and Sandberg (2017b) showed that, for a compressible boundary layer, the wall-normal velocity gradient (and hence its anisotropy) would be dominant at the wall with respect to the other terms of the velocity gradient tensor and it would decrease moving away from the viscous sublayer. In section 5.4.3, it was discussed that the TNTI acts a like a barrier to the development of the turbulent

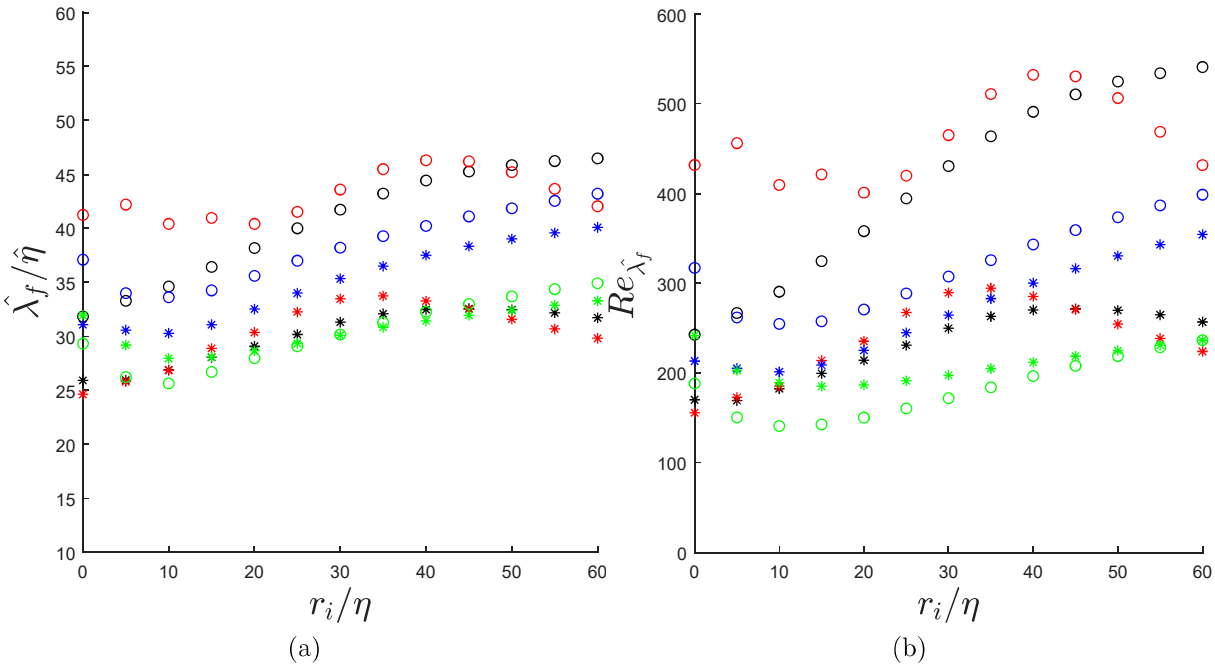


Figure 5.29: Evolution of (a) $\hat{\lambda_f}/\hat{\eta}$ and of (b) $Re_{\hat{\lambda_f}}$ for round ($\circ$) and fractal jet ($*$) ($Re_G = 10,000$, TPIV data). The legend is the same as fig. 5.28

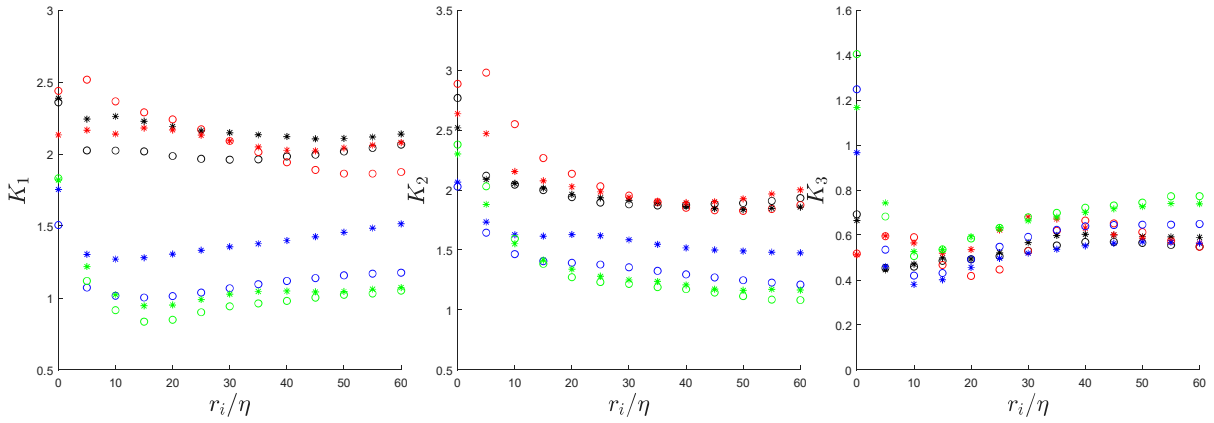
properties. Therefore, the state of anisotropy is examined through three ratios K_i

$$K_1 = 2\frac{\overline{(\partial u_x/\partial x)^2}}{\overline{(\partial u_r/\partial x)^2}},\ K_2 = 2\frac{\overline{(\partial u_x/\partial x)^2}}{\overline{(\partial u_\theta/\partial x)^2}},\ K_3 = 2\frac{\overline{(\partial u_x/\partial x)^2}}{\overline{(\partial u_x/\partial r)^2}}, \tag{5.14}$$

to verify how the velocity gradients evolve from the TNTI towards the turbulent bulk.

As shown in fig. 5.30, the anisotropy is greatest at the interface location at all streamwise locations and for all the three K_i. The trends of K_1 and K_2 appears to decrease moving further downstream, as expected due to the reduced influence of the coherent structures, however an isotropic state where $K_i = 1$ is not yet reached for all ratios. Moreover, at $x/D_e = 2$ the flow is constrained by the presence of two TNTIs as discussed in section 5.4.4, which may not leave enough space to the flow to recover any "bulk" isotropy. In general a plateau or a constant trend is found after a distance of λ_f. It appears that these anisotropy ratios vary mainly inside the TNTI as $\hat{\lambda_f}$ and $\hat{\eta}$. Therefore, this suggests that the local quantities are strongly influenced by the anisotropy of the flow especially inside the TNTI since it acts like a "wall", constraining the movement of the flow. However, outside the TNTI, the ratios stabilise suggesting that away from the TNTI averaging across

the turbulent bulk may still work to estimate the lenghtscales of the flow. Another way to



(a) (b) (c)

Figure 5.30: Evolution of (a) K_1, (b) K_2 and (c) K_3 for round ($\circ$) and fractal jet ($*$) ($Re_G = 10,000$, TPIV data). The legend is the same as fig. 5.28

evaluate these K_i would have been extrapolating points that would be perpendicular or parallel to the interface to calculate the corresponding velocity gradients. However, this proved challenging due to the choice of a $r - \theta$ field of view and the wrinkled interface, which would require interpolating across the field of view. Therefore, this work is left to potentially future studies conducted on a field of view longitudinal to the jet exit, where the points perpendicular to the TNTI would be measured directly. This point is further discussed in chapter 6.

5.6 Small scale evolution across the TNTI

So far, this study has focused on the differences between regions of the flow located at various streamwise locations. Now, the evolution of some of the jet's properties across the TNTI is examined. This is done by recalculating some of the properties at the jet interface and then in regions at a certain distance away from the interface. The intervals chosen were as before $0 - 5\,\eta$, $5 - 10\,\eta$, $10 - 15\,\eta$ and so on up to $55 - 60\,\eta$. An example is shown in fig. 5.31. It is noted that due to the low spatial resolution the findings in the near field of the jet may appear filtered with respect to the stations further donwstream.

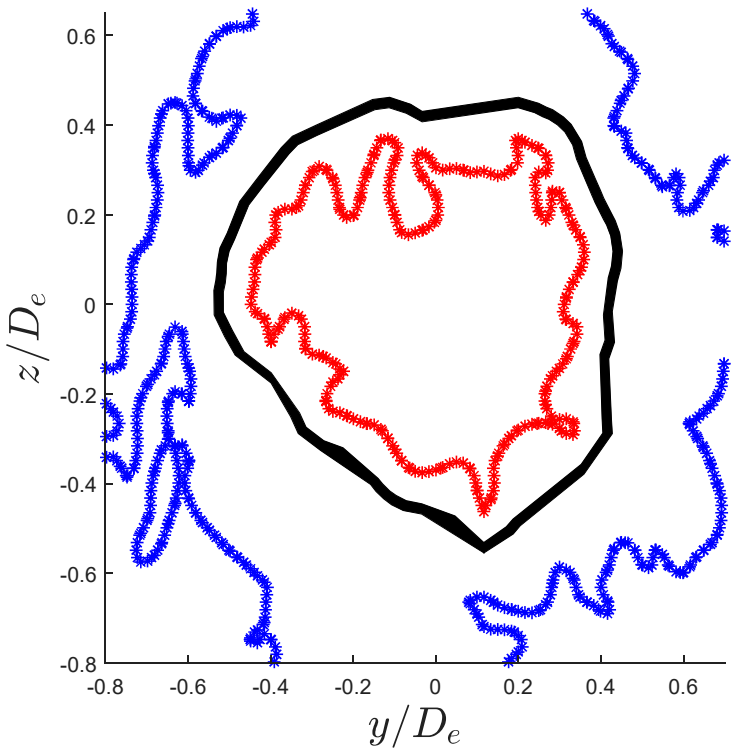


Figure 5.31: Example of an area probed between 15-20 η at $x/D_e = 2$ (black). The ITNTI is shown in red and the OTNTI in blue (Round jet, TPIV data, $Re_G = 10,000$).

In fig. 5.32, the evolution of $-s_{ij}s_{jk}s_{ki}$ is examined. At $x/D_e = 2$, it is found the pdfs have the same shape in regions greater than approximately $\approx \lambda_f$ as shown in figs. 5.32a and 5.32b. At $x/D_e = 10$ and $x/D_e = 25$, the pdfs have the same negative tail (strain destruction) for regions greater then 5η. However, an evolution of the positive side (strain production) is found and the pdf appears to have the same behaviour for regions greater than $\approx \lambda_f$ (figs. 5.32c and 5.32d). Therefore, it appears that the evolution of the jet properties across the TNTI only takes place for the first λ_f away from the interface, after which the jet properties remains comparable. This is in agreement with other works, like the study on a turbulent boundary layer of Bechlars and Sandberg (2017b) who found that the turbulent properties varied significantly near the wall, further showing the "wall" behaviour of the TNTI.

The relationship between strain and enstrophy production across the interface is examined in fig. 5.33. It is found that the jpdf evolves rapidly from the interface towards the turbulent zone. At $x/D_e = 2$, it is found that at the interface there is an almost equal distribution of strain-only and enstrophy-only events (figs. 5.33a and 5.33b). Further

downstream, the jpdf stretches across the $\omega_i s_{ij} \omega_j$ axis moving into the turbulent zone, whilst the extension of strain-dominated regions appears to not vary as much (figs. 5.33c and 5.33d). Along the $-s_{ij}s_{jk}s_{ki}$ axis, the jpdfs appears to extend on the strain production side only, whilst they remain comparable on the destruction one. Again, it is found that the contours of the jpdfs starts collapsing at $\approx \lambda_f$ away from the TNTI.

Now the evolution of the jet properties across the TNTI are examined in terms of the jpdf of Q and R. The data presented in fig. 5.34 suggests that at $\approx \lambda_f$ the contours become comparable between the evolving TNTI and the turbulent bulk region. Examining in detail the contours at the interface location, it is found that at $x/D_e = 10$ and $x/D_e = 25$ all the points are associated with $Q < 0$, indicating that strain dominates over enstrophy at the TNTI. This finding is consistent with the analysis of da Silva and Pereira (2008), who found the same behaviour at the interface location of a plane jet obtained from a DNS of spatial resolution of 2.1η. Therefore, this study suggests even a coarser spatial resolution allows identifying the small scale topology at the TNTI.

A final analysis is conducted to evaluate the topology associated with the dissipation of turbulent kinetic energy in fig. 5.35. At the interface location (magenta contour) at $x/D_e = 10$ and $x/D_e = 25$, the majority of points are aligned with the $-Q_s$ axis, indicating irrotational dissipation (figs. 5.35c and 5.35d). This finding is consistent with the plane jet studied by da Silva and Pereira (2008). Despite the low spatial resolution, a tendency towards strain dominated regions is found at $x/De = 2$ as well, as shown in figs. 5.35a and 5.35b. Moving inside the turbulent zone, all jets show an increase of events associated with Q_ω. Again, at approximately λ_f the contours are superimposed and they approximate the behaviour found previously in the bulk turbulent region of the jets.

Summarising, it has been found that the contours of the jpdf of various microscales properties becomes the same at approximately λ_f. Therefore, these finding suggests the microscale properties vary inside the turbulent sublayer, which scale with λ_f. After that, the microscale properties remains the same as in the turbulent bulk at each streamwise location. Therefore, the present work suggests that the thickness of the TNTI scales with

λ_f, which differs from the recent findings of Silva et al. (2018) (who suggested a thickness of $\approx 17\eta$), but which is in agreement with previous works conducted on other turbulent flows like wakes (Bisset et al., 2002), jets (Westerweel et al., 2005), mixing layers (Attili et al., 2014) and boundary layers (Chauhan et al., 2014b; Borrell and Jiménez, 2016).

5.7 Chapter summary

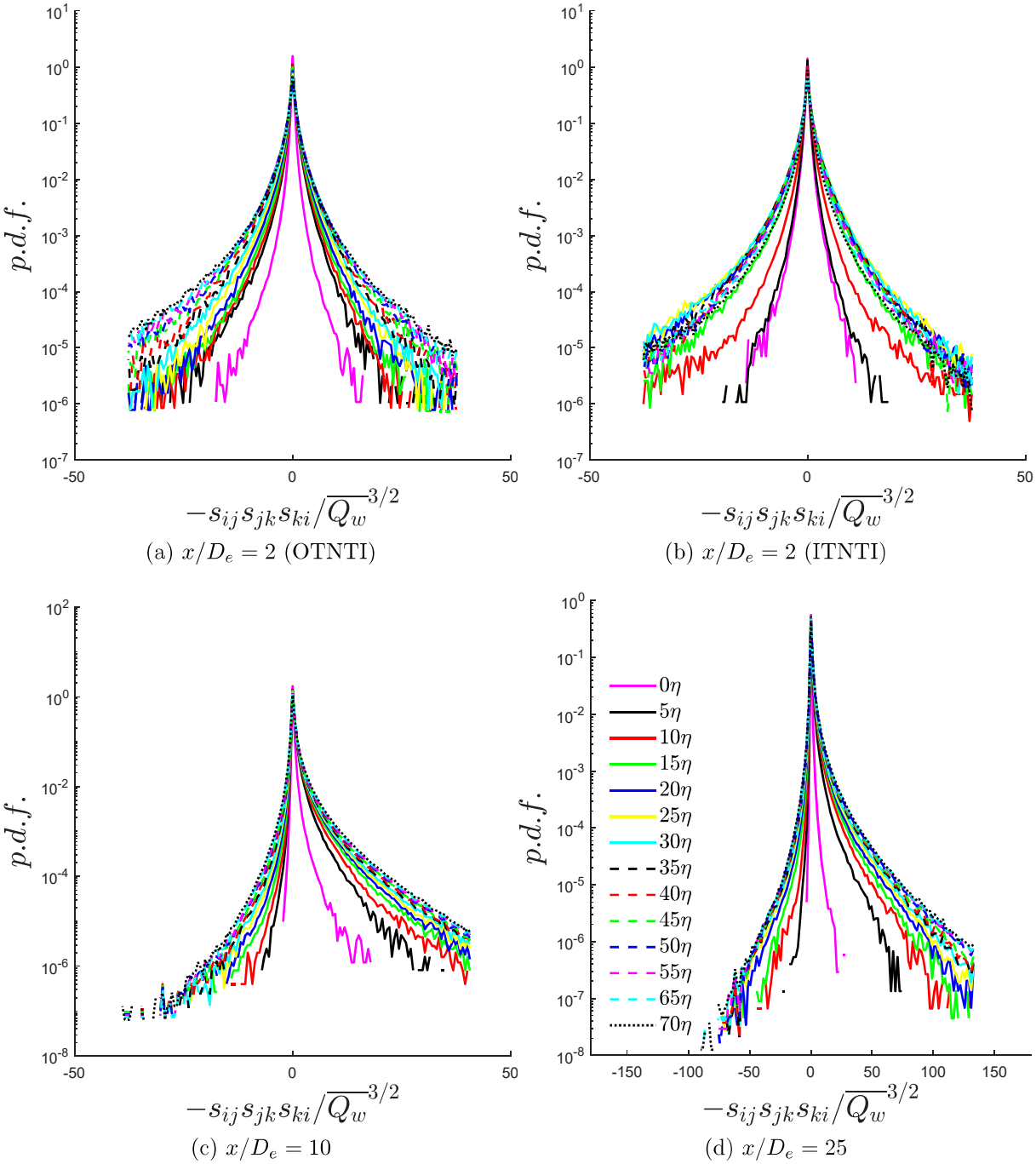
In this chapter, the evolution of the TNTI and of the small scale dynamics has been examined. It was found the break-up of the coherent structures affects the tortuosity of the ITNTI in the near field and also reduces the thickness of the OTNTI in the near field. However, the fluctuations of $\hat{r}$ with respect to its local mean value appear to be comparable for the round and fractal jets if the interface is moving towards the turbulent side, whilst they vary if the TNTI moves towards the non-turbulent one. Overall, it is found that the different exit geometries highly affect the radial excursions of the ITNTI rather than the OTNTI. Despite such differences, the velocity fluctuations at both ITNTI and OTNTI appear to be comparable in the near field for both round and fractal jets. Using a box-counting technique, it was verified that the TNTI follows a scaling of $N \sim B_s^{-6/5}$ in the regions studied, whilst only the fractal jet appears to start approaching the Kolmogorov scaling in the "weakly self-similar" region. Despite $N \sim B_s^{-6/5}$ has been linked before to the presence of non-equilibrium dissipation, the fractal jet was found to have both this type of dissipation and a Kolmogorov scaling.

An analysis of the microstructure of the jet indicated that, in the near field, turbulence is constrained between the ITNTI and of the OTNTI. This inhibits the background *non-local* strain field, which is further demonstrated by the fact that at $x/D_e = 2$ the microscale structure of the jet can be modelled with the restricted Euler equation, in which Π_{ij} is diagonal. Further, the alignment $|\hat{\boldsymbol{e_i}} \cdot \hat{\boldsymbol{\omega}}|$ is studied at the various streamwise locations, finding the role played by the three eigenvector in affecting $s_{ij}s_{ij}$, $-s_{ij}s_{jk}s_{ki}$ and $\omega_i s_{ij} \omega_j$. Comparing the present work with the one of Gomes-Fernandes et al. (2014), it is confirmed

that the $Q-R$ jpdf unfolds from the turbulence production region moving towards the far field. Other similarities are represented by the initial balance between production and destruction of strain and enstrophy and by the evolution of s_2^*. However, some differences are present in the near field, where for a round jet there are two TNTIs and the flow is initially not fully turbulent. In fact, the symmetrical jpdf of $Q-R$ at $x/D_e = 2$ was not found by Gomes-Fernandes et al. (2014). Moreover, the authors found a balance between the pdfs of s_1 and s_3 across all stations studied, whilst in the present work this is found in the near field only and later on the pdf of s_1 is different from s_3. This may indicate that the behaviour of the eigenvalues is flow-dependent.

The analysis then moved towards understanding how the scales varied from the TNTI into the turbulent bulk. It was found that there is a substantial change of $\hat{\lambda_f}$ and $\hat{\eta}$ due to the high anisotropy at the interface. It appears a distance of λ_f is necessary for the lengthscales to have a comparable value spatially. The chapter is concluded looking at the evolution of the microscale structure from the TNTI into the turbulent bulk. It is found that in most cases the the pdfs and the contours of the jpdfs start collapsing after a distance of λ_f away from the TNTI, suggesting therefore the microscale structure of the jet evolves across the interface and then becomes comparable in the turbulent bulk.

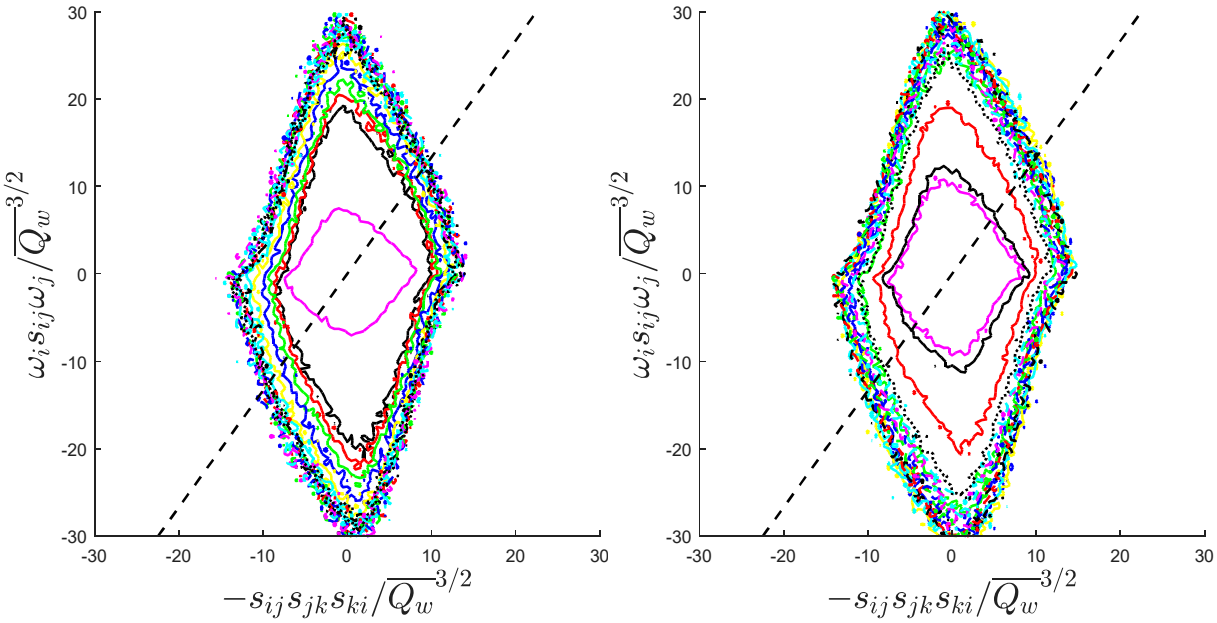
Overall, it appears that breaking up the coherent structures does not affect the fine scales of the flow, which remains comparable between round and fractal jets. The evolution of turbulent properties also takes place across a distance of λ_f for both jets, indicating that the initial conditions may only impact large scale phenomena like mixing, whilst the fine structure of the flow remains unaltered.



(a) $x/D_e = 2$ (OTNTI) (b) $x/D_e = 2$ (ITNTI)

(c) $x/D_e = 10$ (d) $x/D_e = 25$

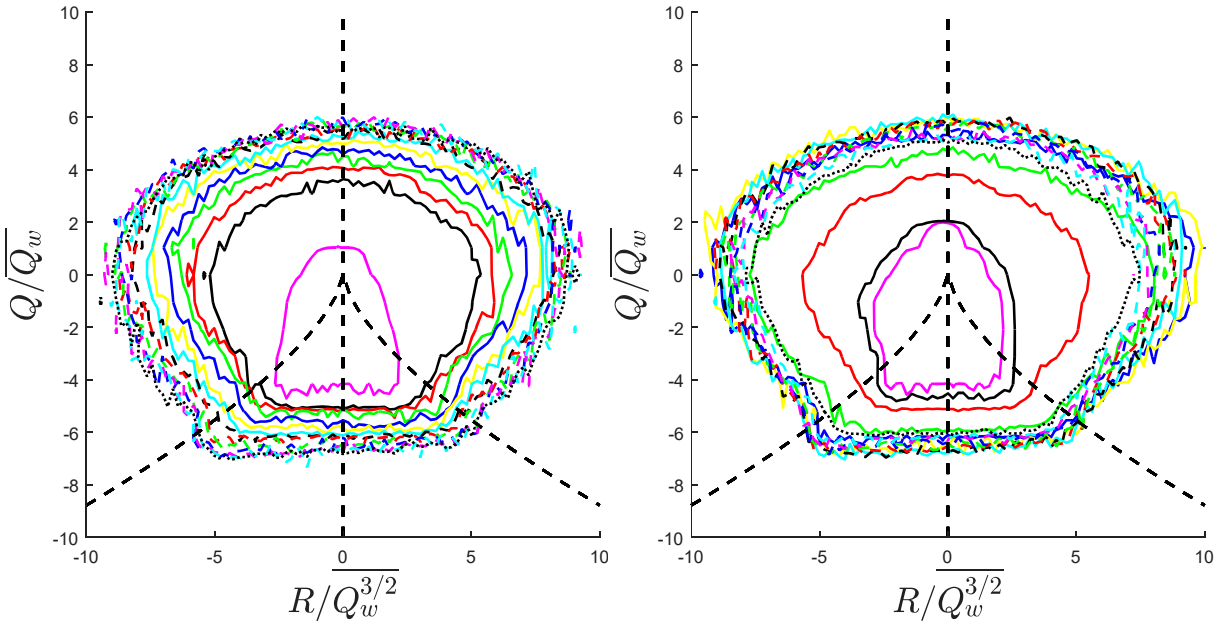
Figure 5.32: Evolution of $s_{ij}s_{jk}s_{ki}$ across TNTI (TPIV data, $Re_G = 10,000$). The data are presented for the round jet only, but comparable results are found for the fractal jet too. The legend in (d) is valid for the rest of the plot of this section.



(a) $x/D_e = 2$ (OTNTI) (b) $x/D_e = 2$ (ITNTI)

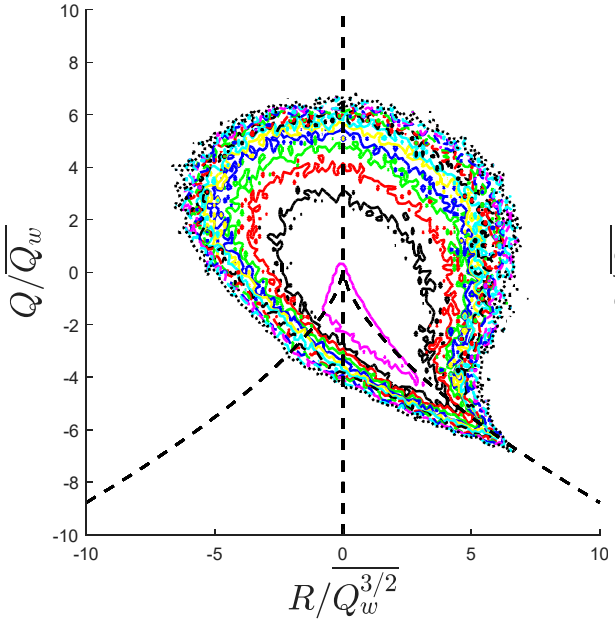
(c) $x/D_e = 10$ (d) $x/D_e = 25$

Figure 5.33: Jpdf of $-s_{ij}s_{jk}s_{ki}$ and $\omega_i s_{ij} \omega_j$. Isocontour 10^{-4} and the data are from round jet (comparable behaviour for fractal jet). The black dashed line marks where $\omega_i s_{ij} \omega_j = -4/3 s_{ij} s_{jk} s_{ki}$, therefore the data above the line corresponds to $R > 0$ and below the line to $R > 0$. (TPIV data and $Re_G = 10,000$).

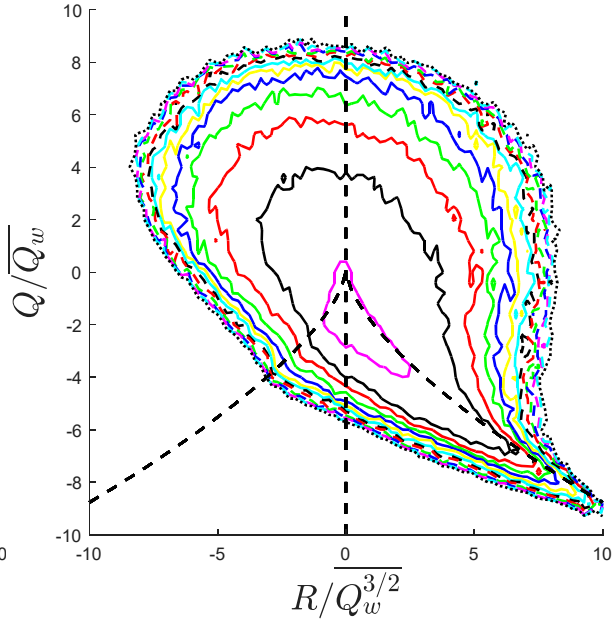


(a) $x/D_e = 2$ (OTNTI)

(b) $x/D_e = 2$ (ITNTI)

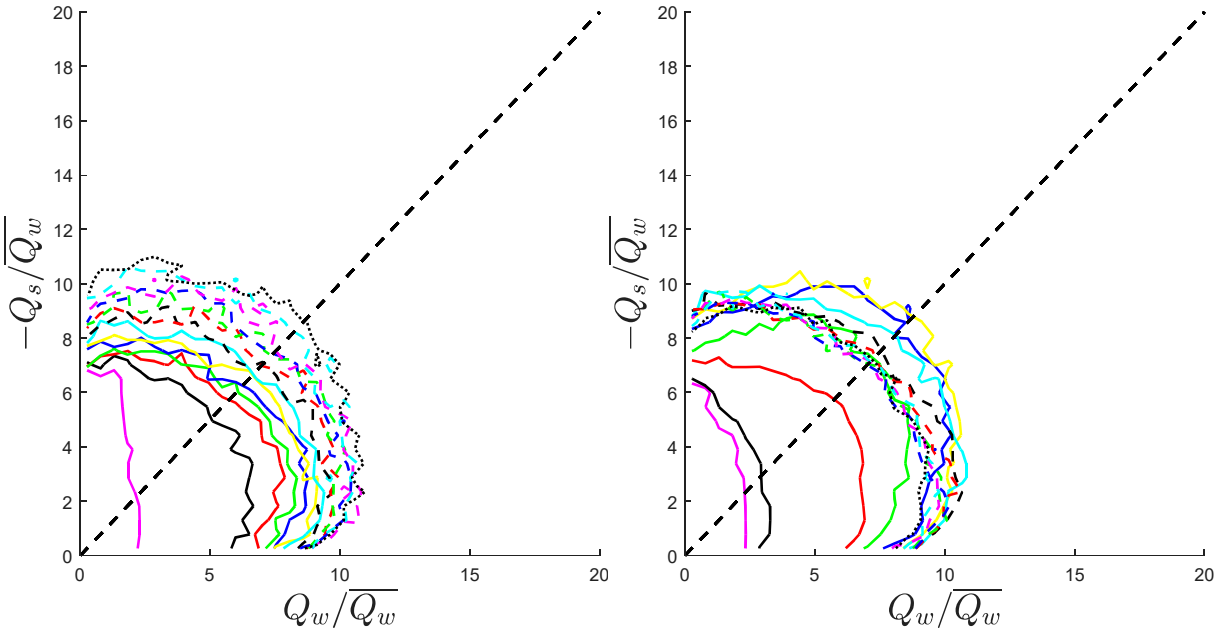


(c) $x/D_e = 10$



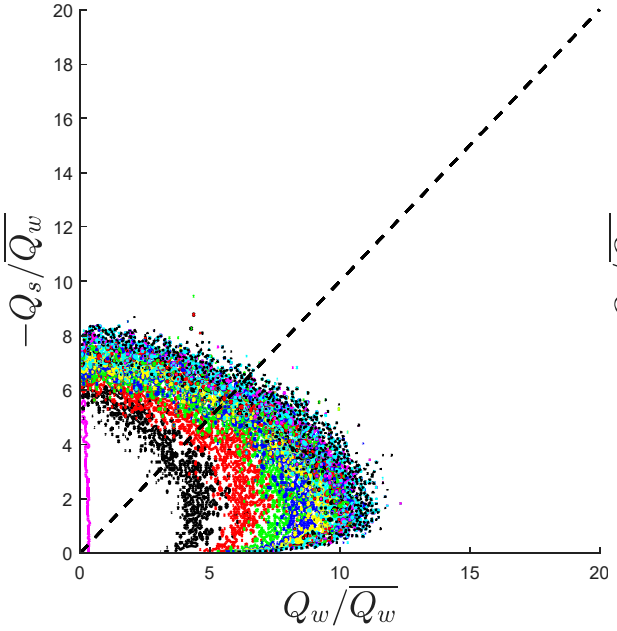
(d) $x/D_e = 25$

Figure 5.34: Jpdf of Q and R, at a isocontour of 10^{-2} for the round jet (a comparable behaviour is found for the fractal jet as well). (TPIV data and $Re_G = 10,000$).

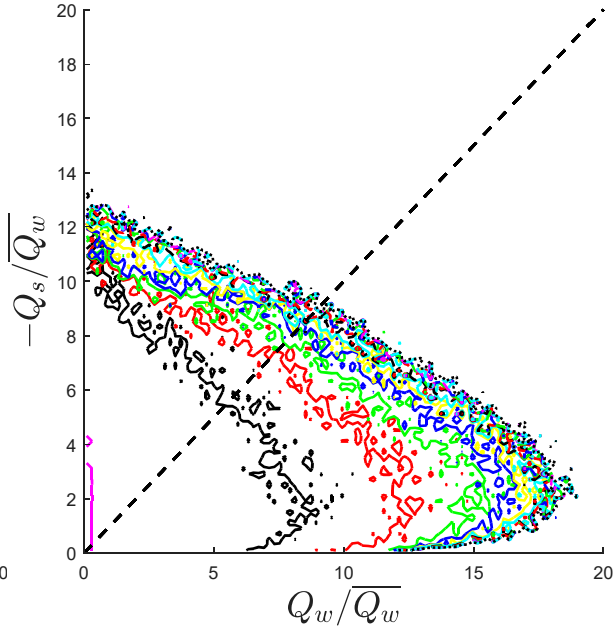


(a) $x/D_e = 2$ (OTNTI)

(b) $x/D_e = 2$ (ITNTI)



(c) $x/D_e = 10$



(d) $x/D_e = 25$

Figure 5.35: Jpdf of $-Q_s$ and Q_ω, at a isocontour of 10^{-4} for the round jet (a comparable behaviour is found for the fractal jet as well). (TPIV data and $Re_G = 10,000$).

Chapter 6

Conclusions and future work

6.1 Conclusions

This thesis has experimentally investigated the role of the coherent structures in the near field and in the evolution of an axisymmetric turbulent jet. This was achieved by suppressing the coherent structures at the jet exit with the aid of a fractal exit geometry. Flow visualisation enabled an immediate identification of the suppression of the Kelvin-Helmholtz vortex rings. Subsequently, calculating two-point correlations of the velocity fluctuation it was possible to further quantify this phenomenon through the lack of a negative anti-correlation of the radial velocity fluctuations in the streamwise direction, representative of coherent azimuthal vorticity. This was further studied with the aid of tomographic PIV, which indicated that the fractal geometry did indeed break the azimuthal component of vorticity and led to the formation of opposite-signed patches of mean vorticity for the radial and streamwise components. Moreover, it was verified that both fractal and square geometry would show axis-switching, indicating it is independent of the state of the coherent structures and that an important role is played by the streamwise vorticity in allowing it to take place.

Further examining the near field, it was found that the suppression of the Kelvin-Helmholtz vortex rings causes a delay of the evolution of the jet properties, as shown by the exten-

sion of the turbulence production region for the fractal jet. It was therefore hypothesised that some of the jet properties would scale in terms of N_{e_x}, the number of eddy turnover times undergone in the time taken by the flow to advect a distance x. The fractal jet was found to develop more slowly, particularly at higher Re_G. Moreover, it was found that after a distance of $N_{e_x} \approx 4$, many of the jet properties become comparable. These include the local entrainment dQ/dx and the radial terms of the time-averaged momentum equation, whilst the streamwise ones appears to take longer to reach the same trend between the different jets. Further, it is found that despite the fractal geometry reducing the entrainment in the near field, the different jets have the same spreading rate in the far field at $Re_G = 10,000$. However, this seems to happen only at this particular Re_G, since at $Re_G = 3,000$ where the coherent structures are more pronounced, the round jet was found to grow at a faster rate. The last section of chapter 4 dealt with the scaling laws of the jet, where it was analytically hypothesised that non-equilibrium dissipation could coexist with self-similar mean velocity and Reynolds stresses. This was verified experimentally, with the aid of planar PIV and hot-wire data. This specific region, where non-equilibrium dissipation was concurrent to self-similar scalings, was renamed "weakly self-similar".

The last part of the thesis (chapter 5) has focused on the TNTI and on the microscale structure of the jet. It was verified that in the near field, where OTNTI and ITNTI are present, the interfaces have the same radial excursions when they move towards the turbulent fluid, whilst when they move towards the non-turbulent one differences are found at the ITNTI only. However the coherent structures are found to increase the thickness of the OTNTI in the near field, whilst the ITNTI remains comparable. The TNTI was then further characterised at various streamwise locations looking at the fractal dimension using the "box-counting" technique. It was found that the TNTI does not follow the Kolmogorov scaling, but rather one that was previously found together with non-equilibrium dissipation.

The analysis then moved to the micro structure of the jet. It was found that the $Q - R$ jpdf would unfold into a tear-drop shape moving from the near field towards the far field.

At $x/D_e = 2$, the presence of two interfaces (the ITNTI and the OTNTI) meant that the turbulence would be somewhat constrained and therefore the *non-local* background strain effects would be hindered. The flow in this region would therefore be well modelled by the restricted Euler equation, where the pressure Hessian Π_{ij} was assumed to be diagonal. Later on, where the turbulence had sufficient space to develop, the non-diagonal part of Π_{ij} would become important again and the restricted Euler equation proved to be ineffective in modelling the flow. A further characterisation allowed understanding the role played by the alignment $|\hat{\boldsymbol{e}}_{\boldsymbol{i}} \cdot \hat{\boldsymbol{\omega}}|$ in promoting the intermittency of $s_{ij}s_{ij}$ and of the strain and enstrophy production/destruction. The last part of the chapter focused on the evolution of the jet lengthscales from the TNTI moving into the turbulent bulk. Due to the high anisotropy at the interface, it was found that the "local" Kolmogorov and Taylor lenghtscales vary significantly from the TNTI moving towards the turbulent bulk. This was found also in the jpdf of Q and R calculated in various regions of the flow. In general, it was found that the jet properties would evolve across a distance of one longitudinal Taylor lengthscale λ_f, after which they would be comparable to the ones calculated in the mean turbulent bulk. This therefore suggests that the TNTI has a thickness of one longitudinal Taylor lengthscale, in agreement with previous literature on wakes (Bisset et al., 2002), jets (Westerweel et al., 2005) and other shear flows (Hunt et al., 2006). Surprisingly, the fine scales of round and fractal jet were found to behave in a comparable manner, suggesting that they are unaltered by the state of the coherent structures.

6.2 Future Work

This thesis has discussed the presence of non-equilibrium dissipation, the structure of the TNTI and it has provided some insights into the flow behaviour when it is constrained between two boundaries at $x/D_e = 2$. The conclusions has pointed to the possibilities of further studies, of which a brief summary is given here:

- *Eddy turnover time*: it was shown in chapter 4 that many of the jet properties would

be comparable for the different jets once a certain number of N_{e_x} had overturned. Despite many studies in the past having investigated the far field of jets and other shear flows, this study has pointed back to the importance of the initial conditions. In fact, since many of the jet properties become comparable after a certain number of N_{e_x}, knowing the initial conditions of a turbulent flow would allow predicting its evolution up to the self-similar state. This study has covered a single type of flow and Re_G, however it would be certainly of great interest understating if a similar evolution in terms of eddy turnover times take place for other turbulent flows and better understanding the initial conditions which then will determine its evolution.

- *Restricted Euler equation*: it was verified in chapter 5 that, for both round and fractal jets, the restricted Euler equation is effective in modelling the flow behaviour in the near field. This may be due to the limited space available for the turbulent structure to develop but also to the importance of the large scale and coherent motions in this region of the flow. It may therefore be of interest verifying if such equation works in other turbulent flows, at least where the coherent structures are dominant and Π_{ij} can be modelled as diagonal, evaluating the conditional mean trajectories in the Q-R space. Finally, from that it would be interesting to observe the influence of the inhomogeneity on the non-diagonal part of Π_{ij}.

- *Non-equilibrium dissipation*: it was verified in chapter 4 that non-equilibrium dissipation was present in the weakly self-similar region of the jet. However two points were yet not covered by this study. One is how the dissipation evolves for an axisymmetric jet from the near field to the weakly self-similar region. The other regards how the jet transitions from a non-equilibrium to a "classical" dissipation. In fact, when an axisymmetric jet is self-similar $Re_{\lambda_f} = \text{constant}$, therefore it may be of interest understanding how the self-similar C_ε and Re_{λ_f} is related to the near field coherent structures and how the two quantities are linked between each other. Moreover, it was suggested by Zhou and Vassilicos (2017) that non-equilibrium dissipation affects the fractal scaling of the TNTI and, as a consequence, it may impact the entrainment rate. Hence, it is certainly of interest understanding how small scale entrainment

processes (nibbling) are affected by this type of dissipation scaling. Moreover, at $x/D_e = 25$ it was found that the fractal jet had non-equilibrium dissipation concurrent to a Kolmogorov scaling of the TNTI. Hence, a deeper understanding of the transition towards a Kolmogorov fractal scaling is needed to establish how this affects the behaviour of the TNTI.

- *Behaviour of the TNTI as a "wall"*: it was discussed in chapter 5 that the TNTI acts like a "wall", constraining the development of turbulent properties in the near field. This was further evidenced by the increased anisotropy at the edge of the interface, where $\hat{\eta}$ and $\hat{\lambda_f}$ were found to be significantly greater than their mean bulk value. An increased anisotropy was measured at the wall for boundary layers by Bechlars and Sandberg (2017a), however it has been found for boundary layers that η reduces at the wall rather than increasing. Therefore, it would be interesting to further explore the similarities between a wall and a TNTI, determining if the different behaviour of the microscales is due to, for example, the viscous diffusion of vorticity across the interface or by other phenomena. Moreover, further work could be focused on the anisotropy of the TNTI itself conducting a tomographic PIV experiment on a volume placed longitudinally to the jet exit, allowing an accurate study of the anisotropy ratios calculated from the velocity-gradient components locally perpendicular and parallel to the TNTI, rather than in a radial and azimuthal direction.

Bibliography

Aleyasin, S. S., Tachie, M. F., and Koupriyanov, M. (2017). PIV measurements in the near and intermediate field regions of jets issuing from eight different nozzle geometries. *Flow, Turbulence Combustion*, 99(2):329–351.

Anand, R. K., Boersma, B. J., and Agrawal, A. (2009). Detection of turbulent/non-turbulent interface for an axisymmetric turbulent jet: Evaluation of known criteria and proposal of a new criterion. *Experiments in Fluids*, 47(6):995–1007.

Antonia, R. A. and Zhao, Q. (2001). Effect of initial conditions on a circular jet. *Experiments in Fluids*, 31:319–323.

Ashurst, W. T., Kerstein, A. R., Kerr, R. M., and Gibson, C. H. (1987). Alignment of vorticity and scalar gradient with strain rate in simulated Navier-Stokes turbulence. *Physics of Fluids Fluids*, 30(8):2343–2353.

Attili, A., Cristancho, J. C., and Bisetti, F. (2014). Statistics of the turbulent/non-turbulent interface in a spatially developing mixing layer. *Journal of Turbulence*, 15(9):555–568.

Baj, P. and Buxton, O. R. H. (2017). Inter-scale energy transfer in the merger of wakes of a multiscale array of rectangular cylinders. *Physical Review Fluids*, 2(114607):1–47.

Batchelor, G. K. (1953). *The Theory of Homogeneous Turbulence*. Cambridge University Press.

Bechlars, P. and Sandberg, R. D. (2017a). Evolution of the velocity gradient tensor

invariant dynamics in a turbulent boundary layer. *Journal of Fluid Mechanics*, 815:223–242.

Bechlars, P. and Sandberg, R. D. (2017b). Variation of enstrophy production and strain rotation relation in a turbulent boundary layer. *Journal of Fluid Mechanics*, 812:321–348.

Betchov, R. (1956). An inequality concerning the production of vorticity in isotropic turbulence. *Journal of Fluid Mechanics*, pages 497–504.

Bisset, D. K., Hunt, J. C. R., and Rogers, M. M. (2002). The turbulent/non-turbulent interface bounding a far wake. *Journal of Fluid Mechanics*, 451:383–410.

Blackburn, H. M., Mansour, N. N., and Cantwell, B. J. (1996). Topology of fine-scale motions in turbulent channel flow. *Journal of Fluid Mechanics*, 310:269–292.

Borrell, G. and Jiménez, J. (2016). Properties of the turbulent/non-turbulent interface in boundary layers. *Journal of Fluid Mechanics*, 801:554–596.

Breda, M. and Buxton, O. R. H. (2017). Near and Far-Field Analysis of an Axisymmetric Fractal-Forced Turbulent Jet. In Örlü, R., Talamelli, A., Oberlack, M., and Peinke, J., editors, *Progress in Turbulence VII*, chapter Part IV, pages 211–217. Springer International Publishing, 1st edition.

Breda, M. and Buxton, O. R. H. (2018a). Effects of multiscale geometry on the large-scale coherent structures of an axisymmetric turbulent jet. *Journal of Visualization*, 21(4):525–532.

Breda, M. and Buxton, O. R. H. (2018b). Influence of coherent structures on the evolution of an axisymmetric turbulent jet. *Physics of Fluids*, 30(035109):1–24.

Brown, G. L. and Roshko, A. (1974). On density effects and large structure in turbulent mixing layers. *Journal of Fluid Mechanics*, 64:775–816.

Burattini, P., Antonia, R. A., and Danaila, L. (2005a). Similarity in the far field of a turbulent round jet. *Physics of Fluids*, 17(025101):1–14.

Burattini, P., Lavoie, P., and Antonia, R. A. (2005b). On the normalized turbulent energy dissipation rate. *Physics of Fluids*, 17(098103):1–4.

Buxton, O. R. H. (2015). Modulation of the velocity gradient tensor by concurrent large-scale velocity fluctuations in a turbulent mixing layer. *Journal of Fluid Mechanics*, 777:1–12.

Buxton, O. R. H., Breda, M., and Chen, X. (2017). Invariants of the velocity-gradient tensor in a spatially developing inhomogeneous turbulent flow. *Journal of Fluid Mechanics*, 817:1–20.

Buxton, O. R. H. and Ganapathisubramani, B. (2009). The classification and composition of fine scale eddies in a turbulent jet. In *47th AIAA Aerospace Sciences Meeting including The New Horizons Forum and Aerospace Exposition*, pages 1–11, Reston, Virigina. American Institute of Aeronautics and Astronautics.

Buxton, O. R. H. and Ganapathisubramani, B. (2010). Amplification of enstrophy in the far field of an axisymmetric turbulent jet. *Journal of Fluid Mechanics*, 651:483–502.

Buxton, O. R. H., Laizet, S., and Ganapathisubramani, B. (2011a). The effects of resolution and noise on kinematic features of fine-scale turbulence. *Experiments in Fluids*, 51:1417–1437.

Buxton, O. R. H., Laizet, S., and Ganapathisubramani, B. (2011b). The interaction between strain-rate and rotation in shear flow turbulence from inertial range to dissipative length scales. *Physics of Fluids*, 23(061704):1–4.

Cafiero, G., Discetti, S., and Astarita, T. (2015). Flow field topology of submerged jets with frctal generated turbulence. *Physics of Fluids*, 27(115103):1–18.

Cantwell, B. J. (1992). Exact solution of a restricted Euler equation for the velocity gradient tensor. *Physics of Fluids A: Fluid Dynamics*, 4(4):782–793.

Chacin, J. M. and Cantwell, B. J. (2000). Dynamics of a low Reynolds number turbulent boundary layer. *Journal of Fluid Mechanics*, 404:87–115.

Chao, J. L. and Sandborn, V. A. (1966). Evaluation of the momentum equation for a turbulent wall jet. *Journal of Fluid Mechanics*, 26:819–828.

Chauhan, K., Philip, J., de Silva, C. M., Hutchins, N., and Marusic, I. (2014a). The turbulent/non-turbulent interface and entrainment in a boundary layer. *Journal of Fluid Mechanics*, 742:1–33.

Chauhan, K., Philip, J., and Marusic, I. (2014b). Scaling of the turbulent/non-turbulent interface in boundary layers. *Journal of Fluid Mechanics*, 751:298–328.

Cheng, W. P. and Cantwell, B. J. (1996). Study of the velocity gradient tensor in turbulent flow. Technical report, University of Stanford.

Chertkov, M., Pumir, A., and Shraiman, B. I. (1999). Lagrangian tetrad dynamics and the phenomenology of turbulence. *Physics of Fluids*, 11(8):2394–2410.

Chong, M. S., Perry, A. E., and Cantwell, B. J. (1990). A general classification of three-dimensional flow fields. *Physics of Fluids A: Fluid Dynamics*, 2(5):765–777.

Chong, M. S., Soria, J., Perry, A. E., Chacin, J. M., Cantwell, B. J., and Na, Y. (1998). Turbulence structures of wall-bounded shear flows found using DNS data. *Journal of Fluid Mechanics*, 357:225–247.

Comte-Bellot, G. (1976). Hot-Wire Anemometry. *Annual Review of Fluid Mechanics*, 8(1):209–231.

Corrsin, S. and Kistler, A. L. (1954). Free-stream boundaries of turbulent flows. Technical report, NACA.

da Silva, C. B., Hunt, J. C. R., Eames, I., and Westerweel, J. (2014a). Interfacial Layers Between Regions of Different Turbulence Intensity. *Annual Review of Fluid Mechanics*, 46(1):567–590.

da Silva, C. B. and Pereira, J. C. F. (2008). Invariants of the velocity-gradient, rate-of-strain, and rate-of-rotation tensors across the turbulent/nonturbulent interface in jets. *Physics of Fluids*, 20(055101):1–18.

da Silva, C. B. and Pereira, J. C. F. (2009). Erratum: Invariants of the velocity-gradient, rate-of-strain, and rate-of-rotation tensors across the turbulent/nonturbulent interface in jets [Phys. Fluids 20, 055101 (2008)]. *Physics of Fluids*, 21(019902):1–2.

da Silva, C. B., Rodrigo, R. T., and Guillem, B. (2014b). Characteristics of the turbulent/nonturbulent interface in boundary layers, jets and shear-free turbulence. *Journal of Physics: Conference Series*, 506(012015):1–19.

da Silva, C. B. and Taveira, R. R. (2010). The thickness of the turbulent/nonturbulent interface is equal to the radius of the large vorticity structures near the edge of the shear layer. *Physics of Fluids*, 22(121702):1–4.

Dahm, W. J. A. and Dimotakis, P. E. (1987). Measurements of entrainment and mixing in turbulent jets. *AIAA Journal*, 25(9):1216–1223.

Dairay, T., Obligado, M., and Vassilicos, J. C. (2015). Non-equilibrium scaling laws in axisymmetric turbulent wakes. *Journal of Fluid Mechanics*, 781:166–195.

De Silva, C. M., Philip, J., and Marusic, I. (2013). Minimization of divergence error in volumetric velocity measurements and implications for turbulence statistics. *Experiments in Fluids*, 54(7):1–17.

Dimotakis, P. E. (2000). The mixing transition in turbulent flows. *Journal of Fluid Mechanics*, 409:69–98.

Discetti, S. and Astarita, T. (2012). Fast 3D PIV with direct sparse cross-correlations. *Experiments in Fluids*, 53:1437–1451.

Elsinga, G. E., Ishihara, T., Goudar, M. V., Da Silva, C. B., and Hunt, J. C. R. (2017). The scaling of straining motions in homogeneous isotropic turbulence. *Journal of Fluid Mechanics*, 829:31–64.

Elsinga, G. E. and Marusic, I. (2010). Universal aspects of small-scale motions in turbulence. *Journal of Fluid Mechanics*, 662:514–539.

Elsinga, G. E., Scarano, F., Wieneke, B., and van Oudheusden, B. W. (2006). Tomographic particle image velocimetry. *Experiments in Fluids*, 41(6):933–947.

Elsinga, G. E., Westerweel, J., Scarano, F., and Novara, M. (2011). On the velocity of ghost particles and the bias errors in Tomographic-PIV. *Experiments in Fluids*, 50:825–838.

Fiscaletti, D., Attili, A., Bisetti, F., and Elsinga, G. E. (2016a). Scale interactions in a mixing layer the role of the large-scale gradients. *Journal of Fluid Mechanics*, 791:154–173.

Fiscaletti, D., Elsinga, G. E., Attili, A., Bisetti, F., and Buxton, O. R. H. (2016b). Scale dependence of the alignment between strain rate and rotation in turbulent shear flow. *Physical Review Fluids*, 1(064405):1–14.

Friehe, C. A., Van Atta, C. W., and Gibson, C. H. (1972). Jet turbulence: dissipation rate measurements and correlations. In *Turbulence Shear Flows, AGARD Conference Proceedings*, volume 93, pages 1–7.

Ganapathisubramani, B., Lakshminarasimhan, K., and Clemens, N. T. (2007). Determination of complete velocity gradient tensor by using cinematographic stereoscopic PIV in a turbulent jet. *Experiments in Fluids*, 42:923–939.

Ganapathisubramani, B., Lakshminarasimhan, K., and Clemens, N. T. (2008). Investigation of three-dimensional structure of fine scales in a turbulent jet by using cinematographic stereoscopic particle image velocimetry. *Journal of Fluid Mechanics*, 598:141–175.

George, W. K. (1989). The Self-preservation of turbulent flows and its relation to initial conditions and coherent structures. In George, W. K. and Arndt, R., editors, *Advances in Turbulence*, pages 39–74. Hemisphere, New York.

George, W. K. and Hussein, H. J. (1991). Locally axisymmetric turbulence. *Journal of Fluid Mechanics*, 233:1–23.

Gibson, M. M. (1963). Spectra of turbulence in a round jet. *Journal of Fluid Mechanics*, 15:161–173.

Gomes-Fernandes, R., Ganapathisubramani, B., and Vassilicos, J. C. (2014). Evolution of the velocity-gradient tensor in a spatially developing turbulent flow. *Journal of Fluid Mechanics*, 756:252–292.

Goto, S. and Vassilicos, J. C. (2015). Energy dissipation and flux laws for unsteady turbulence. *Physics Letters, Section A: General, Atomic and Solid State Physics*, 379:1144–1148.

Goto, S. and Vassilicos, J. C. (2016). Local equilibrium hypothesis and Taylor's dissipation law. *Fluid Dynamics Research*, 48(021402):1–17.

Grinstein, F. F. (2001). Vortex dynamics and entrainment in rectangular free jets. *Journal of Fluid Mechanics*, 437:69–101.

Gutmark, E., Schadow, K. C., and Parr, T. (1989). Noncircular jets in combustion systems. *Experiments in Fluids*, 7:248–258.

Hamlington, P. E., Schumacher, J., and Dahm, W. J. A. (2008). Direct assessment of vorticity alignment with local and nonlocal strain rates in turbulent flows. *Physics of Fluids*, 20(111703):1–5.

Hearst, R. J. and Lavoie, P. (2014). Decay of turbulence generated by a square-fractal-element grid. *Journal of Fluid Mechanics*, 741:567–584.

Herman, G. T. and Lent, A. (1976). Iterative Reconstruction Algorithms. *Computer Biological Medision*, 6:273–294.

Ho, C. and Gutmark, E. (1987). Vortex induction and mass entrainment in a small-aspect-ratio elliptic jet. *Journal of Fluid Mechanics*, 179:383–405.

Holzner, M. and Lüthi, B. (2011). Laminar Superlayer at the Turbulence Boundary. *Physical Review Letters*, 106(134503):1–4.

Hunt, G. R. and Kaye, N. G. (2001). Virtual origin correction for lazy turbulent plumes. *Journal of Fluid Mechanics*, 435:377–396.

Hunt, J. C. R. (1994). Atmospheric Jets and Plumes. In Davies, P. A. and Valente Neves, M. J., editors, *Recent Research Advances in the Fluid Mechanics of Turbulent Jets and Plumes*, pages 309–334. Springer Netherlands, Dordrecht.

Hunt, J. C. R., Eames, I., and Westerweel, J. (2006). Mechanics of inhomogeneous turbulence and interfacial layers. *Journal of Fluid Mechanics*, 554:499–519.

Hussain, A. K. M. F. (1986). Coherent structures and turbulence. *Journal of Fluid Mechanics*, 173:303–356.

Hussain, F. and Husain, H. S. (1989). Elliptic jets. I - Characteristics of unexcited and excited jets. *Journal of Fluid Mechanics*, 208:257–320.

Hussein, H. J., Capp, S. P., and George, W. K. (1994). Velocity measurements in a high-Reynolds-number, momentum-conserving, axisymmetric, turbulent jet. *Journal of Fluid Mechanics*, 258:31–75.

Ishihara, T., Kaneda, Y., and Hunt, J. C. R. (2013). Thin Shear Layers in High Reynolds Number TurbulenceDNS Results. *Flow, Turbulence and Combustion*, 91:895–929.

Iyogun, C. O. and Birouk, M. (2009). Effect of sudden expansion on entrainment and spreading rates of a jet issuing from asymmetric nozzles. *Flow, Turbulence and Combustion*, 82:287–315.

Jiménez, J., Wray, A. A., Saffman, P. G., and Rogallo, R. S. (1993). The structure of intense vorticity in isotropic turbulence. *Journal of Fluid Mechanics*, 255:65–90.

Kaminski, E., Tait, S., and Carazzo, G. (2005). Turbulent entrainment in jets with arbitrary buoyancy. *Journal of Fluid Mechanics*, 526:361–376.

Kolmogorov, A. N. (1941). The local structure of turbulence in incompressible viscous fluid for very large Reynolds numbers. *Doklady Akademii Mak SSSR*, 31:538–541.

Kwon, Y. S., Hutchins, N., and Monty, J. P. (2016). On the use of the Reynolds decomposition in the intermittent region of turbulent boundary layers. *Journal of Fluid Mechanics*, 794:5–16.

Lindgren, B. and Johansson, A. V. (2002). Design and evaluation of a low-speed wind-tunnel with expanding corners. Technical report, Royal Institute of Technology, Stockholm (Sweden).

Maas, H. G., Gruen, A., and Papantoniou, D. (1993). Particle tracking velocimetry in three-dimensional flows. *Experiments in Fluids*, 15:133–146.

Mandelbrot, B. B. (1982). *The fractal geometry of nature*. W. H. Freeman and Company.

Mathew, J. and Basu, A. J. (2002). Some characteristics of entrainment at a cylindrical turbulence boundary. *Physics of Fluids*, 14(7):2065–2072.

Mazellier, N. and Vassilicos, J. C. (2010). Turbulence without RichardsonKolmogorov cascade. *Physics of Fluids*, 22(075101):1–25.

Melina, G., Bruce, P. J. K., and Vassilicos, J. C. (2016). Vortex shedding effects in grid-generated turbulence. *Physical Review Fluids*, 1(044402):1–27.

Mi, J., Kalt, P. A. M., Nathan, G. J., and Wong, C. Y. (2007). PIV measurements of a turbulent jet issuing from round sharp-edged plate. *Experiments in Fluids*, 42:625–637.

Mi, J. and Nathan, G. J. (2010). Statistical properties of turbulent free jets issuing from nine differently-shaped nozzles. *Flow, Turbulence and Combustion*, 84:583–606.

Mi, J., Nathan, G. J., and Nobes, D. S. (2001). Mixing Characteristics of Axisymmetric Free Jets From a Contoured Nozzle, an Orifice Plate and a Pipe. *Journal of Fluids Engineering*, 123:878–883.

Mi, J., Xu, M., and Zhou, T. (2013). Reynolds number influence on statistical behaviors of turbulence in a circular free jet. *Physics of Fluids*, 25(075101):1–30.

Michaelis, D., Novara, M., Scarano, F., and Wieneke, B. (2010). Comparison of volume reconstruction techniques at different particle densities. In *15th International Symposium on Applications of Laser Techniques to Fluid Mechanics*, pages 1–14, Lisbon, Portugal.

Mistry, D., Dawson, J. R., and Kerstein, A. R. (2018). The multi-scale geometry of the near field in an axisymmetric jet. *Journal of Fluid Mechanics*, 838:501–515.

Mistry, D., Philip, J., Dawson, J. R., and Marusic, I. (2016). Entrainment at multi-scales across the turbulent/non-turbulent interface in an axisymmetric jet. *Journal of Fluid Mechanics*, 802:690–725.

Mungal, M. G., Karasso, P. S., and Lonzano, A. (1991). The Visible Structure of Turbulent Jet Diffusion Flames: Large-Scale Organization and Flame Tip Oscillation. *Combustion Science and Technology*, 76:165–185.

Namer, I. and Ötügen, M. V. (1988). Velocity measurements in a plane turbulent air jet at moderate Reynolds numbers. *Experiments in Fluids*, 6:387–399.

Nedić, J., Ganapathisubramani, B., and Vassilicos, J. C. (2013a). Drag and near wake characteristics of flat plates normal to the flow with fractal edge geometries. *Fluid Dynamics Research*, 45(061406):1–16.

Nedić, J., Supponen, O., Ganapathisubramani, B., and Vassilicos, J. C. (2015). Geometrical influence on vortex shedding in turbulent axisymmetric wakes. *Physics of Fluids*, 27(035103):1–17.

Nedić, J., Vassilicos, J. C., and Ganapathisubramani, B. (2013b). Axisymmetric turbulent wakes with new nonequilibrium similarity scalings. *Physical Review Letters*, 111(144503):1–5.

Nicolaides, D., Honnery, D. R., and Soria, J. (2004). Autocorrelation Functions and the Determination of Integral Length with Reference to Experimental and Numerical Data. *15th Australasian Fluid Mechanics Conference*, 1(December):1–4.

Nomura, K. K. and Post, G. K. (1998). The structure and dynamics of vorticity and rate of strain in incompressible homogeneous turbulence. *Journal of Fluid Mechanics*, 377:65–97.

Novara, M., Batenburg, K. J., and Scarano, F. (2010). Motion tracking-enhanced MART for tomographic PIV. *Measurement Science and Technology*, 21(035401):1–18.

Obligado, M., Dairay, T., and Vassilicos, J. C. (2016). Nonequilibrium scalings of turbulent wakes. *Physical Review Fluids*, 1(044409):1–10.

Ohkitani, K. and Kishiba, S. (1995). Nonlocal nature of vortex stretching in an inviscid fluid. *Physics of Fluids*, 7(2):411–421.

Ooi, A., Martin, J., Soria, J., and Chong, M. S. (1999). A study of the evolution and characteristics of the invariants of the velocity-gradient tensor in isotropic turbulence. *Journal of Fluid Mechanics*, 381:141–174.

Phillips, O. M. (1955). The irrotational motion outside a free turbulent boundary. *Mathematical Proceedings of the Cambridge Philosophical Society*, 51(1):220–229.

Pope, S. B. (2000). *Turbulent Flows*. Cambridge University Press, Cambridge.

Quinn, W. R. (1992a). Streamwise evolution of a square jet cross section. *AIAA Journal*, 30(12):2852–2857.

Quinn, W. R. (1992b). Turbulent free jet flows issuing from sharp-edged rectangular slots: the influence of slot aspect ratio. *Experimental Thermal and Fluid Science*, 5:203–215.

Raffel, M., Willert, C. E., Wereley, S. T., and Kompenhans, J. (2007). *Particle Image Velocimetry: A Practical Guide*, volume 2nd.

Sadeghi, H., Lavoie, P., and Pollard, A. (2015). Equilibrium similarity solution of the turbulent transport equation along the centreline of a round jet. *Journal of Fluid Mechanics*, 772:740–755.

Shakouchi, T., Iriyama, S., Kawashima, Y., Tsujimoto, K., and Ando, T. (2014). Flow characteristics of submerged free jet flow from petal-shaped nozzle. *Journal of Fluid Science and Technology*, 9(3):1–7.

Silva, T. S., Zecchetto, M., and da Silva, C. B. (2018). The scaling of the turbulent/non-turbulent interface at high Reynolds numbers. *Journal of Fluid Mechanics*, 843:156–179.

Soria, J. (1996). An investigation of the near wake of a circular cylinder using a video-based digital cross-correlation particle image velocimetry technique. *Experimental Thermal and Fluid Science*, 12(2):221–233.

Soria, J., Sondergaard, R., Cantwell, B. J., Chong, M. S., and Perry, A. E. (1994). A study of the fine-scale motions of incompressible time-developing mixing layers. *Physics of Fluids*, 6(2):871–884.

Sreenivasan, K. R. and Meneveau, C. (1986). The fractal facets of turbulence. *Journal of Fluid Mechanics*, 173:357–386.

Sreenivasan, K. R., Ramshankar, R., and Meneveau, C. (1989). Mixing, entrainment and fractal dimensions of surfaces in turbulent flows. *Proceedings of the Royal Society A:*, 421:79–108.

Tanaka, T. and Eaton, J. K. (2007). A correction method for measuring turbulence kinetic energy dissipation rate by PIV. *Experiments in Fluids*, 42:893–902.

Taylor, G. I. (1938). The spectrum of turbulence. In *Proceedings of the Royal Society of London.*, pages 476–490. The Royal Society.

Tennekes, H. and Lumley, J. L. (1972). *A First Course in Turbulence*. M.I.T. Press, Cambridge, Massachusetts; London, 1st edition.

Thiesset, F., Antonia, R. A., and Djenidi, L. (2014). Consequences of self-preservation on the axis of a turbulent round jet. *Journal of Fluid Mechanics*, 748(R2):1–11.

Townsend, A. A. (1966). The mechanism of entrainment in free turbulent flows. *Journal of Fluid Mechanics*, 26:689–715.

Townsend, A. A. (1976). *The Structure of Turbulent Shear Flow.* Cambridge University Press, New York, 2nd edition.

Tsinober, A. (2009). *An Informal Conceptual Introduction to Turbulence.* Springer, 2 edition.

Tsinober, A., Kit, E., and Dracos, T. (1992). Experimental Investigation of the Field of Velocity-Gradients in Turbulent Flows. *Journal Of Fluid Mechanics*, 242:169–192.

Valente, P. C. and Vassilicos, J. C. (2012). Universal dissipation scaling for nonequilibrium turbulence. *Physical Review Letters*, 108(214503):1–5.

van Reeuwijk, M. and Craske, J. (2015). Energy-consistent entrainment relations for jets and plumes. *Journal of Fluid Mechanics*, 782:333–355.

Vassilicos, J. C. (2015). Dissipation in Turbulent Flows. *Annual Review of Fluid Mechanics*, 47:95–114.

Violato, D. and Scarano, F. (2011). Three-dimensional evolution of flow structures in transitional circular and chevron jets. *Physics of Fluids*, 23(124104):1–25.

Westerweel, J., Elsinga, G. E., and Adrian, R. J. (2013). Particle Image Velocimetry for Complex and Turbulent Flows. *Annual Review of Fluid Mechanics*, 45(1):409–436.

Westerweel, J., Fukushima, C., Pedersen, J. M., and Hunt, J. C. R. (2005). Mechanics of the Turbulent-Nonturbulent Interface of a Jet. *Physical Review Letters*, 95(174501):1–4.

Westerweel, J. and Scarano, F. (2005). Universal outlier detection for PIV data. *Experiments in Fluids*, 39:1096–1100.

Wieneke, B. (2008). Volume self-calibration for 3D particle image velocimetry. *Experiments in Fluids*, 45:549–556.

Wilczek, M. and Meneveau, C. (2014). Pressure Hessian and viscous contributions to velocity gradient statistics based on Gaussian random fields. *Journal of Fluid Mechanics*, 756:191–225.

Wolf, M., Holzner, M., Lüthi, B., Krug, D., Kinzelbach, W., and Tsinober, A. (2013). Effects of mean shear on the local turbulent entrainment process. *Journal of Fluid Mechanics*, 731:95–116.

Worth, N. a., Nickels, T. B., and Swaminathan, N. (2010). A tomographic PIV resolution study based on homogeneous isotropic turbulence DNS data. *Experiments in Fluids*, 49:637–656.

Wygnanski, I., Champagne, F. H., and Marasli, B. (1986). On the large-scale structures in two-dimensional, small-deficit, turbulent wakes. *Journal of Fluid Mechanics*, 168:31–71.

Xu, M., Pollard, A., Mi, J., Secretain, F., and Sadeghi, H. (2013). Effects of Reynolds number on some properties of a turbulent jet from a long square pipe. *Physics of Fluids*, 25(035102):1–19.

Yule, A. J. (1978). Large-scale structure in the mixing layer of a round jet. *Journal of Fluid Mechanics*, 89(03):413–432.

Zaman, K. B. M. Q. (1996). Axis switching and spreading of an asymmetric jet: the role of coherent structure dynamics. *Journal of Fluid Mechanics*, 316:1–27.

Zhou, J., Adrian, R. J., Balachandar, S., and Kendall, T. M. (1999). Mechanisms for generating coherent packets of hairpin vortices in channel flow. *Journal of Fluid Mechanics*, 387:353–396.

Zhou, Y. and Vassilicos, J. C. (2017). Related self-similar statistics of the turbulent/non-turbulent interface and the turbulence dissipation. *Journal of Fluid Mechanics*, 821:440–457.